# Manipulation of Colloidal Crystallization

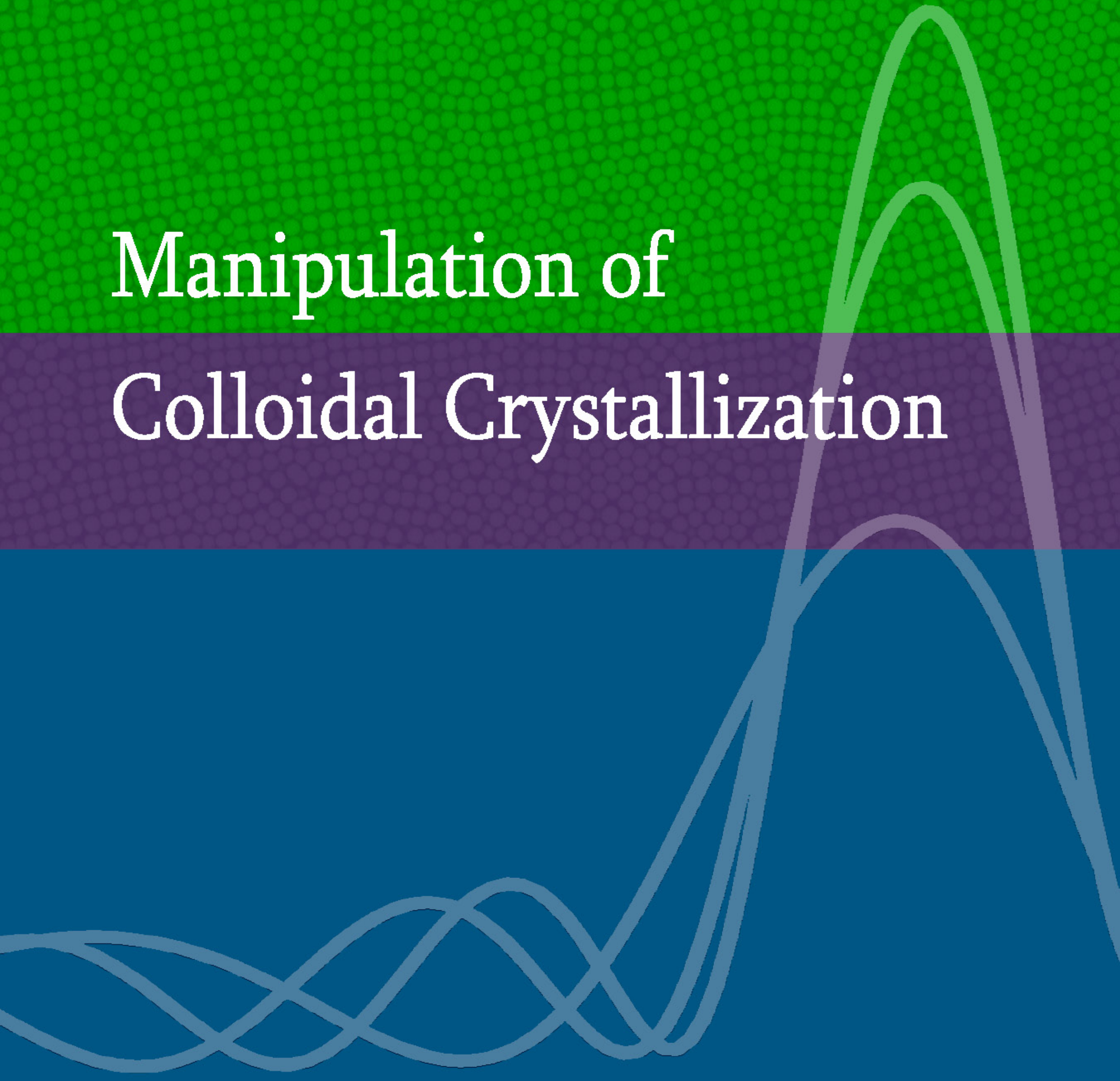

Esther Vermolen

# Manipulation of colloidal crystallization

**Cover:** front - SEM image of a colloidal crystal created by spin coating
back - Colloidal crystal nucleus grown around a 2D seed structure
bookmarker - SEM image of a dried binary colloidal crystal with NaCl structure
lay-out by Sander Vermolen & the author

PhD thesis, Utrecht University, the Netherlands, November 2008.
ISBN: 978-90-393-4915-1
A digital version of this thesis is available at http://www.colloid.nl

# Manipulation of colloidal crystallization

---

## Beïnvloeding van colloïdale kristallisatie

(met een samenvatting in het Nederlands)

## Proefschrift

ter verkrijging van de graad van doctor aan de Universiteit Utrecht op gezag van de rector magnificus, prof. dr. J.C. Stoof, ingevolge het besluit van het college voor promoties in het openbaar te verdedigen op maandag 24 november 2008 des middags te 2.30 uur

door

Esther Christianne Maria Vermolen

geboren op 14 april 1982 te Arnhem.

**Promotor** Prof. Dr. A. van Blaaderen

The work described in this thesis was performed in the Soft Condensed Matter group in the Debye Institute for NanoMaterials Science at the Utrecht University. This research was supported by NanoNed, a national nanotechnology program coordinated by the Dutch Ministry of Economic Affairs, flagship NanoPhotonics, project 7149.

*La maladie principale de l'homme est la curiosité inquiète*
*des choses qu'il ne peut savoir*

Blaise Pascal (1623-1662)

*Pensées* (1670)

◆

# Contents

# 1

# Introduction to colloidal crystals

In this thesis the results are shown of a study of colloidal crystallization and of the development of techniques for manipulating colloidal crystallization. Colloidal crystallization is not only studied as a model system for molecular condensed matter systems, but also because of the interesting (photonic) applications of colloidal crystals. In this chapter we will give an introduction to colloids, colloidal crystals and their applications. At the end of this chapter, an outline is given of the experimental work which is described in this thesis.

## 1.1 Colloids

The word “colloid” originates from the Greek word $\kappa o\lambda\lambda\alpha$, which means ‘glue’ and was first used by Thomas Graham in 1861 for glue-like substances (arabic gum, gelatine) that could be separated from water by letting the mixture diffuse through a membrane [1]. Nowadays, the term “colloidal” refers to a wide range of systems consisting of a continuous medium and a dispersed phase of which the dispersed particles (colloids) are in a loosely-defined size range, typically between 1 nm and 1 $\mu$m. The lower limit of the size range is primarily set by the requirement that the dispersion medium can be treated as a homogeneous background which causes an effective interaction between the dispersed colloids. When the particles become relatively too small, each medium molecule should be treated individually to correctly predict the behavior. The upper limit of the size range is set by the fact that colloids experience Brownian motion, which enables them to redistribute kinetic energy. Brownian motion was first observed by Robert Brown, who studied plant pollen in water. The theoretical explanation for the observed motion, based on the collision of solvent molecules with the particles, was given by Albert Einstein [2], in combination with the experimental verification by Jean Baptiste Perrin. Colloids up to a few micrometer do still experience Brownian motion, while larger objects move according to the laws of mechanics alone and are classified as granular matter.

Colloids and the medium in which they are suspended can be in the gas, liquid or solid phase. Depending on the thermodynamic phase of the colloids and the medium, the colloidal system is named foam (gas in liquid), aerosol (solid/liquid in gas), emulsion (liquid in liquid) or suspension (solid in liquid). In everyday life, colloidal systems are ubiquitous, although they are usually not recognized as separate phases. Examples of colloidal systems are: smoke, fog, paint, milk, mayonnaise and clay. The experimental and theoretical study of colloidal dispersions gives a better understanding of the flow behavior (rheology) and phase behavior of these omnipresent systems.

Colloidal systems are furthermore studied as a model system for atomic and molecular phase behavior [3]. Due to Brownian motion, colloids sample the thermodynamic phase space in a similar way as atoms and molecules [4]. Hard-sphere colloids (which only interact when they mutually touch) can exhibit a fluid phase and a solid phase, only depending on the volume fraction. When compressed fast enough, a hard-sphere dispersion can even form a glassy state [5]. In systems interacting via a hard-sphere potential, the crystallization is driven by entropy alone, since there is no energetic contribution to the free-energy.

The advantage of studying colloidal model systems instead of the "real" atomic systems lies in the fact that colloids can be visualized in real-space with, for example, confocal microscopy. Furthermore, the motion of the colloids is over-damped in the solvent, giving an experimentally accessible time-scale, enabling tracking of individual colloidal trajectories.

Colloidal systems are very versatile model systems, since the interaction potential can be tuned by physical and chemical modification of the particle or solvent. The interaction between colloids can in most cases be described by the so-called Derjaguin-Landau-Verweij-Overbeek (DLVO) potential, which sums the Van der Waals interaction and the electrostatic interaction of the surface charges and the solvent (counter)ions in the double layers. Refractive index matching the solvent with the particles can minimize the Van der Waals interaction. The electrostatic repulsion can be tuned by changing the pH of the solvent (thereby changing the surface charge) or by changing the amount of ions in the solvent, which can screen the surface charge. In this way, the interaction potential can be changed from long-range repulsive to short-range attractive [6]. Sterically stabilized particles, with polymer chains on the surface, have a short-range repulsive interaction, which gives a hard-sphere like interaction. This system can be changed from long-range repulsive at low ion concentration to a hard-sphere potential at high salt concentration [7]. Recently, also a plus-minus interaction was found between two types of PMMA particles and between silica and PMMA particles in a binary dispersion [8]. External fields can also change the interactions between the colloids. For example, an external electric field can induce dipolar interactions between the colloids [9].

All these different interactions influence the phase behavior of the colloids, giving rise to other crystal phases than the normal random hexagonal close packed crystal, that hard-sphere colloids form [10–12]. Besides by influencing colloid-colloid interactions, control over the crystal structure that is formed can also be gained by external fields, such as sedimentation in a gravitational field, spin coating, compression by dielectrophoretic forces and crystallization on a structured surface (epitaxial growth). All these techniques for controlling colloidal crystallization will be discussed in Chapter 2.

The interest in controlling colloidal crystallization originates first of all from their use as atomic model system: control over colloidal crystallization allows us to study, for example, nucleation and epitaxial growth, which both play an important role in many molecular crystallization processes. Secondly, some colloidal crystal structures can have fundamentally and practically interesting photonic properties, because of their fundamental length scale which is on the order of the wavelength of visible light, as will be explained in the next section. Binary colloidal crystals open in this respect a whole new range of possibilities, as will be discussed in Section 1.3.

## 1.2 Photonic crystals

Photonic crystals are structures with a periodically varying refractive index, with a spatial period on the order of the wavelength of light [13, 14]. Because of this wavelength-matching periodicity, light can interact strongly with the varying potential landscape in the structure by constructive and destructive interference of light which in the limit of single scattering is referred to as Bragg reflection. Similar structures, optimized for interference effects, can be found in nature. They cause the beautiful iridescence of, for example, butterfly wings (of which the scales are multilayered arrays) [15] and natural opals (which consist of self assembled colloidal crystals). In science, photonic crystals are well known for the possible occurrence of a photonic band gap, similar to an electronic band gap in semiconductors. This band of frequencies that cannot propagate in the structure, can lead to inhibition of spontaneous emission and localization of light in a cavity. The applications of photonic crystals range from low and high reflection coatings and omni-directional mirrors to low-loss waveguiding and integrated photonic circuits.

In the seventies, two papers by Bykov [16] and Ohtaka [17], that almost got no attention, already discussed the principle of light emission in structures with a strong modulation of the dielectric function, their electromagnetic eigenmodes, the photonic band structure and the possibility of the realization of a band gap. But only after the publications by Yablonovitch on the inhibition of spontaneous emission [18] and by John on localization of electromagnetic waves [19], the concepts received the scientific attention they deserved.

Because the fabrication of photonic crystals (especially for the visible spectrum) lags far behind the theoretical background, photonic band structure calculations are used for finding structures with a large photonic band gap. High dielectric contrast, high connectivity within one phase and a near-circular Brillouin zone appear to be important factors. No band gap was found for a direct face centered cubic (fcc) structure [20, 21], due to a degeneracy at the W-point. This degeneracy could be lifted by using aspherical particles. It was predicted that the diamond structure has a complete photonic band gap by Ho et al. [22]. Following this finding, Yablonovitch et al. created a structure with diamond symmetry by drilling three sets of holes under angles of 35.26° in a solid wafer [23]. Their structure had a photonic band gap between 10 and 13 GHz. Other experimentally realizable structures with diamond symmetry were proposed [24, 25], but no band gap structure for the visible spectrum of light has been created up till now.

### 1.2.1 Photonic band structure

A free travelling light wave has a linear dispersion relation $\omega = ck$, where $\omega$ is the frequency, the slope $c$ is the speed of light and $k = 2\pi/\lambda$ is the wavevector, with $\lambda$

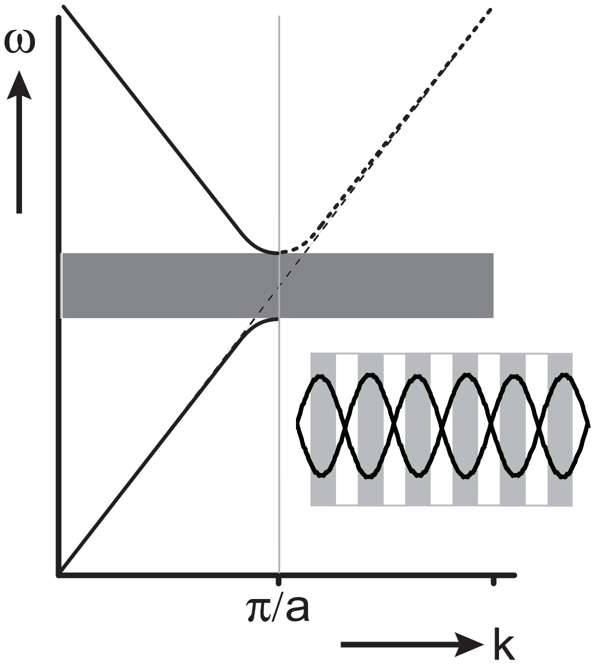

**Figure 1.1:** Construction of the photonic band structure diagram of a 1D photonic crystal (inset). Due to standing waves at $k = \pi/a$, the dispersion relation is bent away from the dispersion relation of a free travelling wave (straight dashed line). The resulting band gap (gray band) represents the frequencies that cannot propagate in the photonic crystal. Due to Bloch's theorem, the bands outside the first Brillouin zone (above $k = \pi/a$) can be folded back into the first Brillouin zone. The final dispersion relation of light in the 1D photonic crystal is given by the thick solid line.

representing the wavelength. When this light wave hits a structure with a periodically varying refractive index in one dimension (a 1D photonic crystal), it can form a standing wave, with a group velocity of zero. There can be two non-degenerate standing waves: one with the nodes in the high refractive index regions and one with the nodes in the low refractive index regions. The dispersion relation of light in this structure splits up at the $k = \pi/a$ point into two frequencies, where the slope of the dispersion relation goes to zero (because of the zero group velocity of the standing wave), as is shown in Figure 1.1. In between these two points, there is a band of frequencies that cannot exist in this periodic structure, also referred to as a photonic band gap. The higher the refractive index contrast, the wider the photonic band gap, since the energy difference between the two standing waves becomes larger. The position (in frequency) of the photonic band gap is determined by the average refractive index of the structure.

Because of the distribution of the power over the different refractive index regions, the band above the band gap is usually referred to as the “air band”, while the band below the band gap is called the “dielectric band” (analogous to the conduction and valence bands in semiconductors).

Since the refractive index function $\epsilon(r)$ is periodic, Bloch's theorem tells us that the waves can be completely characterized by their behavior in the first Brillouin zone, the primitive cell of the reciprocal lattice. Therefore, the band structure of the 1D photonic crystal discussed above can be folded back to the region between $k = 0$ and $k = \pi/a$, yielding the band structure diagram for a 1D photonic crystal (Figure 1.1). Introducing a defect into the photonic crystal (for example replacing one of the low refractive index slabs of the 1D photonic crystal with the high refractive index material) can give a defect mode in de forbidden photonic band gap. Light of the frequency of this mode then can exist in the defect, but not in the structure around it, so the defect forms a cavity for this light.

Similar to this simple 1D example discussed above, we can construct photonic band structure diagrams for materials with a refractive index varying in two or three dimensions (2D or 3D photonic crystals). The band structure diagram for 2D and 3D structures is constructed for the lines between the critical points, the points of high symmetry in the Brillouin zone. In general (except for some rare cases [26]), all the maxima and minima of the dispersion bands are on the lines between the critical points, so we do not have to probe the full 2D/3D space of the reduced Brillouin zone.

### 1.2.2 The photonic “master equation”

To study the dispersion relations of more complicated structures than the 1D photonic crystal discussed above, we must start with the Maxwell equations

$$\begin{aligned} \nabla \cdot \mathbf{B} &= 0 \qquad & \nabla \times \mathbf{E} + \tfrac{1}{c}\tfrac{\partial \mathbf{B}}{\partial t} &= 0 \\ \nabla \cdot \mathbf{D} &= 4\pi\rho \qquad & \nabla \times \mathbf{H} - \tfrac{1}{c}\tfrac{\partial \mathbf{D}}{\partial t} &= \tfrac{4\pi}{c}\mathbf{J} \end{aligned} \tag{1.1}$$

where **E** and **H** are the macroscopic electric and magnetic field, **D** and **B** are the displacement field and the magnetic induction field and $\rho$ and **J** are the free charge and current densities.

From the Maxwell equations a Hermitian eigenvalue problem can be derived for homogeneous dielectric media [13]. In the derivation it is assumed that there are no free charges, $\rho = 0$, and no free currents, $J = 0$ (which holds for all dielectric media, but breaks down for metallic materials). To relate **D** to **E** and **B** to **H**, the following assumptions are made:

- the electric field strengths are small enough that **D** is linearly related to **E**
- the material is isotropic, such that **D** and **E** are related via a scalar dielectric constant $\epsilon(r, \omega)$
- the frequency dependence of $\epsilon(r)$ can be ignored
- for low-loss dielectrics, only the real part of $\epsilon(r)$ is considered
- for the dielectric materials considered, the magnetic permeability is close to unity.

These assumptions lead to the relations: $\mathbf{D} = \epsilon(r)\mathbf{E}$ and $\mathbf{B} = \mathbf{H}$. The time dependence can be separated out by expanding the fields into a set of harmonics, which together reduce the Maxwell equations to

$$\begin{array}{rclcrcl} \nabla \cdot \mathbf{H}(\mathbf{r}) & = & 0 & \quad & \nabla \times \mathbf{E}(\mathbf{r}) + \frac{i\omega}{c}\mathbf{H}(\mathbf{r}) & = & 0 \\ \nabla \cdot \mathbf{D}(\mathbf{r}) & = & 0 & \quad & \nabla \times \mathbf{H}(\mathbf{r}) - \frac{i\omega}{c}\epsilon(\mathbf{r})\mathbf{E}(\mathbf{r}) & = & 0 \end{array} \tag{1.2}$$

The first two divergence equations impose that there are no point sources of displacement and magnetic fields and furthermore, that the waves are transverse. The last two curl equations can be combined to the so called ‘master equation’:

$$\nabla \times \left(\frac{1}{\epsilon(\mathbf{r})}\nabla \times \mathbf{H}(\mathbf{r})\right) = \left(\frac{\omega}{c}\right)^2 \mathbf{H}(\mathbf{r}) \tag{1.3}$$

By identifying the left side of the equation as an operator $\Theta$, the master equation can be rewritten in a form which is more recognizable as an eigenvalue problem, where applying the operator $\Theta$ to $\mathbf{H}$ gives a scalar times $\mathbf{H}$:

$$\begin{array}{rcl} \Theta\mathbf{H}(\mathbf{r}) & = & \left(\frac{\omega}{c}\right)^2 \mathbf{H}(\mathbf{r}) \\ \text{where } \Theta\mathbf{H}(\mathbf{r}) & = & \nabla \times \left(\frac{1}{\epsilon(\mathbf{r})}\nabla \times \mathbf{H}(\mathbf{r})\right) \end{array} \tag{1.4}$$

The master equation is written in terms of $\mathbf{H}$ instead of $\mathbf{E}$ to have a Hermitian operator. The master equation can be solved in a similar way as the Schrödinger equation in quantum mechanics, with an additional difficulty that the different directions in the master equation are never separable.

A nice feature of the electromagnetic master equation for photonic crystals is the fact that the solutions are scalable. If we scale the length scale of a structure by a constant factor, we can multiply the frequencies in the dispersion relation by the same factor to retain the same solutions of the equations. Therefore, the frequencies are often expressed in terms of $c/a$, the speed of light divided by a lattice parameter of the structure. In this way the dispersion relation is applicable for any structure with the considered size ratios, symmetry and dielectric contrast.

### 1.2.3 Band structure calculations

For this thesis, band structure diagrams were calculated using two different methods, such that the results could be compared. The first method is based on truncated plane wave decomposition, which was implemented in an MIT Photonic Bands software package [27]. MPB computes fully-vectorial eigenmodes of Maxwell’s equations with periodic boundary conditions by preconditioned conjugate-gradient minimization of the block Rayleigh quotient in a plane wave basis [28].

The other calculations were done using the Korringa-Kohn-Rostoker (KKR) method. Since this method uses an expansion in spherical waves, it is optimized for lattices of spheres. The KKR method was implemented in a Fortran program by Stefanou et al. [29] and Alexander Moroz [30].

## 1.3 Binary colloidal crystals

Binary colloidal crystals, consisting of two types of colloidal spheres (of different sizes and/or different materials) have opened a new field of research. Different characteristics can be build into the crystal, which have great potential for applications. Selective removal of one of the types of colloids yields a very open crystal structure, which is advantageous for photonic structures. Furthermore, the growth mechanism of the binary colloidal crystals can shed light on the growth mechanism of atomic and molecular binary crystals such as salts.

The first binary colloidal crystal was identified by Sanders and Murray in 1978 [31]. They studied a Brazilian gem opal by electron microscopy and found a band in which large (L) and small (S) particles with size ratio $\gamma = \sigma_S/\sigma_L = 0.58$ were mixed. In some parts the mixture consisted of binary superstructures with long range order. The binary structures in the opal had an $LS_2$ and $LS_{13}$ stoichiometry [32]. Based on packing efficiency they predicted that only NaCl, with stoichiometry LS, and the $LS_2$ structure $AlB_2$ can be stable, depending on the size ratio $\gamma$ [33].

Since the discovery of the binary opal, several binary colloidal systems have been found to crystallize in superstructures, where the structure depends on the size ratio of the particles, the number ratio, the total concentration of particles and the interactions between the particles in the system. The first binary colloidal crystal found under laboratory conditions, was made in an electrostatically repelling system of latex spheres in water by Hachisu and Yoshimura [34]. In charge stabilized systems, crystals were found with stoichiometry $LS_2$, resembling the atomic analogues $AlB_2$ [34, 35], or the intermetallic compound $MgCu_2$ for $\gamma = 0.62 - 0.7$ [35]. Other stoichiometries were $LS_{13}$, similar to $NaZn_{13}$ [34, 35] and $LS_5$ (with atomic analogue $CaCu_5$) for size ratios 0.56 and 0.66 [35]. For the $LS_4$ stoichiometry found at $\gamma = 0.48$ no atomic analogue is known [36]. Recently, the spontaneous crystallization of the binary Laves phase $MgZn_2$ was found in a glass-forming binary Lennard-Jones liquid with a size ratio of $\gamma = 0.82$ [37].

The formation of binary crystals in hard-sphere systems (where the particles only interact when they are touching) has been studied extensively by computer simulations [38–41]. In a system consisting of sterically stabilized poly(methyl methacrylate) (PMMA) spheres, Bartlett et al. studied the behavior of binary hard-sphere mixtures experimentally with different size and number ratios. They found the same structures as found in the Brazilian opal for the size ratio $\gamma = 0.58$ [42]. For size ratio $\gamma = 0.62$ [43], they found an $LS_{13}$ structure under certain conditions. A size ratio of $\gamma = 0.31$ did not give any binary crystal structures, since the dispersion almost completely size segregated [44, 45]. The size ratio of $\gamma = 0.52$ was studied by Hunt et al., giving the same structures as found for $\gamma = 0.58$ [46]. They also found a new binary colloidal crystal structure with stoichiometry LS for $\gamma = 0.39$, analogous to either NaCl or NiAs. Another LS structure consisting of hard spheres, CsCl, was found for $\gamma = 0.736$ [47]. However, these crystal structures disappeared over time, indicating that they were metastable.

In mixtures of attracting particles consisting of poly(4-vinylpyridine) and polystyrene microgels, NaCl and $MgCu_2$ structures were identified by Ma et al. [48] for size ratios of 0.43 and 0.73, respectively. The CsCl structure, found in a hard-sphere system with particles of similar size but differing polymer concentration by Underwood et al. [49], is also attributed to cross-attractions between the particles. Stronger attraction, as found between oppositely charged PMMA colloids, yields a whole new range of tunability of the crystal structures, containing NaCl and CsCl for size ratio 1 and $CaF_2$, $ReO_3$, $LS_4$, $LS_6$ and $LS_8$ for size ratio 0.31 [8, 50].

When the size ratio becomes too small, no crystal structures are found in binary dispersions. The depletion interaction (or excluded volume interaction) causes the dispersion to phase separate into a close-packed crystal of the large spheres and a fluid of small spheres. This behavior has been observed in experiments [44, 45, 51, 52], simulations [53] and theory [54, 55]. When the size ratio goes to 1, a disordered solid solution becomes the most stable phase at high concentrations [56–59].

In all the cases mentioned above, the crystals were obtained by letting a dispersion equilibrate. In most cases homogeneous nucleation leads to small crystal domains in a random direction. By directing the structure, for example by letting it crystallize on a templated wall (epitaxial growth), the size of the crystal domains can be increased by fixing the orientation. In this thesis we show two approaches to growing hard-sphere binary crystal structures on a directing template, namely NaCl (Chapter 3) and $MgCu_2$ (Chapter 4). Both structures are interesting for photonic applications, since their structure (or sub-structure) can have a photonic band gap.

## 1.4 Scope of this thesis

In this thesis we aim at controlling colloidal crystallization, with a focus on making 3D photonic crystals with a band gap in the visible range of the light spectrum. In Chapter 2, we first describe the different techniques which we used to influence colloidal crystallization: sedimentation, epitaxial growth on several different template structures, dielectrophoretic compression and spin coating.

In Chapter 3 and Chapter 4, we focus on two types of binary colloidal crystals, NaCl and $MgCu_2$, which both are equivalents of an atomic crystal, but are mostly interesting for their photonic properties. The photonic properties of the $MgCu_2$ structure and its single-component constituents are studied in Chapter 5. Not only dielectric structures are discussed here, but also band structures for metallo-dielectric colloidal structures, with a metal shell or metal core were calculated.

In Chapter 6, the results are shown of a nucleation study of colloidal systems. Nucleation in a colloidal dispersion was induced by small optically trapped 2D seed structures of different symmetries.

In Chapters 7 and 8, two different methods for making single-component colloidal crystals are studied: compression by dielectrophoretic forces on a templated surface and spin coating (with and without a templated surface) and their applicability for making photonic crystals is discussed. In the last chapter we concentrate on the mechanism which causes the control over the crystal orientation by spin coating.

# 2

# Control over colloidal crystallization via external fields

In this chapter, several external fields are treated with which colloidal crystallization can be manipulated. First, simple sedimentation is discussed. Crystallization by sedimentation can be extended by applying a structure on the bottom of the sample wall. Several ways of making a structured surface are dealt with. Furthermore, a template can be held in the bulk of a sample by optical tweezers. The principle behind trapping with optical tweezers and the used setup are explained. Then the theory behind the technique of dielectrophoretic compression, used in several chapters in this thesis, is described. In the last part of this chapter, another assembly method to produce colloidal crystals is discussed: spin coating colloidal dispersions.

## 2.1 Introduction

The volume fraction of colloids in a dispersion is an important parameter which can influence the thermodynamical state of the dispersion. For hard-sphere systems, in which the colloids only interact via an excluded volume term, this is even the only determining thermodynamic variable [5]. In the process of growing colloidal crystals, the volume fraction is therefore an important parameter to control, preferably in situ. Three known methods to control the volume fraction of colloids in a dispersion are gravity, temperature gradients and dielectrophoretic forces.

In a temperature gradient [60], the osmotic pressure on one side of the sample becomes higher. Therefore, the colloids move to the other side of the sample to equilibrate the pressure. The response to the temperature gradient depends on diffusion and thus, is slow. Furthermore, temperature gradients are limited by the melting and boiling points of the dispersing solvents. In the work described in this thesis we therefore decided to use gravity and dielectrophoresis as main external fields to control the volume fraction of the dispersions.

In gravity, the colloids are distributed inhomogeneously over the sample until the gravitational force is balanced by the osmotic pressure. This process is usually slow and non-switchable, which makes control over the volume fraction limited. The influence of the gravitational force on a colloidal dispersion is discussed in Section 2.2.

Sedimentation of colloids on a flat wall normally yields face centered cubic (fcc) or random hexagonally close packed (rhcp) crystals, with the hexagonal layers parallel to the wall. To gain more control over crystal structure and orientation, the wall of a sample container can be structured with a hole array or a colloidal template. Also, a seed-template can be made in the bulk of the sample to induce and study crystal nucleation. The fabrication of structured walls and seed-templates is explained in Section 2.3. The optical tweezers setup, used for the creation of the seed-templates, is discussed in Section 2.4.

Dielectrophoretic compression, discussed in Section 2.5, enables a direct control and large range of attainable volume fractions in a single sample, which are prerequisites for the study of nucleation near a template as described in Chapter 6. For the fabrication of large single-domain colloidal crystals dielectrophoresis has also proven to be a useful technique, as will be discussed in Chapters 3 and 7.

A final technique, used in this thesis to influence crystal growth, is spin coating. This technique, at first developed to make thin polymer films, is fast and is already used industrially in the production of integrated circuits, an important advantage for applications. On the other hand, the speed of the process is a drawback when one wants to study the underlying mechanism. The theoretical background of spin coating, but also the gaps in our knowledge, are discussed in the final section of this chapter.

## 2.2 Sedimentation in a gravitational field

The local volume fraction of a colloidal dispersion is influenced by the earth gravitational field when the density of the colloids is different from the density of the solvent. When the density of the colloids is higher than the density of the medium, the colloids sink, while otherwise they float. In both cases the term ‘sedimentation’ is used and for the upwards movement also the terms ‘flotation’ and ‘creaming’ are found in literature. By density matching the colloids with the dispersion solvent, using a mixture of two (or more) fluids, the effects of the gravitational field can be minimized.

The sedimentation speed $v_0$ for colloids with radius $R$ and density $\rho_p$ in a medium with viscosity $\eta$ and density $\rho_m$ can be derived by equating the gravitational force ($mg = 4/3\pi R^3\rho_p g$) with the sum of the friction force ($6\pi\eta R v$) and the buoyant force by Archimedes' principle ($4/3\pi R^3\rho_m g$). The result is

$$v_0 = \frac{2}{9}R^2(\Delta\rho)\frac{g}{\eta} \tag{2.1}$$

with $\Delta\rho$ the buoyant density of the particle, which shows that small particles sediment significantly slower than large particles. The influence of the gravitational field on colloidal crystallization as compared to diffusion is given by the ratio between the gravitational energy and the thermal energy, which is expressed in the Péclet number:

$$Pe = \frac{2Rv_0}{D_0} \tag{2.2}$$

where $D_0$ is the diffusion coefficient, given by $D_0 = kT/6\pi\eta R$. At a lower Péclet number, the colloids have more time to diffuse around and therefore, crystals with fewer defects form. To facilitate the growth of high quality colloidal crystals at higher Péclet numbers, the sedimentation can be slowed down by balancing it with an electric field [61] or the time to diffuse can be increased by lowering the initial volume fraction of particles [62, 63]. The Péclet number is independent of the viscosity of the dispersion, therefore, using a more viscous dispersion slows down the whole crystallization process, but the crystal quality does not increase.

The difference in sedimentation speed of small and large particles or of particles with different densities can be used advantageously for separating two species in a dispersion. The sedimentation speeds can then be increased by replacing the earth gravitational force with a much larger centrifugal force in a centrifuge. The difference in sedimentation speeds is however disadvantageous for experiments with binary systems.

When hard-sphere colloids sediment on a flat wall, the first layer will form a close-packed hexagonal layer. The next hexagonal layers can lie on three different positions above the first. When the stacking can be labelled ABAB, the structure is called hexagonal close-packed (hcp), while an ABCABC structure is called face centered cubic (fcc). The free energy difference between these structures only on the order of $10^{-4}$ $\mathrm{k_bT}$ per sphere at the volume fraction of melting [64–66], therefore sedimented colloidal crystals usually have a random hexagonal close-packed (rhcp) structure [63]. The presence of the wall influences the nucleation process: it leads to layering of the liquid [67] and eventually to prefreezing and wetting of the surface [68, 69]. Experimentally, close to the wall, more hcp stacking was found [62].

## 2.3 Templates for epitaxial growth of colloidal crystals

Using a templated surface on the bottom of a sedimentation sample container, the sedimented colloidal crystal can be dictated to have certain a crystal orientation and crystal structure, which can even be metastable [70–75]. Growing crystals on another crystal is called epitaxial growth if the structure of the template crystal is followed. Precrystallization on a substrate patterned with a fixed array of spheres has been studied by computer simulations by Heni and Löwen [76, 77]. They found that a fluid near a patterned wall crystallizes well below the bulk freezing point. When the pattern is distorted from the ideal pattern, a finite number of crystalline layers crystallizes, while at ideal triangular and hcp (110) patterns complete wetting was found. Also finite structured templates can induce epitaxial crystal growth, as studied by Cacciuto and Frenkel [78]. The template structures used in the experiments in this thesis are described in the sections below.

### 2.3.1 Writing templates by electron beam lithography

The basic idea behind electron beam lithography is to coat a substrate with a resist, chemically change the resist on the places where the resist is exposed to the electron beam and then selectively remove the exposed or non-exposed areas of the resist. When the non-exposed areas are removed in the development stage, the resist is called a ‘negative resist’, while a resist where exposed areas are removed is called a ‘positive resist’.

For making hole arrays for epitaxial colloidal growth, we used the positive resist poly(methyl methacrylate) (PMMA). Round no. 1 glass cover slides (Menzel) with a diameter of 22 mm, which were coated with a transparent conducting layer of indium tin oxide (ITO) by Thin Film Devices (Anaheim, US) were used for writing templates with e-beam lithography. The glass slides were cleaned by sonicating in isopropanol for 1 minute and by subsequent rinsing with clean isopropanol.

A PMMA layer was spin coated on the glass slides on a Delta 10 (BLE Laboratory Equipment) spin coater. Two solutions and accompanying spin speeds were used:

- a 4% w/w solution of 950k PMMA in chlorobenzene was spin coated at 700 rpm for 5 seconds and then at 1300 rpm for 40 seconds,
- an 8% w/w solution of 950k PMMA in anisole was spin coated at 5000 rpm for 60 seconds.

The PMMA coated glass slides were baked on a hot plate at 175 °C for at least 45 minutes. The thickness of the resulting layer of PMMA was determined by measuring the profile of an intentional scratch with a surface profiler (KLA Tencor Alphastep 500). Both solutions yielded a PMMA layer of about 700 nm for the mentioned spin speeds.

The patterns were written using an electron beam lithography system JEOL JSM-6460 with a Raith Elphy-Plus Pattern generator, in which the coordinates of an array of dots could be read from a GDSII-file. Every hole was written by single exposure. After electron beam writing, the pattern was developed by immersing the substrate in a 1:3 volume mixture of methyl isobutyl ketone (MIBK) and isopropanol for 90 seconds and then rinsed with pure isopropanol to stop the development.

### Prevent sticking by PHS coating

We observed that colloids (both PMMA and silica) tend to stick to the area of the hole arrays of templates, while they did not stick to the unwritten areas. This was verified by making *xyt*-scans of edges of templates, such that half of the image was filled with the template. From these *xyt*-scans could be concluded that the movement on the template was clearly much slower than elsewhere. This sticking could be partly prevented by adsorption of poly(hydroxy stearic acid) (PHS)-PMMA comb-graft stabilizer on the templates. This stabilizer is also used to stabilize PMMA particles after the synthesis. The stabilizer was normally stored in a mixture of ethyl acetate and butyl acetate, but since this appeared to dissolve the untreated PMMA hole array area, we transferred it to dodecane. The PMMA template was coated by keeping the slide in the solution for about 2 minutes and rinsing with dodecane afterwards. This clearly reduced the sticking of colloids to the templated area.

### Prevent dissolution by post-baking

During the writing step, not only the PMMA in the direct focus of the electron beam is affected. Due to scattering of the electrons and generation of secondary electrons, also the area next to an exposed area will be slightly changed chemically. This is called the *proximity effect*. We found that the whole area in which a hole array was written was more sensitive for dissolution in the solvents which we used in our colloidal dispersions, especially in the ethoxylated trimetylol propane triacrylate (ETPTA) monomer and in cyclohexyl bromide (CHB). To prevent dissolution of the template, we post-baked the templated substrates on a hot plate at 85 °C for at least 30 minutes. Also adsorption of the PHS-PMMA stabilizer to prevent sticking turned out to be not necessary anymore after this prolonged baking-step.

## 2.3.2 Replicating templates using soft lithography

In the soft lithography technique we used, micro-transfer molding [79], a master pattern was replicated in two steps. First the negative of the pattern was written into a soft mold, after which this mold was pressed into the final material, leaving a copy of the original pattern.

### Making a soft-lithography mold from a master pattern

The master patterns we used were made in glass plates as described by Jacob Hoogeboom in Ref. [73], Chapter 2.2.2. The molds were made from poly(dimethyl siloxane) (PDMS). The PDMS precursor and curing agent (Dow Corning Sylgard 184) were mixed in a 10:1 weigth ratio, after which bubbles were removed by short centrifugation. To prevent sticking of the PDMS mold to the master plate, a solution of dishwasher soap in water was poured over the master plate, after which the plate was dried by a flow of nitrogen. Then, a large drop of PDMS precursor mixture was placed next to the pattern and filled the holes in the pattern by slowly flowing over it. The master plate was then placed in the oven at 100 °C to cure the mold, after which the mold could easily be removed.

#### Making a soft-lithography mold from a PMMA e-beam pattern

A soft-lithography mold can also be made directly from the PMMA patterns, written by electron beam lithography as described in 2.3.1. Since the PMMA patterns melt when heated to 100 °C, the PDMS cannot be cured the same way. The polymerization of the PDMS, however, also slowly takes place without heating. Therefore, a mold was created by leaving a drop of PDMS precursor on the pattern for 3 days, after which it was solid enough to be removed from the plate. Then the mold was post-cured in the oven at 100 °C for 1 hour to give a negative of the written pattern.

#### Replicating the original master pattern using the PDMS mold

The relief pattern of the mold, the copy of the original pattern, was made in a polyurethane UV glue (Norland Optical Adhesive 68). A small drop of glue was placed on a glass cover slide (Menzel no. 1), after which the mold was pressed into the drop. The glue was then exposed to long wavelength UV light ($\sim$350 nm) through the mold for at least 2 hours to cure.

### 2.3.3 Creating colloidal epitaxial templates of spheres on a surface

Instead of using hole arrays to direct the first layer of colloids to the desired positions, one can also stick the first layer of colloids one-by-one. This was done by using an optical tweezers setup as depicted in Figure 2.3. A glass sample cell of which the top glass surface was coated with positively charged 3-aminopropyl triethoxysilane (APS) was filled with a very diluted dispersion of silica colloids in ethanol. The colloids sedimented to the bottom of the cell, where they could be trapped in single beam optical tweezers, after which the sample was moved downwards (with respect to the beam focus) and the (negatively charged) colloid was pushed against the (positively charged) APS coated surface, where it stuck. To avoid distortion of the pattern by the surface tension of the drying front which passes by, the patterned substrates were dried by critical point drying (CPD). In a critical point dryer (Bal-Tec CPD 030), the substrate was kept under ethanol after opening the cell. The ethanol in the chamber of the CPD was replaced by liquid $CO_2$. The $CO_2$ was then heated under pressure to bring to its critical point (31 °C, 73.8 bar), where the liquid becomes a vapour with the same density, thereby avoiding a gas-liquid interface.

The advantage of this method for creating templates is the fact that it gives complete freedom over the pattern you want to create and it does not depend on the fact that colloids should order in the holes of the template, the first layer of colloids is ordered already. A disadvantage is that only a small area can be templated in a reasonable amount of time, although the method can certainly be automated.

### 2.3.4 2D Template structures in the bulk of a dispersion

Using the optical tweezers setup, shown in Figure 2.3, not only single particles can be trapped. The focus of the laser beam can be moved in the plane perpendicular to the light path by switching the frequency in the Acousto-Optic Deflectors (AODs). By switching

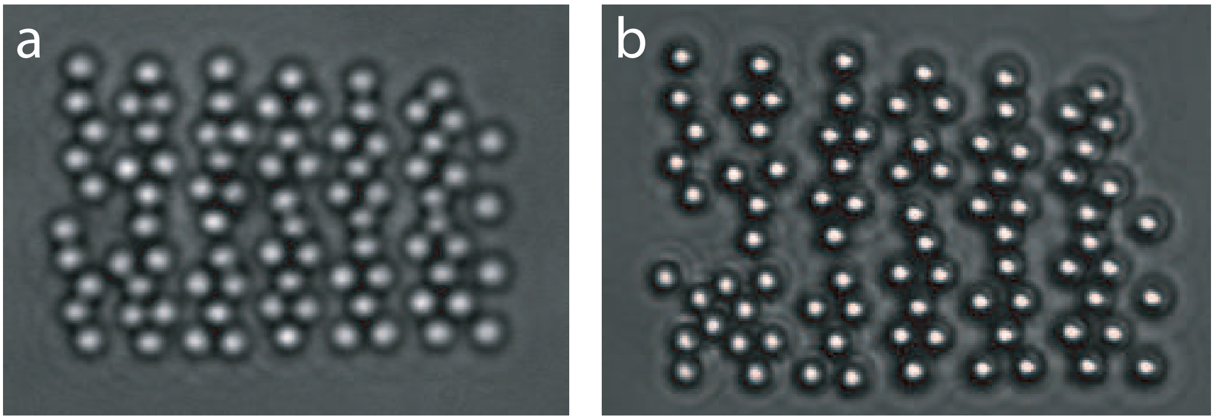

**Figure 2.1:** Photos of a structure of silica colloidal spheres stuck to an APS-coated surface by optical tweezers. (a) Before controlled drying, in ethanol (b) After controlled drying in air. Some spheres have moved and some additional spheres can be seen after drying, but most of the structure is still intact.

the frequency of the AODs fast enough that the particles do not move significantly by Brownian motion in between the visits of the laser beam, a 2D array of particles can be trapped. This effectively ‘time-shares’ the laser beam.

For studying nucleation near a small template (Chapter 6), the sample cell, consisting of two no. 1 glass cover slides with spacers in between, was filled with a dispersion of two different kinds of particles:

- host particles, with the same refractive index as the medium
- tracer particles, with a higher refractive index than the medium

The host particles were not influenced by the laser, since their refractive index was matched by the refractive index of the solvent. The tracer particles were trapped in the light of the laser beam. Time-sharing the laser beam between different points in one plane enabled us to create a 2D template of tracer particles in a bulk of host particles that could be imaged in 3D.

## 2.4 Optical tweezers

Optical tweezers are a non-invasive tool, based on a tightly focussed laser, with which single particles on the order of the wavelength of light can be trapped and moved. In 1970, forces on micrometer sized objects exerted by a laser beam were first identified by Arthur Ashkin [80, 81]. In 1986 he demonstrated the trapping of dielectric particles in a single-beam gradient force optical trap [82].

Optical trapping was first applied in biological sciences to trap viruses and bacteria [83], which was later extended to e.g. cell sorting [84], measuring cell motility [85] and studying protein folding [86]. In physics, optical tweezers are also used for trapping and cooling atoms, which in 1997 resulted in the Nobel Prize for Steven Chu, who was a co-author of the 1986 paper of Ashkin.

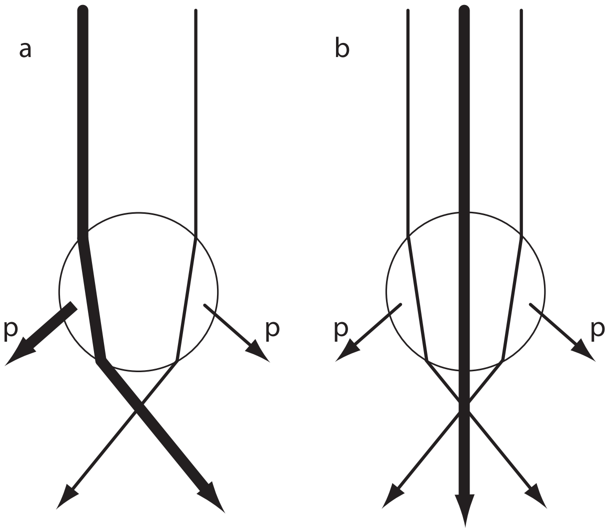

**Figure 2.2:** Schematic representation of the momentum transfer that causes the gradient force on a particle in a Gaussian shaped laser beam. The arrows depict light rays, where the thickness represents the intensity. (a) If a particle (with a higher refractive index than the medium) is off-center in a Gaussian laser beam, on one side more light is refracted than on the other side, giving a force to the high intensity region. (b) If the particle is in the center, the momentum transfers cancel out and there is no net gradient force. In order to get similar restoring forces confining the particle in the direction of propagation, the light needs to be tightly focused.

In this work, optical tweezers have been used to trap a small template of host particles in the bulk of refractive index matched host particles (Chapters 2.3.4 and 6). Furthermore, optical tweezers have been used to create templated surfaces by sticking colloidal particles to a coated wall (Chapter 2.3.3).

### 2.4.1 Theory of optical trapping

The principle of optical tweezers is based on the fact that a particle in the field of a tightly focussed laser beam experiences a force similar to the dielectrophoretic force in an electric field gradient as described in Section 2.5. In a simplified picture for larger particles one can decompose the total force in the particle in a “scattering force”, along the optical axis and a “gradient force”, which is the dielectrophoretic force and which is directed along the electric field gradient, where the direction depends on the sign of the dielectric contrast between the particle and the medium. The scattering force always pushes the particles out of the focus of the laser beam, but the gradient force can pull the particle towards the focus when $\epsilon_p > \epsilon_m$ as is schematically shown in Figure 2.2. The particle is trapped at the point where the gradient and scattering forces balance, on the optical axis, just beyond the focal point (disregarding spherical abberations).

Optical forces on a particle which is much larger than the wavelength can be calculated using simple ray optics. For very small particles (the Rayleigh regime), the particle can be treated as an induced dipole that scatters light elastically [87]. However, optical tweezers are mostly used in the intermediate regime, where the particles are of the same order as

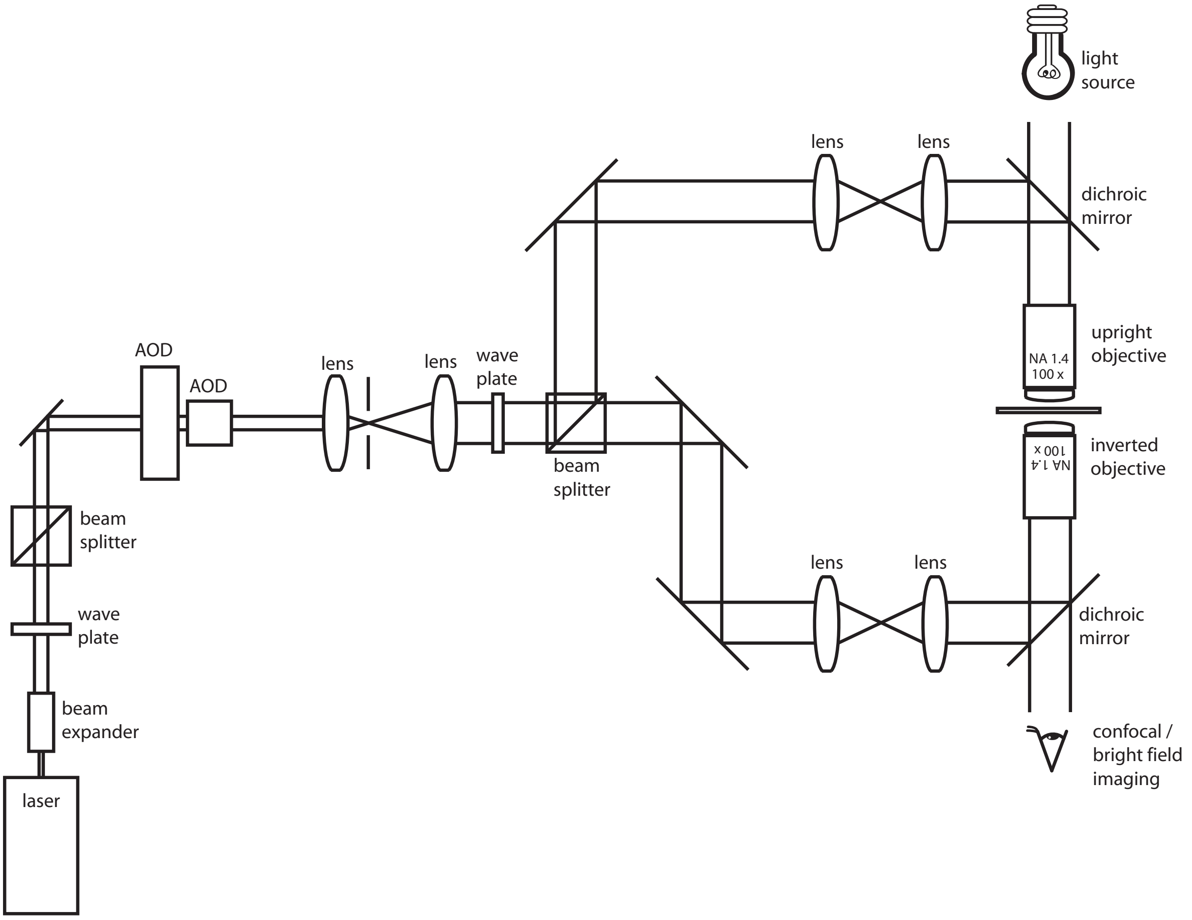

**Figure 2.3:** Schematic diagram of the optical tweezers setup.

the wavelength of the trapping light. Since in this limit the decomposition of the forces into a gradient and scattering force loses its meaning, full Mie theory has to be used to describe the trapping [88–90],

## 2.4.2 Experimental methods

In the optical trapping setup, used in this work (Figure 2.3) [91], the Nd:YVO$_4$ trapping laser (Spectra Physics, Millenia IR, 10 W, cw) has a wavelength of 1064 nm. The absorption of this wavelength is low in most materials that we use. Furthermore, this wavelength is far from the excitation wavelengths of the fluorescent dyes which are incorporated in the particles and it is not detected by the photomultiplier tubes used as confocal microscopy detectors.

The laser beam is expanded six times in a beam expander (EXP, Melles Griot) and then attenuated by a combination of a half-lambda zero-order wave plate (Newport) and a beam splitter, after which the horizontally polarized light is directed to a beam dump. Via a mirror (Newport), the light is coupled into two perpendicular Acousto Optical Deflectors (AODs, IntraAction Corp. DTD-276HB6). The AODs consist of a crystal bound to a piezoelectric material over which an rf-voltage is applied. The sound wave travels through the crystal, forming a grating-structure in the crystal. The spacing in the grating, and thus the angle of the diffracted light, is related to the frequency of the applied voltage. The amount of light in the first order diffracted beam depends on the voltage amplitude and the angle of incidence. The first order diffracted beam is selected using a diaphragm. The AODs are controlled with Direct Digital Synthesizers (DDSs, Novatech Instruments Inc. DDS8m 100 MHz) and amplifier, which in turn are controlled by a LabVIEW program (National Instruments). Using this program, the beam can be time-shared between several points to create an array of traps.

The light is expanded again using two lenses (Melles Griot, $f$=120 mm and $f$=250 mm), after which a half-lambda wave plate in combination with a polarizing beam splitter cube determines the fraction of light that is going through the upper beam path and through the lower beam path. In both beam paths, a pair of lenses (Melles Griot, $f$=80 mm) on $xyz$-stages controls the angle under which the light enters the back focal plane of the objectives and therefore allows manual $xyz$-control over the position focus of the laser beam. The laser light passes through two dichroic mirrors (ChromaTech) on a body of an inverted microscope (Leica, DMIRB), which reflect the laser light into the objectives, but at the same time allow for imaging with visible wavelengths (bright field or confocal microscopy). Confocal and bright field imaging are both done through the inverted objective, while the upright objective can be used as a condenser for bright field illumination. The upright objective is placed on an $xyz$-stage with microscrews for accurate positioning. The height of the inverted objective can be accurately controlled with the computer with a piezo microscope objective scanner (Physik Instrumente, Pifoc P-721.20).

For the upright objective we used a 100× (0.7-1.4 NA) objective. For the inverted objective, we used a 100× (0.7-1.4 NA) objective or a 63× (1.4 NA) objective. The sample was mounted on the microscope stage, which was equipped with motorized actuators (Newport, 850G-LS, low speed closed-loop motorized actuators) and a high resolution $xyz$-piezo stage (Physik Instrumente, P-563.3CD) with a range of $300\times300\times300$ $\mu$m$^3$.

For confocal imaging we used a commercial confocal scan head (Leica NT) attached to the side port of the microscope stage. Instead of the Leica $z$-scanner, which is usually used for $xyz$-scans, we controlled the piezo lens scanner (PIFOC, Physik Instrumente) on which the inverted objective was mounted, with the Leica scan head. For bright field imaging we used a halogen light source coupled in through the upright objective and a CCD camera on the front port of the microscope stage (UNIQ, UP-600 or Evolution QEi Fast Cooled Mono 12-bit, MediaCybernetics).

## 2.5 Dielectrophoretic compression

### 2.5.1 Theory of dielectrophoresis

Dielectrophoresis is the translational motion of neutral matter caused by polarization effects in a nonuniform electric field [92]. Particles acquire a dipole moment when their dielectric constant ($\epsilon_p$) is different from the dielectric constant of the medium ($\epsilon_m$). The dipole moment of the particle is then attracted to (for $\epsilon_p > \epsilon_m$) or repelled from (for $\epsilon_p$

$< \epsilon_m$) the areas with a high electric field. The colloids migrate towards the energetically more favorable area until the energy gain is balanced by the osmotic pressure which is built up.

The force on small homogeneous neutral particles with a field-induced dipole moment **p** in an external electric field **E** is [93]

$$\begin{aligned} \mathbf{F}_{\text{diel}} &= (\mathbf{p} \cdot \nabla)\mathbf{E}_e \\ &= (\alpha \upsilon_0 \mathbf{E}_e \cdot \nabla)\mathbf{E}_e \\ &= \tfrac{1}{2}\alpha \upsilon_0 \nabla |\mathbf{E}_e|^2, \end{aligned} \tag{2.3}$$

where $\alpha$ is the polarizability and $\upsilon_0$ is the volume of the particle. The last step is proven in [92] p.16. For very low particle concentrations and high field frequencies (we only used fields of 1 MHz to prevent polarization of the double layer of ions around the colloids), this equation can be rewritten in terms of an effective dielectric constant of the particle in the suspension, $\epsilon_{\text{eff}}$, using the Clausius-Mossotti relation:

$$\begin{aligned} &\mathbf{F}_{\text{diel}} = -\tfrac{1}{2}\upsilon_0 \epsilon_{\text{eff}} \epsilon_0 \nabla \mathbf{E}_e^2(\mathbf{r}) \\ \text{with} \quad &\epsilon_{\text{eff}} = 3\beta\epsilon_m \\ \text{and} \quad &\beta = \tfrac{(\epsilon_p - \epsilon_m)}{(\epsilon_p + 2\epsilon_m)}. \end{aligned} \tag{2.4}$$

The $\epsilon_{\text{eff}}$ depends on the dielectric constants of the particle and the medium (which are both frequency-dependent) and on the volume fraction of the particles ($\phi$).

For higher volume fractions, the electric field in a particle is influenced by the dipole field of neighboring particles. For a low dielectric contrast between the medium and the particle ($|\beta\phi| \ll 1$), the volume fraction dependence can be approximated using a volume fraction dependent effective dielectric constant [94]

$$\epsilon_{\text{eff}}(\phi) = 3\frac{\beta\epsilon_m}{(1-\beta\phi)^2} \tag{2.5}$$

The balancing force comes from the osmotic pressure $\Pi$, built up by the accumulation of particles, which for low volume fractions is described by the Van 't Hoff equation $\Pi = nk_BT$ [95],

$$\Pi = nk_BT, \tag{2.6}$$

where $n$ is the number of particles per unit volume, $k_B$ is the Boltzmann constant and T is the absolute temperature. If there is an osmotic pressure gradient $\nabla\Pi$, the average osmotic force per particle reads [92]

$$\mathbf{F}_{\text{os}} = -\frac{1}{n}\nabla\Pi = \frac{-kT}{n}\nabla n. \tag{2.7}$$

If the system is in equilibrium, the osmotic force and the dielectrophoretic force balance.

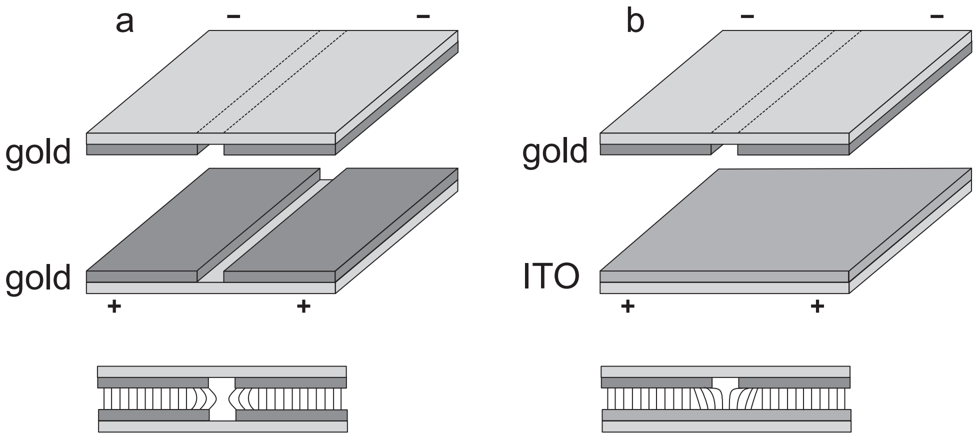

**Figure 2.4:** Schematic picture of the cells used for compression of a colloidal dispersion by dielectrophoretic forces. (a) Double-slit geometry with gold electrodes on both sides (b) Single-slit geometry with one gold electrode and one ITO electrode. Below the cell is a schematic side view of the cell with an impression of the electric field lines.

### 2.5.2 Experimental methods

In all dielectrophoresis experiments we used variations of a 'slit-like' geometry as described by Leunissen [96–98]. The designs we used are shown in Figure 2.4.

The gold electrodes were made by sputter coating a 3 nm layer of chromium on a 22 mm × 22 mm no. 1 glass cover slip (on a Cressington 208hr sputter coater equipped with a thickness meter) to increase the wetting of gold on the glass. Then, a 10 nm layer of gold was sputter coated on top. A gold electrode of this thickness is still transparent enough for confocal microscopy. The slit in the electrode was covered with a glass capillary (0.2 mm × 0.2 mm, 0.1 mm × 2 mm or 0.1 mm × 1 mm) during sputter coating. The width of the slit was determined using bright field microscopy.

For the single-slit geometry, we used an indium tin oxide (ITO) electrode on one side of the sample cell. This electrode was coated on no. 0 glass cover slips (Menzel) by Thin Film Devices, USA.

The glass slides were glued together with no. 71 Norland optical adhesive, with spacers, cut from no. 00 cover slips (thickness 55 - 80 $\mu$m), in between. T2 thermocouple alloy wires (diameter 50 $\mu$m, Goodfellow) were connected to the electrodes with silver paint (Jeol) and on the other side wrapped around normal electric wires. After filling the cell with the dispersion, the cell was closed with the more viscous no. 68 Norland optical adhesive.

The field we applied was a high frequency electric field (1 MHz), which has the advantage that it polarizes the colloidal particle itself, but not the double layer of ions around it.

## 2.6 Spin coating

Spin coating is a fast method for making large uniform thin films. The thickness of the film can be tuned by changing the spinning speed and spinning time, which makes the technique very versatile. Recently, the application range of spin coating was extended to colloid science by dispersing colloidal particles in the solution which is spun around, yielding large colloidal crystals. In the case of a non-volatile solvent, a monomer can be used as dispersant to allow for a polymerization step to make the resulting colloidal crystals permanent [99]. In the case of more volatile solvents, the crystals are dried during spinning [100]. In this work we used spin coating in a polymer solution in Sections 4.5.1 and 4.5.2 and spin coating in volatile media is studied in Chapter 8.

### 2.6.1 Theory of spin coating

In describing the process of spin coating usually four stages are identified:

1. deposition of the fluid on the wafer,
2. acceleration, in which the fluid acquires the same velocity as the wafer and a lot of fluid is expelled,
3. spinning at constant velocity, in which the film gradually becomes thinner and viscous forces dominate,
4. spinning at constant velocity, where evaporation dominates.

The evaporation actually already starts in stage 2, but for an idealized theoretical description, these stages were separated. The physics of the third stage has been described theoretically by Emslie et al. [101], making the following assumptions: the fluid is Newtonian, the process is cylindrical symmetric, there is only flow in radial direction, there is no evaporation and the final film is uniform in thickness. The centrifugal force is then balanced by the viscous force:

$$-\rho r \omega^2 = \eta \frac{\partial^2 \upsilon_r(z)}{\partial z^2}, \tag{2.8}$$

where $\rho$ is the fluid density, $\omega$ the angular velocity, $\eta$ the fluid viscosity, $\upsilon_r(z)$ is the velocity of the fluid in radial (outward) direction and $z$ is the height above the substrate. Assuming a no-slip condition at the substrate ($\upsilon_r(0) = 0$) and zero stress at the top surface ($\frac{\partial \upsilon_r}{\partial z}\big|_h = 0$), a parabolic velocity distribution results:

$$\upsilon_r(z) = \frac{\rho r \omega^2 h^2}{\eta} \left( \frac{z}{h} - \frac{1}{2} \left( \frac{z^2}{h^2} \right) \right). \tag{2.9}$$

From this velocity profile, Emslie et al. derived the thickness of the final film as a function of the spin speed and time

$$h(t) = \frac{h_0}{(4Kh_0^2 t + 1)}, \tag{2.10}$$

where $h_0$ is the film thickness at time zero and the constant $K$ is defined as

$$K = \frac{\rho\omega^2}{3\eta}. \tag{2.11}$$

The thinning rate of the film is

$$\frac{\partial h}{\partial t} = -2Kh^3. \tag{2.12}$$

Meyerhofer [102] discussed evaporation of the solvent during spinning and added a constant evaporation rate term $e$ (in ml/s/cm$^2$) to the thinning rate, giving:

$$\frac{\partial h}{\partial t} = -2Kh^3 - e. \tag{2.13}$$

While actually the evaporation is already present from the beginning, Meyerhofer divides the processes at constant velocity into two stages: one where the viscosity dominates and one in which the evaporation dominates, with the transition point at the moment where the evaporation rate and the viscous flow rate are equal. With this assumption, he predicts the final layer thickness to be

$$h = c_0 \left( \frac{e}{2(1-c_0)K} \right)^{\frac{1}{3}} \tag{2.14}$$

It has been shown that the evaporation $e$ above a spinning disc is proportional to $\sqrt{\omega}$.

The model described above works fine for several Newtonian fluids. However, colloidal dispersions are non-Newtonian, the viscosity is therefore a function of the shear rate. Furthermore, in the fast-evaporating dispersions, the viscosity of the dispersion also changes while the solvent evaporates. The evaporating fluid in turn gives rise to capillary forces, drawing the particles together. All these effects make it hard to build a theoretical description of spin coating a concentrated dispersion in a volatile medium. We will come back to these issues in Chapter 8.

# 3

# Fabrication of large binary colloidal crystals with a NaCl structure using a combination of external fields

Binary crystals are a perfect starting point for creating ordered structures of particles with different characteristics, which have great potential for applications, including three-dimensional photonic band gap materials. Binary crystals made from particles with sizes of a few hundred nanometers and larger have been created in colloidal systems, but their formation is usually described as being slow and difficult, which is attributed to the difference in sedimentation rates of the two species in a dispersion.

The binary colloidal crystal with a NaCl structure can have a photonic band gap of 9% between bands 8 and 9 for an inverse structure of air spheres in silicon, which is significantly larger than the band gap of a similar face centered cubic structure.

In this chapter, the fabrication is described of hard-sphere-like binary colloidal crystals with NaCl structure using combinations of the following external fields: electric, gravitational and dielectrophoretic fields and a structured surface (colloidal epitaxy). We were able to produce large, oriented binary colloidal crystals, with a well-defined stacking, which could be used for the realization of a photonic band gap in the visible.

Using confocal microscopy, defects in the NaCl lattice were imaged, which were caused by impurities or by stress release in the crystal. Both defects were shifts of the lattice over the (111) plane.

After fabrication, we were able to dry the produced NaCl structures, demonstrating feasibility of infiltration with a high-index material, which is an essential step towards photonic crystal fabrication.

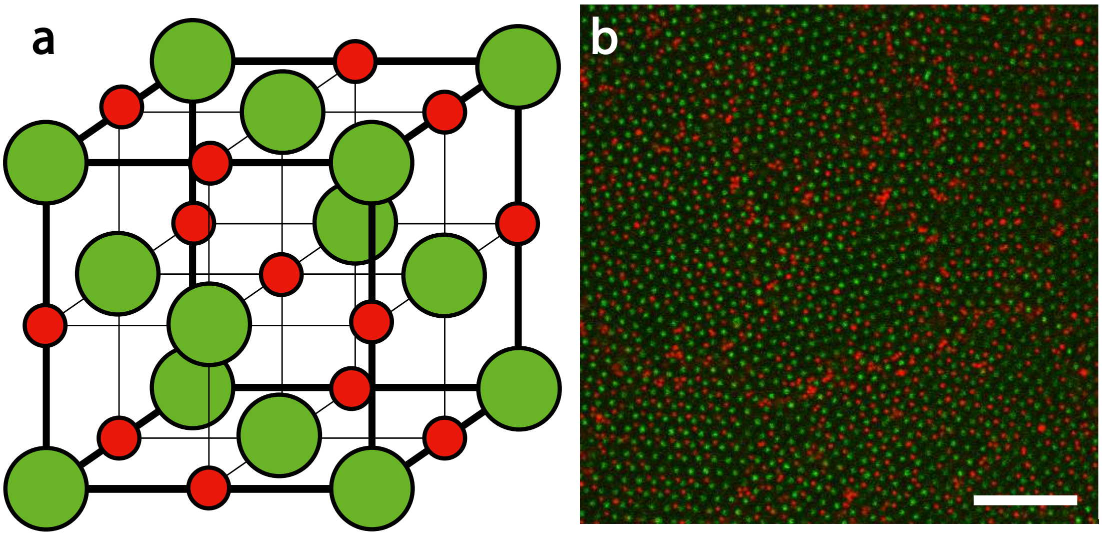

**Figure 3.1:** NaCl unit cell and a confocal image of a hexagonal layer in a NaCl crystal grown by sedimentation. (a), Schematic representation of the conventional unit cell of the NaCl structure, where the green spheres represent the large colloids and the red spheres represent the small colloids, both in their own fcc structure. (b), Confocal scanning $xy$-image of a NaCl crystal grown by sedimentation. Only the fluorescent cores of the particles are visible in the confocal images. The scale bar is 10 $\mu$m.

## 3.1 Introduction

Because of the interesting fundamental physical aspects and the wide range of photonic applications, the creation of a 3D photonic crystal with a complete photonic band gap in the visible region of the spectrum of light is the pursuit of many researchers in the last decade [14]. However, the experimental fabrication remains a challenge up till now. The binary colloidal NaCl structure can have a complete photonic band gap, with a relative gap width between bands 8 and 9 for an inverse NaCl structure of air spheres in silicon of 9% [103]. This is significantly higher than the 5% for an inverse face centered cubic (fcc) lattice of the same materials.

Another incentive to make a NaCl colloidal crystal, is the fact that binary colloidal crystals offer greatly increased potential for tuning material properties for applications, as they allow the positioning of particles with quite different characteristics on one lattice. Recently, examples of tunability have become available in several binary systems of nanoparticles [104–106]. For larger, micron-sized colloids it is believed that gravity and slow crystallization hinder the formation of binary crystals [107, 108].

Here we present methods for growing binary colloidal crystals with a NaCl structure from relatively heavy, hard-sphere-like, micron-sized silica particles, exploring the following external fields: electric, gravitational and dielectrophoretic fields, and a structured surface (colloidal epitaxy). A combination of these fields yielded large, oriented single crystals without stacking disorder. The binary colloidal crystals could be dried allowing reversal of refractive-index contrast.

The binary sodium chloride (NaCl) crystal structure consists of spheres of two different radii ($\sigma_\mathrm{L}$ and $\sigma_\mathrm{S}$), both ordered in a face centered cubic (fcc) structure, where the small particles are in the octahedral holes of the fcc crystal of the large spheres (Figure 3.1a). For a close-packed fcc crystal of the large spheres, the radius of the small spheres ($\sigma_\mathrm{S}$) has to be smaller than $0.41\sigma_\mathrm{L}$ for them to fit in the octahedral holes, but larger than $0.22\sigma_\mathrm{L}$, the radius of the tetrahedral holes in the fcc crystal. The stability of the NaCl structure in binary hard-sphere dispersions has been studied both theoretically [58, 109] and by simulations [41, 53, 110]. From these studies it can be concluded that NaCl is at least stable in the size ratio range $0.22 < \sigma_\mathrm{S}/\sigma_\mathrm{L} < 0.42$. Experimentally, NaCl structures have been observed in nanosphere systems [105, 111] and oppositely charged colloidal systems [50]. A colloidal NaCl structure has been fabricated by layer-by-layer growth [112], but this method is time-consuming and is not suitable for more than a few layers. Hard-sphere NaCl crystals have also been grown following homogeneous nucleation from a binary dispersion [46, 113], but the stacking order of the larger spheres could not be determined or was only determined very locally. Similarly as for single-component hard-sphere crystals, the stacking sequence of the close-packed planes of the large spheres can be $ABA$ which gives a hexagonally close packed (hcp) structure, or $ABC$, giving an fcc structure. If the octahedral holes are filled up with small spheres, the corresponding binary crystal structures are that of NiAs or NaCl, respectively. The free-energy difference between NiAs and NaCl is in the same order as the free-energy difference between hcp and fcc [114]. Therefore, experimentally, a random mixture of both stacking sequences is expected. Control over the stacking in this binary crystal is therefore crucial for the determination of the crystal structure and its application.

## 3.2 Experimental methods

### 3.2.1 Particle synthesis and dispersions

We synthesized two sizes of monodisperse core-shell silica spheres. The small spheres, of which the core was labelled with RITC dye, were grown according to the method described by Verhaegh et al. [115] with three adaptations to prevent aggregation and secondary nucleation: the time between the addition of Tetra Ethoxy Silane (TES) and the addition of dye was adjusted to 8 minutes, the labelled cores were kept in the Stöber mixture of ammonia and ethanol until a 20 nm unlabelled shell was grown and the centrifugation speed was limited to $50g$. The large spheres, of which the core was labelled with FITC dye, were grown from existing cores using the Giesche seeded growth [116]. The RITC-labelled colloids had a diameter of 412 nm the polydispersity in size was 5%. The FITC-labelled colloids had a diameter of 1.37 $\mu$m the polydispersity in size was 3.3%. Both particle sizes were determined from Static Light Scattering (SLS) data.

The silica particles were transferred from the ethanol synthesis mixture to the dispersion solvent (DMSO or a glycerol/water mixture) by several centrifugation steps. The glycerol/water mixture was made in a ratio such that it matched the refractive-index of the particles. The starting volume fraction of the DMSO dispersions was 22-24%, the starting volume fraction of the glycerol/water dispersions was 20-22%.

### 3.2.2 Sample cell design

The experiments where an external electric field was applied, were done in sample cells where two 50 $\mu$m diameter nickel wires were placed parallel, 1.3 mm apart, between a no. 1 cover slide and an object glass (Figure 3.2a). The sides of the cell parallel to the wires was closed with candle wax. The other sides were closed with two-component glue (Bison Epoxy Rapide) after filling the cell. The final sample volume was typically 1.3 mm × 2 cm × 50 $\mu$m.

Sedimentation experiments on a template were done in a sample cell made of two cover slips, with two no. 00 glass strips as spacers. On the bottom of the lower cover slide, the square array of holes was made by soft lithography [73] in Norland Optical Adhesive 68, which was cured with a UV lamp (wavelength around 350 nm) for 2 hours. The cell was closed with Norland Optical Adhesive 68. The sample compartment was typically 1 cm × 1 cm × 100 $\mu$m.

The compression by dielectrophoresis was done in a sample cell (Figure 3.2b) with parallel plate electrodes about 140 $\mu$m apart, with a 1 mm slit in both electrodes. The electrodes were made by sputter coating a 10 nm layer of gold on top of a 3 nm layer of chromium (to increase the wetting of the gold) on a cover slide. Two no. 00 glass strips were used as spacers. Also in this cell, a template was made on the bottom of the lower cover slide using soft lithography. The sample compartment was similar in size to the sample cells for sedimentation on a template.

### 3.2.3 Sample characterization

The 3D structure of all samples was imaged using a Confocal Scanning Laser Microscope (Leica, type NT or SP2). The fluorescent dye FITC was excited with the 488 nm line of an Ar-laser, the dye RITC was excited with the 543 nm line of a green HeNe-laser. On the SP2 confocal the signals of these different dyes can be sequentially scanned line by line.

One of the samples, grown by sedimentation on a wall structured by soft lithography with a square template, was dried and imaged using Scanning Electron Microscopy (SEM, Phenom, FEI Company). The crystal was removed from the substrate and imaged from the bottom side (against the gravity direction).

### 3.2.4 Image analysis

The stacking parameter of the structure $\alpha = 1 - \frac{\kappa}{P-2}$ was determined from $xz$-scans, where $\kappa$ is the number of twinning planes and $P$ is the number of planes. This gives $\alpha = 1$ for fcc lattices and $\alpha = 0$ for hcp lattices.

We calculated the number ratio $f_N^{crystal}$ in the crystal by determining the coordinates of the particles of several confocal $xyz$-stacks using IDL software based on similar methods as described by Crocker and Grier [117]. The number of small particles (excluding the groups of small particles in vacancies of the crystal of large particles) was divided by the number of large particles to give the number ratio. The number ratios of multiple images were averaged to give $f_N^{crystal}$.

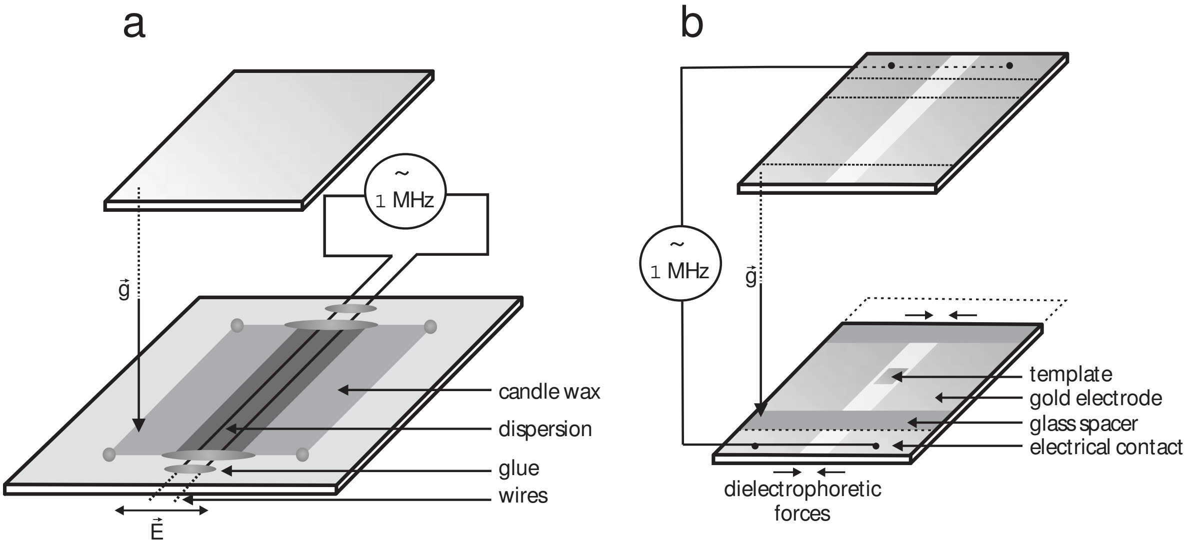

**Figure 3.2:** (a), Sample cell used for crystal growth by sedimentation, directed by an electric field. (b), Sample cell used for crystal growth by compressing with dielectrophoretic forces, directed by a templated bottom wall.

## 3.3 Results and discussion

### 3.3.1 Sedimentation of the binary mixture

We first studied a binary mixture of silica spheres in dimethyl sulfoxide (DMSO) under compression by gravity. The silica spheres, having a size ratio of $\sigma_S/\sigma_L = 0.3$, had a core that was labelled with a fluorescent dye, fluorescein isothiocianate (FITC) for the large, 1.37 $\mu$m diameter spheres and rhodamine isothiocianate (RITC) for the small, 0.41 $\mu$m diameter spheres (for synthesis details, see Section 3.2.1), thus allowing imaging into separate channels in confocal laser scanning microscopy. The refractive-index matching silica dispersion had a steep, almost hard-sphere like interaction potential, resulting from charges on the surface and residual counterions in the dispersion [62]. These first experiments resulted in binary structures with small crystal domains (of the order of 20 $\mu$m $\times$ 20 $\mu$m) in which hexagonal (111) planes of large spheres were parallel to the bottom wall for most of the domains (Figure 3.1b). This orientation, which we will refer to as the "(111)-orientation" is favored by sedimentation on a flat bottom wall [73].

We determined the stacking parameter of the structures as described in Section 3.2.4. For the sedimented binary structures, a stacking parameter $\alpha$ around 0.7 was found, indicating that the structure has a lot of randomness in its stacking sequence of (111) planes, but with a preference for an fcc structure. The binary crystals formed did not have a pure NaCl structure but consisted instead of a mixture of NaCl and NiAs. These stacking errors and also the small domain size, can be disadvantageous for their use in photonic applications.

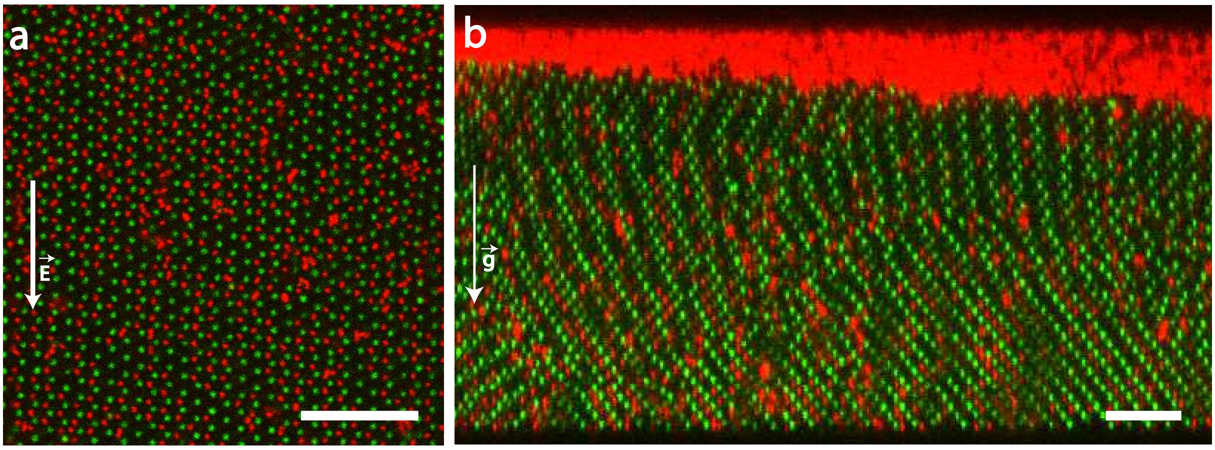

**Figure 3.3:** Confocal scanning image of a NaCl crystal grown in an external electric field. (a), $xy$-scan of the (111)-plane. (b), $xz$-scan of crystals with their (111) plane horizontal. Only the fluorescent cores of the particles are visible in the confocal microscopy images. All scale bars are 10 $\mu$m.

### 3.3.2 Electric-field-induced binary crystals

To increase the domain size of the crystals and obtain additional control over the orientation of the crystals, the crystallization of the sedimenting binary mixture was directed by a horizontal external electric field, perpendicular to gravity (Figure 3.2a). A 1 MHz oscillating electric field of 200 V peak-peak was used between wires which were 1.3 mm apart. The 1 MHz AC field ensured that the double layer around the colloids did not polarize [12, 118], while the low electric field amplitude made sure that only the large colloids obtained a significant dipole moment $\vec{p}$, which is proportional to the particle volume. In earlier work it has been shown that for single-component dispersions at high field strengths the dipolar interactions favor a body centered tetragonal (bct) colloidal crystal lattice [9, 10]. However, for low fields where gravity and dipolar energy start to compete [12, 119], one finds oriented fcc crystals [9]. It was also found that frequently turning the sample upside down caused complicated sedimentation behavior [120], which resulted in annealing of the crystals. The same observations were made with our binary system. We observed crystals oriented with the hexagonal planes parallel to the substrate near the bottom of the cell (Figure 3.3), such that the strings in these planes were along the field direction in addition to a higher stacking probability of fcc than hcp ($\alpha \simeq 0.7$). Moreover, turning the sample upside down resulted in larger single crystal regions with a size of roughly 30 $\mu$m × 30 $\mu$m.

Using confocal microscopy, we studied the crystallization process in time, which started in the bulk already after 10 minutes due to the induced dipole moments of the large colloids. Heterogeneous crystallization from the bottom wall upwards took over when the dispersion was compressed further by gravity. This combination of homogeneous and heterogeneous crystallization (which was not observed in the single-component case [12]), resulted in crystals with the (111)-plane parallel to the lower glass wall near the bottom of the sample and a varying orientation of the crystals higher up in the sample. However, as

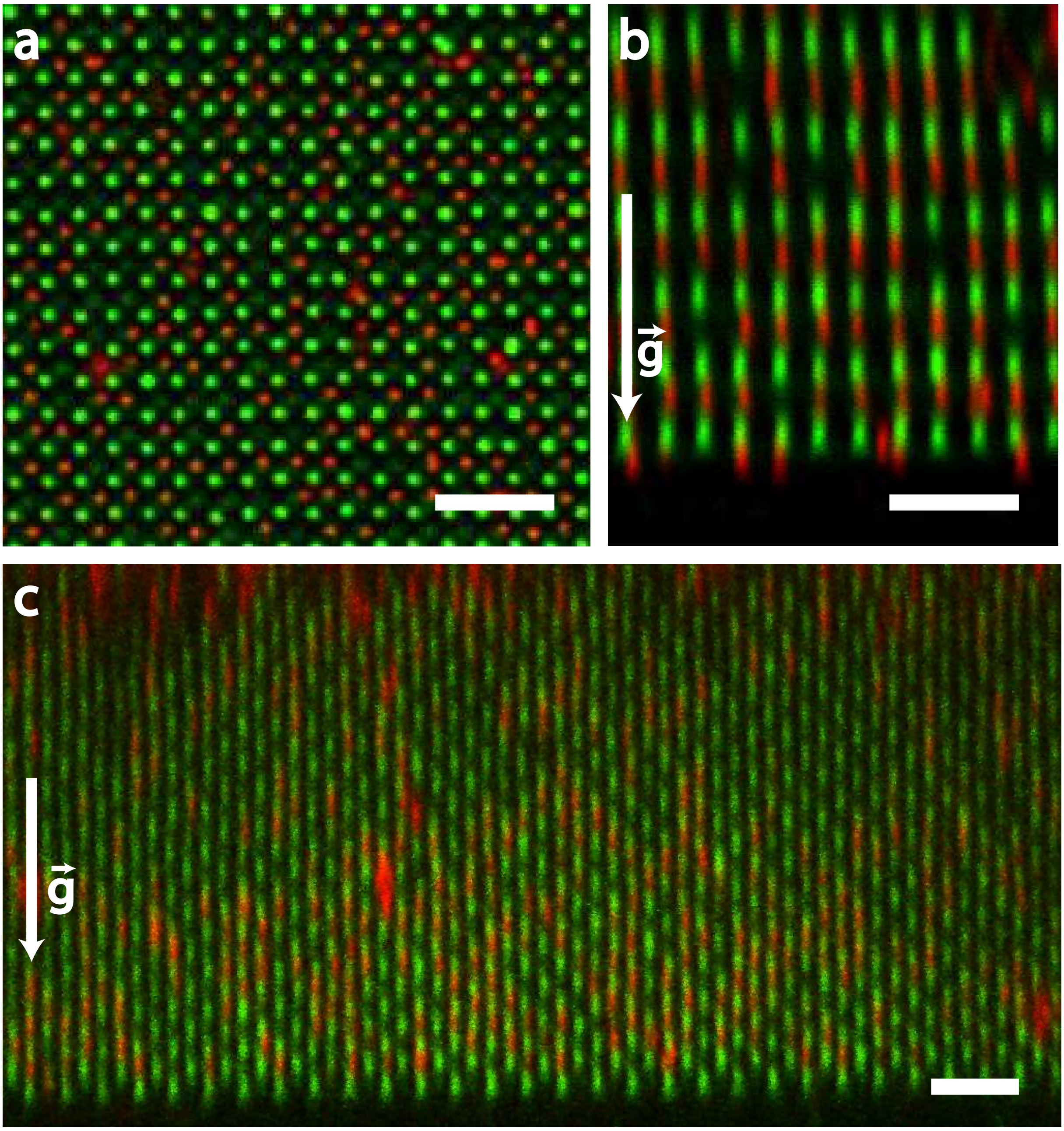

**Figure 3.4:** Confocal scanning images of a NaCl crystal grown on a template by compression with dielectrophoretic forces. (a), $xy$-scan of the (100)-plane. (b), $xz$-scan of the (110)-plane. **c**, $xz$-scan of the (100)-plane. Only the fluorescent cores of the particles are visible in the confocal microscopy images. Note that not all smaller spheres are visible, because they are often out of the confocal plane. All scale bars are 5 $\mu$m.

before the close-packed strings aligned in the direction of the electric field (Figure 3.3a). Similarly as was observed with the close packed crystals grown in [12], it was found that the inter-particle distance in the direction of the electric field was slightly smaller than in the other directions. However, this distortion, caused by the softness in the inter-particle potential, was small (the ratio between the particle distances in the different directions was 0.97).

Due to the different sedimentation rates of the two sizes of colloids, there were many small particles on top of the crystals and fewer than the stoichiometric amount at the bottom. Consequently, not all octahedral holes were filled with small particles and the ratio of the number of small particles to the number of large particles in the crystal, $f_N^{crystal}$, was not equal to 1 as would be optimal. We determined the number ratio in the crystal from confocal microscopy data as described in Section 3.2.4. By changing the initial number ratio between large and small particles in the dispersion, we could increase the parameter $f_N^{crystal}$ in the crystals directed by the electric field from 40% for an initial number ratio of $N_\mathrm{S}/N_\mathrm{L} = 1$ to 89% for $N_\mathrm{S}/N_\mathrm{L} = 10$. However, the number of vacancies in the crystal of the large particles also increased from 1.5% to 5 %. From confocal microscopy images it was apparent that small particles were causing the formation of more point defects on lattice sites of large particles.

### 3.3.3 Epitaxial growth of a binary colloidal crystal

Controlling the orientation of colloidal crystals can also be done in another way, by sedimentation on a structured wall [70, 74], referred to as *colloidal epitaxy*. This method yielded binary crystal domains which were as large as the template, which in our case was a two-dimensional hole array made by soft lithography and therefore extended over several hundreds of micrometers in both dimensions. By choosing an appropriate template, the desired crystal structure could be selected. In our case, the (100) fcc face (a square structure with a spacing of 1.42 $\mu$m, only slightly larger than the close packing distance between the larger particles) directed the growth of the large particles such that only an fcc structure formed, yielding one single binary crystal. The NiAs (hcp-stacked) structure cannot grow on this template, since a square face does not exist in the hcp structure. The dispersions for these sedimentation experiments, contained a glycerol/water mixture (matching the index of refraction of the silica spheres) instead of DMSO as solvent. The lattice parameters of the resulting crystals were not distorted in any direction, the spacing in the (100) plane stayed 1.42 $\mu$m in both horizontal directions up to at least the fifth layer. The highest $f_N^{crystal}$ we obtained using sedimentation on a square template was 60% for $N_\mathrm{S}/N_\mathrm{L} = 10$.

### 3.3.4 Compression by dielectrophoretic forces

To increase $f_N^{crystal}$ further, we used a technique recently introduced as the “electric bottle” [97, 121]. We compressed the binary dispersion horizontally by dielectrophoretic forces created by electric field gradients, thereby leaving less time for the dispersion to separate under gravity. The compression cell was formed by two horizontal plate electrodes with a slit in both electrodes. The cell design is shown in Figure 3.2b. When a 1 MHz oscillating electric field of 30 V (peak-peak) is applied between the electrodes which are about 140 $\mu$m apart, there is a significant field gradient at the edges of the slit. This field gradient applies a pressure to the enclosed dispersion and forces the colloids, which have a dielectric constant which is lower than that of the liquid, into the field-free region in the slit. We used the same glycerol/water solvent mixture as in the sedimentation experiments on a template, the colloids were compressed in the millimeter wide slit, where the template was on the bottom of the slit. This way, $f_N^{crystal}$ could be increased to 73%, yielding a large, template-sized NaCl single crystal without lattice distortion. The (100)-oriented NaCl crystal in the slit was 25 layers thick. Confocal microscopy images of the crystal in the slit are shown in Figure 3.4.

### 3.3.5 Defects in the epitaxially grown NaCl crystals

The spacing of the hole array, used for the epitaxial growth of the NaCl binary colloidal crystals, is chosen as close as possible to the effective radius of the spheres in the dispersion. However, as was shown by Hoogenboom [73], the growth of a crystal is very sensitive to the spacing of an epitaxial template. A mismatch of a few percent leads to stress in the crystal, and a mismatch of a template and a crystal can even completely prevent a crystal with the intended crystal face from nucleating at the template [70, 75].

In our samples, the stress in the crystals, probably due to the mismatch of the template and the ideal crystal or by defects, expressed itself in the defects which primarily were visible in the (100) planes. Confocal microscopy images of the (100) planes show clear defect lines under 45° with the horizontal, above or below which the (100) plane is not in focus of the microscope (see for example Figure 3.5). Parts of the crystal are shifted along the (111) planes, bringing them out-of-plane along the (100) plane.

Similar stress release is found around a large defect sphere (Figure 3.6), where a wedged part of the crystal to the top right of the sphere (under 45°) is shifted out of the (100) plane along the (111) planes. At the beginning of the defect, a few lines are shifted, which grows out into a whole strip of crystal being shifted out of plane. In the schematic picture at the bottom of Figure 3.6, the direction of the shift is indicated with a grey arrow. This direction is parallel to the intersection line of the (110) plane and the (111) plane, both indicated with (differently) dashed lines. The same defects are found in single-component fcc crystals grown by dielectrophoretic compression on a square template in Chapter 7.3.1.

### 3.3.6 Drying the colloidal crystal for obtaining inverse crystals

Plane wave band structure calculations were performed before by Thijssen [103] for the inverse NaCl structure showing that the relative gap width is significantly larger than for an inverse fcc structure. The photonic band structure for an inverse NaCl structure with a size ratio $\sigma_S/\sigma_L$=0.3 (where the small spheres are in the middle of the octahedral holes of the large spheres) and a refractive index contrast of 12 is shown in Figure 3.7a. The photonic band structure contains a band gap between bands 8 and 9, with a relative gap width of 8.2%.

The dispersion, which was used in this study, had a size ratio of $\sigma_S/\sigma_L$=0.3, which is smaller than the size ratio for a completely close-packed structure. Thus, in principle,

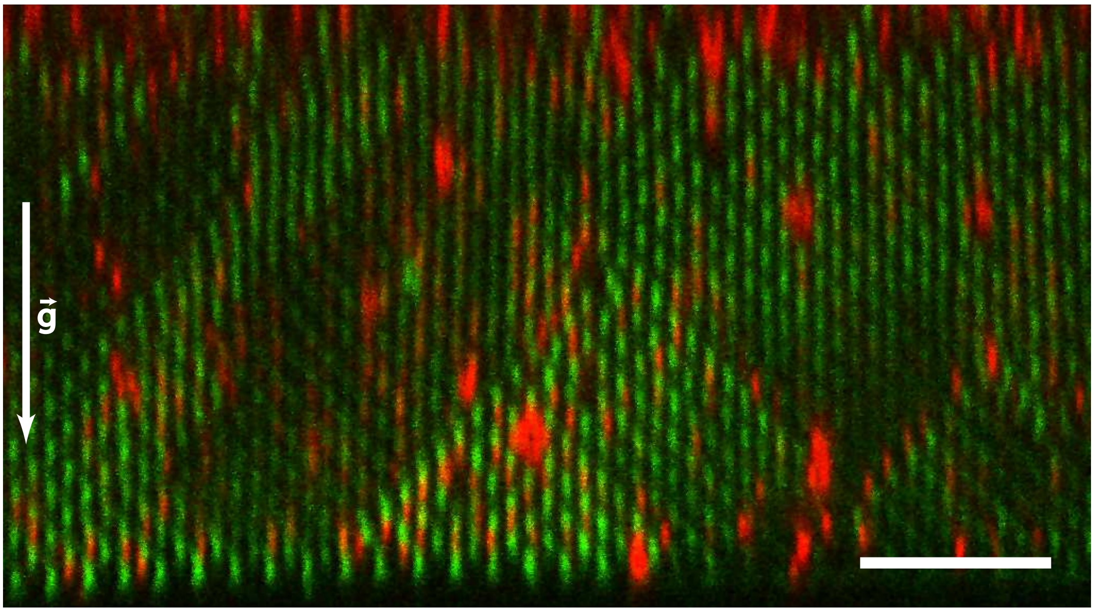

**Figure 3.5:** Confocal $xz$-scan of the (100)-plane of a NaCl crystal grown on a template by compression with dielectrophoretic forces. Only the fluorescent cores of the particles are visible in the confocal microscopy images. Note that not all smaller spheres are visible, because they are often out of the confocal plane. The scale bar is 10 $\mu$m.

the small spheres are rattling in the lattice of the large spheres. The disorder induced by the "rattling" cannot be incorporated in the photonic band structure calculations, but the effect of the difference in size ratio for a sphere in the middle of the octahedral hole has been calculated with MIT Photonic Bands software using 32 x 32 x 32 grid points to discretize the real space unit cell. The dependence of the relative gap width on the size ratio is plotted in Figure 3.7b, from which can be concluded that the optimum size ratio is around 0.2.

Inversion of the structure for refractive-index contrast enhancement can only be performed after drying the structure. To demonstrate the feasibility of inverting the index contrast for our binary crystals, necessary to achieve a band gap, a crystal, grown by colloidal epitaxy, was dried from a glycerol/water dispersion. Scanning Electron Microscopy (SEM) images of this crystal are shown in Figure 3.8.

## 3.4 Conclusions

In conclusion, we demonstrated that the crystallization of binary colloidal crystals with a NaCl structure from a binary hard-sphere dispersion can be manipulated using several external fields (and combinations thereof), i.e. gravity, electric field, epitaxial template and dielectrophoretic compression. With application in the field of photonics in mind, we aimed at oriented, defect-poor NaCl crystals with large domains and without stacking faults. Combining epitaxial growth on a directing template with dielectrophoretic compression to avoid demixing of the dispersion by gravity, we obtained thick, oriented pure

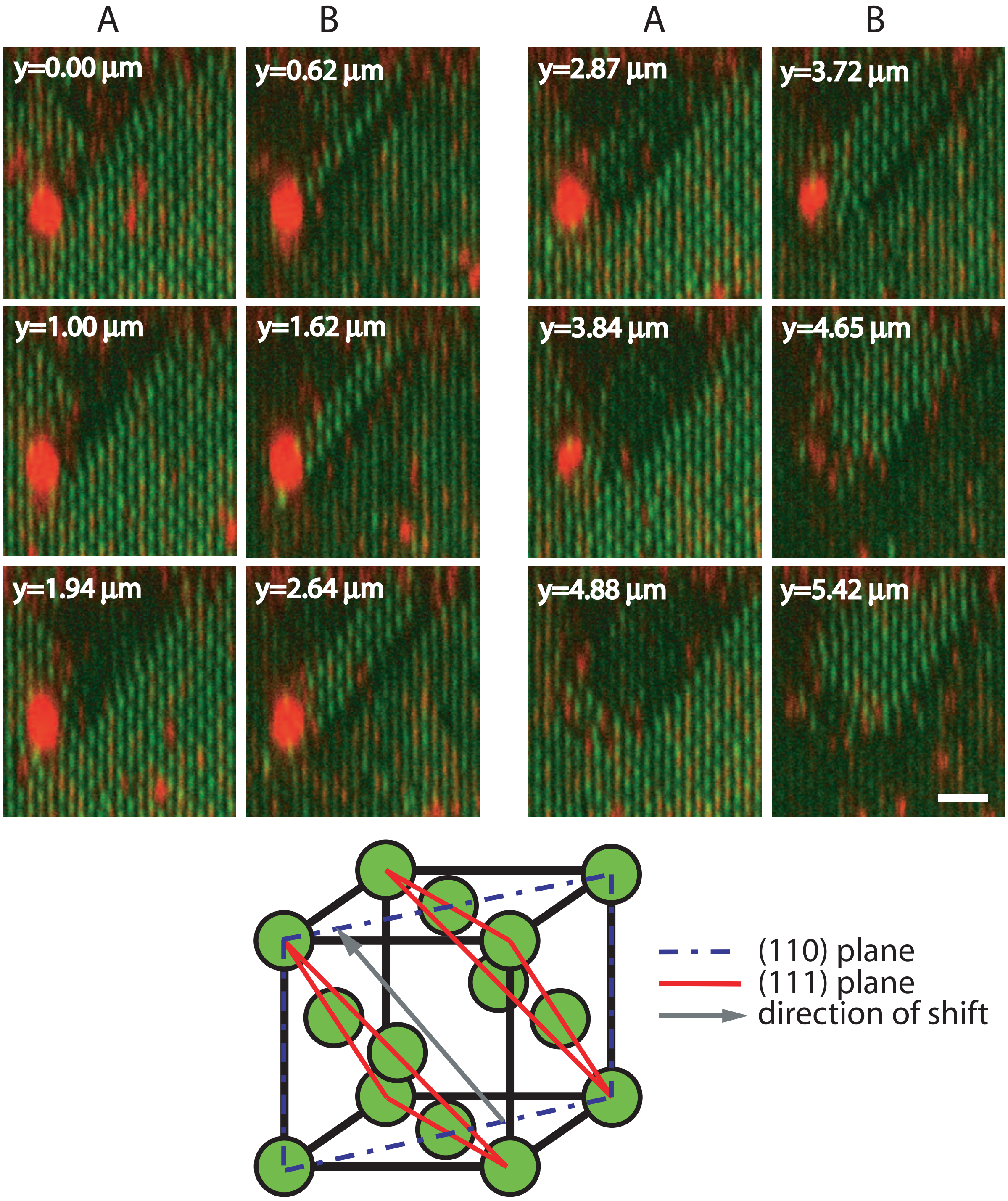

**Figure 3.6:** Confocal $xz$-images at different $y$-values around a large defect sphere (in red, the fact that it is a large sphere became clear from the $xzy$-movies), showing stress release by the shift of a wedged shaped part of the crystal out of the (100) plane, along the (111) planes. In columns (A), the normal crystal is in focus, while in column (B), the wedge shaped crystal is in focus. The scale bar in the right lower corner is 5 $\mu$m. The schematic image at the bottom illustrates the direction of the shift of the crystals. For clarity only the large spheres are depicted, which form an fcc-lattice. The dash-dot-dash lines indicate the (110) plane, the dashed lines indicate the (111) plane. To release stress, the crystal slid over the (111) plane in the direction of the intersection between the (110) plane and the (111) plane. This direction is indicated with the grey arrow.

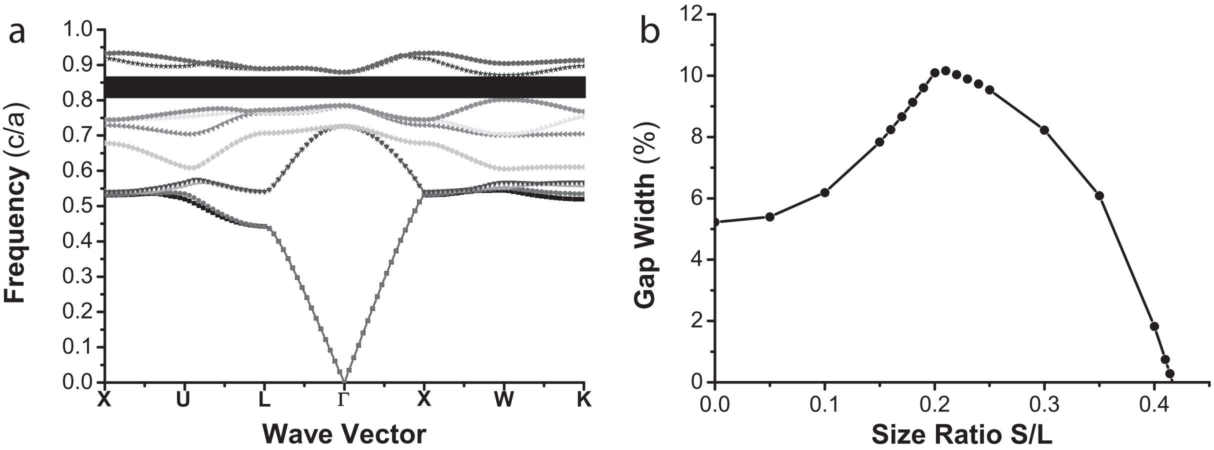

**Figure 3.7:** (a) Photonic band structure diagram of an inverse binary NaCl structure of air spheres ($\epsilon$=1) in silicon ($\epsilon$=12) with a size ratio between the two types of spheres of 0.3. The photonic band gap between bands 8 and 9 of approximately 8.2% is indicated by the black rectangle. (b), Graph containing relative width of the photonic band gap versus the size ratio of the large and small spheres. The size ratio is varied, while the position of the center of the small sphere is fixed in the center of the octahedral hole of the fcc lattice of the large spheres.

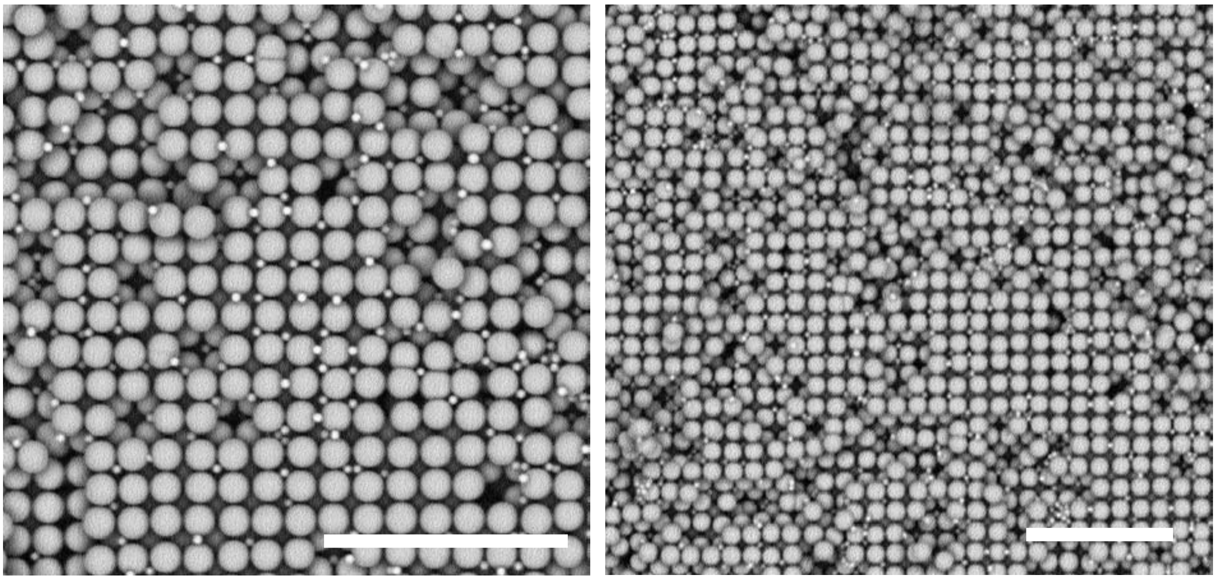

**Figure 3.8:** SEM images of the bottom of a dried binary colloidal crystal with a NaCl structure grown by sedimentation on a square template. Since the SEM images were taken of the bottom layers of the crystal, the fraction of small particles is quite low. Furthermore, some small and large particles were lost in the process of removing the crystals from the substrate. The scale bars are 10 mm.

NaCl single crystal with a relatively high number ratio $f_N^{crystal}$. This result could still be improved upon in future experiments by combining the last method with an additional horizontal electric field as described before. By switching off the field afterwards and letting the crystal relax to avoid a small lattice distortion in the electric field direction, further optimization is still possible. However, this combination of all four external fields needs a more advanced electrode arrangement and accurate fine-tuning of experimental procedures to speed up the crystallization on the bottom wall, while avoiding homogeneous nucleation in the bulk.

## 3.5 Acknowledgements

This work was done together with Anke Kuijk, who did the synthesis of the colloidal spheres of both sizes, the experiments in the electric field and the sedimentation experiments (with and without template). The photonic band structure calculations were performed by Job Thijssen. Initial electric-field-induced experiments were done by Michiel Hermes. We thank Dannis 't Hart for the fabrication of the cores for the FITC labelled silica spheres. Dannis 't Hart, Carlos van Kats and Arnout Imhof are acknowledged for useful discussions on colloid synthesis. Jacob Hoogenboom is thanked for the fabrication of the masters for the soft lithography.

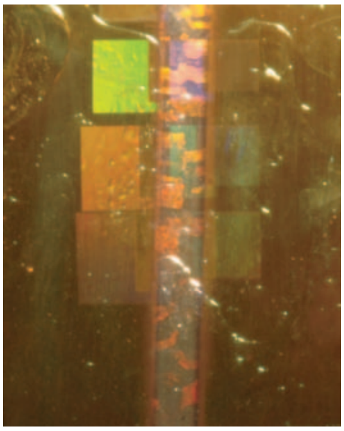

Figure 7.1

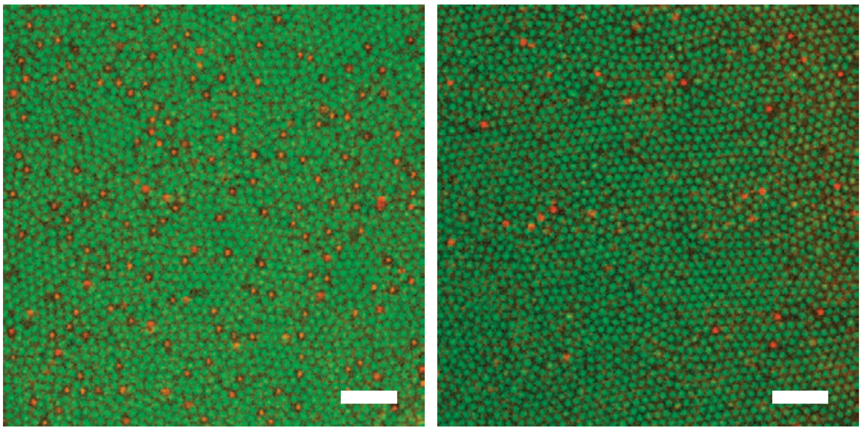

Figure 8.14

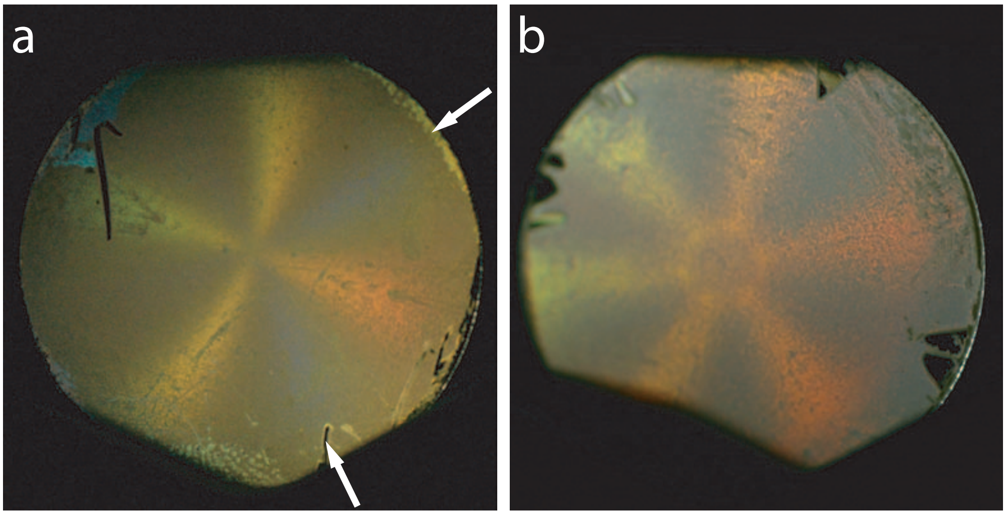

Figure 8.1

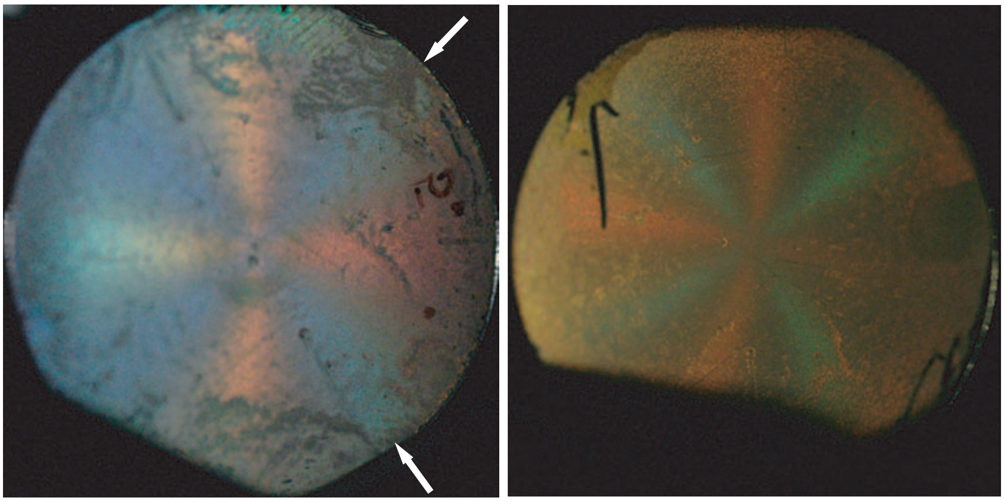

Figure 8.4

# 4

# A new method for growing a diamond or pyrochlore colloidal photonic crystal via the binary $MgCu_2$ Laves structure

We present a new method for fabricating colloidal crystals with a diamond or pyrochlore structure from the binary colloidal Laves phase $MgCu_2$. The correct Laves phase can be selected by epitaxial growth on a (110) face, flattened against a wall, of the $MgCu_2$ structure, which dictates the stacking and can be realized more easily experimentally. The stability of the Laves phases and the effect of growth near a structured wall is checked by computer simulation. Experimentally, two binary $SiO_2$ systems and two binary PMMA systems were subjected to several external fields and interaction parameters, which did not result in the formation of one of the Laves phases yet. Glass formation and separation of the two species interfered with crystallization of a binary structure.

## 4.1 Introduction

Photonic crystals are structures with a periodically varying refractive index, with a spatial period in the order of the wavelength of light. The same way as electrons interact with an atomic lattice, light can interact with a photonic crystal. Therefore, a lot of work is going on with specially designed photonic crystals to achieve the same kind of control over photons as we have in steering the flow of electrons with semiconductors in transistors and diodes. Photonic modes can be shifted by the periodic structure of a photonic crystal, resulting in ranges of frequencies that cannot propagate in a certain direction, called photonic stop gaps. When a photonic stop gap persists for all directions of the photonic structure, the structure has a photonic band gap. Structures with an (almost) complete photonic band gap open the way for fundamental studies on, for example, inhibition of spontaneous emission and they are interesting for the realization of photonic analogues of electronic circuits, including low-loss waveguides, optical diodes and transistors (for recent reviews see [14, 122, 123]).

Despite the fundamental interest and the applications in photonics, three dimensional photonic crystals with a band gap in the visible region of the light spectrum have not been fabricated up till now. The most promising candidates for opening up a large band gap at relatively low refractive index contrasts are the diamond [22, 124, 125] and pyrochlore [126–128] structures, for which a band gap opens up at a refractive index contrast around 2 between bands 2 and 3. Several methods for the experimental realization of the diamond and pyrochlore structure have already been proposed, including direct laser writing [129] and the laborious method of nanorobotic manipulation of colloids [130].

A more suitable method for creating a photonic crystal with a band gap in the visible, is self-assembly of colloidal spheres [131–133], for which per definition the periodicity is in the right size range. However, the usual colloidal dispersions self-assemble in a gravitational field into a face centered cubic (fcc) structure, which only has a band gap for the inverted structure between bands 8 and 9 starting from a dielectric index contrast of about 2.9 [20, 134–136]. Materials with such a high dielectric contrast and no absorption in the visible range are not readily available. The fact that this band gap opens between higher bands, also makes it less stable against disorder [137, 138]. Several methods have been proposed for self-organization of colloids in a diamond structure. In one of these methods the interaction potential of the colloids is made non-spherical [139] by making attracting or repelling patches [140] or by attaching DNA to the colloids [141]. Another method proposes to self-assemble microspheres into tetrahedral clusters [128, 142], which in turn can form diamond or pyrochlore structures. [143]. A very laborious route towards pyrochlore lattices is suggested by Garcia-Adeva [127], who proposes to use layer-by-layer growth as shown by Velikov et al. [112]. Here we propose a new method to create the diamond or pyrochlore structure by self-assembly of simple spherically symmetric colloids via a binary colloidal crystal.

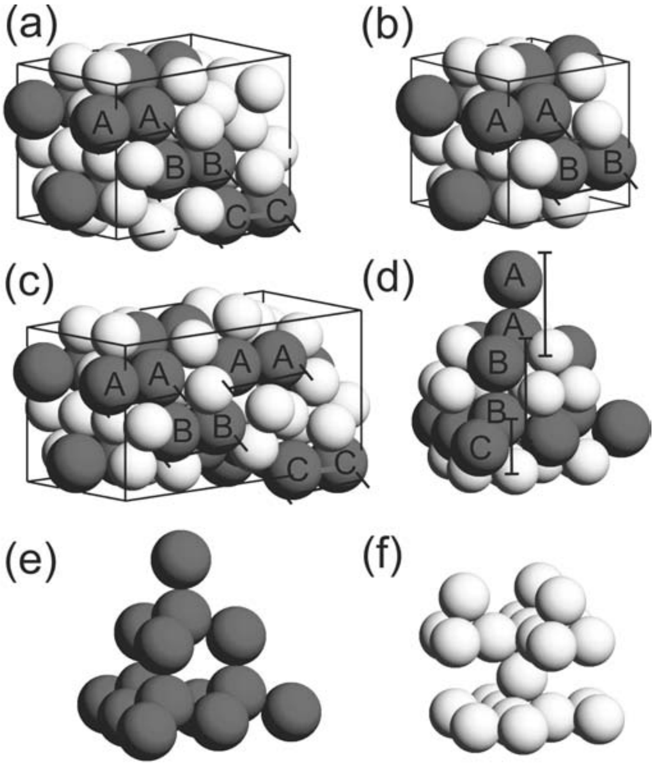

**Figure 4.1:** Binary Laves crystal structures, where the large spheres are depicted dark grey and the small spheres are depicted light grey: (a) $MgCu_2$ (b) $MgZn_2$ (c) $MgNi_2$. The $MgCu_2$ structure (d) is a combination of the diamond (e) and a pyrochlore (f) structure.

## 4.2 The binary Laves phase $MgCu_2$

One of the problems in growing diamond and pyrochlore structures from simple colloids is the fact that the structures are very open, with a low filling fraction, making the structure less stable. In our method, we get around this problem by growing a binary crystal, with a high volume fraction. A suitable binary structure for growing both diamond and pyrochlore is the $MgCu_2$ structure, one of the three binary Laves phases. The three Laves phases are shown in Figure 4.1 a-c. All three structures have hexagonal layers of large spheres, stacked in different fashions: $AABBCC$ for $MgCu_2$, in $AABB$ for $MgZn_2$ and $AABBAACC$ for $MgNi_2$. The holes in between the large spheres are filled with small spheres in alternating hexagonal and kagomé layers.

The $MgCu_2$ structure consists of small and large particles with a size ratio at close packing of $\gamma = \sigma_S/\sigma_L = (\sqrt{2}/\sqrt{3}) \approx 0.816$, where $\sigma_L$ is the diameter of the large sphere and $\sigma_S$ is the diameter of the small spheres. The large spheres are on the sites of the diamond lattice, which is equivalent to two interpenetrating fcc lattices and the small spheres are in the holes in between the diamond lattice, on the sites of a pyrochlore lattice (Figure 4.1 d-f). At close packing, all small spheres are touching and all large spheres are touching, but they are not mutually touching. The diamond and the pyrochlore structures are therefore both self-supporting and their packing fraction is 34% and 37%, respectively. The packing fraction of the $MgCu_2$ structure at close-packing is 71%, which

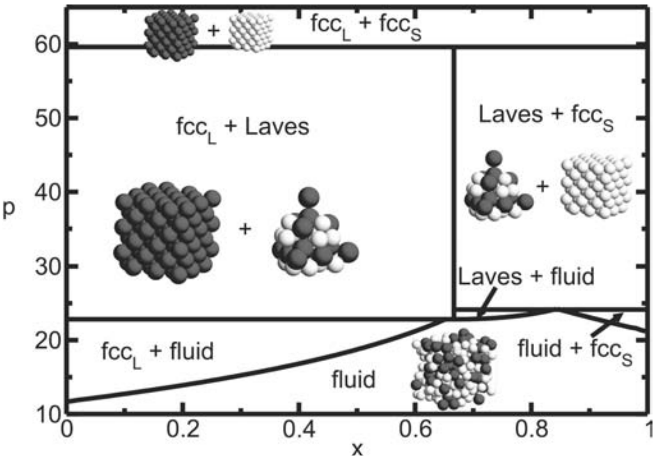

**Figure 4.2:** Phase diagram of binary hard spheres with size ratio of $\gamma = 0.82$.

is a bit lower than the packing fraction of a close-packed fcc structure of 74%. By using different materials for the two components in the binary $MgCu_2$ crystal, one of the two components can be removed in a later stage. Selective removal of one component from a binary crystal has proved successful before by Vlasov et al. by dissolution [144] and by Velikov et al. by burning [112].

## 4.3 Stability of the Laves phases

The Laves structures have been observed experimentally in mixtures of attracting particles consisting of poly(4-vinylpyridine) and polystyrene microgels for size ratios of 0.43 and 0.73, respectively [48] and in charge stabilized systems for size ratios 0.62-0.7 [35]. Recently, also in simulations, the spontaneous crystallization of the binary Laves phase $MgZn_2$ was found in a glass-forming Wahnström binary Lennard-Jones liquid [37]. Here, we studied the stability of hard-sphere Laves structures.

To study the stability of the $MgCu_2$ phase, a phase diagram was calculated for a binary mixture of hard spheres with a size ratio of 0.82 in the reduced pressure $p = P\sigma_L^3/\mathrm{kT}$, composition $x$ representation, where $x = N_S/(N_S + N_L)$ is the number fraction of small spheres, k is the Boltzmann constant and T is the absolute temperature. The phase diagram (Figure 4.2) is obtained from Gibbs free energy data, where the free energies of the Laves phases are calculated using Monte Carlo (MC) simulations and the free energies of the fluid and the fcc phases are taken from analytical results [145, 146]. The phase diagram mainly consists of coexistence regions where the tie lines are horizontal. For example in the region marked '$\mathrm{fcc_L}$+Laves', the stable system has an fcc crystal of large spheres in coexistence with Laves structures. The pressure region where the Laves structures are stable $p = 22.8 - 59.6$ corresponds to packing fractions $\eta = 0.59 - 0.66$. For hard spheres, the size ratio range in which the Laves structures are stable is $\gamma = 0.74 - 0.84$. For soft repulsive interparticle potentials, this stability range shifts to lower values.

The relative stability of the three different Laves phases was studied by calculating their Helmholtz free energies [147] with extrapolation to the infinite-system limit [148].

The free-energy difference between the three structures turned out to be on the order of $10^{-3}$kT per particle (at $\eta = 0.6$ and a size ratio of 0.82). Due to this small energy difference we expect to see a mixture of all three Laves phases in experiments.

## 4.4 Selective epitaxial growth of $MgCu_2$

Since only the $MgCu_2$ Laves phase is suitable for creation of diamond or pyrochlore structures, the growth of this phase has to be made more favorable than the growth of the other two phases. The difference between the three phases is comparable with the difference between the fcc structure and the hexagonal close packed (hcp) structure: they both consist of hexagonal layers, only the stacking is different. It has been shown before by Hoogenboom et al., that the hcp structure can be obtained in pure form by directing the growth by an epitaxial template with a pattern of a plane orthogonal to the hexagonal planes [74, 75]. This plane reflects the *ABAB* stacking of hcp and therefore excludes the growth of the fcc structure. We found a similar plane in the $MgCu_2$ structure, the (110) plane, orthogonal to the hexagonal and kagomé planes, which dictates the *AABBCC* stacking. The plane is shown in the inset (a) in Figure 4.3.

In a simulation, we have studied a binary mixture with volume fraction $\eta = 0.555$ on a wall which is templated with a structure which resembles the (110) face of $MgCu_2$, but with all spheres touching the wall. This pattern can be made experimentally by sticking spheres to a glass wall with optical tweezers as described in Section 2.3.3. The spacing of the spheres in the template corresponds to $\eta = 0.59$, the $MgCu_2$ bulk freezing density. MC simulations were done in the canonical (NVT) ensemble with 4,077 particles, with patterned walls at $z = 0$ and $z = 35\sigma_\mathrm{L}$ and periodic boundary conditions in the other two directions. Figure 4.3 shows a snapshot of the simulation along the $z$-direction together with the equilibrium density profile. We clearly observed 7-8 crystalline layers close to the wall and a fluid phase in the middle, i.e. spontaneous crystallization of the $MgCu_2$ phase is observed on the template below bulk coexistence. This simulation illustrates the feasibility of the proposed method.

## 4.5 Towards experimental realization of the Laves structures

From the phase diagram calculated for a binary hard sphere system of spheres with a size ratio of 0.82 (Figure 4.2), it can be seen that the Laves structures are thermodynamically stable for a large range of parameters. Also for size ratios which deviate slightly from this ideal value of 0.82, the Laves structures are found in simulation. This also comes out of recent more extensive simulations looking into stability of many binary crystal structures in the size range of interest [149]. When a colloidal system changes from a hard to a soft potential, the effective radius of the small spheres increases relatively more than the effective radius of the large spheres. Consequently, the size ratio of a soft system is effectively larger than the ratio of the radii of the dry spheres. This is an explanation for the fact that the Laves phases are also found in simulations of soft systems, but for

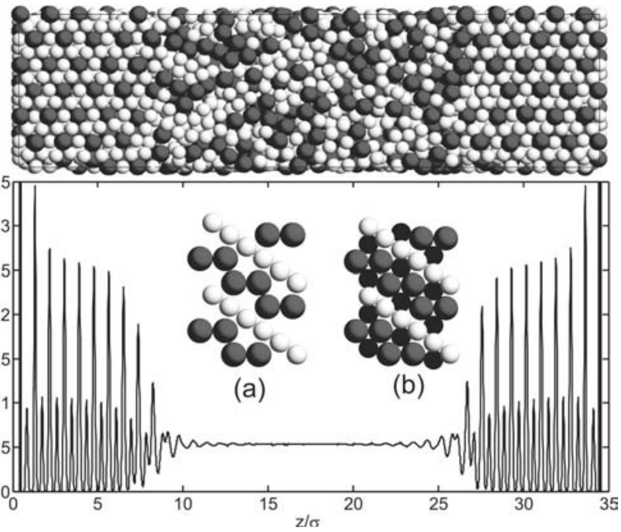

**Figure 4.3:** Density profile and a snapshot of the simulation of a binary hard sphere system of small (light grey) and large (dark grey) spheres in between walls patterned with small and large spheres in the pattern of a (110) $MgCu_2$ face (Structure 1). Structure 2 shows the wall pattern plus the first plane of mobile small spheres just above the template in black.

lower size ratios. In this section, we show the results of sedimentation, spin coating, shearing and dielectrophoresis for four different dispersions, which can be tuned from hard to soft, thereby screening a range of effective size ratios. Since a Laves phase was not formed in any of the dispersions irrespective of the external fields used, we will explain the experimental difficulties which were encountered and we will discuss some changes to the present methods, to increase the chance for successful growth of the Laves phases in the future.

## 4.5.1 Experimental methods

### Binary dispersions

Four different dispersions, one of silica particles and two of poly(methyl methacrylate) (PMMA) particles, were used to probe several points in the phase space that was explored by simulation, as described in Section 4.3.

For the first mixture of silica particles we used particles which both had a fluorescently labelled core and an unlabelled shell. The large particles were labelled with the dye fluorescein isothiocianate (FITC). The small particles were 860 nm in diameter with a core of about 200 nm. The large particles were 1.2 $\mu$m in diameter with a core of 400 nm. The hard sphere size ratio for these particles is 0.72, which is slightly too low for the formation of the Laves phases. However, we have seen that the effective size ratio in the solvents is higher. For example, the effective size ratio in the ethoxylated trimethylol propane triacrylate (ETPTA) monomer is 0.78, as derived from confocal images of single crystals of the two particles. The effective close-packed radius is obtained from a random hexagonal close packed (rhcp) crystal formed by sedimentation assuming compression by gravity till close-packing.

The second silica dispersion also consisted of core-shell particles. The large particles were labelled with FITC. The core had a diameter of 830 nm, the total diameter was 1.48 $\mu$m as determined by transmission electron microscopy (TEM). The small particles were labelled with the dye rhodamine isothiocianate (RITC) in a core of approximately 200 nm in diameter. The total diameter of the small particles was 1.14 $\mu$m, as determined by TEM. The hard sphere size ratio for these particles is 0.77.

All FITC labelled silica particles were synthesized via a modified Stöber-method and the cores were grown out via a Giesche seeded growth procedure [116]. The RITC labelled particles were synthesized according to the method described by Verhaegh et al. [115]. The silica particles, described above, were dispersed in one of the following solvents (depending on the method in which they were used): ethanol, glycerol/water, DMSO/water or the ETPTA monomer (MW. 428, Aldrich), with 1-2% (w/w) of photoinitiator 2-hydroxy-2-methyl-propiophenone (Darocur 1173, 97%, Aldrich).

The first PMMA dispersion was made of completely labelled spheres, where the small spheres were labelled with RITC and the large spheres with 7-nitrobenzo-2-oxa-1,3-diazole (NBD). The small spheres had a diameter of 2.0 $\mu$m and the large spheres had a diameter of 2.4 $\mu$m. The hard sphere size ratio of this system is 0.83, which is within the range that can form Laves phases according to simulations.

The second PMMA dispersion was similar to the first, with different radii: the small spheres had a diameter of 1.7 $\mu$m and the large spheres had a diameter of 2.5 $\mu$m. The hard sphere size ratio of this system is 0.68, which is lower than the range of sizes that form Laves phases in simulation. Therefore, we used this system only with a soft potential, in dispersions without added salt or at low salt concentrations, which effectively makes the size ratio higher.

The PMMA particles were dispersed in a solvent mixture of cyclohexyl bromide (CHB) and cis-decahydronaphthalene (decalin), with which the density or the refractive index of the particles can be matched at different volume ratios of the mixture. The charge of the particles and the softness of the potential between the particles can be tuned by adding the salt tetrabutyl ammonium bromide (TBAB).

The dispersions were made in a number ratio of $x = N_\mathrm{S}/(N_\mathrm{S}+N_\mathrm{L}) = 2/3$ or, similarly, $N_\mathrm{L}$:$N_\mathrm{S}$=1:2, which agrees with the stoichiometry of $MgCu_2$, unless stated differently.

### Sedimentation

The dispersions were allowed to sediment in three different experimental setups:

- a capillary of 0.1 mm × 2.0 mm cross section was filled with the dispersion by capillary forces, after which it was sealed with Norland Optical Adhesive 68 or closed by melting the ends. The capillaries were kept in horizontal orientation.

- a capillary was filled and closed the same way, but then kept in vertical orientation to have a longer sedimentation height.

- a 22 mm diameter no. 1 round cover slip was glued to a bottomless flask with Norland No. 68 optical adhesive and filled with about 1-2 mm of the dispersion.

### Sedimentation on a $MgCu_2$ template

To test whether the crystallization of $MgCu_2$ can be induced by a templated surface, as is shown in simulation (Section 4.4), we combined sedimentation with epitaxial growth. A 22 mm diameter no. 1 round cover slip was templated with an electron beam lithography template in PMMA as described in Section 2.3.1. The pattern of the holes resembled the (110) plane of $MgCu_2$ (see Section 4.4), however, with equally sized holes. This templated slide was glued to a bottomless flask with Norland Optical Adhesive 68. The flask was then filled with about a millimeter of dispersion.

### Shear experiments

To study crystallization of binary dispersions induced by shear, the binary dispersions were sheared in two ways: 10 $\mu$l dispersion was sheared by hand between two round glass cover slides (a 22 mm diameter no. 1 bottom slide and a 16 or 18 mm diameter no.1 top slide).

Alternatively, about 50 $\mu$l dispersion was sheared in the High Precision Parallel Plate Oscillating Shear Cell (HIPPOS), which is described by Wu [150, 151]. This shear cell can be mounted on top of an inverted confocal microscope. The dispersion was sheared between two glass slides (Kleener & Bison, 24 mm x 50 mm no. 1 glass slides), the gap between the slides can be tuned from 20 $\mu$m to 200 $\mu$m. The speed of the plates relative to each other was kept between 5 and 100 $\mu$m/s in our experiments, with an amplitude of 600 $\mu$m. The ratio of the absolute speeds of the plates could be varied to put the zero-velocity plane (the plane in the dispersion with zero absolute speed) in the focal plane of the confocal.

### Spin coating

The dispersions were spin coated on a round cover slide which was cleaned with chromosulfuric acid to remove contamination and to make the surface hydrophilic. A droplet of about 15-20 $\mu$l dispersion was spinned on the slide in the spin coater (model P6700, Specialty Coating Systems, USA) at different spin speeds. When the dispersion was spin-coated in the monomer ETPTA, the monomer was polymerized with the short wave UV lamp for a few minutes.

### Dielectrophoretic compression

Dispersions were compressed in a dielectrophoretic cell, consisting of two parallel plate electrodes with a thin electrode-free slit in the middle of one of the electrodes. At the edge of the slit, an electric field gradient pushes the colloidal particles into the slit. The principles of dielectrophoretic compression are explained in Chapter 2.5, the cell design is shown in Figure 2.4.

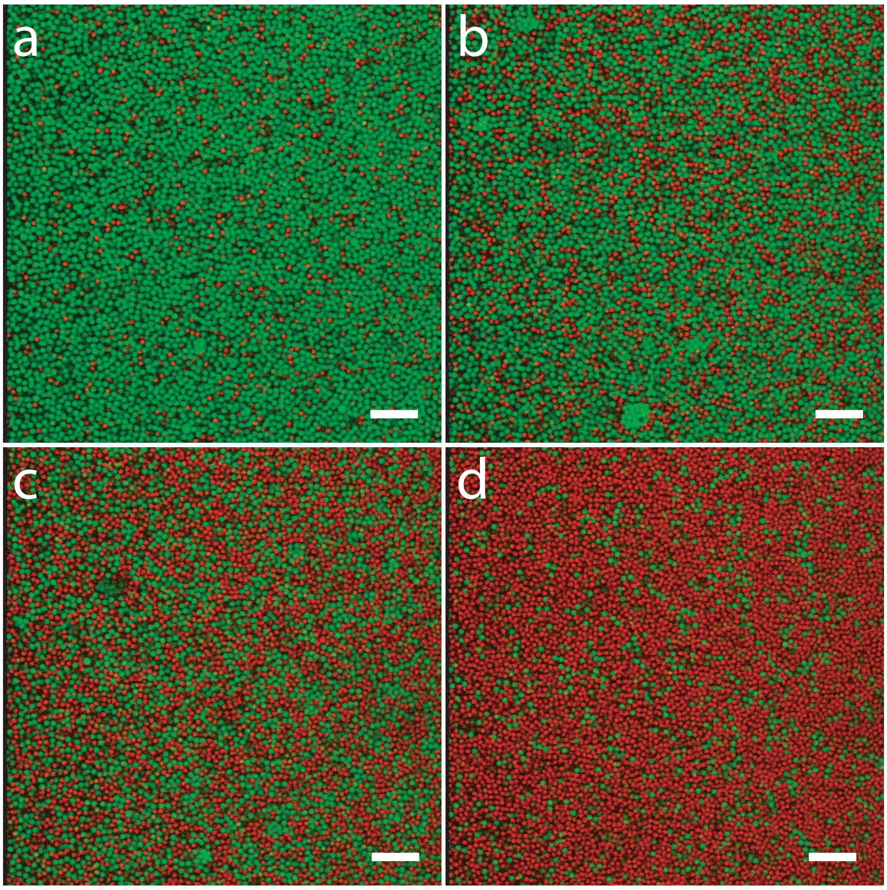

**Figure 4.4:** A range of number ratios in a horizontal capillary filled with a dispersion of 2.4 $\mu$m (green) and 2.0 $\mu$m (red) PMMA particles in a mix of CHB, saturated with TBAB and 21.1% w/w cis-decalin with $\phi = 0.29$. (a) is in the bottom of the sample, (d) on the top of the sample and the other two are in between. The total height was 100 $\mu$m. The scale bars are 20 $\mu$m.

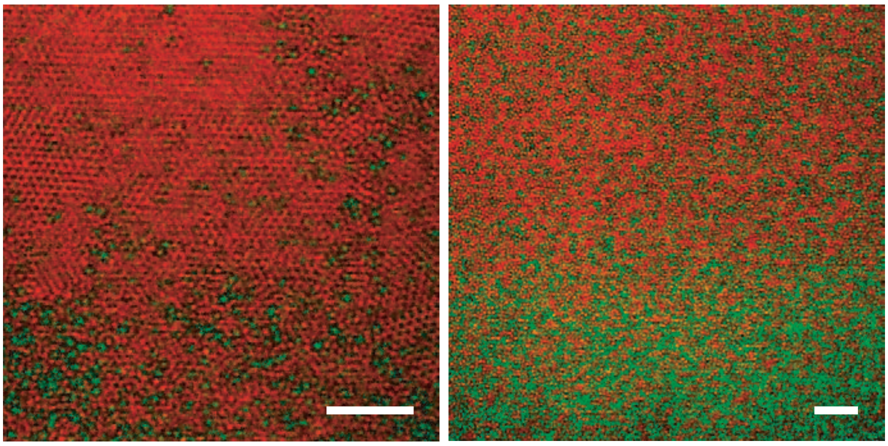

**Figure 4.5:** Sharp transitions in a vertical sedimenting sample of 0.86 $\mu$m and 1.2 $\mu$m silica spheres in DMSO/$H_2O$. The scale bars are 10 $\mu$m.

### Confocal Laser Scanning Microscopy

The 3D structure of all samples was imaged using a Confocal Scanning Laser Microscope (Leica type NT or SP2). The fluorescent dye FITC was excited with the 488 nm line, the RITC dye was excited with the 543 nm line. On the SP2 confocal the signals of these different dyes can be scanned sequentially for better resolution of the signal. The scan head of the NT confocal can be placed on a tilted microscope frame to enable scanning in (sedimenting) samples, that have to be in vertical position. In all the confocal images the red particles depict the small species (RITC dye) and the green particles depict the large particles (NBD or FITC dye).

## 4.5.2 Results and discussion

### Sedimentation

As explained in Chapter 2.2, the sedimentation speed of colloidal particles in a fluid is proportional to $R^2$. Therefore, in the binary dispersion used in this study, the large colloids sediment roughly 1.5 times faster than the small ones (assuming similar density). Of course we are well aware of the fact that this single particle argument could very well be too simplistic as it does not take into account the complex many body effects of hydrodynamics in concentrated binary systems and also does not take into account local density differences caused by variations in concentrations of the different species [152].

The difference in sedimentation velocity is clearly seen in all horizontal capillary samples with a hard-sphere or repulsive interaction between the colloids. On the bottom of the sample cell, there were more large particles, while on the top of the sample cell there were more small particles. For example, in Figure 4.4 a range of number ratios is seen in a sample of 2.4 $\mu$m and 2.0 $\mu$m PMMA particles in a mix of CHB, saturated with TBAB and 21.1% w/w cis-decalin with $\phi = 0.29$.

The exception to the continuous change of number ratios over height is found near the walls of the sample cell for the hard-sphere dispersions of 0.86 $\mu$m and 1.2 $\mu$m silica spheres in ETPTA monomer or in glycerol, and also in the hard-sphere (salt saturated) dispersions of 2.4 $\mu$m and 2.0 $\mu$m PMMA particles in CHB. In these dispersions, the wall is primarily occupied with small particles. This effect is probably due to shear near the wall, as will be discussed in Section 4.5.2.

In the vertical capillaries, also a change of number ratios over height is seen, as expected. In some samples, a glass is found at every height, with more large particles at the bottom of the sediment (at the top of the sample if the particles sediment upwards) and more small at the top of the sediment. The designation glass or gel was given by the experimental observation of the absence of long time self diffusion. In many samples, however, the number of small particles at the bottom of the sediment was so small that about 1-2 mm of fcc$_\mathrm{L}$ structure formed, which can also be clearly seen by eye, from the Bragg scattering of the crystal domains and the presence of Bragg peaks in the Fourier plane of the focal region which is visible with the Bertrand lens. Similarly, 1-2 mm of fcc$_\mathrm{S}$ structure was found on the top of the sediment. The transition between the glass region and the single fcc crystals was clearly discernable, both with the confocal and with the naked eye. Confocal images of the sharp transitions between these concentration regions are shown in Figure 4.5. The images were made on a 90° tilted confocal microscope frame, such that the gravitational field was parallel to the imaging plane, in a sedimented $\phi = 0.3$ dispersion of 0.86 $\mu$m and 1.2 $\mu$m silica spheres in DMSO/$H_2O$ (20 volume % $H_2O$).

The formation of the single-component $fcc_L$ crystals at the bottom of the sediment, below the glass is somewhat remarkable, since there is a discontinuous jump in the density of the small and large spheres. A possible explanation is that at the bottom of the sample a critical concentration was reached where the large spheres could crystallize fast enough with respect to sedimentation and glass formation, that the crystallizing system expelled the small particles from the crystal. Another possible explanation is that the discontinuity is due to the fact that it is very hard to put a capillary microscopically vertical, so the sedimenting particles hit the wall of the capillary, giving different sedimentation behavior than expected. A third explanation for an inhomogeneous distribution of small and large spheres can be found in Rayleigh-Taylor-like sedimentation instabilities as described below.

In studying glass formation, the concentration gradient found by letting a binary dispersion sediment can be used advantageously [153]. For the analysis described in this work, we studied two types of experimental binary systems, sedimented in a vertical capillary by confocal microscopy. We studied the local bond orientational order and the radial distribution function both in 2D and in 3D, at different heights in the sample. From these data we could conclude that the compositional change in the vertical capillary is ideal to study phase behavior as a function of composition in a binary dispersion, from a substitutional crystal to a glass.

The hard-sphere-like dispersions of both silica and PMMA colloids did not yield any binary crystals. These systems formed single-component fcc crystals on the top and on the bottom of the samples, with a binary glass in the mixed regions. We therefore turned to dispersions with soft potentials, since these dispersions are known to crystallize faster than systems with a harder potential. A dispersion of 2.4 $\mu$m and 2.0 $\mu$m PMMA particles in CHB solvent without added TBAB salt, developed opposite charges by preferential uptake of ions from the solution, as is described in [8]. This resulted in a well mixed dispersion (Figure 4.6a), which did not evolve to a height dependent composition change, but which also did not form binary crystals, since it fell out of equilibrium in a binary gel state [154].

At medium salt concentration of 130 $\mu$M TBAB (formed by mixing one part of CHB which is saturated in TBAB and one part of pure CHB), the dispersion of 2.4 $\mu$m and 2.0 $\mu$m PMMA particles in CHB formed a mixed fcc on the bottom (Figure 4.6b) and a binary glass on the top of the sample cell. The mixed fcc, also referred to as a solid solution, forms because of the high effective size ratio of the two types of colloids, they effectively have almost the same size.

In the dispersion of 2.5 $\mu$m and 1.7 $\mu$m PMMA particles in CHB/decalin (27.2% w/w decalin) with medium salt concentration, we have seen nucleation of small $fcc_L$ crystals, as is shown in Figure 4.6c.

Besides a changing number ratio with height and time caused by different sedimentation speeds, inhomogeneities of the two types of colloids in the horizontal plane was caused by sedimentation instabilities, reminiscent of the Rayleigh-Taylor instabilities in

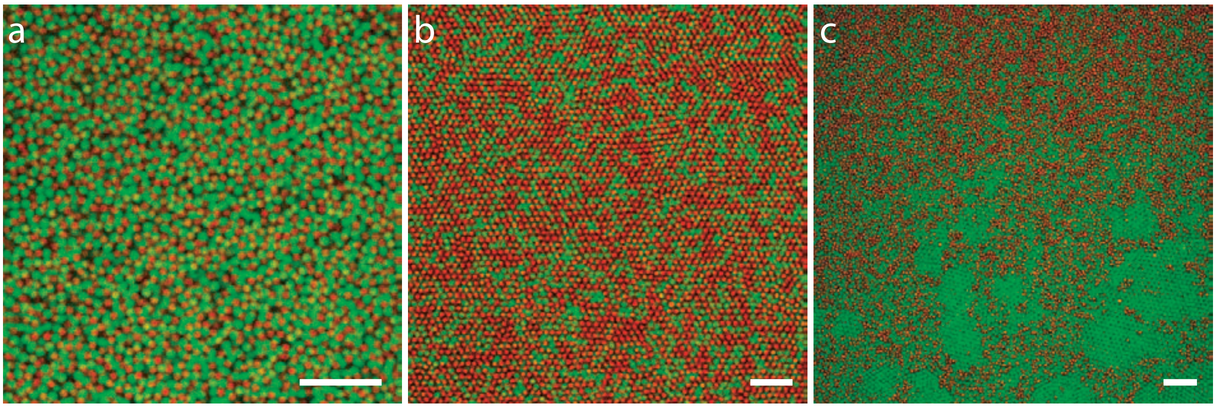

**Figure 4.6:** (a) Oppositely charged dispersion of 2.4 $\mu$m and 2.0 $\mu$m PMMA particles in CHB solvent without added TBAB salt in a gelled state. (b) Mixed fcc crystal (solid solution) in a dispersion of 2.4 $\mu$m and 2.0 $\mu$m PMMA particles in CHB, at a medium salt concentration. (c) Small $\mathrm{fcc_L}$ nuclei formed in a dispersion of 2.5 $\mu$m and 1.7 $\mu$m PMMA particles in CHB/decalin (27.2% w/w decalin) with medium salt concentration. The scale bars are 20 $\mu$m.

two-layered liquids. When a dispersion was left to sediment for a while in one direction for example while closing the sample cell (after which one of the species is more present at the bottom of the sample than the other) and then turned around, the density difference of a layered system can develop, giving a network-like structure. This can be seen in Figure 4.7 in images made of the silica dispersion of 0.86 $\mu$m and 1.2 $\mu$m spheres in DMSO/$H_2O$ and for both PMMA dispersions in a CHB/decalin mixture. These patterns were very similar to experiments recently reported for a one-component system made to sediment from an inhomogeneous starting condition. These patterns were explained both theoretically and by computer simulations that included full hydrodynamics [155]. As a result of these sedimentation instabilities, the binary mixture ends up in an inhomogeneous state, which is disadvantageous for the formation of binary crystals.

Since sedimentation leads to changing number ratios with time and the spatial coordinate in the direction of gravity, which decreases the chance of forming binary crystals, we have tried to match the density of the PMMA colloidal particles with the density of the solvent. However, for the 2.5 $\mu$m and 1.7 $\mu$m PMMA spheres we found that the densities of the two types of colloids were too far apart to find a matching solvent for both. There was quite a large regime in which the colloids are sedimenting in different directions. For the system of 2.4 $\mu$m and 2.0 $\mu$m PMMA spheres, we found that a density matching solvent was so far off matching the refractive index that confocal imaging became impossible.

The effect of the different sedimentation speeds of the two types of colloids in a binary dispersion can be used advantageously to create a number ratio gradient over the height of a sample, as discussed by Royall et al. [153]. In one experiment, many number ratios can be tested quite conveniently, for instance, in the case of an investigation on the effects of structure in glass formation in binary systems. Of course, if the formation of the gradient is slow enough that in some regions binary crystallization can occur it is also an efficient way to test the number ratio at which crystallization is fastest for a certain

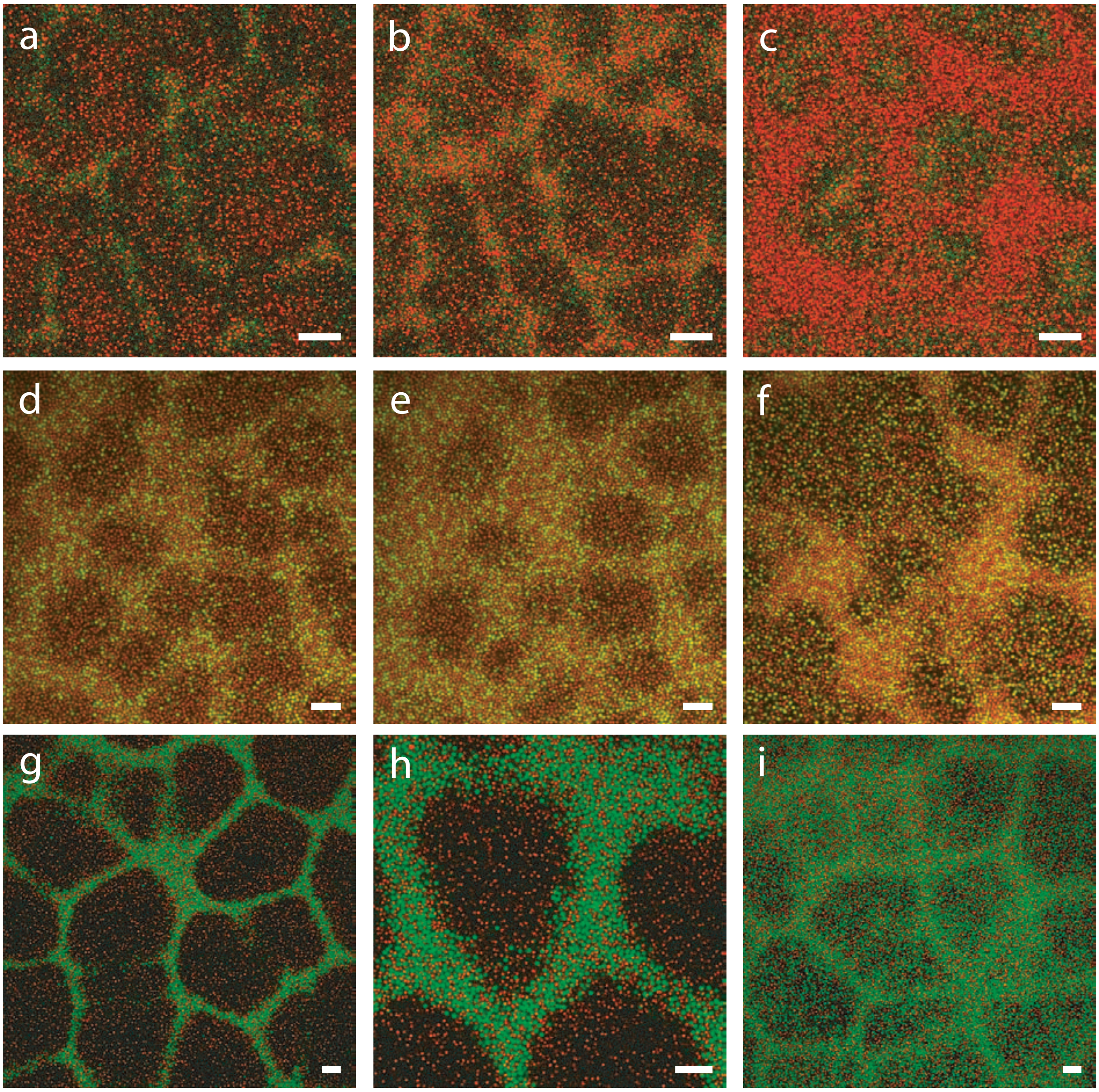

**Figure 4.7:** Rayleigh-Taylor-like sedimentation instabilities observed in (a,b,c) a $\phi = 0.3$ dispersion of 0.86 $\mu$m and 1.2 $\mu$m silica spheres in DMSO/$H_2O$, (d,e,f) a $\phi = 0.29$ dispersion of 2.4 $\mu$m and 2.0 $\mu$m PMMA spheres in CHB/decalin (27.2% w/w decalin) saturated with TBAB salt, (g,h,i) a $\phi = 0.3$ dispersion of 2.5 $\mu$m and 1.7 $\mu$m PMMA spheres in CHB/decalin (27.2% w/w decalin) in a TBAB salt gradient. The red spheres represent the small particles, the green spheres represent the large particles. The scale bars are 20 $\mu$m.

volume fraction.

A more suitable situation for binary crystallization could be created, if density matching alone is not enough (or cannot be achieved because densities of the different particles is not close enough), by taking a solvent which is as close to matching as possible and then eliminating gravity to first order by slowly rotating the sample around its horizontal axis in a carrousel, as was proposed by Bartlett et al. [107]. The angular velocity should in this case be high enough that the dispersion does not have the time to separate under gravity, but slow enough that the rotationally induced shear gradient and centrifugal force do not influence the binary crystallization process.

### Sedimentation on a $MgCu_2$ template

Preliminary sedimentation experiments on a $MgCu_2$ template were performed with a $\phi = 0.025$ $SiO_2$ dispersion of 1.48 $\mu$m and 1.14 $\mu$m particles (with a hard-sphere size ratio of 0.77) in a mixture of glycerol and water in a volume ratio of 6.5:1. Dispersions in monomer ETPTA were also tried, but this solvent dissolved the PMMA e-beam template. The glycerol dispersion did partially go into the holes of the template. The intended (110) plane of the $MgCu_2$ structure did not nucleate on this template. Probably this is due to the fact that the holes were equally sized and large enough for both the large and the small particles to go in. As expected, also the next layers did not adopt a $MgCu_2$ structure.

### Shear experiments

A dispersion of 860 nm and 1.2 $\mu$m diameter silica particles (as described in Section 4.5.1) in a number ratio of 2:1 with a volume fraction of $\phi = 0.5$ in monomer ETPTA and photoinitiator was sheared in the HIPPOS using an oscillatory shear. Immediately after closing the cell, there were almost no large particles at the bottom of the sample cell. We attribute this unexpected observation to the shear which was applied to the dispersion upon closing the sample cell, squeezing the dispersion to the sides. We do not understand this effect of shear, but we hypothesize that it results from the fact that the small spheres can become trapped between the wall and large spheres which are also touching the wall, while large spheres cannot become trapped this way.

Shearing at $\dot{\gamma} = 0.05$ s$^{-1}$ and $\dot{\gamma} = 0.1$ s$^{-1}$ (with a plate separation of 100 $\mu$m) did not have an observable effect on the order in the samples. When shearing at a relative speed of the plates of $\dot{\gamma} = 0.2$ s$^{-1}$, the large particles in the layer just above the bottom layer grouped in small, elongated clusters. These clusters grouped further in time, forming long bands perpendicular to the flow direction, through the full width of the cell (Figure 4.8a and 4.8b). The close packed lines of the large particles in the bands were parallel to the flow direction (as expected for a single-species dispersion). The bands (which were only in the layer just above the bottom layer) also persisted when the zero velocity plane was shifted and when the speed of the plates was increased to $\dot{\gamma} = 1$ s$^{-1}$. At the turning point of the shearing motion, the band were disrupted slightly, but they were quickly reformed after the shearing speed became steady again.

This result was reproduced in another sample of the same dispersion. For this sample, we started shearing at $\dot{\gamma} = 1$ s$^{-1}$ from the beginning. This time the bands of large particles extended over several (∼3) layers instead of only the second layer.

Shearing the same dispersion by hand for about 1 minute did not give clear structure to the dispersion. Only the top and bottom plate again were occupied with significantly more small than large particles. Also a small air bubble, which was accidently incorporated in the sample was completely covered by the small particles.

After shearing the dispersion of 2.0 $\mu$m and 2.4 $\mu$m PMMA particles in a mixture of CHB saturated with TBAB and 21% (w/w) of cis-decalin by hand for about five minutes, in most places only one or two layers remained. These layers showed clear separation of the large and the small particles into large clusters.

Separation in shear cells can be due to a similar mechanism as the Rayleigh-Taylor-like flow instabilities seen during sedimentation. The horizontal variant of Rayleigh-Taylor instabilities are called Saffman-Taylor instabilities. The instabilities formed in the shear cell are probably a combination of Rayleigh-Taylor and Saffman-Taylor instabilities.

### Spin coating

A drop of 18 $\mu$l dispersion of 860 nm and 1.2 $\mu$m diameter silica particles in a number ratio of 2:1 with a volume fraction of $\phi = 0.5$ in monomer ETPTA and photoinitiator was spin coated first at a rate of 300 rpm for 1 minute to spread the droplet and then at a rate of 2000 rpm for several minutes, after which the sample was polymerized with UV light.

The spin coated samples had a dense part on the bottom of mixed dispersion without clear structure, above which voids of empty polymer could be seen. The top layer of polymer was filled with a hexagonally ordered layer of colloids (randomly mixed in size), which were attached to the top surface of the monomer by surface tension. The fact that the top surface was ordered was also seen when studying spin coating single-component dispersions in volatile media (Chapter 8) and was also found by Wu for single-component dispersions in ETPTA. The top layer in these cases can act as a template from which crystallites can grow downwards. The layers below the top layer did not crystallize for this binary case because the binary crystallization rate is too low.

### Dielectrophoretic compression

We compressed a dispersion of 860 nm and 1.2 $\mu$m diameter silica particles with a volume fraction of $\phi = 0.3$ in DMSO/$H_2O$ (20 volume % $H_2O$) in a dielectrophoretic compression cell formed by one slide coated completely with an ITO electrode and another slide, covered with a gold layer except for a slit of about 400 $\mu$m wide (as in Figure 2.4a). The gap between the two slides was about 100 $\mu$m. We applied an oscillating voltage of 13 V peak-peak over the electrodes with a frequency of 1 MHz. The resulting inhomogeneous electric field drives the colloids into the field-free slit by dielectrophoretic forces because of the difference between the dielectric constants of the solvent and the particles.

Applying the voltage over the cell, did repel the particles from the edge of the electrode into the slit, as is shown in Figure 4.9. However, the dispersion did not crystallize in the slit but formed a glass within two hours.

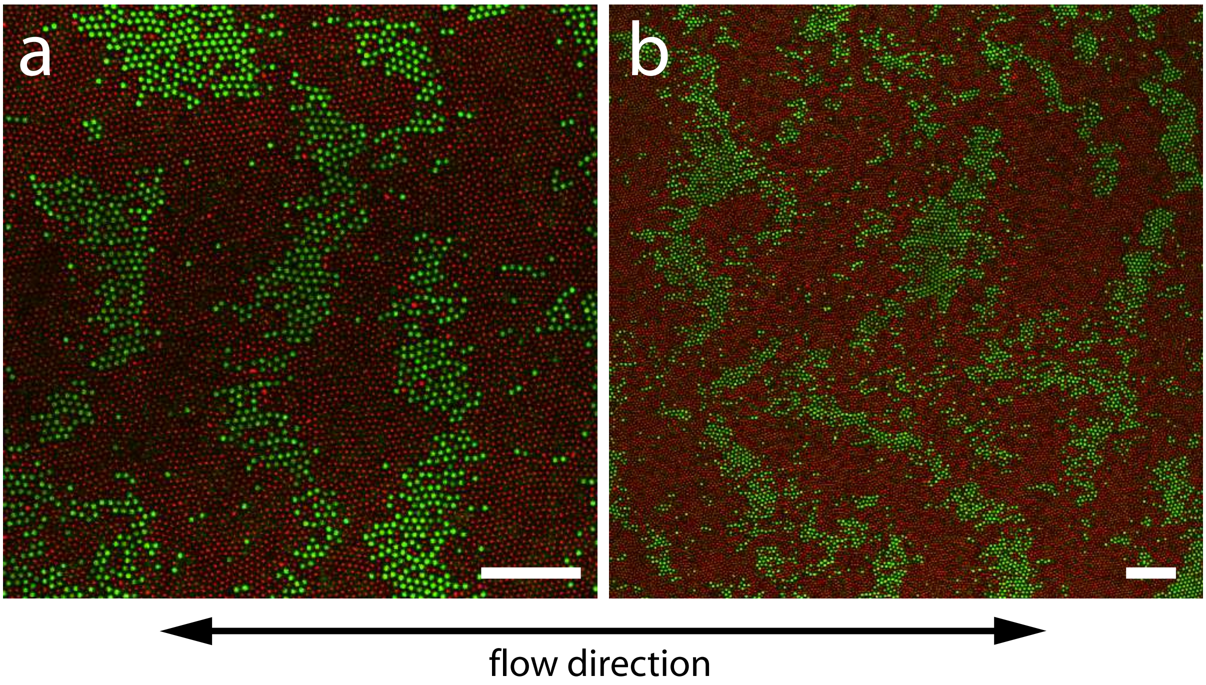

**Figure 4.8:** Confocal images of shear induced bands of large particles (green) perpendicular to the shear direction (the shear-amplitude direction was horizontal in these pictures). The scale bars are 20 $\mu$m.

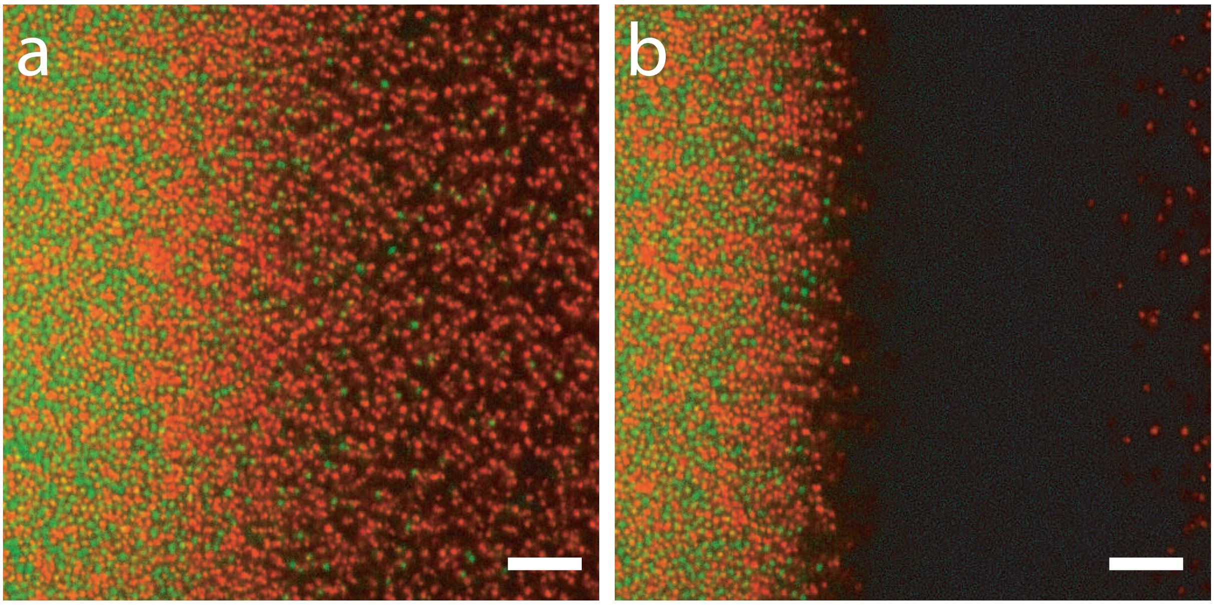

**Figure 4.9:** Confocal $xy$ images of the compression of a binary $SiO_2$ dispersion of 860 nm and 1.2 $\mu$m diameter silica particles in DMSO/$H_2O$ (20 volume % $H_2O$) by dielectrophoretic forces. On the left side of the image is the slit and on the right side are the electrodes. Image (b) is taken some time after image (a). The scale bars are 10 $\mu$m.

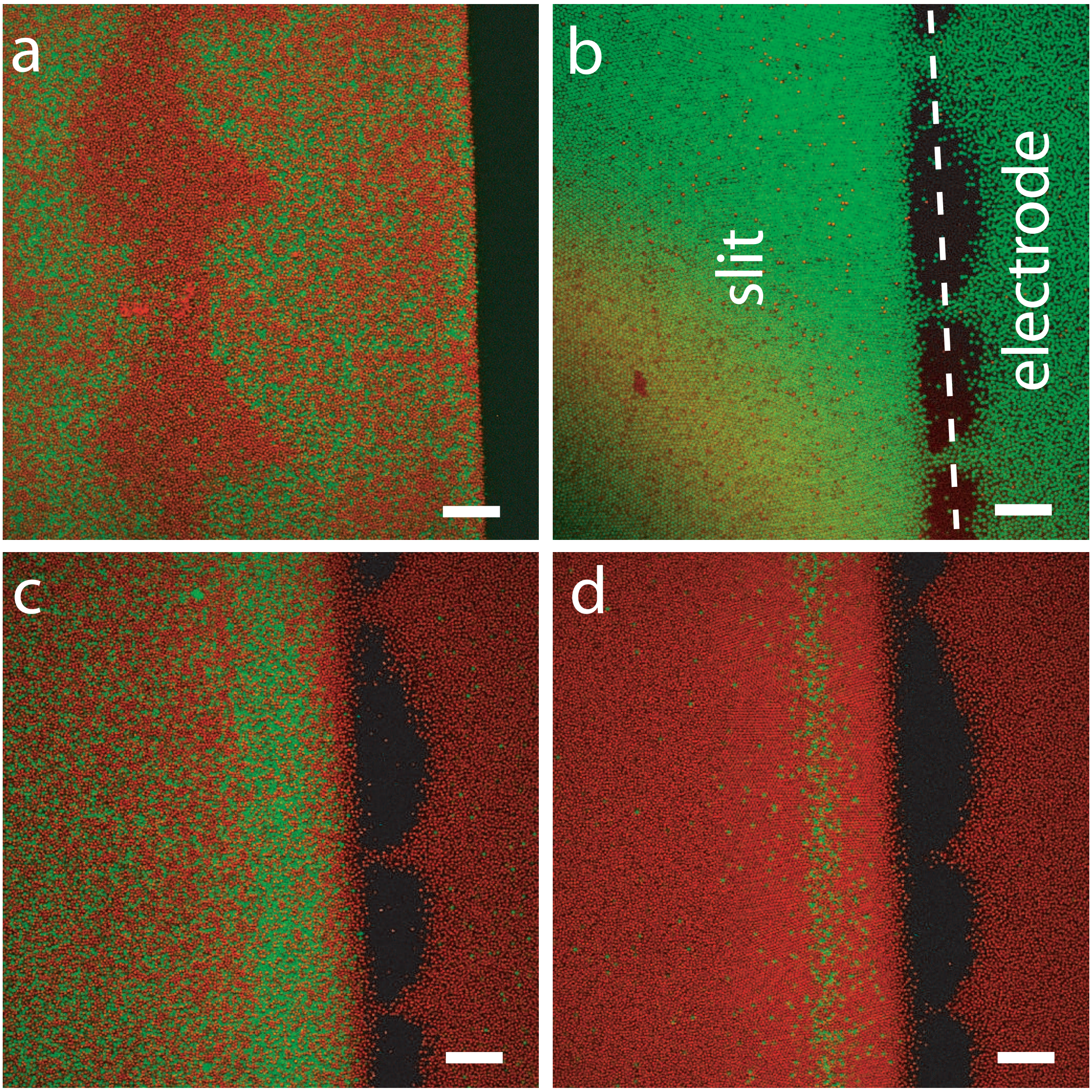

**Figure 4.10:** Confocal $xy$ images of the compression of a binary PMMA dispersion of 2.0 $\mu$m and 2.4 $\mu$m diameter spheres in a CHB/decalin mixture (21% w/w cis-decalin) saturated with TBAB salt by dielectrophoretic forces. (a) After fast compression at 50 V peak-peak, a band of only small particles has been formed in the middle of the slit. The whole image is in the slit of the electrodes. (b,c,d) Compression at 10 V peak-peak. At the left side of the image is the slit and on the right side is the electrode. Image (b) is at the bottom and image (d) is at the top, with (c) in between. The scale bars are 40 $\mu$m.

We also compressed a PMMA dispersion of 2.0 $\mu$m and 2.4 $\mu$m diameter spheres in a CHB/decalin mixture (21% w/w cis-decalin) saturated with TBAB salt in a compression cell as described above. Applying a voltage of 50 V peak-peak over the cell compressed the dispersion too fast, resulting in a region of only small spheres in the middle of the cell (Figure 4.10a), probably due to electro-hydrodynamic instabilities, similar to the flow instabilities during shear.

Compression at a lower voltage of 10 V peak-peak, did not give demixing due to electro-hydrodynamic instabilities. However, now the dispersion did get the chance to sediment, giving an fcc crystal of the large spheres (with some defects of small spheres) on the bottom of the sample and an fcc crystal of the small spheres at the edge of the slit at the top of the sample, as can be seen in Figure 4.10b,c,d. In the figure, the left side of the image is in the slit and the right side is between the electrodes. In Figure 4.10c, the region just inside the slit shows a clear overpopulation by large spheres, from which it can be concluded that the large particles are compressed harder into the slit than the small particles, as expected.

## 4.6 Conclusions

In this chapter a new method was presented for creating colloidal crystals with a diamond and pyrochlore structure, which both have great potential for obtaining a photonic band gap in the visible. The method relies on the formation of the binary colloidal crystal with $MgCu_2$ structure by self-assembly, where the correct stacking is directed by epitaxial growth on a structured wall. The thermodynamic stability of the $MgCu_2$ structure and the other binary Laves phases is checked by computer simulation and found stable for a relatively large regime of size ratios and pressures.

Experimentally, four different binary colloidal systems were used to probe several points in the experimental parameter space. The silica dispersions, in which gravity plays a large role, became easily separated by difference in sedimentation speed and additionally by gravitational instabilities and shear effects. Binary crystals could not form because the changes in composition of the two species both in space and time were too fast compared to the crystallization rate. The PMMA dispersions displayed the same separation of particle species and even density matching (as close as possible for the PMMA particles with slightly different densities) did not solve the problem. Besides separation of species, also glass formation interfered with the crystallization.

Application of other external fields, i.e. spin coating, shear and dielectrophoretic compression, did not yet result in the formation of a binary Laves phase. Fast dielectrophoretic compression gave electro-hydrodynamic flow instabilities, which separated the dispersion and are not understood, while during slow compression the dispersion separated due to gravity. Also the dielectrophoretic forces on the small and large particles are different, leading to inhomogeneous distributions of particles.

From this we can conclude that all external fields tested here should be minimized as much as possible when aiming for formation of binary crystals, since external fields lead to flow and sedimentation instabilities and the forces resulting from the fields are size-dependent. Minimizing gravity is complicated by the difference in density of most colloidal dispersions from different synthesis batches. Complete density matching is therefore impossible. Further minimization of gravitational influence can be done by slowly rotating a sample around the horizontal axis [107].

## 4.7 Acknowledgements

This work was done together with Antti-Pekka Hynninen, who performed computer simulations necessary to construct the phase diagram and investigate the effect of a template. We thank Carlos van Kats, Peter Vergeer, Jacob Hoogenboom, Yu Ling Wu and Dannis 't Hart for the synthesis of the silica particles and Didi Derks, Mirjam Leunissen, Teun Vissers, Johan Stiefelhagen and Peter van Oostrum for the synthesis of the PMMA particles. Furthermore we are grateful to Carlos van Kats for the help with the seeded growth of the 1.48 $\mu$m FITC particles and to Yu Ling Wu for the help with the shear experiments in the HIPPOS and the spin coating experiments.

# 5

# Photonic band structure calculations of dielectric and metallodielectric Laves structures

The photonic band structures of the experimentally realizable close-packed colloidal binary Laves structures, and both constituent structures separately, have been studied using the Korringa Kohn Rostoker (KKR) method implemented in a Fortran program and using MIT Photonic Bands software. The comparison of these two methods opens the possibility to study the validity and the convergence of the results, which have been an issue for diamond related structures in the past. For the combined binary Laves structures and for the constituent structures of $MgZn_2$ and $MgNi_2$, no significant photonic band gaps have been found. Band gaps only open for the constituent structures of $MgCu_2$, i.e. diamond and pyrochlore, but not for the close-packed $MgCu_2$ structure itself. The closing of the band gap of a diamond structure upon inserting small particles at the pyrochlore lattice sites, forming $MgCu_2$, is studied as a function of the size ratio of the spheres. At a size ratio of 0.58, the band gap between bands 2 and 3 closes, because the air band and the dielectric band can no longer be separated in phases with a different dielectric contrast. For dielectric diamond and pyrochlore structures, the largest band gaps open between bands 2 and 3 for the direct structures at a dielectric contrast of 5. For inverse structures, this gap opens at a contrast of 10 and 12 for pyrochlore and diamond, respectively. Complete photonic band gaps are also found between bands 8 and 9 for both structures. The KKR calculations systematically give a lower value for the gap width than the MPB calculations. This difference can partly be ascribed to a convergence issue in the MPB code when a contact point of two spheres coincides with the grid.

Adding a metallic core or metallic shell to the dielectric particles, increases the band gap significantly up to more than 70% for a diamond structure of silica spheres with a silver shell.

## 5.1 Introduction

Photonic crystals are structures with a periodically varying dielectric constant, the spatial period being of the order of the wavelength of light. Similar to the way that electrons are influenced by the atomic lattice of a semiconductor, photonic modes can be shifted by the periodic structure of a photonic crystal, resulting in ranges of frequencies that cannot propagate in a certain direction, called photonic stop gaps. When a photonic band gap persists for all directions of the photonic structure, the structure has a photonic band gap. Structures with an (almost) complete photonic band gap open the way for fundamental studies on, for example, inhibition of spontaneous emission and they are interesting for the realization of photonic analogues of electronic circuits, including low-loss waveguides, optical diodes and transistors (for recent reviews see [14, 122, 123]).

Motivated by the interesting possible photonic applications and fundamental physical aspects, many studies have focused in the last two decades on designing three-dimensional photonic crystals with a photonic band gap. Until now, the most promising candidates for opening up a large band gap at relatively low refractive index contrasts are the diamond [22, 124, 125] and pyrochlore [127, 128] structures. Several methods for the experimental realization of the diamond and pyrochlore structure have already been proposed [128–130, 139, 141, 143, 156], including the recent method to fabricate both the diamond and the pyrochlore structure from the binary Laves structure $MgCu_2$ [156]. In the $MgCu_2$ structure, the large (Mg) sphere component forms a diamond structure, while the small (Cu) sphere component forms a pyrochlore structure. Therefore, when the $MgCu_2$ structure is fabricated from spheres of different materials, one of the materials can be selectively removed, yielding the desired photonic colloidal crystal. This method is a promising route for the experimental fabrication of these colloidal structures and may even lead to a photonic band gap in the visible, because a photonic band gap opens up in diamond and pyrochlore for relatively low contrast, thus allowing a broader range of materials to be used. The other related Laves structures ($MgZn_2$ and $MgNi_2$) have free energies very close to that of $MgCu_2$ and are also composed of arrangements of the small and large spheres in tetrahedrons.

The photonic properties of the diamond structure of dielectric spheres have been thoroughly investigated using both plane-wave calculations [124] and the Koringa-Kohn-Rostoker (KKR) method [125]. However, for the pyrochlore structure, only plane-wave calculations have been performed, while it is known that there can be a discrepancy between the two methods [22, 103, 125, 134, 136, 157]. Furthermore, previous photonic calculations on pyrochlore structures have focused on maximizing the photonic band gap, for example, by considering non-close-packed structures, focusing less on feasibility of the experimental realization. To complete our knowledge on the photonic properties of the experimentally realizable crystal structures related to the binary Laves structures, we present here plane-wave and KKR calculations for the photonic band diagrams of close-packed, dielectric Laves structures and their one-component constituent structures. We were interested in all constituent structures (not only diamond and pyrochlore) as they consist of tetrahedral arrangements of spheres and it has recently been shown that even an “amorphous” diamond photonic crystal structure, consisting of atoms with tetrahedral bonding symmetry, but no long-range order (like in a glass of silicon), has a large photonic band gap [158].

Infiltrating colloidal structures with a high-dielectric material yields inverted structures (with low-dielectric spheres in a high-dielectric background), which in some cases have a larger gap width than the direct structures (e.g. fcc [135]). Therefore, also the inverted pyrochlore and diamond structures are considered here. Comparing the results from both calculation methods also sheds new light on the convergence of band structure calculations of diamond related structures.

Metal inclusions in the spheres of a photonic crystal or metal shells around the spheres are known to enhance the gap width. In 2000, Zhang et al. [159] stated that any periodic structure of ideal metal particles or metalshell particles has a band gap above a certain filling fraction.

In 2001, Wang et al. considered a photonic crystal with a face centered cubic structure made of dielectric spheres with a real metal coating [160]. They show that these structures can have very large band gaps. Because the penetration depth of the metal is only several tens of nanometer, a dielectric particle with a metal shell will have the same effect as a very large metal particle, which are much harder to synthesize.

In 2002, Moroz has shown that a photonic crystal with a large band gap can be made from a low-refractive-index material by placing small inclusions of low absorbing metal in diamond-like structures [125]. The effect on the gap width was the largest if both spheres in the unit cell contained an identical metal core, but the absorption is smaller with a metal core in only one of the spheres (giving a zinc-blende structure). The gap widths found in the metal-core diamond structures are an order of magnitude larger than the metal-shell fcc structures.

Here we look at the effect on the gap width for metal inclusions in the pyrochlore structure. Furthermore, we study the photonic band structure of pyrochlore and diamond structures made of spheres with a metal shell around a dielectric core. The complex dielectric constants were chosen according to Reference [161]. The band structure calculations sets the imaginary part to zero, to be able to determine whether a photonic band gap exists in the absence of absorption. The influence of the absorption of the metal spheres on the transmission and reflection spectra, which can be significant, should be studied with finite slab calculations which explicitly take into account both the real and imaginary parts of the dielectric constants. Spherical harmonics were included up to angular momentum index $l_{max} = 9$.

## 5.2 Band structure calculations

Photonic band structure diagrams were calculated up to band 10 for dielectric contrasts ranging from 2 to 20 using the photonic analogue of the Koringa-Kohn-Rostoker (KKR) method [30, 125, 138]. This method is optimized for crystals of spheres, but can be used for scatterers of any arbitrary shape [162–164]. Spherical harmonics were included up to angular momentum index $l_{max} = 9$. The convergence of the method for increasing angular momentum cut-off was checked (Fig. 5.1a). We compared our KKR results to plane-wave calculations, employing a unit cell, discretized by a grid of $32 \times 32 \times 32$ points, performed

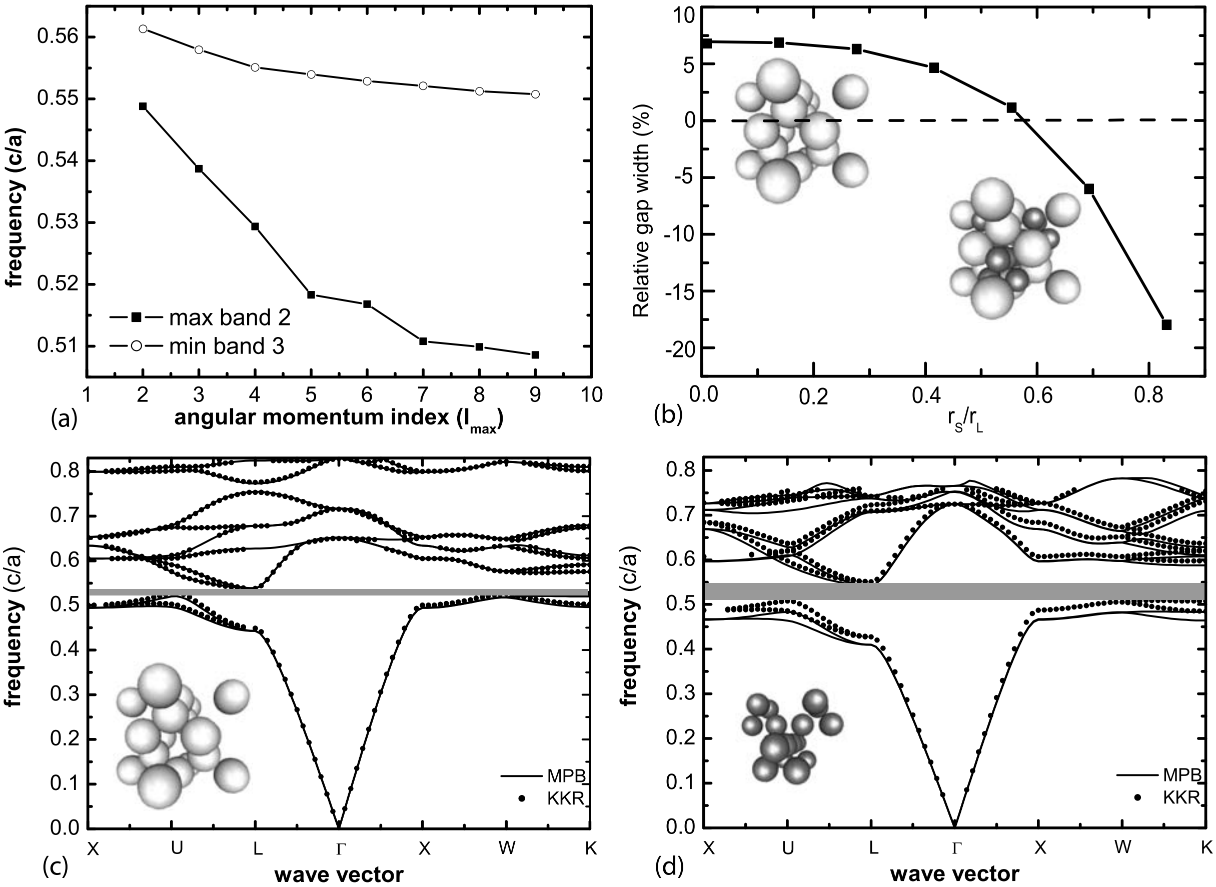

**Figure 5.1:** (a) Convergence of the maximum frequency of band 2 and the minimum frequency of band 3 of the KKR band structure of the direct pyrochlore crystal of close-packed silicon spheres in air (dielectric contrast 12) with increasing values of $l_{max}$. (b) Relative gap width of various $MgCu_2$ structures. The large spheres are close-packed, the small sphere radius is varied. A size ratio of $r_S/r_L = 0$ corresponds to diamond, $r_S/r_L \approx 0.82$ corresponds to close-packed $MgCu_2$. All spheres consist of silicon ($\epsilon = 12$), the surrounding medium is air ($\epsilon = 1$). For negative relative gap widths, the maximum of the lower band is higher than the minimum of the higher band, therefore, the structure has no band gap. The line is a guide to the eye. (c-d) Band structure diagrams calculated by the plane-wave method (solid lines) and the KKR method (symbols) of (c) a direct diamond crystal and (d) a direct pyrochlore crystal, both of silicon spheres in air (dielectric contrast 12).

using the MIT Photonic Bands (MPB) software package [28]. This package computes fully-vectorial eigenmodes of Maxwell's equations with periodic boundary conditions by preconditioned conjugate-gradient minimization of the block Rayleigh quotient in a plane-wave basis [27]. For the calculations presented here, we used MPB 1.4.2, modified to calculate the effective dielectric constant of Wigner-Seitz real-space unit cells instead of the parallelepiped unit cells spanned by the lattice vectors. We did not find any major differences (only differences below 0.2% in the relative gap width) between calculations that were performed with or without this patch.

We emphasize that the structures for which band diagrams have been calculated have not been optimized in any way. Optimization might be achieved for instance by using incomplete filling, which increases gaps for inverse fcc structures [165], or by slightly sintering the structures [166]. Both enhancement methods result in structures with overlapping spheres and are experimentally realizable. Although the KKR method can be used for scatterers of arbitrary shape [162–164], our implementation allows to calculate photonic band diagrams only for muffin-tin scatterers (not overlapping scatterers), photonic band diagrams of structures with overlapping spheres cannot be calculated with our code.

## 5.3 Results

For both the pyrochlore and the diamond structures, we have found band gaps between bands 2 and 3 and between bands 8 and 9 (Fig. 5.1c and 5.1d). We have focused on the band gap between bands 2 and 3, because this band gap is relatively larger and it is more stable against disorder and defects [137]. Figure 5.2 shows the relative gap width of the photonic band gap between bands 2 and 3, as a function of the dielectric contrast, for both the direct and inverse structures at the maximum sphere packing fraction (of 34% and 37%, respectively) calculated by using both the KKR-method and the MPB software. The relative gap width is defined as the ratio of the gap width and the midgap frequency. The inverse structures have a relatively narrow band gap, which opens up for dielectric contrasts higher than 10 and 12 for pyrochlore and diamond, respectively. KKR and MPB agree on the relative gap width within 0.5% for the inverse structures.

The direct structures possess large photonic band gaps for moderate dielectric contrasts. The two calculation methods agree on the midgap frequency and on the value of the dielectric contrast at which the gap opens, which is around a dielectric contrast of 5 for both the diamond and the pyrochlore structure. This is much lower than the required contrast of 8.4 for an inverse face-centered cubic (fcc) structure [135]. The large difference in the calculated relative gap width for higher dielectric contrasts in direct diamond and direct pyrochlore is discussed in Section 5.3.1.

Using the MPB software, we did not find full band gaps for any of the binary Laves structures in the dielectric contrast range of 2 to 20. Neither did we find any significant gaps for the single small/large particle constituents of the $MgZn_2$ and $MgNi_2$ structures. We only found a 3.9% gap for the small sphere constituent of the $MgNi_2$ structure between bands 8 and 9, for a close-packed structure of silicon spheres in air (dielectric contrast 12).

To clarify the transition between the diamond structure, which has a band gap, and the

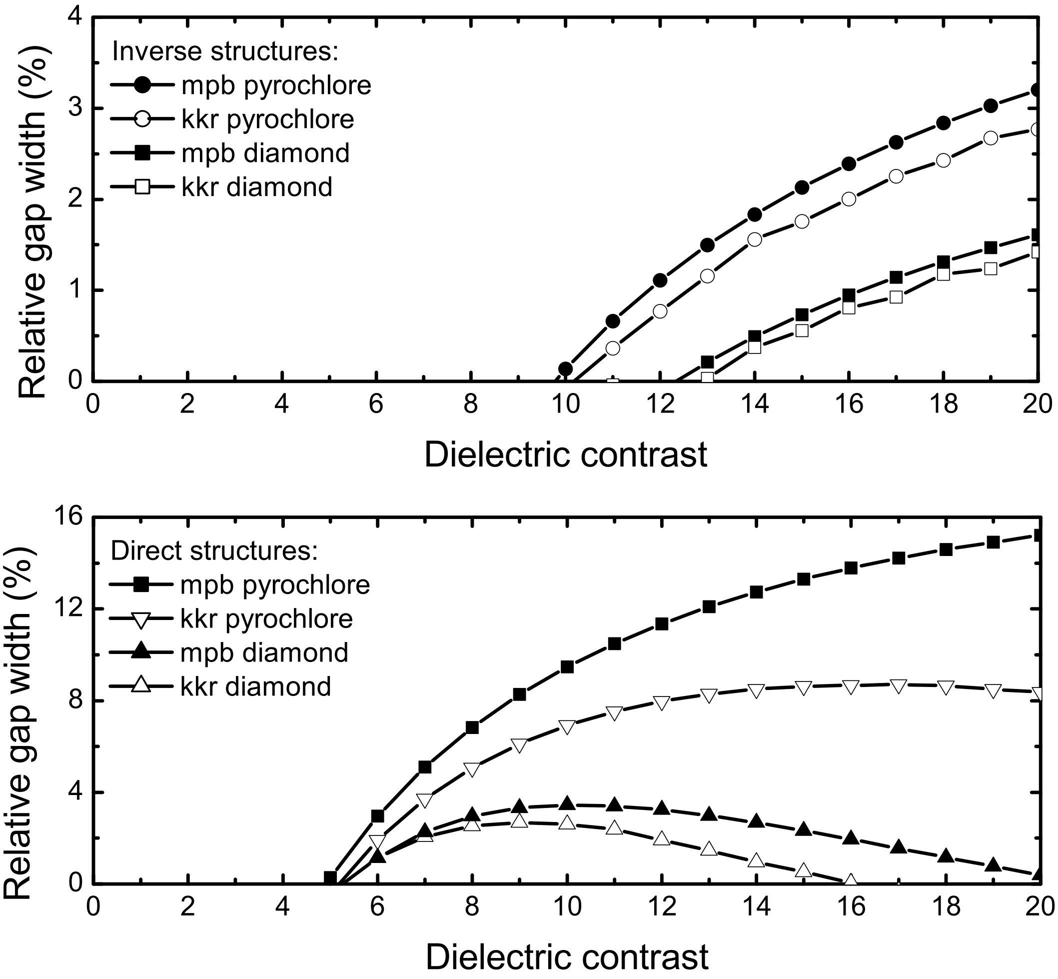

**Figure 5.2:** The relative gap width of the photonic band gap between bands 2 and 3, as a function of the dielectric contrast, for the direct diamond and pyrochlore structures and their inverse structures at the maximum sphere packing fraction (of 34% and 37%, respectively), calculated by using both the KKR-method ($l_{max} = 9$) and MPB software (resolution 32 for the inverse structures and the direct pyrochlore structure and resolution 28 for the direct diamond structure, see Section 5.3.1). Note the difference in scale on the vertical axes.

binary $MgCu_2$ structure, without band gap, we looked at how the band gap of the diamond structure of large spheres closes upon insertion of the small spheres of the pyrochlore structure, thus forming $MgCu_2$. We started with a close-packed diamond structure of large spheres of silicon ($\epsilon$=12) in air ($\epsilon$=1) and increased the size of the small particles ($\epsilon$=12). The resulting graph is shown in Fig. 5.1b. The band gap closes at a small-to-large size ratio of $r_S/r_L = 0.58$, while close-packed $MgCu_2$ is formed at a size ratio of $r_S/r_L = \sqrt{\frac{2}{3}} \approx 0.82$. The closing of the band gap can be ascribed to the increasing dielectric fraction together with a lack of connectivity of the dielectric phase, which makes it impossible to concentrate the field energy of successive bands in different dielectric phases and thus results in a featureless density of states (DOS).

### 5.3.1 Convergence of diamond and pyrochlore band structure calculations

Comparing the KKR and plane-wave photonic band structure calculation methods in Fig. 5.2 shows that the KKR method systematically gives lower values for the relative gap width than the plane-wave method. Furthermore, the difference for the direct pyrochlore and diamond structures is much larger than the difference for the inverse structures. We examined the convergence of MBP and KKR more closely to find a possible cause of the discrepancy. Increasing the value of $l_{max}$ in the KKR method shows that the results converge to one value for both the direct and the inverse structure, although the calculations for the direct structures converge slower than the calculations for the inverse structures. However, plotting the relative gap width versus the resolution in the MPB calculations (where resolution$^3$ equals the number of plane waves included in the calculation) for a close-packed direct diamond structure of silicon spheres in air (Fig. 5.3a) revealed an oscillating line, where the lower and the higher values slowly converge to one value. The oscillation period depends on the choice of the origin of the sphere coordinates with respect to the grid points. With one of the two spheres in the diamond unit cell centered on the grid origin, the oscillation period is 8, with high values for resolutions that are multiples of 8 and low values for resolutions that are multiples of 4, but not of 8. Similar oscillations, but with a period of 2, are found when the origin is on the contact point of the two spheres in the unit cell, i.e. when the structure has inversion symmetry.

A clue for this oscillation can be found in the coincidence of a sphere-contact point with an MPB grid point. When the origin is on one of the spheres, the contact point is at $(\frac{1}{8}, \frac{1}{8}, \frac{1}{8})$. This contact point coincides with a grid point when the resolution is a multiple of 8, giving a high value for the relative gap width. The contact point is exactly in the middle of a grid box when the resolution is a multiple of 8, but not of 4, giving a low value.

For an origin at a quarter of the line between the two spheres in the diamond unit cell (halfway the center of one sphere and the contact point of the two spheres), the convergence-curve is shown in Fig.5.3b. The clear local maximum and minimum can be explained in the same fashion: The contact point of the two spheres in this case is at $(\frac{1}{16}, \frac{1}{16}, \frac{1}{16})$. At a resolution of 8, this contact point is exactly in the middle of a grid box, yielding a low value for the relative gap width, while at a resolution of 16, the grid and

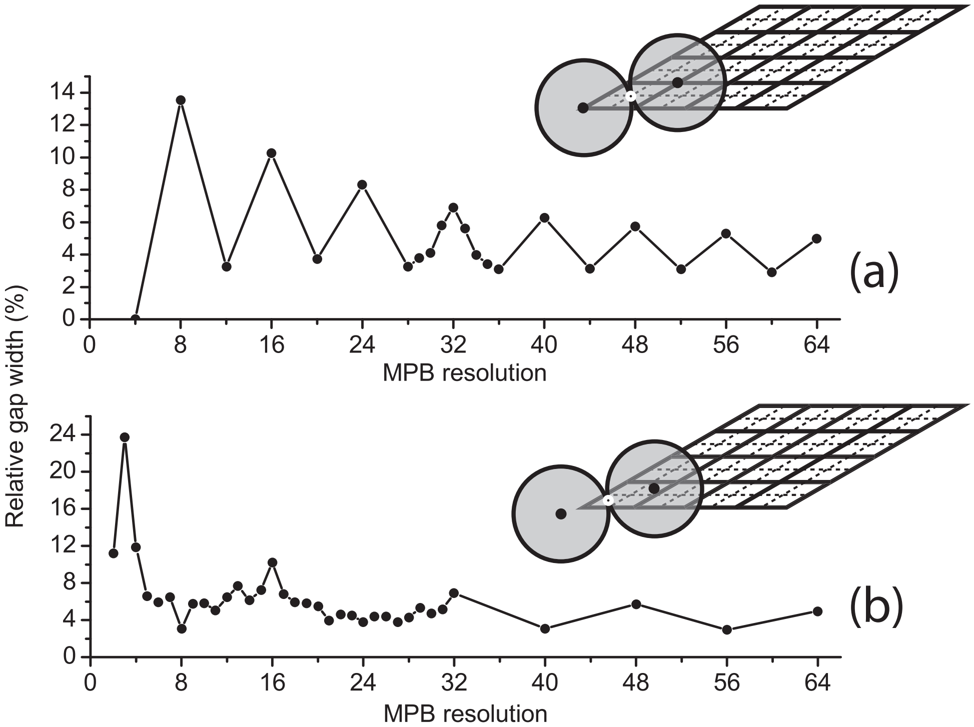

**Figure 5.3:** Relative gap width of a close-packed diamond structure of silicon spheres in air as a function of the chosen resolution in the MPB software with the origin of coordinates on one of the spheres (a) or with the origin halfway between the center of the sphere and the contact point of with the other sphere (b). The insets are 2D representations of the positions of the spheres and their contact point (white circle) with respect to the grid of the unit cell for resolution 4 (solid grid) and resolution 8 (solid+dashed grid).

the contact point coincide, giving a high value.

We have performed additional MPB-calculations (not shown here) to investigate the dependence of the relative gap width on the coincidence of a contact point of two spheres and a grid point. These suggest that this dependence may be caused by the procedure with which MPB calculates the dielectric tensor for each grid point. However, the exact cause of the oscillations in the convergence is currently under investigation. Unfortunately, we therefore cannot conclude at this moment whether the high or the low values which are calculated by the MPB program are closer to the actual value, we can only state that the lower values are closer to the values resulting from the calculations using the KKR method and that using both methods is recommended to check for consistency if numerical accuracy is important.

### 5.3.2 Pyrochlore structure of dielectric spheres with a metal core

For a direct pyrochlore structure consisting of 300 nm spheres with a silver core (with core radius/total radius ratio of $r_{core}/r = 0.5$) in air, the relative gap width (the ratio between

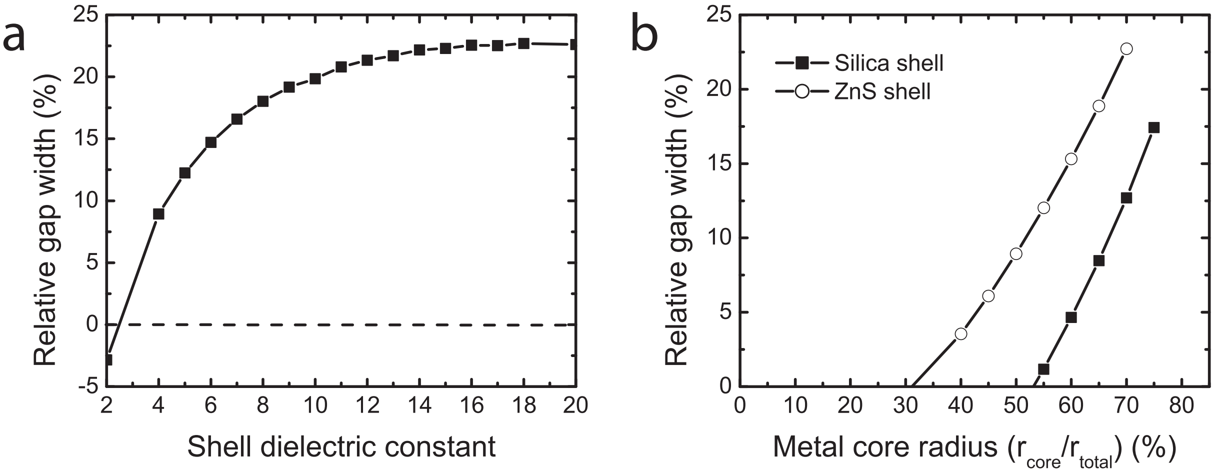

**Figure 5.4:** Relative gap width of a direct pyrochlore structure of dielectric spheres with a silver core with total radius $r = 300$ nm (a) as a function of the shell dielectric constant with a metal core radius of $r_{core}/r = 0.5$, (b) as a function of the metal core radius for spheres with a silica shell or with a ZnS shell. For negative relative gap widths, the maximum of band 2 is above the minimum of band 3 and there is no photonic band gap.

the width of the gap and the midgap frequency) between bands two and three increases steeply with increasing shell dielectric constant, after which it levels off at a gap width around 22% (Figure 5.4a). This behavior is similar to the dielectric constant dependence found for diamond by Moroz [125]. For both metallo-dielectric structures the gap width is an order of magnitude larger than for the pure dielectric structures.

The band gap already opens for a dielectric constant below 3. For a realistic shell material as silica (dielectric constant 2.1) or ZnS (dielectric constant 4), the gap opens for a relative core radius of $0.50 < r_{core}/r < 0.55$ and $r_{core}/r = 0.3$, respectively (Figure 5.4b). For a diamond structure, Moroz [125] found gap opening at $r_{core}/r = 0.48$ for silica shells and $r_{core}/r = 0.28$ for ZnS shells, so a slightly lower metal filling fraction is needed to open a band gap in a diamond structure than in a pyrochlore structure.

For dielectric photonic structures, the relative gap width is independent of the sphere radius. Since, if there is no dispersion, the physical length of the structure and the wavelength scale because of the linearity of Maxwell's wave equations. However, this behavior is remarkable for structures for which the dielectric constant depends on the wavelength. Moroz found this so called 'scaling behavior' for the metallodielectric close-packed zinc-blende structure [125]. When the dielectric constant of the metal at the midgap frequency of the photonic band gap becomes sufficiently large, such that there is no significant difference with a perfect metal ($\epsilon$ = -$\infty$), the relative gap width becomes independent of the sphere radius for a given metal filling fraction. In Figure 5.5, the dependence of the relative gap width on the sphere radius is plotted for a direct pyrochlore structure of silica spheres with a silver core ($r_{core}/r = 0.5$) in air. The relative gap width is only independent of sphere radius for sphere radii above 200 nm. From that size on, similar scaling behavior is found as for the zinc-blende structure.

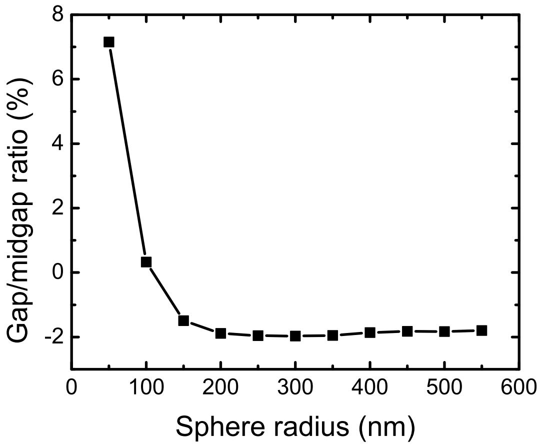

**Figure 5.5:** Relative gap width of a direct pyrochlore structure of dielectric spheres with a silver core and a silica shell with a metal core radius of $r_{core}/r = 0.5$, as a function of the total sphere radius. For negative relative gap widths, the maximum of band 2 is above the minimum of band 3 and there is no photonic band gap.

### 5.3.3 Pyrochlore and diamond structure of dielectric spheres with a metal shell

Adding a silver shell to the dielectric spheres in a pyrochlore, makes a huge difference for the relative gap width of the photonic band gap between bands 2 and 3. While no band gap opens for a close-packed pyrochlore structure of silica spheres, adding a 60 nm silver shell to 240 nm radius spheres, gives a band structure diagram as depicted in Figure 5.6a. Making the silver shell thicker (but keeping the total sphere radius the same), does not change the width of the band gap (Figure 5.6b, because the penetration depth of the light is only a few tens of nanometers. Also the position of the gap does not change: the midgap frequency of this structure was around 3500 nm for all shell thicknesses down to 60 nm ($r_{core}/r = 0.8$).

The dependence of the relative gap width on the total sphere radius does not level off completely, as in the case of the spheres with a metal core (Figure 5.7a). The total sphere radius can however be used to tune the midgap frequency. In Figure 5.7b, the position of the band maximum of band 2 and the band minimum of band 3 are plotted as a function of the particle radius. The telecom wavelength of 1500 nm is indicated with a line.

Similar calculations for the diamond structures gave numerical instabilities in the calculation, which we could not resolve so far, therefore not all data points are available. However, from the data points in Figures 5.6b and 5.7a it can be concluded that the diamond structure behaves similar as the pyrochlore structures, but with a slightly higher relative gap width.

For experimental realization of this metalshell structure, a dielectric coating of the metalshell would be preferable, since otherwise the particles aggregate due to Van der Waals forces. A calculation of the band structure of a close-packed pyrochlore structure

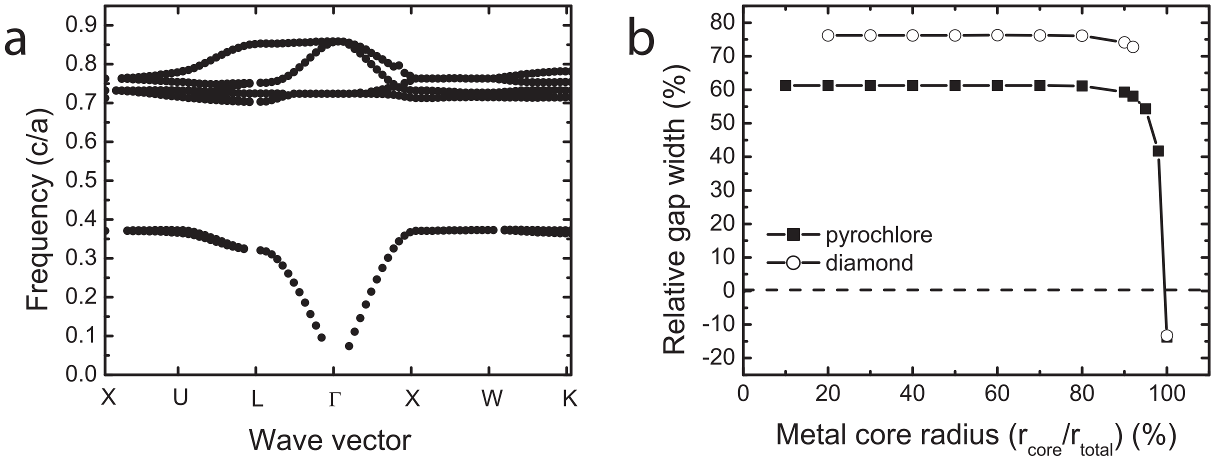

**Figure 5.6:** (a) Band structure diagram of a close-packed pyrochlore structure of silica spheres of 240 nm with a 60 nm silver shell. (b) Relative gap width of a pyrochlore (and diamond) structure of dielectric core/metal shell spheres with a total diameter of 300 nm as a function of the dielectric core radius.

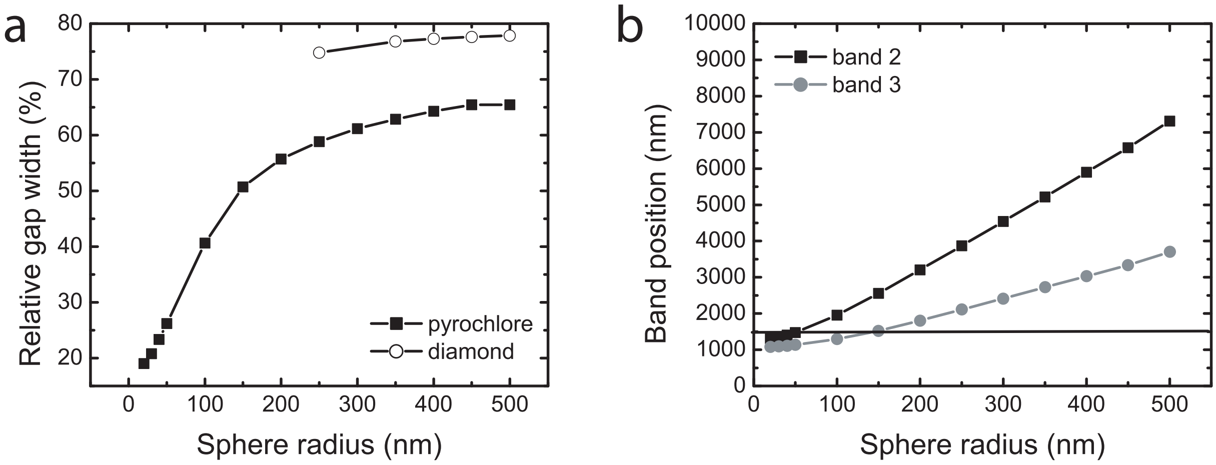

**Figure 5.7:** (a) relative gap width and (b) positions of the maximum of band 2 and the minimum of band 3 as as a function of the total sphere radius for a pyrochlore (and diamond in (a)) structure of dielectric spheres with a silver shell, with a dielectric silica core of which the radius is 80% of the total sphere radius.

of 300 nm radius spheres with a 240 nm silica inner core, a 20 nm silver shell and a 40 nm silica outer shell, showed that there is no band gap between the second and third bands. A better way to make the structure is therefore: self-assembly of pure dielectric spheres and coating a silver shell after self-assembly.

## 5.4 Conclusions and discussion

Band diagrams of various structures related to the binary Laves structures have been calculated using both plane-wave and KKR methods. We have not found significant band gaps for the binary Laves structures. Of the constituent single structures, only those of $MgCu_2$, pyrochlore and diamond give a photonic band gap that is interesting for photonic applications. Since a high filling fraction of dielectric material is disadvantageous for the gap width, the relative gap width was found to be larger for the direct structures than for the inverse structures and the gap width is also larger for pyrochlore than for diamond. Therefore, we conclude that the growth of a $MgCu_2$ colloidal crystal is a suitable starting point for the fabrication of a photonic crystal with a large photonic band gap. However, since no band gaps are found for the constituent structures of the other two Laves structures, selection of the desired Laves structure by epitaxial growth is necessary [156].

KKR and MPB calculations agree upon the conclusions stated above and on the values of the midgap frequencies and of the dielectric contrast needed for a band gap to open. However, for high dielectric contrast, the predicted relative gap widths start to disagree, which is partly caused by the discretization of the unit cell in MPB, especially when there are two curved surfaces in a grid cell, as is the case for touching spheres. In most other photonic structures, such as inverse fcc, this does not lead to severe convergence issues. In diamond, however, the gap width is a very sensitive function of the sphere radius near close-packing. This may lead to the observed dependence of gap width on the position of the sphere centers on the grid.

Adding a metallic core or metallic shell to the dielectric particles, increases the band gap significantly up to more than 70% for a diamond structure of silica spheres with a silver shell. Coating the silver shell with a dielectric coating, however, closes the band gap between the second and third band. We would therefore advice to produce the diamond structure of dielectric spheres (to avoid aggregation by Van der Waals forces between the silver shells) and then coat the structures with silver after crystallization.

## 5.5 Acknowledgements

I want to thank Job Thijssen for all MPB calculations and the useful discussions. I want to thank Alexander Moroz for the KKR program and for the help with the KKR calculations.

# 6

# Studying colloidal crystallization around a finite seed structure

Crystal nucleation in a hard sphere colloidal model system was studied by optically trapping 2D seed structures of tracer particles in a bulk dispersion of refractive index matched host particles. The symmetry and lattice spacing of the seed structures were varied by changing the trapping positions of the time-shared optical tweezers. At the same time, the volume fraction of the host dispersion around the template was controlled by dielectrophoretic forces in an ‘electric bottle’.

Ordering around square and hexagonal seed structures was observed and quantified in terms of 2D hexagonal and square bond orientational order parameters. A nucleus around a square template grew out to a crystallite, giving the opportunity to study the structure and shape of the outgrowing crystal. Because of a mismatch of the template and the bulk fcc crystal, the square fcc (100) planes only grew out above and below the crystal. The sides of the crystal grew out in crystal domains with other orientations. The shape of the nucleus and the final crystallite were not spherical, as is assumed in classical nucleation theory. Although our results are too preliminary to obtain accurate results, taken together with published simulation results, our approach could be used to obtain hard sphere surface tensions on different crystal faces.

In some cases, the seed structure acted as a defect in a crystal grown heterogeneously and under the influence of gravity from the top of the sample cell. At first, crystallization was suppressed around the template. Final crystallization around the template resulted in defect lines and grain boundaries pinned on the template to release the stress. The method used here to study nucleation is also well suited to grow photonic colloidal crystals with doped patterns of particles in the bulk of the crystal.

## 6.1 Introduction

For the study of the structure and growth of crystals, crystal nucleation is one of the most important stages. At this stage, the later structure, form and orientation of a crystal are determined. Therefore, control over the growth of nucleates in a liquid gives control over the end product of crystallization, which is of major technological importance. However, since the short time- and length-scales complicate real-space and scattering studies, nucleation is also the stage which is least understood.

Two types of nucleation can be distinguished:

- Homogeneous nucleation, in which small crystallites grow in the bulk of an undercooled or oversaturated liquid,
- Heterogeneous nucleation, in which crystallites nucleate on a different substance, e.g. the surface of another type of crystal or on a container wall.

Homogeneous nucleation is best understood qualitatively by classical nucleation theory: nuclei are formed continually by thermal fluctuations, but most of the time, the high surface energy cost of the crystallites is not counterbalanced by the small bulk energy gain and the crystallite will melt again. The free energy of the crystallites is expressed by

$$\Delta G = 4\pi r^2 \gamma - \frac{4\pi}{3} r^3 \Delta\mu n \tag{6.1}$$

where $r$ is the radius, $\gamma$ is the surface free energy per unit area of a crystal-liquid interface, $\Delta\mu$ is the chemical potential difference between the liquid and the solid and $n$ is the number density of the crystal. When the crystallite reaches a critical nucleus size at the maximum of $\Delta G$, with $r_c = 2\gamma/(\Delta\mu n)$, it can grow out to a crystal. The classical nucleation theory assumes that the nuclei that are formed are spherical (where $\gamma$ is averaged over all crystal planes) and that the nuclei have the same structure as the bulk crystal (taking the bulk values for the parameters $\Delta\mu$ and $n$).

Colloidal systems are ideal for studying the governing parameters of crystal nucleation, because of the slow time scales and long length scales, which enable 3D real-space imaging on the single particle level using confocal microscopy [167]. Furthermore, colloids serve as good model systems for atomic and molecular systems because of their analogous thermodynamical behavior [3].

The internal structure of the critical nuclei in colloidal systems has been studied by computer simulations using the umbrella sampling technique, finding a face centered cubic (fcc) core and a body centered cubic (bcc) surface layer for a Lennard-Jones system [168] and a random hexagonal close-packed (rhcp) structure for hard spheres [169, 170]. Light-scattering measurements on hard-sphere systems confirmed the rhcp structure of the crystalline regions [5, 171, 172], but it could not resolve this information for crystallites as small as a critical nucleus. Also the real-space study by Gasser et al., using laser scanning confocal microscopy of fluorescently labelled hard-sphere colloids showed a predominant rhcp structure of the critical nuclei [173]. The simulations and the real-space study both found non-spherical critical nuclei, which disagrees with the assumption in classical nucleation theory.

Crystallization can also be induced by a foreign object like a wall or an impurity. A simulation study of heterogeneous crystallization close to a wall [174] showed that the presence of the wall lowers the energy barrier for nucleation with two orders of magnitude. It has also only recently become clear from computer simulations that hard spheres crystals wet a smooth hard wall [175]. However, in this case the pre-wetting transition takes place very close to the bulk freezing transition. Also, a structured surface can induce crystallization at densities below freezing when the structure closely matches the bulk crystal structure. This effect is much larger and can induce a first crystalline layer already 30% below the bulk freezing pressure. This was tested in experiments [62, 63, 70, 74] and confirmed with computer simulations by Heni and Löwen [77].

The effect of heterogeneous crystallization on impurity spheres in a suspension has been studied both by simulation [176] and experiment [177]. Smooth spheres promote crystallization above a minimum size (or actually, below a maximum curvature).

When crystallization is induced by an optically trapped seed structure, as proposed by Vossen [91, 178], which matches the structure of the thermodynamically stable bulk crystal, classifying the type of nucleation becomes tricky. In principle, the situation is closer to heterogeneous crystallization, since the seed itself is a fixed structure, which is not formed by thermal fluctuations. However, the structure is not foreign to the bulk crystal and when the seed is smaller than the critical nucleus, the effect of the thermal fluctuations on nucleation can still be studied. Moreover, it is possible, although not tried in this study, to extrapolate the effects of the tweezers potential to zero by performing experiments as a function of the trapping strength.

Applying a seed structure facilitates the investigation of nucleation by making the formation of a nucleus more likely. Furthermore, the position of the forming nucleus becomes predefined, causing it to always be in the experimental field of view. Because of the use of time-shared optical tweezers to create the seed structure, the spacing and symmetry of the seed structure can be changed during the experiment, which allows probing various seed structures in one experiment. However, the volume fraction of the dispersion, which is a determinative parameter, especially considering hard-sphere systems, is constant during the whole experiment, limiting its versatility .

Cacciuto and Frenkel investigated the effect of a two-dimensional seed structure with in-plane ordering related to the (100), the (110) and the (111) plane of an fcc structure [78]. They concluded that the (111) plane was the most effective in inducing epitaxial crystal growth. However, disorder in the template (comparable to the Lindemann criterion of ~10%), experimentally for example caused by a low trapping power, suppresses the effectiveness of the template. Also a lattice mismatch between the template and the bulk crystal can suppress crystal growth. In principle, Cacciuto and Frenkel studied templates in which the template particles are mutually touching. Experimentally this is difficult to achieve, since the chance of particles hopping from one trap to another becomes too high. Therefore, they also studied an expanded version of the template structure, in which the lattice spacing is made higher in such a way that additional particles can occupy the template lattice, finding that an expanded lattice can induce order in its own plane. This result suggests that the expanded template not only overcomes the experimental trapping difficulty, but also reduces the number of trapped particles needed for inducing nucleation with respect to a compressed template. Furthermore, they found that the effect of a lattice mismatch is smaller in an expanded template. Assuming that the form of the nucleus on the template is a spherical cap, they modified classical nucleation theory. With this modified theory, they could well account for the size of the adsorbed crystallites on the templates. Experimentally, this finding may be used to obtain an estimate of the different crystal-liquid surface tensions on different crystal-face templates in contact the liquid.

Using the recently developed time-dependent dynamic density functional theory (DDFT) [179, 180], crystal nucleation on a fixed 2D seed structure can be studied [181], which is close to the effect of a two-dimensional seed structure fixed by optical tweezers studied experimentally [178, 182].

Following the experimental setup as described by Vossen et al. [91, 178], we extended the experiment with dielectrophoretic compression (Chapter 2.5) to have in situ control over the volume fraction of the dispersion. This setup enables us to follow the nucleation of a colloidal crystal on a seed structure of chosen symmetry and spacing as a function of increasing (or decreasing) volume fraction.

## 6.2 Experimental methods

For the results described in this chapter, several techniques were combined into one experiment: we trapped high-index core-shell tracer particles in the bulk of index-matched host particles by time-shared optical tweezers. At the same time, we compressed the dispersion into a narrow slit by dielectrophoretic forces. The real-space 3D structure of the dispersion was imaged instantaneously using confocal microscopy, allowing a direct study of the nucleation on the trapped seed structure. In this section we describe the dispersions and all the employed techniques.

### 6.2.1 Colloids and dispersions

The host particles, which formed the bulk of the dispersion, were PMMA particles which were completely dyed with 1,1'-dioctadecyl-3,3,3',3'-tetramethylindocarbocyanide perchlorate (DiIC) and sterically stabilized with poly(12-hydroxystearic acid) (PHS). The PHS was not locked to the particles. The host particles were 0.93 $\mu$m in diameter.

To enable trapping of the tracer particles, they needed to have a different refractive index than the host particles and the dispersion medium. Polyelectrolyte coated polystyrene (PS) cores of 0.99 $\mu$m diameter were coated with a layer of poly(allylamine hydrochloride) (PAH) and a layer of polyvinyl pyrrolidone (PVP). Then a silica shell was grown on top, which in turn was coated with 3-(trimethoxysilyl) propyl methacrylate (TPM) and then sterically stabilized with PHS. The final diameter of the tracer particles was 1.1 $\mu$m.

The index of refraction of the PMMA host particles at 1064 nm (the infrared wavelength of the trapping laser) was matched with a solvent mixture of cyclohexyl bromide (CHB) and cis-decalin. The interactions between the particles were tuned to be nearly hard-sphere-like by saturating the solvent with tetrabutylammonium bromide (TBAB).

### 6.2.2 Optical tweezers setup

The optical tweezers setup used in this chapter is described in Chapter 2.4, with an illustration in Figure 2.3. In the experiments described here, the upright objective was used for trapping (and as a condenser for bright field illumination), while the inverted objective was only used for imaging. We always used 100×, 1.4 NA oil immersion objectives for both the upright and the inverted objective positions. By switching the laser beam between different focal positions using acousto-optic deflectors (AODs, IntraAction Corp.), an array of optical traps was created.

During the initial step of filling all traps, the seed structure was imaged by bright field microscopy using a charged coupled device (CCD) camera (UNIQ, UP-600 or Evolution QEi Fast Cooled Mono 12-bit, MediaCybernetics). For imaging the host particles, we switched to Laser Scanning Confocal Microscopy (Leica, type NT). The fluorescent dye DiIC of the host particles was excited with the 543 nm line of a green HeNe-laser. The tracer particles were imaged using their reflection signal.

### 6.2.3 Dielectrophoretic compression

The principle and theory behind dielectrophoretic compression is explained in Chapter 2.5. In an inhomogeneous electric field, particles with a different dielectric constant than the medium acquire a translational motion: particles which are more polarizable than the medium move towards the stronger field, less polarizable particles move towards a lower field. We used this principle to concentrate the particles from the large volume of a sample into a small strip in the middle. This strip was created by a gap in the gold electrodes on the inside of the sample with a double-slit geometry as shown in Figure 2.4a. The PMMA particles used here, had a higher dielectric constant than the CHB/cis-decalin and thus were compressed into the field-free slit.

Several other sample cell designs for dielectrophoresis were tried, both single-slit and double-slit geometries (Figure 2.4). The single-slit geometries have the disadvantage that the high laser power travels through the electrodes. When the laser passes through the gold electrode, this causes heating of the sample, which deteriorates the refractive index matching and eventually can gel the dispersion. With an Indium Tin Oxide (ITO) electrode, the effect was even more drastic: the sample locally gelled, i.e. particles stopped moving and formed an amorphous solid within a few seconds. Besides heating, also the release of free charge carriers could have played a role here [183]. The question remained how the dispersion could gel so quickly. Since it was observed with confocal microscopy that the particle motion stopped within only a few seconds, it was investigated if one of the components of the dispersion polymerized, or if possibly some glue had dissolved in the dispersion.

Letting the glue harden longer before inserting the dispersion did not yield a change, the dispersion still gelled when it was illuminated through the electrode. We also investigated whether CHB or CHB with an added drop of liquid glue or CHB with an added piece of hardened glue could cause gelation upon heating. However, all three did not seem to be the case. It therefore is most likely that the PMMA particles itself gave rise to attractions that caused the system to gel. This agrees with the observation that pre-heated PMMA particles (to about 80°C) stick to each other when pushed together in an electric field [184].

### 6.2.4 Image analysis

The coordinates of the particles of the 2D confocal microscopy images in the $xyz$-stacks were determined using IDL software based on a method as described by Crocker and Grier [117]. For every $xy$-image, a hexagonal and a square order parameter was determined.

The 2D local hexagonal bond orientational order parameter $\Psi_6$ for a single particle can be calculated from the particle coordinates [185]:

$$\Psi_6(r_j) = \frac{1}{N} \sum_k \exp(i6\theta(r_{jk})) \tag{6.2}$$

where $k$ runs over all $N$ neighboring particles of particle $j$ and $\theta(r_{jk})$ is the angle between the vector between particles $j$ and $k$ and a reference axis. In a similar way, we used $\Psi_8$ for determining the amount of square order. Both order parameters are discussed more extensively in Chapter 8.3.4.

The volume fraction in the dispersion is not known at every instant, because of the dielectrophoretic compression and simultaneous sedimentation. Nevertheless, this is an important parameter in the study of nucleation phenomena. To have a quantitative measure for the volume fraction during the experiment, we determined the amount of particles in a 2D slice which is not affected by the template. The amount of particles in a 2D slice of a fluid can be directly related to the volume fraction.

### 6.2.5 Experimental challenges

During the experiments, described in this chapter, we met several challenges. Some of these challenges could be solved, for some we had to compromise.

#### Refractive index matching

To be able to trap the tracers without influencing the host particles, the refractive index of the PMMA hosts was matched with the refractive index of the dispersion at the wavelength of the trapping laser (1064 nm). Accurate matching was complicated by the temperature dependence of the refractive index. The refractive index matching ratio of solvents, which was used here, was determined empirically by checking the influence on the hosts in an empty trap in several solvent ratios. In the ratio of 4% w/w cis-decalin used, no influence of the trapping laser on the host particles was observed.

Since we used a two-component solvent mixture, matching of the refractive index does not coincide with matching the density. For the refractive index matching CHB/cis-decalin mixture, the particles float. Therefore, besides the dielectrophoretic compression, the dispersion was also compressed by gravitational forces against the top wall, favoring a crystal orientation where the (111) plane was parallel with the top wall. To avoid the influence of this heterogeneous nucleation at the wall with the nucleation at the tracer array, the dielectrophoretic compression had to be faster than the gravitational compression.

### Filling the trapping array

During the first stage of the experiment, the sample was moved around to find tracer particles to fill the array with. The tracers were primarily at the bottom because of their higher density. Therefore, the seed structure was held close to the bottom and brought to the middle of the sample after filling all traps by moving the sample downwards. However, moving a trapped array around in a dense dispersion of host particles is not without risk: the risk of losing particles or to have particles moving from trap to trap is significant, especially when the trapping stiffness decreases in a large array because of laser time-sharing. Of course, the laser power was increased when the mobility of the tracer particles in the traps became too large, this could however not be done unlimitedly. The fact that we compressed the dispersion using dielectrophoretic forces after filling the array, and therefore had the opportunity to fill the array in a dilute host dispersion, considerably decreased the risk of loosing particles during this stage of the experiment.

Another trick employed to avoid loosing tracer particles was the fact that we filled the array at a much larger array spacing than the spacing used in the final nucleation experiments. When accidentally an extra particle entered an already filled trap, the particle was removed by releasing the trap (not letting the laser visit the position of this trap) and filling it again.

During the trapping, the edges of the slit had to be avoided, because illuminating the gold electrodes with the laser beam caused heating. We therefore carefully measured the positions of the edges before switching on the laser and stayed within the middle half of the slit. This, however, reduced the searching-area considerably.

The amount of tracers to put in the dispersion was a compromise between searching time (with less tracers, the time to find them increases) and the fact that too many tracers causes them to diffuse into a trap during the experiment (giving two or more particles per trap).

### Imaging of the tracer and host particles

When the whole array of traps was filled with tracer particles, we switched to confocal microscopy imaging. The tracer particles were not fluorescently dyed and were therefore imaged in reflection mode. However, the reflection signal also contained the back-reflecting confocal laser, which interfered with the imaging of the array of tracer particles. The array therefore had to be placed at a position away from the center, where the reflecting beam was not imaged.

The imaging of the hosts deteriorated during the experiment due to bleaching of the fluorescent dyes. The bleaching was even higher than normally during confocal scanning, since the trapping laser beam constantly illuminated the particles around the template at a very high power. The particles around the template could be refreshed by moving the sample, at the risk of losing particles from the template.

## 6.3 Results and discussion

### 6.3.1 Refractive index matching the dispersion

To be able to draw conclusions from the ordering of the hosts around the trapped tracer particles, the influence of the laser of the hosts has to be negligible. To achieve this, the refractive index of the host particles has to be matched with the refractive index of the dispersion at the laser-wavelength of 1064 nm. A rough indication for the refractive index matching is visible in the light transmission camera images, as for example in Figure 6.1: the tracers are clearly visible, while the hosts can only be seen as a slight modulation of the background signal.

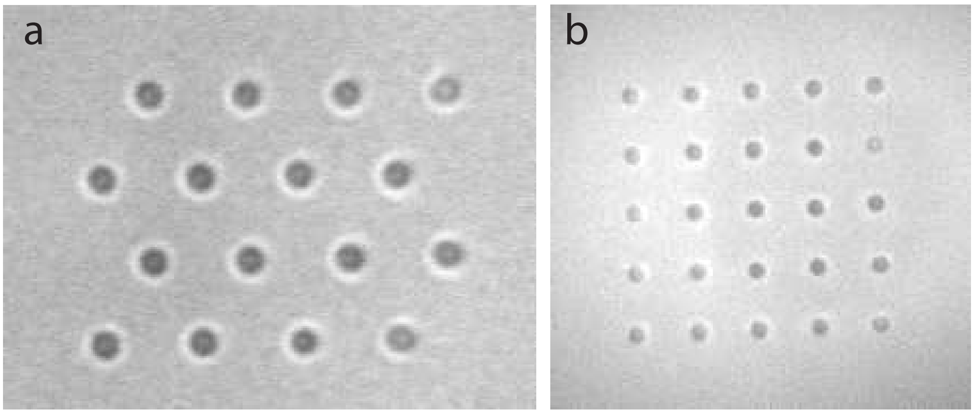

**Figure 6.1:** Structures of tracer particles (dark grey), trapped with optical tweezers. (a) Hexagonal array imaged with the UNIQ, UP-600 CCD camera in transmission-mode. (b) Square array imaged with the Evolution QEi (Fast Cooled Mono 12-bit, MediaCybernetics).

However, the refractive index at 1064 nm (in the infrared spectrum) is not the same as the refractive index at visible wavelengths. Therefore, the refractive index matching of a dispersion was also checked during illumination with the 1064 nm laser. In particular, we trapped a tracer array in a fluid of host particles, where one trap-position was left empty. Imaging the host particles in this configuration and averaging over several images, blurs the moving fluid particles, while the trapped particles (and the particles which freeze in between the trapped particles) are imaged as clear dots. When a host particle is not index-matched well enough, a clear host-dot is found at the position of the empty trap when the refractive index of the dispersion is too low or a hole in the blurred host fluid is found when the refractive index of the dispersion is too high. The ratio of CHB and cis-decalin volume fractions was adjusted till none of the effects were seen.

Nevertheless, during an experiment the refractive index of the particles and the dispersion can change. First of all, the particles swell by uptake of solvent. Preferential uptake of one of the solvents in the solvent mixture can lead to a higher or a lower refractive index than the solvent. Preparing the dispersion at least a day before the experiments lets the particles come into equilibrium in the solvent mixture.

Furthermore, heating by continuous illumination by the trapping laser and also by the confocal laser, causes a decrease of refractive index of both the solvents and the particles.

This decrease is larger for the solvents than for the particles, causing the host particles to become attracted to the trapping laser foci. Heating of the sample was minimized by restricting the laser power to approximately 2 W (power of the laser before attenuation, the actual power on the sample is an order of magnitude lower) and by avoiding the electrodes with the laser beam. Even when taking into account these measures, still sometimes the effect of the laser beam on the hosts was visible after some time. However, for the experiments described below, we made certain that the effect of the laser on the hosts was negligible.

### 6.3.2 Nucleation on a hexagonal template

According to the simulations by Cacciuto and Frenkel [78], the (111) plane of the fcc structure, with a hexagonal structure, is most effective in inducing epitaxial crystal growth. In-plane order can be induced at several lattice distances. In Figure 6.2 the hexagonal lattices are shown that fit with an expanded hexagonal template with lattice spacings of $2d$ and $\sqrt{3}d$. In practice, crystallization starts at a lower volume fraction than the close-packed volume fraction of 74%. Therefore, the best lattice spacing for the seed structure is about 10% larger than the close-packed lattice spacings.

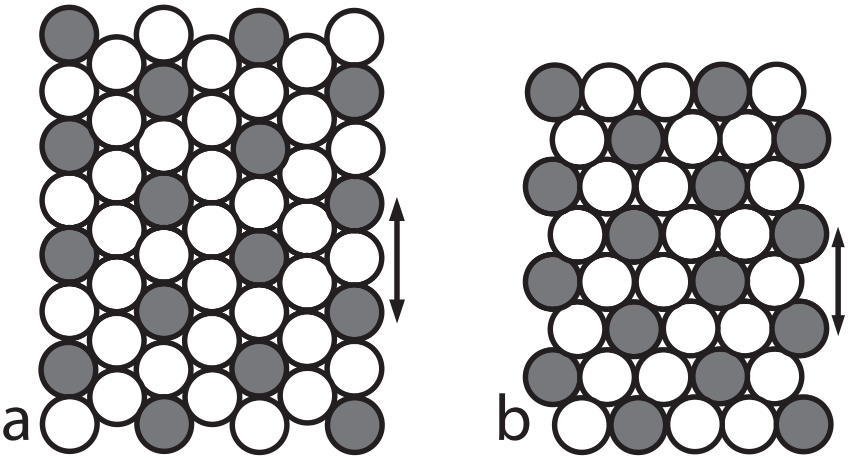

**Figure 6.2:** Schematic representation of hexagonal lattices that fit with an expanded hexagonal template with lattice spacings (indicated with an arrow) of (a) $2d$ and (b) $\sqrt{3}d$. The fixed tracer spheres are grey, while the white spheres are the host particles.

Experimentally, the ordering induced by the template structure can best be studied by averaging several confocal microscopy scans into one image. The resulting image contains sharply depicted spheres which are not moving and blurred moving spheres. Spheres that wet on the template or in between the template particles are depicted as clear spheres, while the fluid around the template is blurred. In Figure 6.3, the ordering in between a hexagonal template with two different lattice spacings is shown. The structure corresponded with the lattice depicted in Figure 6.2. The smaller spacing induced more order than the larger spacing and also the order next to the template was higher for the smaller spacing. The smaller spacing was slightly too small to accommodate the

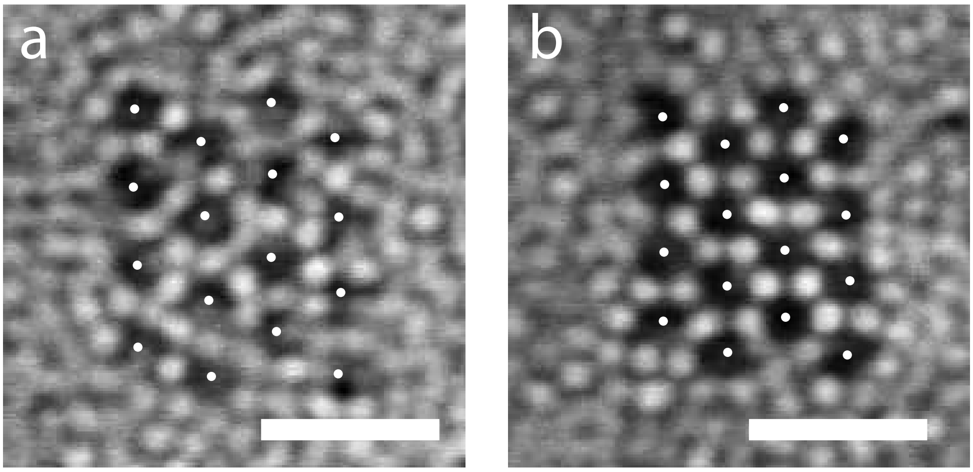

**Figure 6.3:** Confocal microscopy $xy$-images of hexagonal templates with two different lattice spacings: (a) 2.0 $\mu$m and (b) 2.2 $\mu$m. Both images were averaged over 8 scans. The scale bars are 5 $\mu$m.

spheres in between the template spheres. Therefore, the host spheres ordered slightly above and slightly below the trapped tracer particles. These spheres were fixed more in the $z$-direction than in the case for the larger spacing, where the host spheres could easily move in and out of the plane. The higher confinement of the host spheres for the smaller spacing resulted in more order, even disregarding the lattice mismatch.

Above and below the template structure, also freezing of particles was observed. We primarily studied the nucleus grown on the bottom side of the template, since these host particles bleached less than the spheres above, which were permanently exposed to the trapping laser. We studied templates with different lattice spacings, around the two lattice spacings as shown in Figure 6.3 with a step size of 0.1 $\mu$m. The crystalline order on top of the hexagonal templates never extended to more than two layers until crystallization started from the top surface (see Section 6.3.4).

Analyzing the hexagonal bond orientational order parameter ($\Psi_6$) for $xyz$-stacks below the trapped hexagonal templates confirmed the induced order at the level of the template layer and also one layer below. For two different hexagonal templates, the bond orientational order parameter is plotted as a function of the height from the template in Figure 6.4. We compared the order parameter averaged over a whole image (open symbols) with the order parameter in the small area directly above the template. Since there are less particles above the template, the noise in this line is significantly larger. Nevertheless, the increase in order in the template layer and the next layer around $z = 0.8$ $\mu$m can be clearly seen in image 6.4b.

Compressing the dispersion further led to crystallization. However, often, the flat top surface induced crystallization earlier than the slightly fluctuating hexagonal seed structure (the particles were sedimenting upwards because of a small density mismatch with the dispersion). The bulk crystal growing from the top of the sample cell downwards also grew around the template. As a result, the template structure did not act as a seed structure, but as a defect instead. This phenomenon is described in Section 6.3.4.

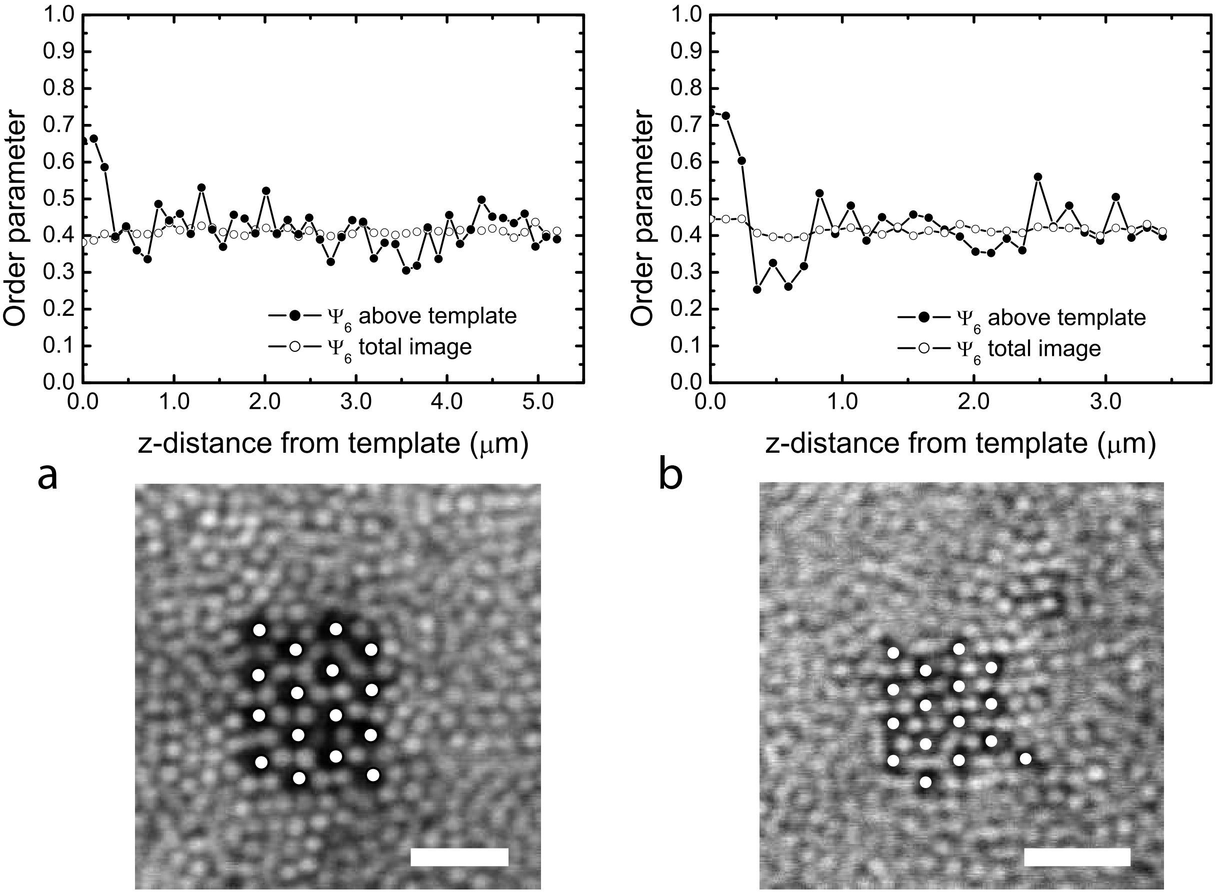

**Figure 6.4:** 2D hexagonal orientational order parameter as a function of the distance from two different hexagonal templates (spacings: (a) 1.9 $\mu$m (b) 1.8 $\mu$m), both consisting of 16 tracer particles (see confocal images below the graphs, the position of the tracer particles are drawn in as white dots as a guide to the eye). The scale bars are 5 $\mu$m.

### 6.3.3 Nucleation on a square template

Although the square template is less effective according to Cacciuto and Frenkel [78], nuclei grown on top (or below) can more be easily distinguished from the crystal grown heterogeneously from the top of the cell. Furthermore, the square lattice will yield exclusively fcc stacking, while the hexagonal template also can accommodate hcp stacking, yielding a randomly stacked rhcp structure.

We made square templates with different spacings, with a step size of 0.1 $\mu$m around the best-fitting lattices as depicted in Figure 6.5. Again, the best lattice spacing for the seed structure is about 10% larger than the close-packed lattice spacings, because of crystallization at volume fractions lower than 74%.

For a lattice spacing of 1.7 $\mu$m, the square lattice as depicted in 6.5b formed. This spacing is slightly higher than the expected spacing of $1.1\sqrt{2}d$, which is probably due to electrostatic repulsion between the particles. Besides in-plane ordering in between the tracer particles (visible in the first column of the averaged images in Figure 6.6), also the next layers below the template showed induced order as can be seen in the second and

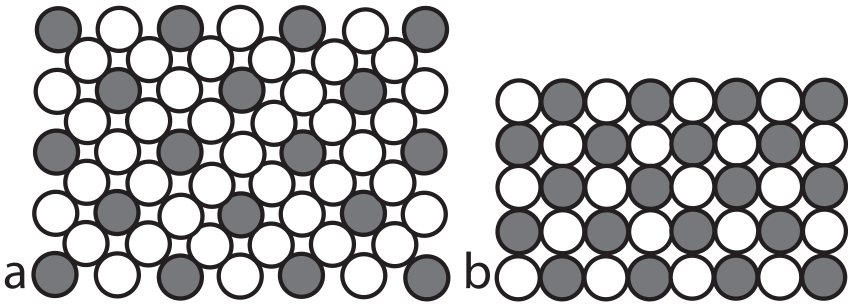

**Figure 6.5:** Schematic representation of square lattices that fit with an expanded square template with lattice spacings of (a) $2d$ and (b) $\sqrt{2}d$. The fixed tracer spheres are grey, while the white spheres are the host particles.

third column of Figure 6.6. The increase in ordering upon compression of the dispersion also becomes clear when comparing images in different rows of Figure 6.6.

To study the formation of the nucleus on the square (100) structure more quantitatively, we derived the square and hexagonal bond orientational order parameters ($\Psi_8$ and $\Psi_6$) from $xyz$-stacks at different host volume fractions. We did not use the $\Psi_4$ order parameter for the square order, because neighbors in a square lattice are not always defined correctly by Delaunay-triangulation [186]. Besides the four neighbors which should be found, also some of the next generation of neighbors (lying under an angle of 45° with the four direct neighbors) are determined as next neighbors. Therefore, we used the $\Psi_8$ parameter instead, which does correctly define the amount of square order [186].

While at the lowest volume fraction only the template layer itself had square ordering, the $\Psi_8$ increased for the next layers below the template as the volume fraction increased. At the same time the $\Psi_6$ decreased at the positions of these frozen square layers. The $\Psi_8$ reached values above 0.8 for the template layers, but this level of ordering is not attained in the next layers because of a slight mismatch of the lattice spacing compared with that of the bulk crystal. This resulted in layers which were slightly buckled close to the template, which in turn led to planes which were partly shifted in the $z$-direction. Moreover, the nucleus did not grow completely straight upwards, but rather grew a bit sidewards.

The $\Psi_8$ and $\Psi_6$ values averaged over 20 scans below the template as a function of the total number of spheres in a 2D slide (at a $z$-distance of 5 $\mu$m from the template) are shown in Figure 6.8. The number of spheres in a 2D image is a direct measure for the volume fraction of the host dispersion. The solid lines represent the order parameters for the particles directly above the template, while the dashed lines represent all particles in a 2D image. The order in the dispersion increased only slightly when the volume fraction of hosts increased, while the $\Psi_8$ clearly increased above the bulk value and at the same time, the $\Psi_6$ decreased below the bulk value.

Because of the slight lattice mismatch, the (1D) sides of the template did not grow out as a (100) face, but instead nucleated a distorted (111) plane. This distorted (111) plane adjusted itself to the bulk lattice spacing in the layers that grew upon it. In the bottom confocal image in Figure 6.7, the transition can be seen from the square symmetry in the middle of the nucleus to the hexagonal symmetry on the four corners, resulting in a four-fold star-shaped nucleus. Later, the star-shaped corners rearranged, exchanging the gradual change from square to hexagonal for a clear grain boundary from square to hexagonal. The close-packed lines of the hexagonal lattice fitted seamlessly to the close-packed lines of the square lattice (Figure 6.9a). The part of the nucleus which had square symmetry had about the same area as the initial square template, but rotated 45°. The final inner nucleus oriented with the (100)-plane horizontal thus did not have the form of a spherical cap on top of the template, but resembled a platelet twisted around the $z$-axis. The total nucleus, including the crystal domains which had grown on top of the distorted inner nucleus (both on top and below the template) had the form of a spheroid (Figure 6.9b).

After growing the nucleus by increasing the volume fraction, de volume fraction of the dispersion was decreased again, which resulted in melting of the nucleus. The melting of the nucleus did not proceed equally fast on all sides, resulting in an irregularly shaped crystal. Since the decrease in volume fraction might also have been inhomogeneous over the sample, we cannot conclude that some planes melt easier than others.

### 6.3.4 Frustration of a crystal by the trapped structure

In the current experiments, we tried to lower the energy barrier for nucleation of a bulk dispersion of host spheres, using a seed structure of trapped tracers particles. At the same time, however, also the walls of the sample cell are expected to induce crystallization below the bulk freezing density. The pre-freezing at a flat wall only starts at a pressure (or volume fraction) a few percent below bulk freezing [175]. Moreover, because of the density mismatch of the host particles with the solvents, the volume fraction of hosts was higher at the top of the sample. Thus, there was a large chance that crystallization took place at the top sample wall before it crystallized at the seed structure. In these cases, we could study the effect of a defect on the crystal growth.

In Figure 6.10 confocal images are shown of a crystal of host spheres grown from the top of the sample cell downwards. While growing, it encountered the trapped seed structure as an obstacle. The crystallization around the template was first suppressed because of the mismatch of the crystal orientation with the template orientation. The crystal grew around the template and released the stress due to the template through defect lines and grain boundaries starting in the trapped structure. In Figure 6.10, the defect lines are indicated with dashed arrows and the grain boundaries are indicated with solid arrows.

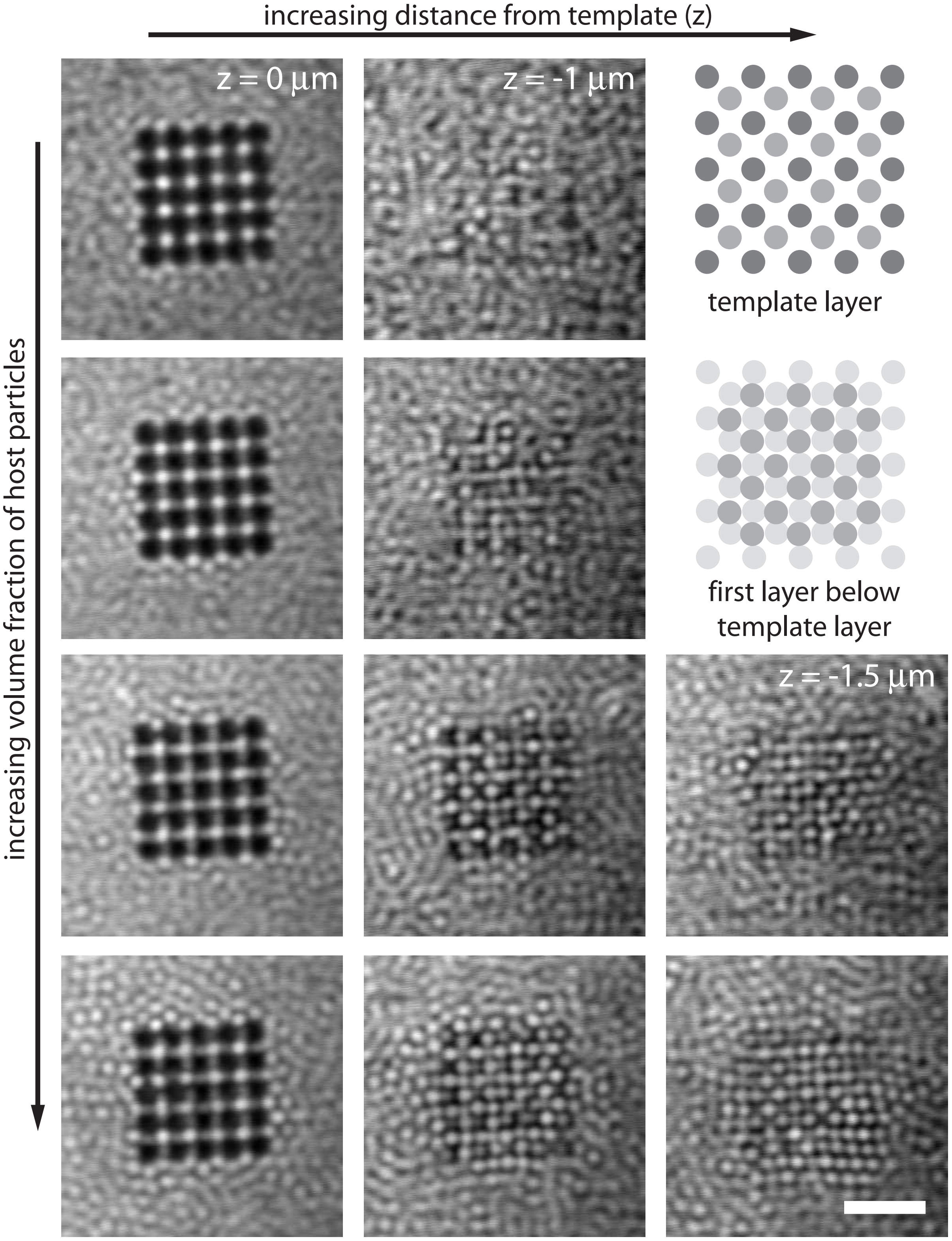

**Figure 6.6:** Confocal images of the host particles on and in between a square template, averaged over 20 images taken 3 seconds apart. Hosts which are solid-like appear as clear dots, while moving particles are blurred. From the top image to the bottom image, the volume fraction of the host particles increases. From left to right, the distance from the template increases. The scale bar is 5 $\mu$m. The top right inset, schematically depicts the expected crystallization of the host particles (grey) between the template particle (black), together forming the template layer. The first layer below the template layer consists of (grey) hosts in a square array on top of the (light grey) template layer.

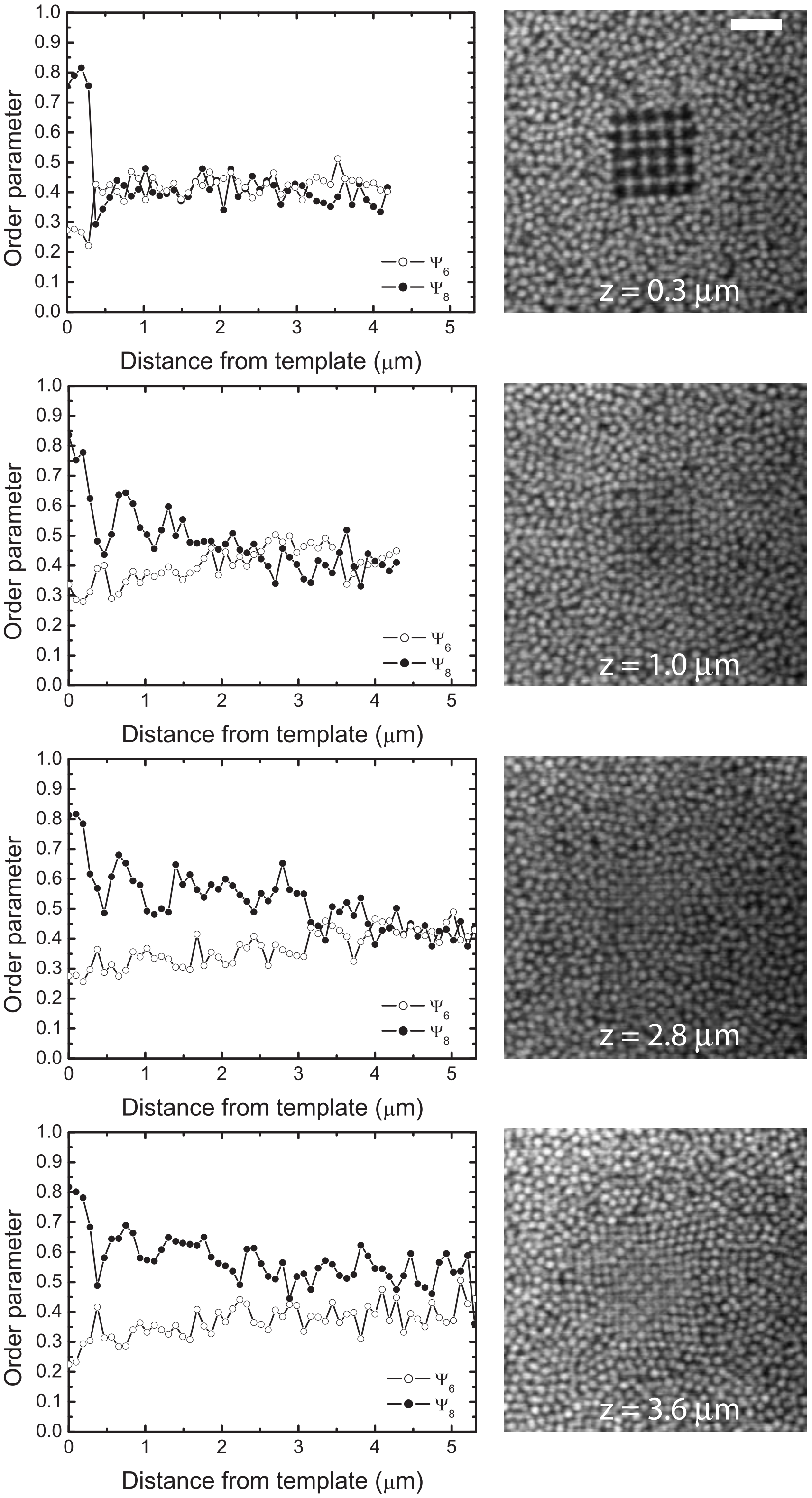

**Figure 6.7:** 2D square and hexagonal orientational order parameter as a function of the distance from a square template, consisting of 25 tracer particles. The 2D order parameters are derived from 2D slices out of 3D confocal microscopy $xyz$-stacks. From the top graph to the bottom graph, the volume fraction of the host particles increases. Next to the graphs, confocal images are shown which originate from the $xyz$-stacks. The distance $z$ from this image to the tracer template is shown in the image. At these heights, the square order was still clearly visible for the corresponding volume fraction of host particles. The scale bar is 5 $\mu$m.

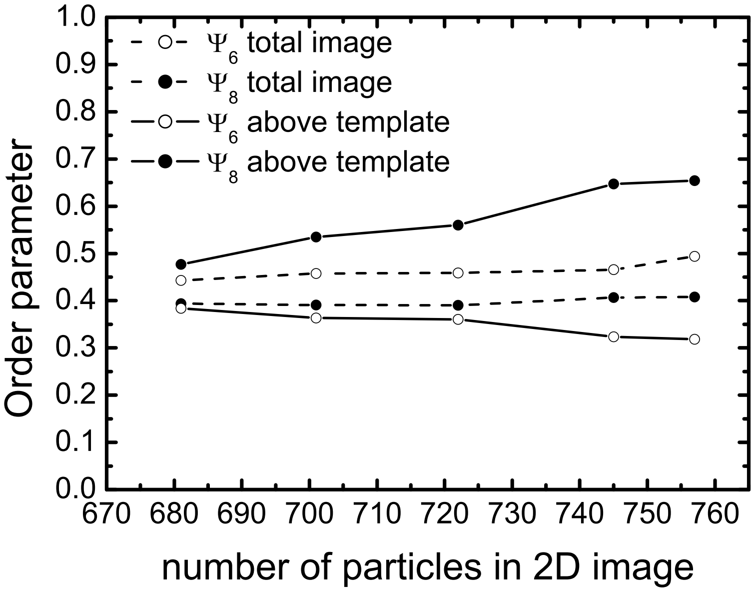

**Figure 6.8:** Graph of the square and hexagonal order averaged over 20 2D images at a height of 0 $\mu$m to 2 $\mu$m below the template structure. The solid lines represent the order parameter in the area above the template, while the dashed lines represent the order parameter in the whole 2D image. The open symbols stand for the $\Psi_6$ values, while the closed symbols stand for the $\Psi_8$ values.

The crystal in Figure 6.10b was hardly frustrated by the square defect structure: the domain orientation was not changed and only two defect lines alleviated the stress. However, the large amount of defect lines and grain boundaries in this crystal in Figure 6.10a indicates the high stress in the crystal due the trapped template. This grain boundary pinning was observed in defect studies by Villeneuve et al. [187].

Coating of the sample cell walls with polydisperse spheres could help to avoid heterogeneous crystallization from the top surface caused by pre-freezing in future experiments.

## 6.4 Conclusions

We studied nucleation on a 2D seed structure, trapped with optical tweezers in the bulk of a dispersion of host particles as a function of the volume fraction of host particles in the dispersion. The combined use of time-shared optical tweezers and dielectrophoretic compression enabled us to control in-situ both the symmetry and spacing of the seed structure and the volume fraction of the dispersion.

We studied seed templates with tracer particles on a square lattice (resembling the (100) plane of the an fcc crystal) or on a hexagonal lattice (resembling the (111) plane of an fcc crystal). The lattice spacing was chosen in such a way that host particles exactly fitted in between the tracer particles. It was found that for both template structures,

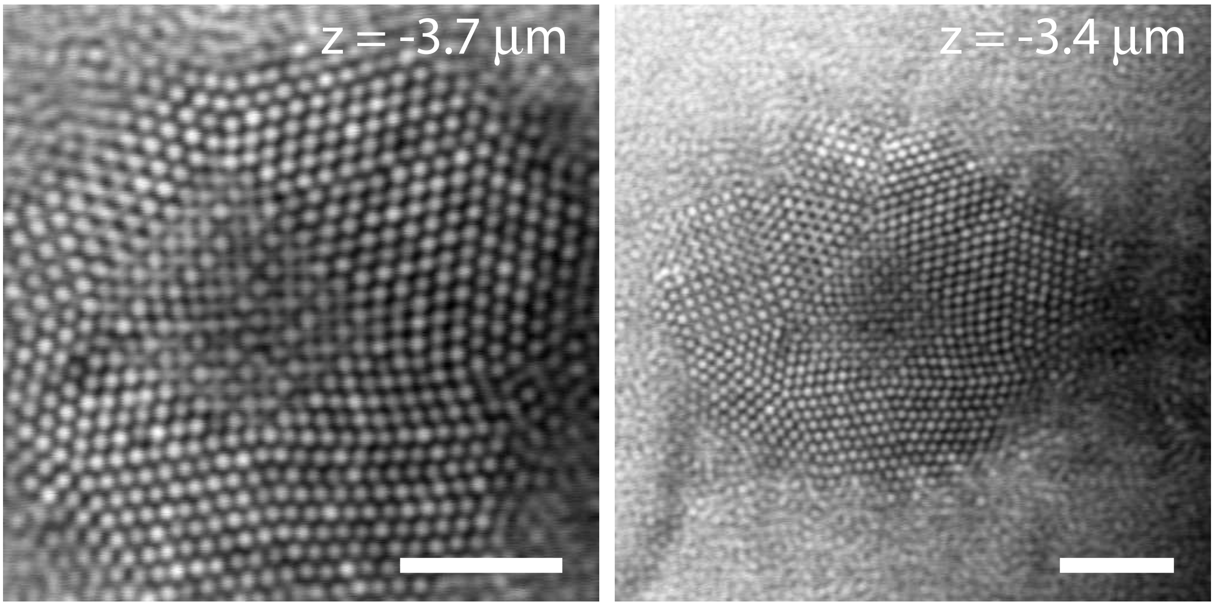

**Figure 6.9:** Confocal images with an overview of the nucleus which was formed around the seeds structure, averaged over 20 images taken 3 seconds apart. Hosts which are standing still appear as clear dots, while moving particles are blurred. The scale bars are 10 $\mu$m.

square and hexagonal, order was induced in the host dispersion, both in plane with the template (to the host particles in between the tracer particles) and also in the layers of hosts just below the template.

On a square seed structure an outgrowing nucleus was formed, which first grew from the template down- and upwards in square-ordered layers. Afterwards, these layers grew out to the sides, however with hexagonal order in the horizontal planes. The final spheroidal crystal contained several domains with different orientations around the initial nucleus which had its (100) plane horizontal. This structure of the nucleus does not agree with the assumptions of classical nucleation theory.

When a crystal, grown from the top surface of the cell encountered the trapped structure, it grew around it while releasing stress in defect lines and grain boundaries. Defect doped crystals, which can have a defect state in the photonic band gap as discussed in Chapter 8.3.6, can be achieved in this manner for a small region of crystal.

## 6.5 Acknowledgements

This work was partly done together with Mirjam Leunissen, who helped to design a dielectrophoresis cell for the present purpose. We want to thank Dirk Vossen for the synthesis of the tracer particles and the initial help with the experiments. Furthermore, we thank Didi Derks for the synthesis of the host particles. Astrid van der Horst en Peter van Oostrum are gratefully acknowledged for the help with and the maintenance of the optical tweezers setup.

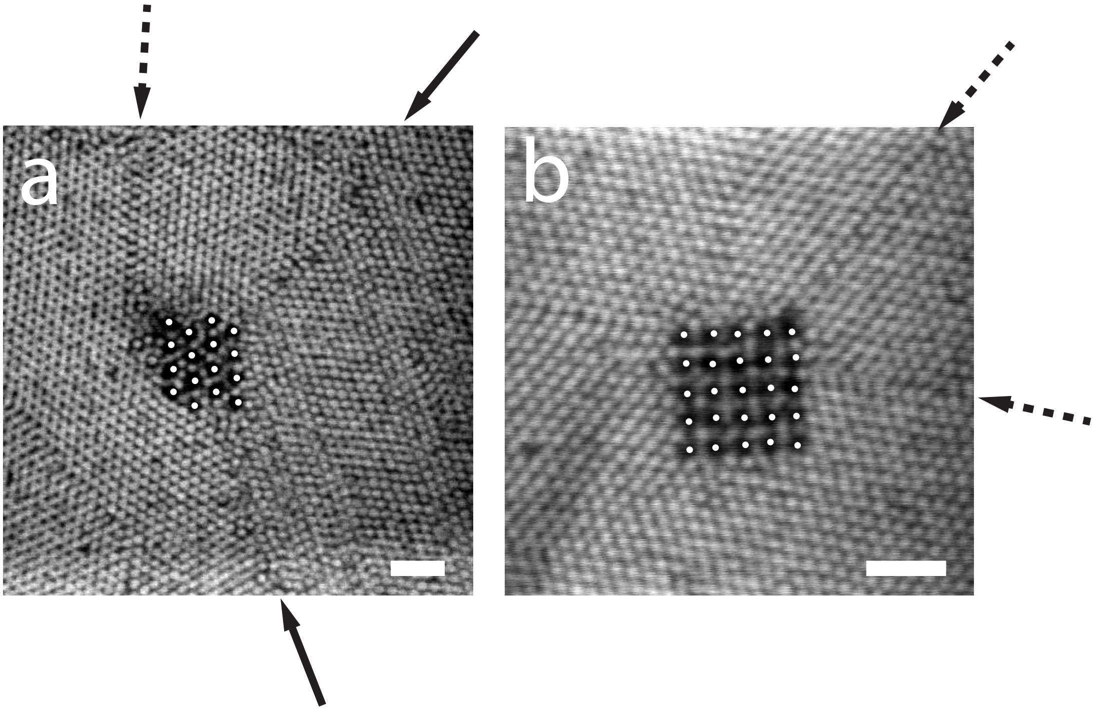

**Figure 6.10:** Confocal images of hosts around a hexagonal (a) and square (b) template which, after compression of the dispersion, frustrated the crystal of hosts which was grown around it. The defect lines in the crystal are indicated with dashed arrows and the grain boundaries are indicated with solid arrows. The position of the tracer particles are drawn in as white dots as a guide to the eye. The scale bars are 5 $\mu$m.

# 7

# Growing large colloidal single crystals by dielectrophoretic compression on a much smaller structured surface

In this chapter we present a new fabrication method for colloidal (photonic) crystals, which combines dielectrophoretic compression with epitaxial growth. By compressing a colloidal dispersion in a field-free slit with a hole array on the bottom, we were able to grow fcc crystals with the (100) plane horizontal. When the field gradient was high enough, the crystals could be pushed forward over the hole array, after which growth on the same single crystal was seen to lead to single crystals much larger than the template. The bottom layers in between the crystal and the hole array were sheared because of this motion. Although we have shown that the method works, the formation and the quality of the crystal is dependent on the smoothness and spacing of the template, the compression speed and the density matching of the dispersion and needs further optimization to see how robust this growth method can be made.

## 7.1 Introduction

Colloidal crystals have gained recent interest as a building block for photonic applications [131–133]. When an ordered colloidal structure has the right symmetry and sufficient dielectric contrast, a photonic band gap can open in the dispersion relation which describes the wave propagation in different crystal directions as a function of frequency. Light of certain frequencies cannot propagate in any direction in the colloidal crystal. However, this property is sensitive to the amount of defects in the crystal: when there are too many defects the photonic band gap closes [188, 189]. Therefore, a method is needed to create colloidal crystals with a low amount of defects and which is furthermore fast and can be easily scaled-up.

The most commonly used techniques to make thicker 3D colloidal crystals rely on self-assembly of colloidal particles, such as controlled drying [144, 190–192], spin coating [99, 100], shear alignment [193, 194] and dielectrophoretic compression [97, 121]. These methods yield random hexagonal close packed (rhcp) or face centered cubic (fcc) structures, in most cases with the hexagonal planes parallel to the substrate.

For photonic applications, one would like to be able to fabricate crystals with different orientations or with different crystal lattices and symmetries. In the colloidal assembly technique called “colloidal epitaxy”, the crystal structure and orientation can be directed using a patterned surface [70–75]. The colloids sediment on the patterned surface, adapting to the symmetry and spacing of the surface pattern. The next layers take over this spacing and symmetry in a similar way. Since the method relies on sedimentation, it is relatively slow, but it can yield good-quality crystals on the bottom of the container. However, the top layers of the sedimented crystal will never crystallize, they stay in the fluid phase. This fluid layer on top of the crystal is undesirable for photonic application, since this layer scatters isotropically.

A different approach to grow colloidal crystals on a patterned surface is layer-by-layer growth [112]. This process has the advantage that different sizes of colloids can be combined into one structure and also that the structure is dried during the process, which facilitates further processing. The multi-step process, however, cannot easily be scaled up to industrial processes. Colloidal epitaxy has been combined also with ‘controlled’ drying, which is a process that is generally much faster than sedimentation. However, it was found that it is only possible to effectively combine these processes for larger spheres, if gravity is also helping to push the particles onto the template [195, 196].

In this chapter we combine the epitaxial growth on a patterned surface with compression of the dispersion by dielectrophoretic forces. This last technique has proven to be a well-controlled and fast way to create high-quality colloidal crystals without the need to rely on gravitational compression [97, 121]. An electric field induces polarization dipoles in the particles, which experience a so-called dielectrophoretic force in an inhomogeneous electric field. This results in the translational motion of the colloids [92]. Leunissen et al. have found an intriguing growth mechanism in which the entire crystal was pushed forward as a whole in a plug flow by the field gradient while it grows, yielding large single crystals [97]. Combining this compression method with a templated bottom surface adds up the advantages of both methods for colloidal crystal fabrication, giving a fast, well-controlled method for growing colloidal crystals with a pre-defined orientation and crystal structure. In this chapter, we will first show that it is possible to epitaxially grow colloidal crystals on a templated surface by dielectrophoretic compression. This is already significantly faster than the normal epitaxial sedimentation process. Then we will demonstrate in preliminary proof-of-principle experiments the possibility of pushing the colloidal crystal off the template without loosing its orientation and structure. By optimization it may be even possible to let the templated region function as a template for a much larger single crystal of the same structure.

## 7.2 Experimental methods

In the experiments described in this chapter, we combine dielectrophoretic compression (Chapter 2.5) with epitaxial growth on templates made by soft lithography (Chapter 2.3.2). The dispersion from which the colloidal crystals were grown is described in Section 7.2.1, the dielectrophoresis sample cell adapted for epitaxial growth is described in Section 7.2.2.

### 7.2.1 Colloids and dispersions

We used nearly density and refractive-index matched dispersions of poly(methyl methacrylate) (PMMA) particles ($\epsilon_p \approx 2.6$), completely labelled with rhodamine isothiocianate (RITC). The diameter of these particles was 1.4 $\mu$m as determined from static light scattering (SLS) data.

The solvent mixture consisted of cyclohexyl bromide (CHB) and cis-decalin, with a 21 weight percentage of cis-decalin ($\epsilon_p \approx 6.0$, $n \approx 1.49$). At this ratio of CHB and cis-decalin, the particles are almost density matched with the dispersion. To obtain hard-sphere-like interactions between the colloids, we saturated the solvent mixture with tetrabutylammonium bromide (TBAB, 260 $\mu$M) to screen the charges on the particles.

### 7.2.2 Sample cell design

The sample cell design is analogous to the sample cell design as described in Chapter 2.5. It consisted of two cover slides (22 mm × 22 mm no. 1 glass cover slip), which were on the inside sputter-coated with a layer of gold (10 nm) as an electrode (with a thin chromium layer (3 nm) underneath to wet the gold). In the middle of the sample, there was an electrode-less slit of 1 or 2 mm wide into which the particles were compressed by the inhomogeneous electric field. Before coating the bottom cover slide with the gold electrode, a soft-lithography template was applied in Norland OA 68 UV glue or Norland OA 71 UV glue as described in Chapter 2.3.2. For the experiments in which the crystal was pushed from the template, the template was applied in such a way that it extended till roughly one quarter of the slit. In other cases, the template extended over the whole slit. The two cover slides were held apart by strips of no. 00 or no. 0 cover slides, creating a cell of about 80-100 $\mu$m high. These strips were glued to the cover slips by Norland OA 71 UV glue. The sample cell was sealed off with Norland OA 68 UV glue. The electrical contacts between the gold electrodes and the T2 thermocouple alloy wires (diameter 50 $\mu$m, Goodfellow) were made with silver paint (Jeol).

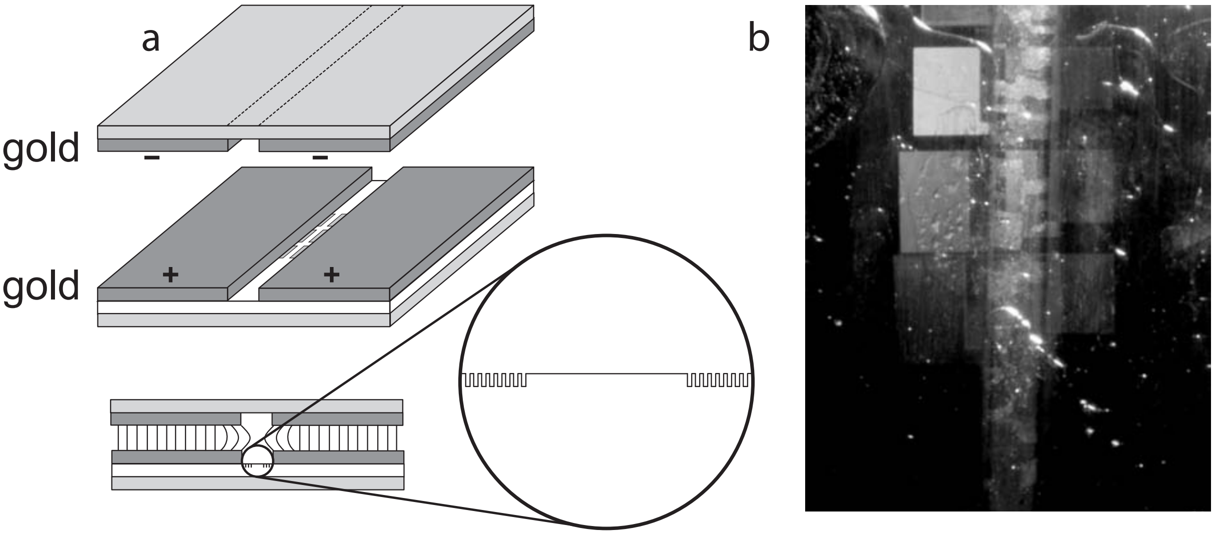

**Figure 7.1:** (a) Schematic representation of the sample cell used for the combined epitaxy-dielectrophoresis experiments. The sample had a double-slit geometry with a partly templated surface on the bottom cover slide. In the side view, the field lines of the inhomogeneous electric field are depicted. The side view of the slit is enlarged in the circle. (b) *(A color version of this figure can be found on page 36)* Photo of the middle of a sample cell with the hole arrays extending over the whole slit (and also partly in the electrode-region). The colored rectangles are caused by the Bragg reflections from the regular template structures, while the irregularly shaped colors are caused by the colloidal domains compressed in the slit.

The field we applied was a high frequency electric field (1 MHz), which has the advantage that it polarizes the colloidal particle itself, but not the double layer of ions around it. We slowly turned up the field with steps of about 5 V per 30 minutes until the crystalline state was reached at the edge of the field-free slit. Depending on the thickness of the cell (and thus the separation of the two plate-electrodes) and the time-span available for the compression, the final voltage needed for the initiation of crystallization within about 4 hours ranged from 25 V to 40 V.

## 7.3 Results and discussion

### 7.3.1 Growing fcc crystals with the (100) plane horizontal

In a dielectrophoresis cell with on the bottom square arrays of holes with different spacings, we managed to grow fcc structures with the (100) plane parallel to the bottom wall. The stacking of the crystals grown on this template is well defined, in contrast to the rhcp structures which are normally grown by sedimentation or dielectrophoretic compression on a flat wall. The pure fcc stacking is advantageous for the photonic properties of the photonic crystal [197, 198].

The fcc structures grew best on the template with a spacing of 1.74 $\mu$m. The quality of the crystals was strongly dependent on the compression speed: fast compression yielded crystals with a higher amount of defects. The defects in the crystals were primarily caused by inhomogeneous compression, which moved one part of a crystal faster than another part of the same crystal.

We examined the motion of the crystals over the template. At slow compression (at a voltage lower than about 10 V), the crystals hardly move over the template, because the compression forces are not enough to push them over the barrier that is caused by the anchoring of the lowest layer in the holes of the template. At higher voltages the dielectrophoretic forces were high enough to overcome the barrier and we could follow the movement of the crystal by bleaching a small rectangular area with the confocal laser and following it in time. Actually, a whole column of particles was bleached when scanning a rectangle at a certain height in the bulk of the sample, giving the possibility to determine the displacement of the crystal at different heights. Two confocal $xy$-images of the (100) plane of a colloidal fcc crystal with a bleached rectangle are shown in Figure 7.2a and 7.2b. The second image is taken half an hour after the first at the same place. The movement of the bleached rectangle implies the movement of the whole crystal. The images were taken during a fast compression, which distorted the crystal structure as can be seen in Figure 7.2b.

The crystal did not move with a continuous speed, it generally moved with discontinuous steps which were multiples of the lattice parameter of the template. In effect, the motion can be described as a regular stick-slip motion. Sometimes different rows of the crystal did not move an equal distance, resulting in deformation of the bleached rectangle, but after each step the defects between the rows annealed and the crystal stayed almost without defects.

A bleached rectangle in the bottom layer was followed during 25 minutes and we made an $xyz$-scan of a bleached column, with a heigth of 12 $\mu$m, afterwards. The bleached rectangle on the bottom moved about 6 $\mu$m during this time in a stepwise fashion, such that it could fall back in the template holes after every step.

In the graph in Figure 7.2 the displacement in $x$ and $y$ of the bleached column after 25 minutes is plotted as a function of the height from the template. The position of the bleached rectangle in the bottom layer is set to zero. From this graph can be deduced that the bottom layer was held back by the template holes and therefore moved 16 $\mu$m less than the top layers. The top crystal moved as a whole, in plug flow as observed before [97] with on average 53 $\mu$m per hour and also a few layers below, a small part of the crystal moved as a whole. The layers in between these two pieces of crystal and in between the lowest crystal and the bottom were sheared. These also ended up to be less crystalline, they were shear melted.

The crystals formed after complete compression, usually filled the slit from the top to the bottom. The stress in the crystal due to a mismatch between the crystal and the template (only templates with a few discrete lattice distances were available) was released by the formation of defects similar to the defects found in the NaCl crystals grown by dielectrophoresis on a square template (Chapter 3.3.5). In the NaCl crystals out-of-plane shifts were observed of parts of the crystal, of which the boundaries were visible as under an angle of 45° with the horizontal in images of the (100) plane. From series of images of the (100) plane, we could conclude that these crystal parts were shifted over the (111) plane.

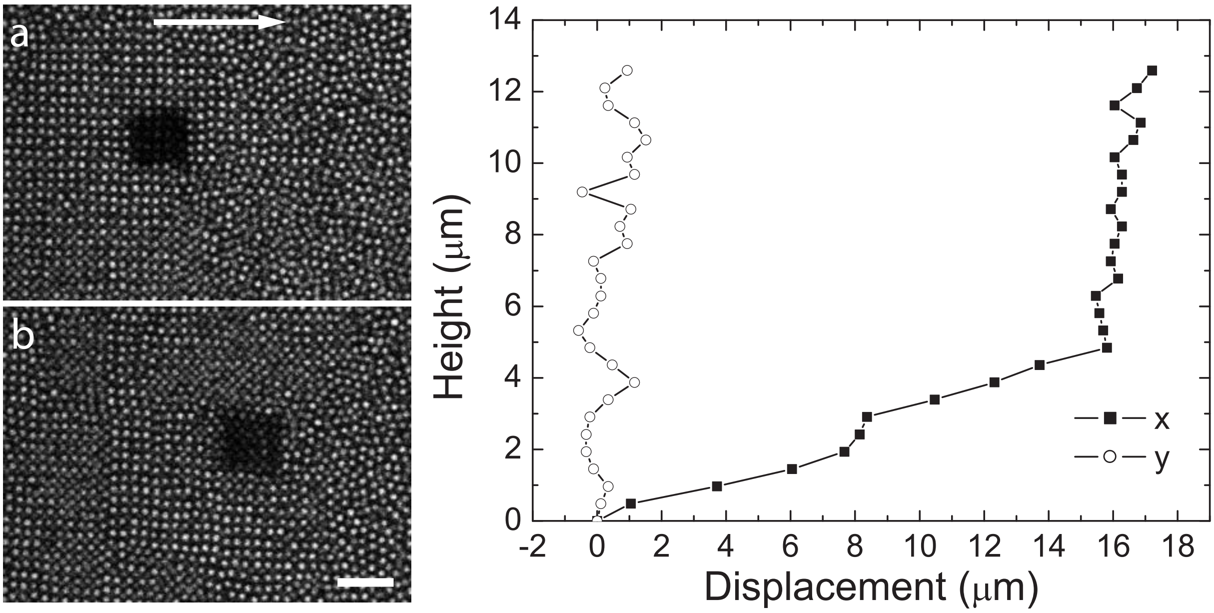

**Figure 7.2:** The confocal microscopy images in (a) and (b) show a bleached area in a colloidal crystal grown on square template, which is pushed forward by dielectrophoretic forces. The image (b) is taken half an hour after image (a) at the same place. The arrow indicates the field gradient direction. The scale bar is 10 *μ*m. In the graph the displacement in $x$ and $y$ of the bleached area is plotted versus the height $z$ from the bottom wall.

In the confocal $xz$-images of the (110) plane of the compressed single-component fcc crystals, defect lines were found under 55° with the horizontal. In Figure 7.3 two of these defect lines can be discerned. The crystal plane stayed in the imaged plane. Therefore, we can conclude that also in these crystals, parts of the crystal slid over the close-packed (111) plane to release stress. These defect lines are the intersection of the (110) plane with the (111) plane along which two pieces of crystal are shifted to release stress.

### 7.3.2 Growing colloidal crystals on an hcp (110) template

As was shown by Hoogenboom et al. [74, 75], also metastable structures can be grown by epitaxial growth on a suitable template. A hole array with a pattern of the (110) plane of a hexagonal close packed (hcp) structure was used to dictate the typical $ABAB$ stacking to a sedimented silica colloidal crystal. The spheres in the (110) plane of hcp are depicted schematically in Figure 7.4. The figure shows on the left the configuration as used for the hcp-template. On the right, the next layer which grows on the template is shown in grey. The dimensions of the template are characterized by the distances $a$ and $c$, which for spheres of close-packed diameter $d$ are given by $a = \sqrt{3}d$ and $c = 2d\sqrt{\frac{2}{3}}$. The second layer of spheres on top of the template layer is shown in grey.

The hcp-structure is metastable in a hard sphere dispersion. A density matched dispersion could therefore also nucleate an fcc structure at the flat top wall of the dielectrophoretic compression cell instead of at the bottom template. However, the energy

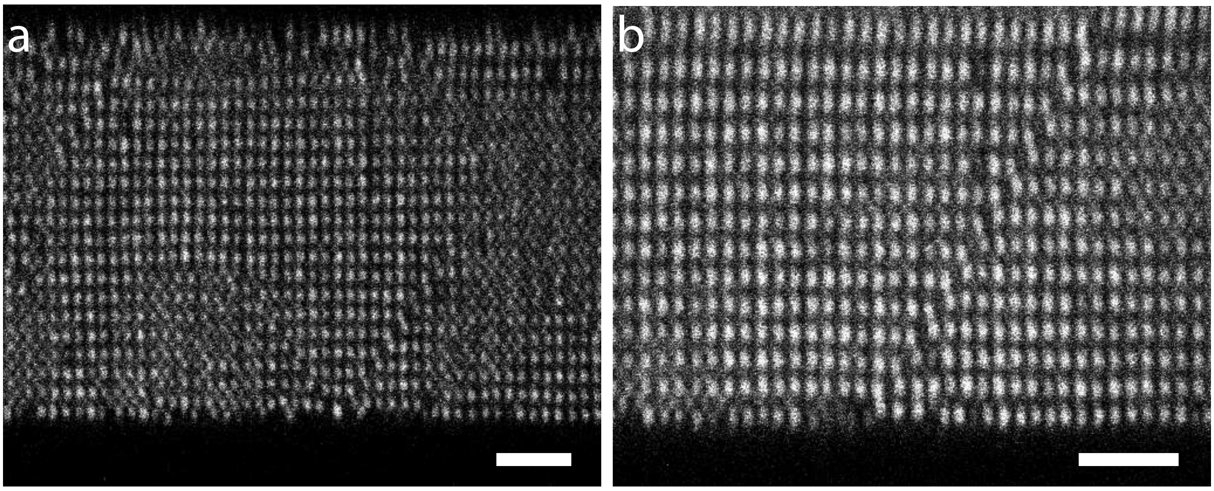

**Figure 7.3:** Confocal microscopy $xz$-images of the (110) plane of an fcc crystal formed by dielectrophoretic compression on a square template. Defect lines under 55° with the horizontal are an intersection of the (110) plane with the close-packed (111) plane over which part of the crystal was displaced to release stress. The scale bars are 10 $\mu$m.

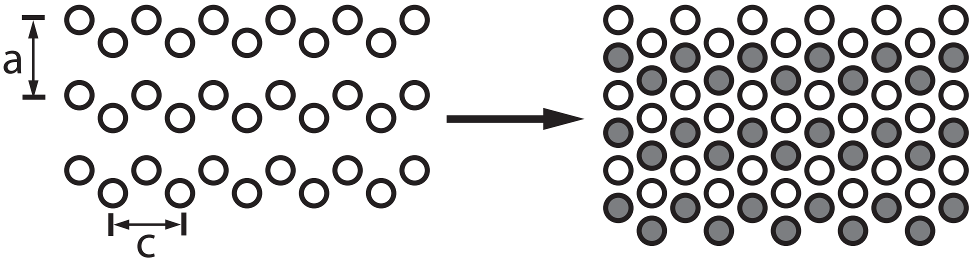

**Figure 7.4:** Schematic representation hcp (110) pattern. The lattice parameters $a$ and $c$ are given in the left image. The right image shows the bottom layer of spheres in white and the next layer which grows on top in grey.

barrier for nucleation at a templated surface is significantly lower than for nucleation at the flat top surface, as long as the templated surface is closely matching the crystal structure [76, 175]. Therefore, theoretically also metastable structures can form in a dielectrophoresis cell with a suitable template on the bottom. In our experiments we used nearly density matched dispersions to facilitate the horizontal movement of the crystals over the template. Since the density of the dispersion is very close to the density of the particles, a small temperature change can invert the sedimentation direction. We found that when the particles are sedimenting upwards, as expected, the particles do not go into the holes of the template early enough to take over the symmetry. A dispersion which is sedimenting slightly downwards is more suitable in this case.

We compressed a dispersion in a cell with several hcp templates on the bottom wall, with varying lattice parameters. When crystallization set in, the bottom particles did take over the hcp pattern of the hole array, but the expected zigzag pattern did not extend further than the second layer because of a misfit of the lattice parameters with the effective diameter of the particle. On the hole arrays corresponding to $d = 1.77$ $\mu$m and $d = 1.68$ $\mu$m (Figure 7.5a), the particles could go too deep in between the particles in the holes, this way a hexagonal pattern formed, which did not pass on the hcp-symmetry. On the hole arrays corresponding to a diameter of $d = 1.50$ $\mu$m, distorted square layers formed, forming an fcc crystal, which is rotated 45° around the $z$-axis with respect to the fcc crystals made on the square templates (Figure 7.5b). The fcc crystal was pushed towards the middle of the slit with a speed of about 60 $\mu$m per hour, which shows that also differently oriented fcc crystals can be pushed without (further) distortion of the crystal.

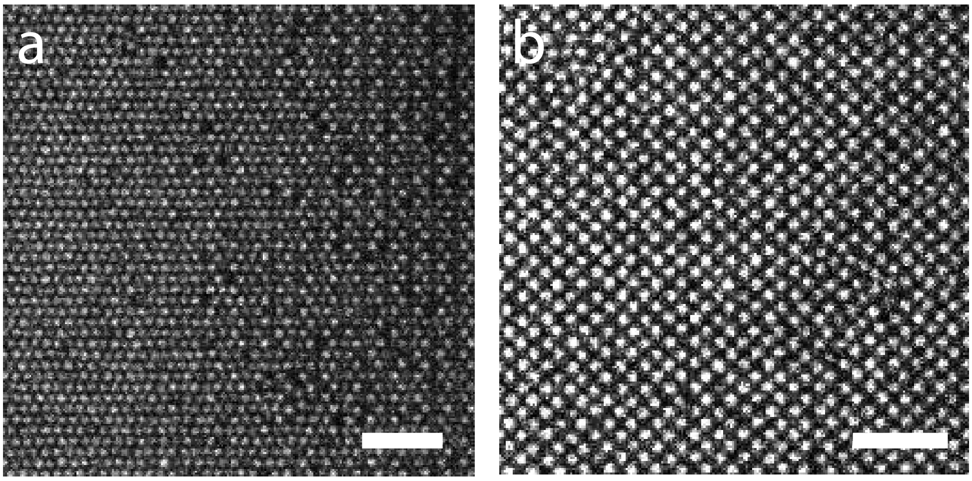

**Figure 7.5:** Confocal images of distorted structures formed on hcp (110) templates corresponding to a close-packing diameter of (a) $d = 1.68$ $\mu$m and (b) $d = 1.50$ $\mu$m. The scale bars are 10 $\mu$m.

### 7.3.3 Growing large colloidal crystals on a small templated surface

By letting the template end at a quarter of the slit-width, we investigated the possibility of growing very large colloidal crystals with a certain orientation and structure, dictated by only a small templated surface. We used the fact that dielectrophoretic forces push the crystal forward, to grow a crystal on top of a template and then push it off the template towards the middle of the compression-slit. The principle is illustrated by Figure 7.6.

The difficulty in pushing the crystal from the template lies primarily in the imperfection of the end of the soft lithography templates. These templates are a replica of hole arrays made by electron beam lithography, which always suffer from the so-called "proximity effect": due to scattering electrons and secondary electrons, not only the holes of the template are changed chemically, but also the area around it. Therefore, after dissolution of the holes, the whole template area is a bit deeper than the initial surface. At the end of the template, the moving crystal thus encounters a threshold which disturbs the crystal structure and often converts it to an fcc structure with the (111) plane horizontal as can be seen in Figure 7.7.

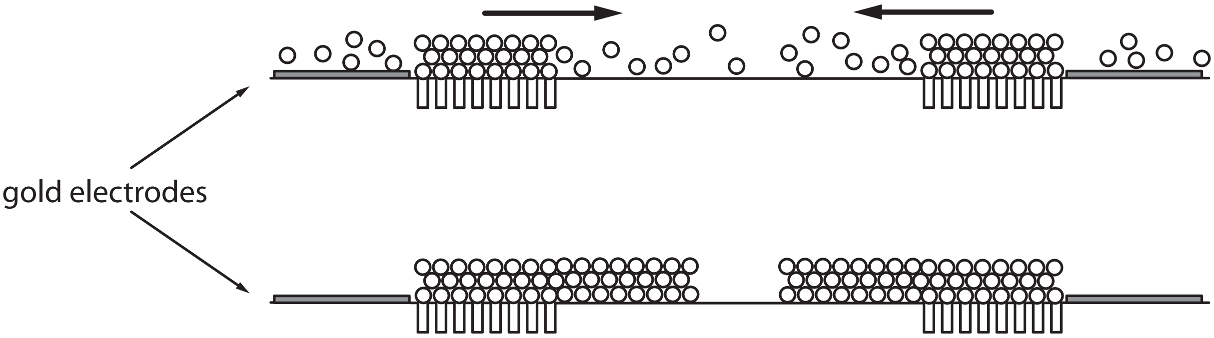

**Figure 7.6:** Schematic representation of the growth of large single-domain colloidal crystals with a predefined orientation by pushing a crystal, formed on a templated bottom wall, forward.

However, it was possible to produce a template which does not have a threshold at the end by not pressing the end of the lithography mask completely in the glue. This way, the holes gradually became less deep towards the end of the template. Using this template we were able to grow an fcc crystal with the (100) plane horizontal, which extended over a much larger horizontal area than the templated surface. $xy$-confocal microscopy images of the crystal grown with the described method are shown in Figure 7.8. These images show that the crystal was not pushed forward homogeneously. After the end of the template, the orientation of the crystal was not corrected by the template anymore and since it was pushed more on one side than on the other, the crystal changed direction.

The misfit of the template (with a spacing of 1.42 $\mu$m) with the crystal resulted in waves in the planes and even slight buckling. The close-packed spacing of the crystals which are not on the template was around 1.8 $\mu$m. This was a result of the fact that the effective diameter of the PMMA particles is larger than the physical diameter because of incomplete screening of the charge on the particles. These preliminary results do have great promise for optimization.

## 7.4 Conclusions

In this chapter we investigated the feasibility of a fabrication method of colloidal (photonic) crystals based on a combination of epitaxial growth and dielectrophoretic compression. This combination of techniques makes it fast and versatile, since it does not rely on (slow) sedimentation and the crystal structure and symmetry can be chosen by choosing an appropriate epitaxial template. Furthermore, if the crystal can be pushed off the template by dielectrophoretic forces, only a small template on the bottom would suffice for the growth of a large single-domain crystal.

We managed to grow an fcc crystal with the (100) plane horizontal on a square template and pushed it forward over the template by dielectrophoretic forces. By monitoring a bleached column of particles, we showed that the bottom layer of particles was anchored in the template and therefore moved less than the layers above. The layers just above the bottom were sheared between the bottom layer and the crystal which moves above it. When the crystal was pushed off the template, the bottom layer lost its square symmetry,

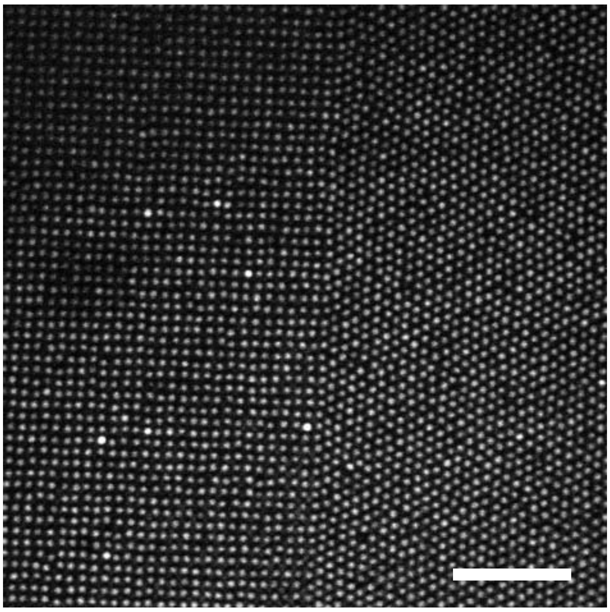

**Figure 7.7:** Confocal *xy*-image of the bottom layer of colloids on a square template which ends halfway the image. The square symmetry is lost directly after the colloids are pushed over the threshold at the end of the template. The scale bar is 20 $\mu$m.

but the crystal above stayed intact.

Although we showed that the principle of the proposed fabrication method works, we also found that the method is sensitive to the smoothness and spacing of the template, the compression speed and the density matching of the dispersion. However, it is not even known yet which depth of holes still induces 3D crystal growth. If shallow holes would still induce epitaxial crystal growth, it would significantly reduce the friction and make the proposed scheme more robust.

As was found for NaCl crystals made by dielectrophoretic compression on an epitaxial template, stress in the crystal, due to a mismatch of the template with the crystal lattice parameters, was released by shifting part of the crystal over the close-packed (111) plane.

## 7.5 Acknowledgements

This work was partly performed together with undergraduate student Floor Kamphorst. Jacob Hoogenboom is gratefully acknowledged for the fabrication of the masters for the soft lithography.

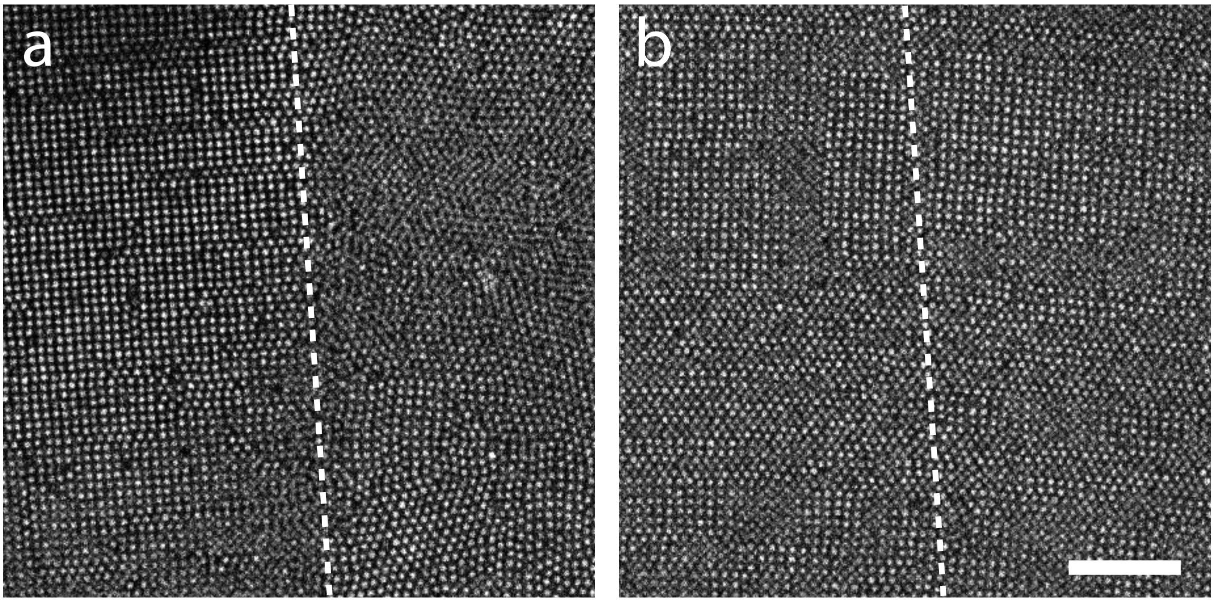

**Figure 7.8:** Confocal images of an fcc crystal with the square (100) face horizontal as a result of the square template on the bottom of the sample cell. The edge of the template is indicated with the dashed line (the template was left of this line). The crystal was pushed off the template towards the right of the images. (a) The bottom layer of the crystal, which lost the square orientation because of shear (b) A few layers above the bottom, the crystal kept its horizontal square symmetry even when pushed over the edge of the template. The scale bar is 20 $\mu$m.

# 8

# Spin coating colloidal crystals from volatile solvents

Spin coating a colloidal dispersion in monomer on a substrate yields colloidal crystals with large domains and good global alignment [99]. Using a volatile solvent as ethanol as dispersion solvent, results in colloidal crystals with a larger refractive index contrast (in air) [100], which is advantageous for the use of these colloidal crystals in photonic applications. Also, the orientation of the face centered cubic crystals can be tuned, when using a volatile medium. The mechanism behind the formation of these crystals and the parameters that determine their orientation are unknown. In this chapter, the colloidal crystals formed by spin coating colloids dispersed in ethanol are studied using several techniques, both in reciprocal space (white light diffraction, laser diffraction) and in real space (scanning electron microscopy, confocal microscopy). The colloidal crystals have an orientation with the (111) plane horizontal at low spin speeds and low concentrations and an orientation where the (200) plane is horizontal at higher concentrations and at higher spin speeds. The formation of crystals with different orientations can be ascribed to the alignment of the highly permeable {220} planes along the two important fluid flow directions (radial and azimuthal). From confocal microscopy images it can be concluded that the ordering starts at the top surface, where the final particle density and the degree of ordering is higher than at the bottom. Polystyrene defects could be incorporated in the crystal, which is useful to study photonic defect states. Spin coating a dispersion on a templated substrate, aligned the crystals only for high spin speeds and the imposed order did not continue upwards for more than two layers. This is in line with the observation that crystallization starts at the top of the sample.

## 8.1 Introduction

For the production of photonic colloidal crystals, a crucial aspect is the quality of the crystal in terms of concentration of lattice defects and short- and long-range order [132]. Furthermore, up-scaling possibilities and production speed will determine the practicality of a technique. Most colloidal self-assembly processes, such as sedimentation and controlled drying, are slow processes. Especially controlled drying is sensitive to several parameters (such as humidity and temperature). Most self-assembly processes also yield intrinsic growth imperfections, such as stacking defects and cracks [197, 199].

The spin coating technique was developed initially for the fabrication of thin polymer films. Tuning the parameters spin speed and spin time give an easy control over the film thickness. The technique was first introduced for colloidal self-assembly by Jiang et al. in 2004, who spin coated thin films of silica colloids dispersed in a monomer that acted as the solvent in which the charged stabilized particles crystallized and subsequently were embedded in by polymerization [99]. Studies of the resulting colloidal crystals, showed that in some cases the inter-particle distance was $\sqrt{2}$ times their diameter. A good explanation for the repeated occurrence of this specific inter-particle distance was not given. A drawback of the method of Jiang et al. is the fact that before these colloidal crystals can be used in photonic applications, that rely on strong interactions of the crystal with light, the refractive index contrast has to be enhanced by selective etching, burning or dissolution. Another drawback is the fact that this method is mostly suitable for inorganic particles, since selective removal is difficult for organic particles in an organic medium.

In 2006, Mihi et al. presented a related spin coating method to produce colloidal-crystal films, using a more volatile medium [100]. The colloidal crystals fabricated this way already have a significant refractive index contrast. Further contrast enhancement by, for example, silicon infiltration can be achieved without prior etching steps. Spin coating silica or polystyrene dispersions yielded large colloidal face centered cubic (fcc) crystals, of which the orientation could be controlled: in a certain parameter range the fcc crystals, which normally are oriented with the (111) plane horizontally, were oriented with the (200) plane* parallel to the substrate. The domain size was small in most cases (10 $\mu$m x 10 $\mu$m), but by optimizing the mixing ratios of the dispersion solvents ethylene glycol, water and ethanol, domain sizes of around 100 $\mu$m x 100 $\mu$m were obtained of the fcc crystals with their (111) plane horizontal. The thickness of the colloidal films depended on the particle concentration and spin speed. A physical mechanism for the occurrence of differently oriented fcc crystals was not given. It was reported that for both crystal planes lines of touching spheres were oriented such that they were pointing outward from the center of the rotation, thus providing the samples with the rotational symmetry reflecting the rotation of the sample.

One mechanism which leads to differently oriented fcc crystals is confinement, as is shown in experiments [186, 200–202] and in simulation [203]. In confined geometries consisting of a top and bottom plate, a finite number of layers fit between the two plates. The dispersion tries to accommodate the highest packing fraction which minimizes the free

---

*In this chapter the unsimplified ($hkl$) values (200) and (220) are used instead of (100) and (110), because this will be crucial for the calculation of the distances between the planes.

energy at high osmotic pressures. At some plate separations, a stack of square symmetric (200) layers fits better than a stack of hexagonal symmetric (111) layers. With increasing plate separation, the best fitting structure alternates between square and hexagonal symmetric layers, with a buckled structure in between. If this mechanism leads to the different orientations of the spin coated crystals, a similar alternation is expected with increasing spin speed (because it is expected that an increasing spin speed causes a continuous decrease in the film thickness).

Another mechanism giving rise to crystals with different crystal orientations for different conditions was presented by Ishii et al. for self-assembly in a fluidic cell. The mechanism was based on the permeability of the crystal to liquids for different crystal directions [204]. When flow is a significant factor in the self-assembly process, crystals tend to orient with the planes with the highest fluid permeability (the lowest friction) perpendicular to the flow. In the process of spin coating colloidal films, the exact fluid flows are not known. However, the assumption that the fluid flow in radial direction is highest as a consequence of the radial acceleration, is commonly accepted. This would mean that the (220) plane (which has the lowest friction according to Ishii et al. [204]) should be perpendicular to the radial direction in the spin coating process at higher spin speeds.

Mihi et al. showed that nicely ordered colloidal crystals with large domains can be obtained through spincoating of a dispersion containing the slowly evaporating ethylene glycol [100]. The resulting crystals, however, were only found in one orientation: with the (111) plane horizontal. We are more interested in the mechanism that is responsible for the occurrence of different crystal orientations. Different crystal orientation were primarily found to occur with dispersions containing ethanol. We therefore focussed our study mostly on the structure of colloidal crystals spin coated from pure ethanol dispersions, investigated with different techniques: white light illumination, laser diffraction, scanning electron microscopy (SEM) and confocal microscopy. Using these techniques, we probed the ordering of the crystals from global to local and investigated possible mechanisms for the reorientation of the crystals.

For a comparison, we also studied some crystals spin coated in a mixture of ethylene glycol and water instead of ethanol. A preliminary investigation to see if aligning the small crystal domains could be improved by using a templated substrate is presented in Section 8.3.8.

Finally, we also describe a characterization of the photonic properties of the formed colloidal crystal films using Fourier Transform Infra-Red (FTIR) spectroscopy. This investigation included testing the experimental feasibility of intentionally including PS defects in the structure, in order to produce photonic defect states in a photonic band gap. These point defects could act as microcavities if incorporated in a photonic crystal with a (complete) band gap [205].

## 8.2 Experimental methods

In this section, the experimental materials and methods are discussed, which were used to make the colloidal crystals and to characterize them.

### 8.2.1 Colloidal particles and dispersions

Three types of silica colloids were used, all with a fluorescently labelled core and an unlabelled shell. The core of the particles was labelled with the dye fluorescein isothiocianate (FITC). The first batch of particles was 1038 nm in diameter with a polydispersity of 2.5%, the second batch of particles was 808 nm in diameter with a polydispersity of 5%, the third batch was 1480 nm in diameter. The first two diameters were determined by Static Light Scattering, the last by SEM. All FITC labelled silica particles were synthesized via a modified Stöber-method and the cores were grown out via a Giesche seeded growth procedure [116].

In some experiments, we also added polystyrene (PS) spheres to a silica dispersion to study defect states in the Bragg peak. The PS spheres had a diameter of 776 nm and they were coated with a 10 nm silica shell, giving a total diameter of 796 nm. Because of this silica shell, the PS defects had the same interaction with each other and with the silica spheres as the mutual silica spheres. The PS particles were added to a silica dispersion in a number ratio of $SiO_2$:PS = 19:1.

The particles were dispersed in ethanol by several centrifugation steps. In Section 8.3.5 another dispersion solvent was used: a mixture of ethylene glycol and water (4:1 weight ratio), which is less volatile and more viscous.

### 8.2.2 Spin coating

The substrates for the spin coating process were 22 mm diameter no. 1 round glass cover slides. To increase wetting of the ethanol dispersions, the slides were cleaned with chromosulfuric acid. For the ethylene glycol containing dispersions, the hydrophilicity had to be increased even more by cleaning the slides in a piranha solution.

The spin coater (model P6700, Speciality Coating Systems, USA) contained a sample holder of about 15 mm diameter in which ridges make sure that the vacuum reaches also the outside of the sample slide. However, since our sample slides were very thin, the vacuum pulled the slide into the grooves of the holder, yielding a nonuniform colloidal crystal film after spin coating a dispersion. To improve the uniformity of the film, the cover slide was placed on top of a thick microscope slide (cut to a square of about 3 cm x 3 cm) with a small drop of water in between. The thick microscope slide was kept on the spin coater by vacuum, while the thin cover slide was retained on top by capillary forces up to a spin speed of about 5000 rpm.

The best results were obtained when the spin coater was brought to the desired speed first, after which a dispersion was applied to the middle of the spinning cover slide with a pipet. Within a few seconds (in the case of ethanol dispersions) to a few minutes (in the case of ethylene glycol dispersions) the sample became opaque, indicating that the solvent had evaporated.

We also spin coated a few dispersions on substrates which were templated with a square array of holes. The square arrays of holes were made by soft lithography (described in Chapter 2.3.2) in poly-urethane UV glue (Norland OA 68). The substrate and the hardened glue were made hydrophilic by glow discharge (exposing them to a plasma for 15 seconds), this increased the wetting of the dispersion on the substrate.

### 8.2.3 Sample characterization

The diffraction behavior of the samples was studied and imaged under white light illumination. The diffraction pattern gives an indication of the order, both orientationally and position wise, of the colloidal crystals as will be discussed in Section 8.3.1.

For sample characterization by more local laser diffraction, a green HeNe laser (Melles Griot) was directed to the sample via a mirror and aperture, after which the transmitted diffraction peaks were visualized on a screen with a circular black spot in the middle, to block the primary beam. Images of the diffraction pattern were made with a Nikon D70 single-lens reflex digital camera with a Nikkon AF-S 18 mm to 70 mm lens. The sample area probed by the laser diffraction was about 1 mm$^2$.

The top surface of the sample was imaged using a Philips XL30FEG Scanning Electron Microscope. This real-space imaging technique gives more local information than the white light illumination and laser diffraction.

The 3D structure of all samples was imaged using a Confocal Scanning Laser Microscope (Leica type NT or SP2). The fluorescent dye FITC was excited with the 488 nm line. The PS spheres were imaged in reflection. To avoid scattering by the colloidal silica spheres at the colloid-air interface, we infiltrated the samples with a DMSO-water mixture (80:20 w/w), which matches the refractive index of the silica spheres.

Transmission and reflection spectra of the spin coated samples were recorded with a Fourier transform infrared (FTIR) spectrometer (Bruker Vertex 70) coupled to a microscope (Bruker Hyperion 2000). A 4×/0.10 NA objective was used as condenser, giving a spot diameter of 150 $\mu$m. The sample was illuminated with a near-infrared source using a KBr beamsplitter and the spectra were measured with an MCT-D326 detector (liquid-nitrogen cooled detector on the microscope, scanner velocity 20 kHz). Reflection spectra were calibrated using a silver mirror. To avoid Fabry-Pérot fringes due to the thin glass cover slip underneath the sample, we adhered the thin glass cover slip to a thick microscope slide with immersion oil that refractive index matches the two glass slides.

## 8.3 Results and Discussion

The crystals formed by spin coating were examined with a number of methods to determine the structure and degree of order. In this section, first the results are discussed of two methods which probe the reciprocal space of the crystals by looking at the scattering of light. The results of the two direct methods Scanning Electron Microscopy and Confocal Scanning Laser Microscopy are discussed afterwards. Then the structure of the samples made on a templated substrate and in a different dispersion medium is described. At the end of this section, possible causes of the observation of the occurrence of different crystal orientations are discussed.

### 8.3.1 Reflection from spin coat samples: four/six-armed star(s)

We first turn to the visual observation of the diffraction colors on a spin coated colloidal crystal on a circular glass wafer. This method can be used to quickly determine the orientation of a crystal over a large area without the help of any experimental apparatus.

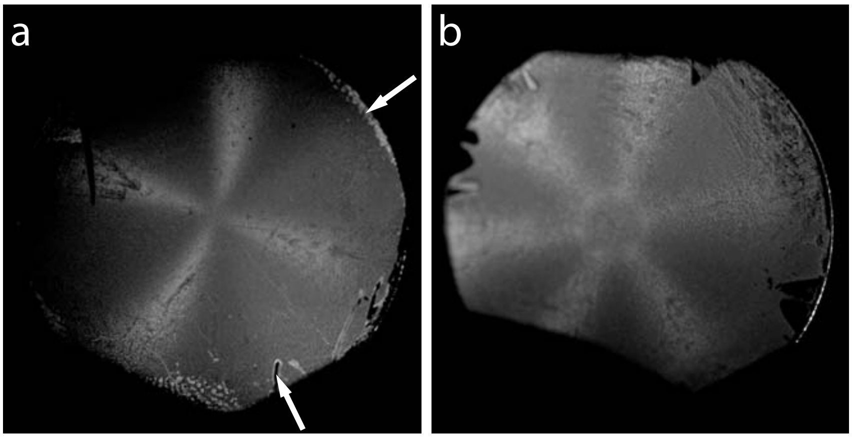

**Figure 8.1:** *(A color version of this figure can be found on page 36)* Photos of two different spin coated colloidal crystals of 1038 nm particles on a circular cover slip (22 mm diameter) illuminated under an angle with a white light source on which a (a) four armed star (volume fraction 30%, spin coated at 5000 rpm) and a (b) six armed star (volume fraction 21%, spin coated at 3000 rpm) are visible. The arrows indicate arms of the less clear secondary square star.

Some spin coated colloidal crystals on a circular wafer exhibit a clear reflection pattern. On some of the wafers, equally spaced strongly reflecting sectors were visible, where the number of reflecting sectors depends on the orientation of the crystal. For an fcc, twinned fcc, or more randomly stacked crystal with a hexagonal (111) plane parallel to the glass surface, a six armed star was observed if the order was good enough, while for an fcc crystal with a (200) plane parallel to the glass surface, a four armed star appeared for high enough quality of order. Examples of both diffraction stars are shown in Figure 8.1.

### Six armed star

The origin of the six armed star for hexagonally ordered lattices (fcc lattice with the (111) face parallel to the bottom surface) was explained by Ruhl et al. [206]. They discuss in this paper also radially oriented crystals, but in their case these were obtained by compression molding. One of the hexagonal (111) layers of the crystal is oriented horizontally and there is always a “string” of colloids in the hexagonal layer pointing radially outward. Besides the (111) plane, which is horizontal, also the (022) plane, the $(\bar{1}11)$ plane and the (200) plane are intersecting the string of spheres that is pointing outwards. In Figure 8.2 the string of spheres is depicted with the white spheres. The planes intersecting this string of spheres and the angles which these planes make with the (111) plane are depicted below the structure.

The spacing $d_{hkl}$ between the $(hkl)$ planes and the angle $\phi_{hkl}$ with the (111) plane is given by

$$\begin{aligned} d_{hkl} &= \tfrac{a}{\sqrt{h^2+k^2+l^2}} &&= 2r\sqrt{\tfrac{2}{h^2+k^2+l^2}} \\ \cos\phi_{hkl} &= \tfrac{h+k+l}{\sqrt{3(h^2+k^2+l^2)}} \end{aligned} \tag{8.1}$$

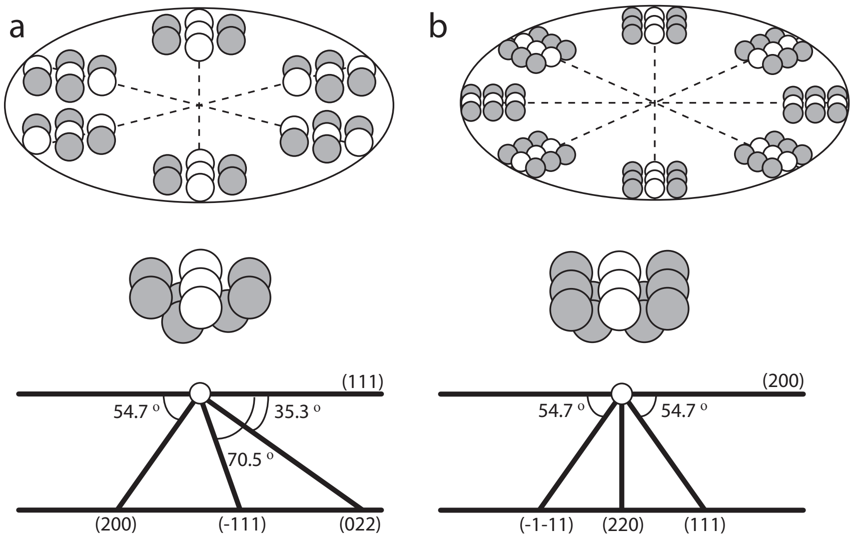

**Figure 8.2:** Schematic representation of the alignment of the close-packed strings in the horizontal plane (white) on the sample substrate and of the orientation of all planes in the fcc-lattice going through the close-packed strings of spheres which point outwards from the center of the spin coat samples, for an fcc lattice oriented (a) with the hexagonal (111) plane horizontal or (b) with the square (200) plane horizontal.

where $a$ is the lattice constant of the square fcc unit cell and $r$ is the radius of the particles. Light that travels through the film at an angle $\alpha$ with the normal, will be diffracted from a plane $(hkl)$ if it satisfies Bragg's law

$$\lambda_{hkl} = 2nd_{hkl}\sin(\phi_{hkl} + (90^\circ + \alpha)). \tag{8.2}$$

Light which falls on the sample perpendicular to the string of spheres can in principle be diffracted by all planes running through the string. However, since the colloidal crystal of Ruhl et al. was embedded in a polymer film, light outside the cone formed by incoming angle $\alpha_{\mathrm{tir}} = \arcsin(1/n)$ cannot leave a film with refractive index $n$ to the surroundings with refractive index 1 (air), due to total internal reflection[†]. This makes it impossible for visible light coming from above, to diffract at the (200) or $(\bar{1}11)$ face and leave the sample again on the same side.

The reflection from the horizontal (111) plane does not depend on the in-plane rotation of the sample. At a given angle of the light with the (111) plane, one color is diffracted and the rest is transmitted, independent of the orientation of the strings of particles to the light.

Diffraction by the (022) plane does depend on the orientation of the crystal with respect to the incident light. In a single crystal, illuminated under a very large angle, the reflection from the (220) plane shows up only in three in-plane orientations of the crystal, 120° apart. Because of total internal reflection, only light that comes in under a very

---

[†] I defined $\alpha$ to be the angle with respect to the normal, contrary to the definition of $\delta$ in the article of Ruhl et al. [206], which is defined with respect to the (111) plane.

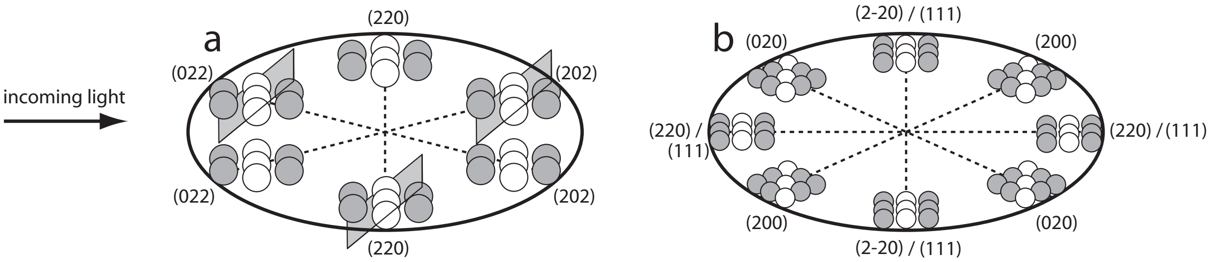

**Figure 8.3:** Schematic representation of the orientation of the spin coated crystal at the different azimuthal angles that can diffract the incoming light of certain wavelengths. Light which comes in from the left can be diffracted, from planes running through the white line of spheres, resulting in a diffraction star. For the case that the (111) plane is horizontal (a), light coming from the left can reflect on the (022) planes of crystals under three azimuthal angles. These (022) planes are drawn in as grey planes. When the stacking of the crystals is twinned, every 60° occurs a sector of crystal with the (022) plane in the right direction, forming a six-armed star. For the case that the (200) plane is horizontal (b), the light is diffracted on both tilted (111) planes, if no internal reflection is assumed. Otherwise, light is diffracted from the vertical (220) and (200) planes.

large incident angle can diffract at the (022) plane and leave the film again without total internal reflection.

In the radially aligned crystal made by compression molding, and also in a spin coated crystal, the orientation of the fcc crystal changes gradually around the sample (Figure 8.2). There is always a string of spheres pointing towards the center of the sample. With light incident from one direction, it can be reflected from three narrow sectors on the sample pointing radially outward. When the crystal is twinned (the $ABC$-stacking is inverted to an $CBA$-stacking) there are three other in-plane angles under which the light can be reflected, resulting in a six-armed star (Figure 8.3). The same reasoning applies therefore to all close packed crystals with stacking errors. Only for pure fcc and pure hcp crystals one expects to see three arms. The wavelength of the light that is reflected depends on the distance between the planes and on the incoming angle of the light.

### Four armed star

When the fcc crystal is not oriented with its (111) plane horizontal, but with the (200) plane, the close-packed strings of the (200) plane point radially outward (as is shown in Figure 8.2b). The planes that run through this string of spheres are the (220) plane and the (111) and $(\overline{11}1)$ planes. The family of {111} planes is under an angle of 54.7° with the (200) planes. This means that, if there is total internal reflection as in the case of the polymer films of Ruhl et al. [206], there is no diffraction from the {111} planes. However, as our material is not a homogeneous slab of matter but contains index variations on length scales comparable to the wavelength, total internal reflection is only an approximation. Assuming no total internal reflection, diffraction from the family of {111} planes would cause four strongly reflecting sectors (Figure 8.3), as observed. However, if our colloidal crystal would act like a dielectric film with an effective refractive index, the diffraction

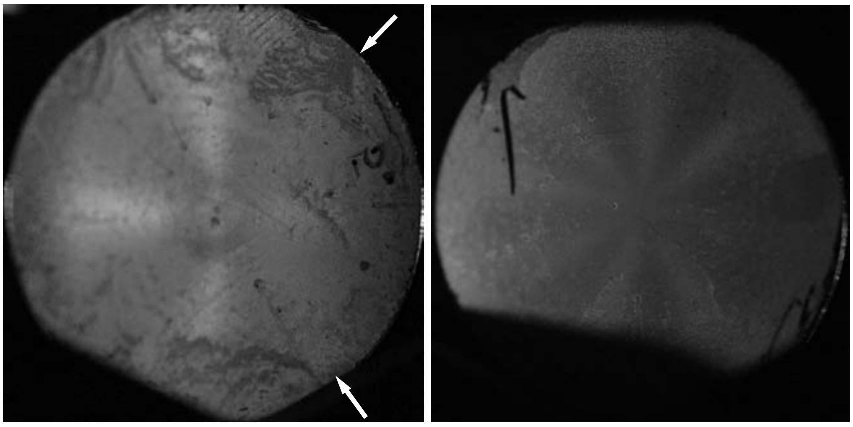

**Figure 8.4:** *(A color version of this figure can be found on page 36)* Photos of spin coated colloidal crystals both made of a dispersion 1038 nm particles (volume fraction 25% and 30%), spin coated at 5000 rpm, on a circular cover slip (22 mm diameter) illuminated under an angle with a white light source on which a double four-armed star is visible, one coming from the {220} (and possibly {111}) planes and one from the {200} planes. The arrows indicate arms of the less clear secondary square star. The sample on the right is the same sample as in Figure 8.1a.

from the {111} planes becomes unlikely.

The (220) plane, perpendicular to the horizontal, can also cause a diffraction star. Incoming light from above the sample under an angle with the normal, can reflect from the vertical (220) plane and exit the sample on the other side. The diffraction star would then be visible on the other side than the light source. This would also cause a four armed star, since the vertical (220) plane is perpendicular to the incoming light for four azimuthal angles on the samples (Figure 8.3). Reflection of the diffracted light at the glass plate under the sample could even make this diffraction star visible on the same side of the sample as the light source.

Besides this (220) plane, also two planes of the {200} family are perpendicular to the horizontal plane. These planes can cause a similar four-armed star, in between the arms of the (220)-diffraction star, but at a different wavelength because the plane-spacing is different. Evidence of the coexistence of these two stars of different colors is illustrated in Figure 8.4.

### Spin speed and concentration dependence

Checking many samples, made at different spin speeds and from different dispersion concentrations, for a diffraction star resulted in Table 8.1 for the 1.0 $\mu$m diameter particles and Table 8.2 for the 0.8 $\mu$m diameter particles.

From the tables, a clear trend can be deduced: a four-armed star is more often visible on samples made at higher concentrations and at higher spin speeds. In some samples both stars could be discerned, where a six-armed star was more clear on the bottom, while a four-armed star was visible on the top of the sample.

**Table 8.1:** Bragg diffraction pattern on the sample in white light illumination for different spin speeds and different volume fractions of the dispersion of 1038 nm diameter particles, where '-' denotes no clear diffraction, $\circ$ is azimuthal-angle-independent diffraction (one color over the whole sample), $*$ denotes a six-armed diffraction star and $\times$ denotes a four-armed star. The superscript shows the number of layers for some of the samples.

| | 500 rpm | 1000 rpm | 2000 rpm | 3000 rpm | 4000 rpm | 5000 rpm |
|---|---|---|---|---|---|---|
| 5% | $\circ^1$ | $\circ^1$ | | $\circ^1$ | $\circ^1$ | |
| 10% | | $\circ^3$ | $\circ^2$ | | $\circ^1$ | |
| 19% | | $\circ$ | $\circ^5$ | $*^3$ | $*^2$ | |
| 21% | | $-^7$ | $\circ^4$ | $*$ | $*^3$ | $\times^3$ |
| 25% | | $-^7$ | $*^5$ | | $*^4$ | $\times^3$ |
| 30% | | | $*^6$ | | $*^5$ | $\times^4$ |

**Table 8.2:** Bragg diffraction pattern on the sample in white light illumination for different spin speeds and different volume fractions of the dispersion of 796 nm diameter particles, where $*$ denotes a six-armed diffraction star and $\times$ denotes a four-armed star. If the symbol is between brackets, the star was less clearly visible.

| | 2000 rpm | 3000 rpm | 4000 rpm |
|---|---|---|---|
| 15% | $*$ | $*$ | $(\times)$ |
| 25% | $(*)$ | $*/\times$ | $*/\times$ |
| 35% | $(*)$ | $*/\times$ | $*/\times$ |

### 8.3.2 Laser diffraction

Laser diffraction was done at normal incidence of the beam on the sample. Two laser diffraction patterns of a sample with a six-armed star and a sample with a four-armed star are shown in Figure 8.5a and 8.5b. Clearly, the 2D symmetries present in the diffraction stars recur in the laser diffraction patterns. In the square diffraction pattern, two groups of peaks can be discerned at different distances from the center, corresponding to diffraction from differently spaced lines in the square lattice, with a spacing of $2r$ and a spacing of $\frac{1}{2}\sqrt{2}(2r) \sim 0.70 \cdot (2r)$. As expected, the sample on which both a square and a hexagonal star were visible, shows both diffraction patterns on top of each other, where the peaks with six-fold symmetry are slightly further out than the peaks with four-fold symmetry (Figure 8.5c). The spacing between lines of particles in the 2D hexagonal (111) planes is $\frac{1}{2}\sqrt{3}(2r) \sim 0.87 \cdot (2r)$, while the spacing between lines of particles in the 2D square (200) planes, corresponding to the diffraction spots with square symmetry visible in this image is $2r$.

The new information that can be deduced from these diffraction patterns, is the fact that the in-plane long-range ordering, demonstrated by the diffraction stars, is also present more locally, on the millimeter scale of the laser spot. Displacing the laser spot around the center of the sample at the same radial distance, resulted in a rotation of the diffraction pattern (Figure 8.6). This rotation confirms the radially aligned crystal structure and the length scale at which this is already manifesting itself.

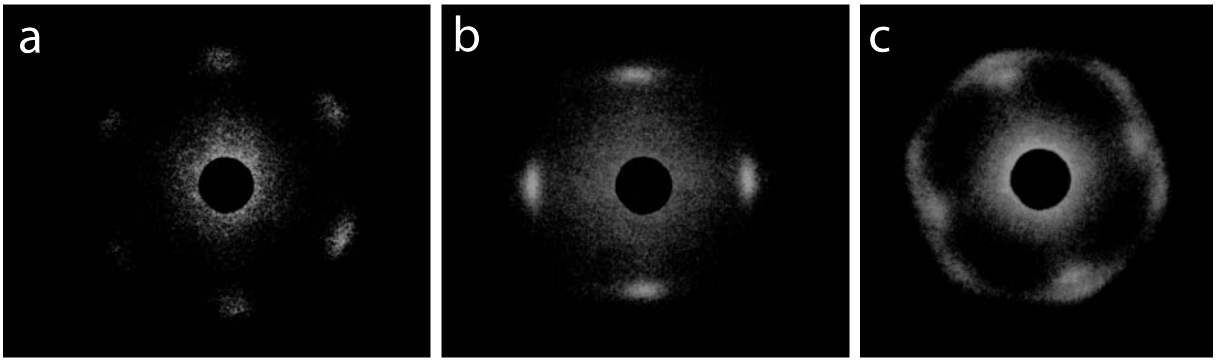

**Figure 8.5:** Laser diffraction pattern of (a) a sample with a six-armed diffraction star, (b) a four-armed diffraction star and (c) both a six-armed and a four-armed diffraction star.

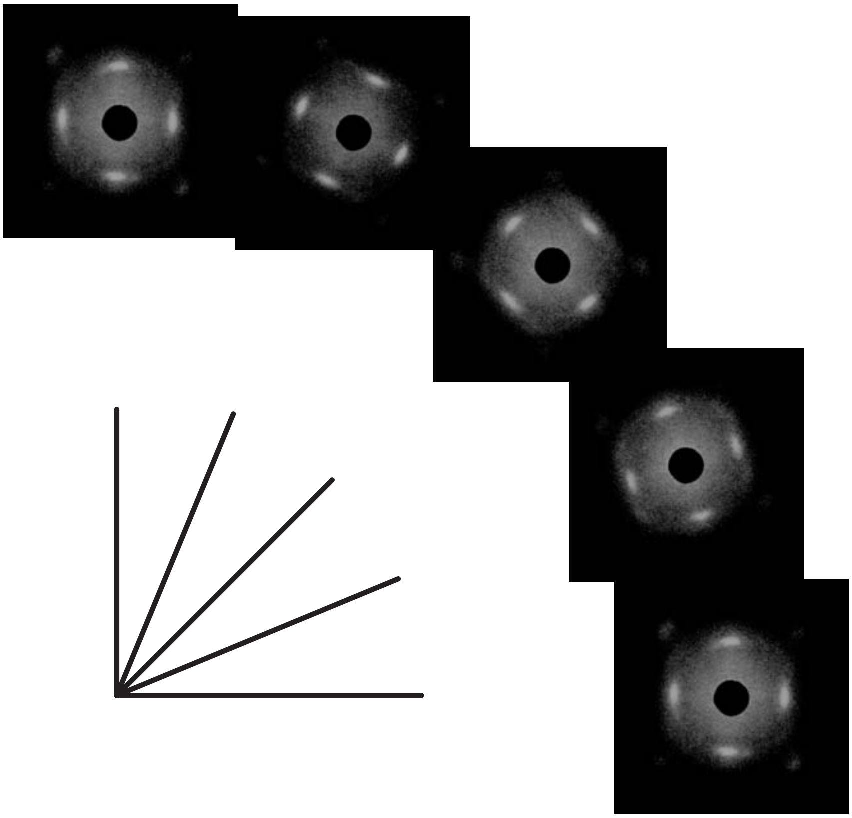

**Figure 8.6:** Diffraction patterns at different azimuthal angles on a sample with a four-armed diffraction star, demonstrating the radially aligned crystal structure.

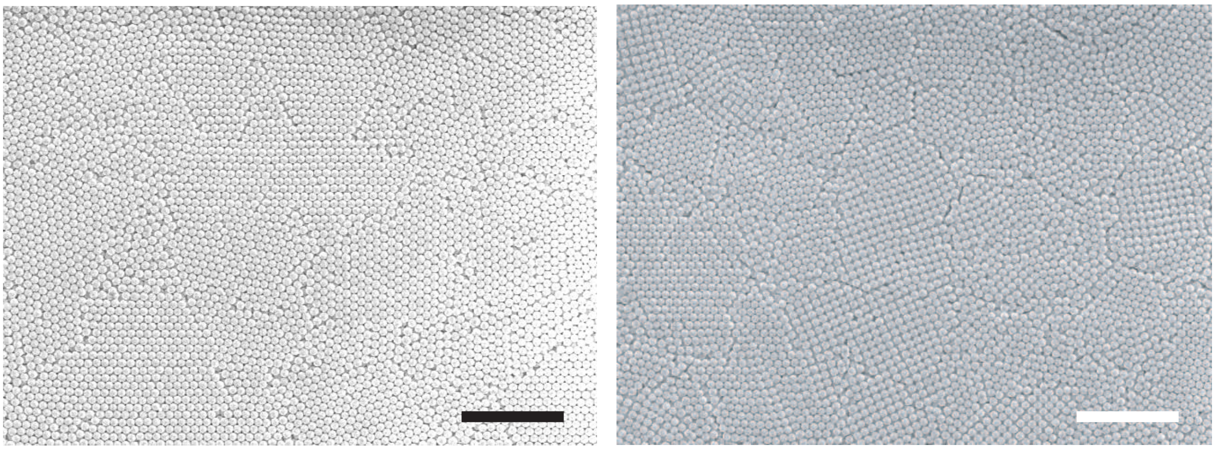

**Figure 8.7:** SEM images of the top surface of spin coated silica spheres: (a) a dispersion of 808 nm particles with a volume fraction of 15% spin coated at 3000 rpm and (b) a dispersion of 808 nm particles with a volume fraction of 35% spin coated at 4000 rpm. The scale bars are 10 $\mu$m.

### 8.3.3 Scanning Electron Microscopy

Using Scanning Electron Microscopy (SEM), the top surface of the spin coated colloidal crystals was imaged. The hexagonal and square symmetries found by white light illumination and laser diffraction recur in the small domains visible in the SEM images in Figure 8.7. For a dispersion with a volume fraction of 15%, spin coated at 3000 rpm, only hexagonal ((111) plane horizontal) domains were found. For a dispersion with a volume fraction of 35%, spin coated at 4000 rpm, more square ((200) plane horizontal) domains were found, however, still also many hexagonal domains were present.

An overall preferential alignment of the domains along the radial direction is expected because of the occurrence of a diffraction star. However, from these SEM images, we can not conclude that the close-packed strings of particles in the domains of one symmetry are aligned along one direction. Most square domains are roughly aligned in the same direction, but several hexagonal domains clearly are not, since, next to alignments with strings of particles aligned in an outward direction from the center, orthogonal alignments exist within one image (Figure 8.7).

The rougher surface (as compared to Figure 8.7), that is visible in a zoomed-out image in Figure 8.8 of 1 $\mu$m particles, spin coated at 5000 rpm from a 30% dispersion, probably originates from the difference in in-plane spacing for the two different orientations. The spacing of (111) planes is $\frac{2}{\sqrt{3}} \sim 1.15$ times the spacing of (200) planes.

We scanned several samples from the middle to the outside of the sample, finding no significant changes in alignment, crystal orientation or spacing between particles.

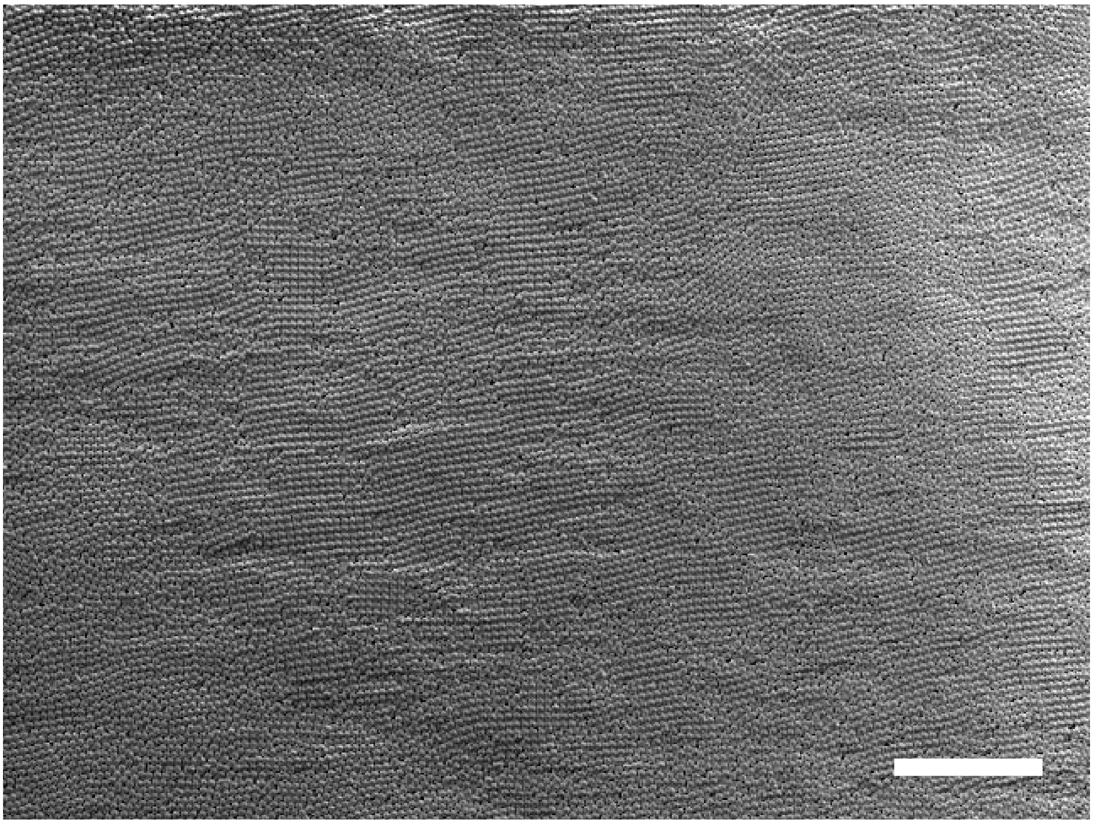

**Figure 8.8:** SEM image of the top surface of spin coated 1 $\mu$m diameter silica spheres from a dispersion with a volume fraction of 30% at a spin speed of 5000 rpm. The scale bar is 20 $\mu$m.

### 8.3.4 Confocal Laser Scanning Microscopy

Using confocal laser scanning microscopy, the real space ordering in a colloidal crystal can be imaged in three dimensions. Contrary to SEM imaging, confocal microscopy can also image the bottom and bulk layers of a sample, which can increase the insight into the formation process of the spin coated colloidal crystals.

Using confocal microscopy, the number of layers of every sample was determined. This ranged from 1 layer for low concentrations ($\sim 5\%$) and/or high spin speeds ($> 4000$ rpm) to 7 layers for high concentrations and/or low spin speeds.

The bottom layers, imaged by confocal microscopy, reflect the same symmetry in the horizontal plane as concluded from white light illumination, laser diffraction and SEM imaging: at higher spin speeds or higher concentrations, the square symmetric (200) plane of the fcc structure dominates over the hexagonal symmetric (111) plane. Figure 8.9 displays the hexagonal order and the square order in the bottom layers of two different samples. The Fourier transforms of both images are shown as an inset. The hexagonal order of Figure 8.9a is not reflected in the Fourier transform because all domains are not aligned along one director, resulting in a powder-like diffraction spectrum. The square order of Figure 8.9b is clearly visible in the Fourier transform. The square domains are thus better aligned than the hexagonal domains.

In Figure 8.10, several confocal microscopy images are shown of the top and bottom of a sample made at 4000 rpm. The bottom layers are clearly less dense than the top layers and furthermore, the top layers are more ordered. These observations suggest that the ordering starts at the top layers, where the particles are fixed to the fluid-air surface due to surface tension. This ordering is imposed on the lower layers when the fluid level lowers (by evaporation or flow caused by centrifugal forces).

The fact that the bottom layer is less dense can have two causes: the colloids stick to the substrate and therefore have random positions (random sequential adsorption), or the crystal formation process starts at the top surface and is so fast that the bottom particles have no time to become denser and order. The second explanation (or a combination of both) is most likely, since in some samples clearly some ordering is present in the bottom layer, as can be seen in Figure 8.9 and 8.10a. Crystallization from the top surface downwards was also observed by Li et al. [207]. They produced a free-standing silica 3D colloidal crystal at a water-air interface by letting the air evaporate. Similar crystal nucleation at the top surface was observed by Wu [150] when spin coating colloids dispersed in the monomer ETPTA.

It was also observed that there is more hexagonal ordering on the bottom than on the top. This is in agreement with the fact that in white light illumination sometimes a six-armed star was visible on the bottom, while a four-armed star was visible on the top of the sample. The hexagonal order is probably caused by interaction with the bottom wall which favors the densely packed hexagonal ordering.

#### Order parameters and degree of alignment

The degree of hexagonal or square ordering can be obtained from confocal images by deriving bond orientational order parameters from particle coordinates. In an $xy$ confocal image, the coordinates of the particles can be obtained by the method of Crocker and

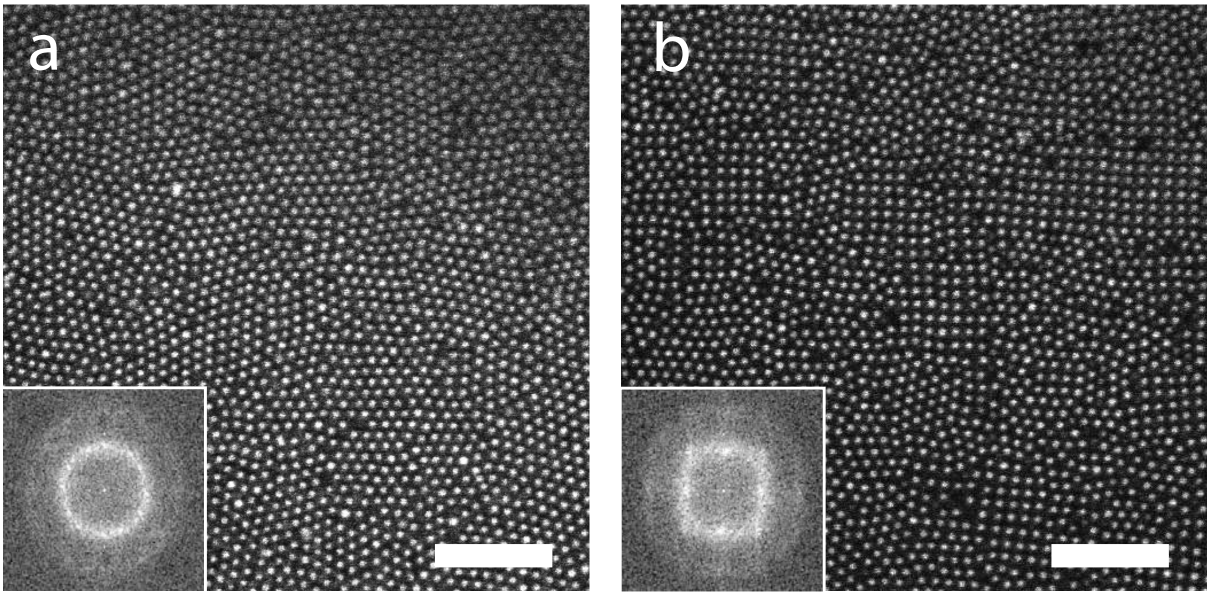

**Figure 8.9:** Confocal microscopy images of bottom layers of (a) a 10% dispersion of 1038 nm particles, spin coated at a speed of 2000 rpm and (b) a 30% dispersion of 1038 nm particles, spin coated at a speed of 4000 rpm . The insets show Fourier transforms of both images. The scale bars are 10 $\mu$m.

Grier [117]. For every particle, the neighboring particles were defined using Delaunay-triangulation, which is the equivalent of defining the region of space that is closest to each particle (the Voronoi cell) [186]. Triangles are drawn by drawing lines between all particles, such that no particle is inside the circumcircle of any triangle. All connected particles after triangulation are defined as neighbors.

The 2D local hexagonal bond orientational order parameter $\Psi_6$ for a single particle can be calculated from the particle coordinates of its neighbors [185]:

$$\Psi_6(r_j) = \frac{1}{N} \sum_k \exp(i6\theta(r_{jk})) \tag{8.3}$$

where $k$ runs over all N neighboring particles of particle $j$ and $\theta(r_{jk})$ is the angle between the vector between particles $j$ and $k$ and a reference axis (Figure 8.11a). This equation essentially sums the angles $\theta(r_{jk})$ times six, where the multiplication of the angles by six reduces all vectors to a sextant of the circle. Summing the angles of all neighbors gives a vector $\Psi_6$, which is longer if all angles are the same, and is longest if the neighbors form a perfect hexagon (Figure 8.11b-c). The resulting $\Psi_6$ is a complex vector, where the absolute value (or length) defines the amount of local order and from the ratio between the real and the imaginary part, the angle can be derived under which the hexagon is aligned with the reference axis.

Summing the absolute values of the local hexagonal bond orientational order parameters of all particles, gives a degree of hexagonal order in the image. However, this sum of *absolute* values does not take into account the alignment of the hexagons with respect to each other. Since the overall alignment of the domains is a crucial parameter in spin

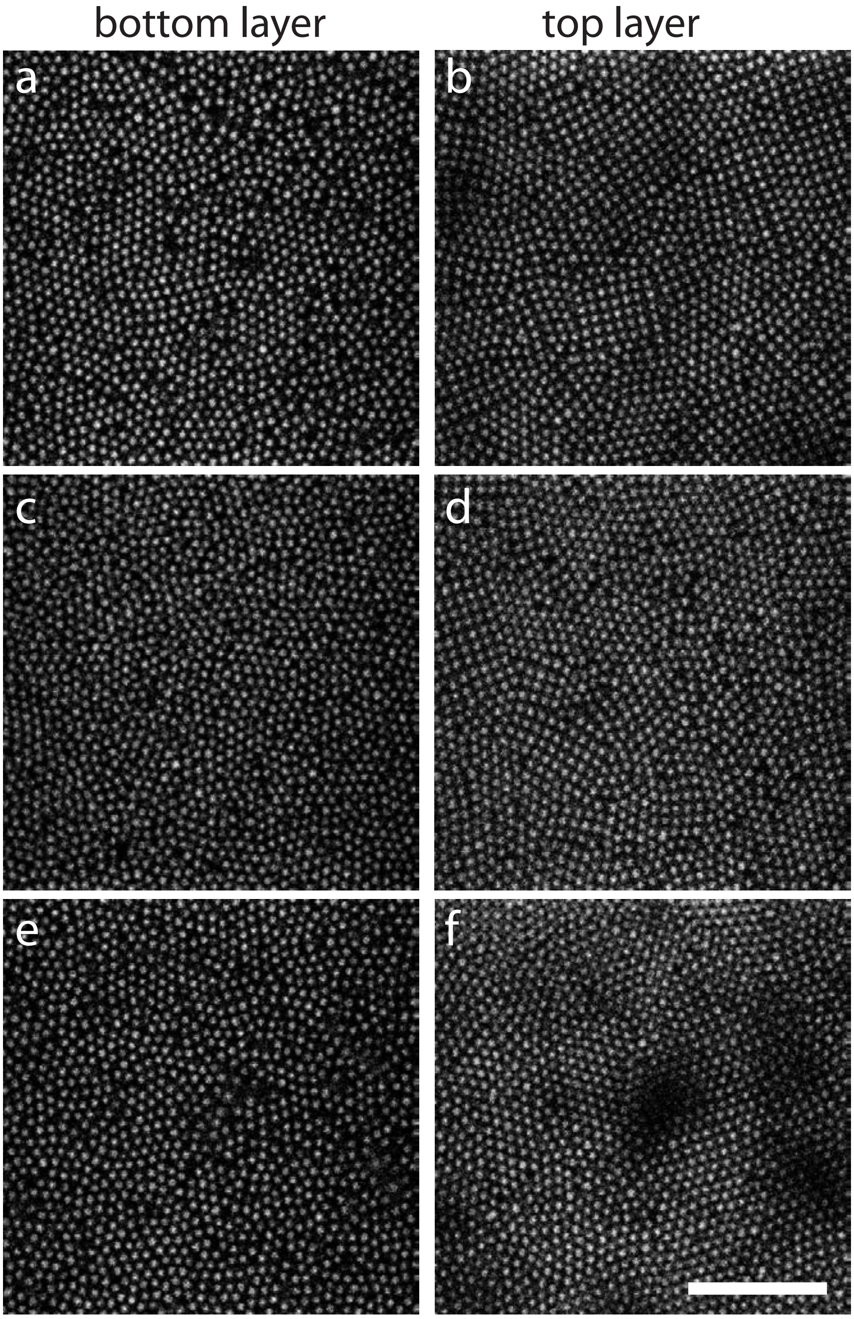

**Figure 8.10:** Confocal microscopy images of bottom layers and top layers of a 25% dispersion spin coated at a speed of 4000 rpm. The scale bar is 10 $\mu$m.

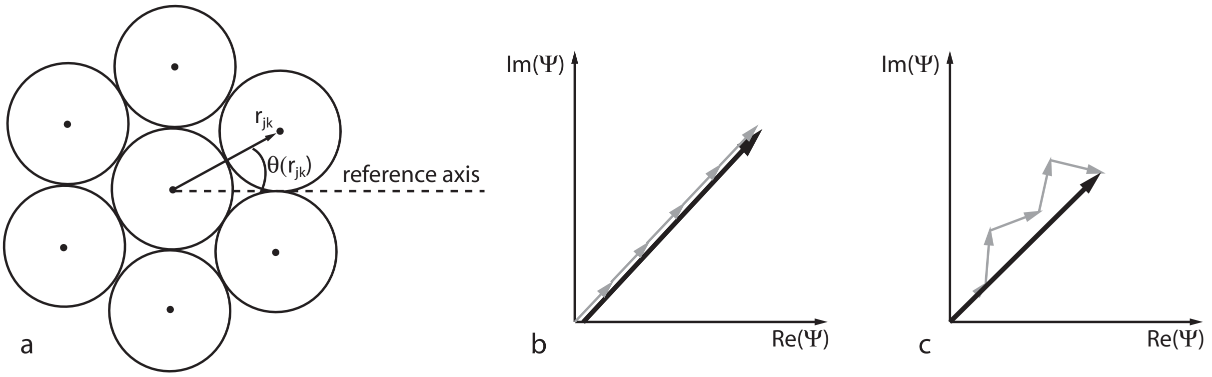

**Figure 8.11:** Schematic representation of the hexagonal bond orientational parameter $\Psi_6$. a) The local bond order parameter of a single particle is defined by summing the six-fold of all angles $\theta(r_{jk})$ of the bond-vectors between this particle and its neighbors with a reference axis. b) If all hexagons are aligned in the same direction, the overall absolute $\Psi_6$ value becomes large, while c) if the alignment is less well defined, the absolute $\Psi_6$ value becomes smaller.

coating, this parameter was probed by summing all *complex* values of the local hexagonal bond orientational order parameters. Summing the complex values for all particles in a confocal image gives a complex vector of which the length defines the range of the hexagonal order in the image. The orientational order parameter, found after summing all absolute values, will be called 'local $\Psi_6$' hereafter, whereas the orientational order parameter, found after summing all complex values, will be called 'global $\Psi_6$'. All order parameters are normalized by dividing by the number of particles. The value of $\Psi_6$ (between 0 and 1) gives a degree of global alignment of the hexagonally ordered domains. However, this global parameter is limited to the view of the confocal image (usually less than 100 $\mu$m) and therefore probes the order on a different length scale than the global alignment found by laser diffraction and white light diffraction.

By replacing all numbers '6' in the local hexagonal bond orientational order parameter by '4', a bond order parameter $\Psi_4$ could be defined for determining the square order in the spin coat samples. However, neighbors in a square lattice are not always defined correctly by Delaunay-triangulation [186]. Besides the four neighbors which should be found, also some of the next generation of neighbors (lying under an angle of 45° with the four direct neighbors) are determined as next neighbors. Therefore, we used the $\Psi_8$ parameter instead, which does correctly define the amount of square order [186].

The graphs in Figure 8.12 show the global $\Psi_6$ and local $\Psi_6$, and the global $\Psi_8$ and local $\Psi_8$, as a function of concentration or spin speed for the 1038 nm particles. All points were determined by averaging over at least five confocal images at different positions, only from the bottom of the samples. All confocal images were taken at the same zoom, such that an equal area was taken into account (which could otherwise influence the global order parameter).

The local order was clearly much higher than the global (aligned) order, as expected. This difference was larger for the hexagonal order than for the square order, which indicates better global alignment of the square domains than of the hexagonal domains, which was also found from the Fourier transforms in Figure 8.9.

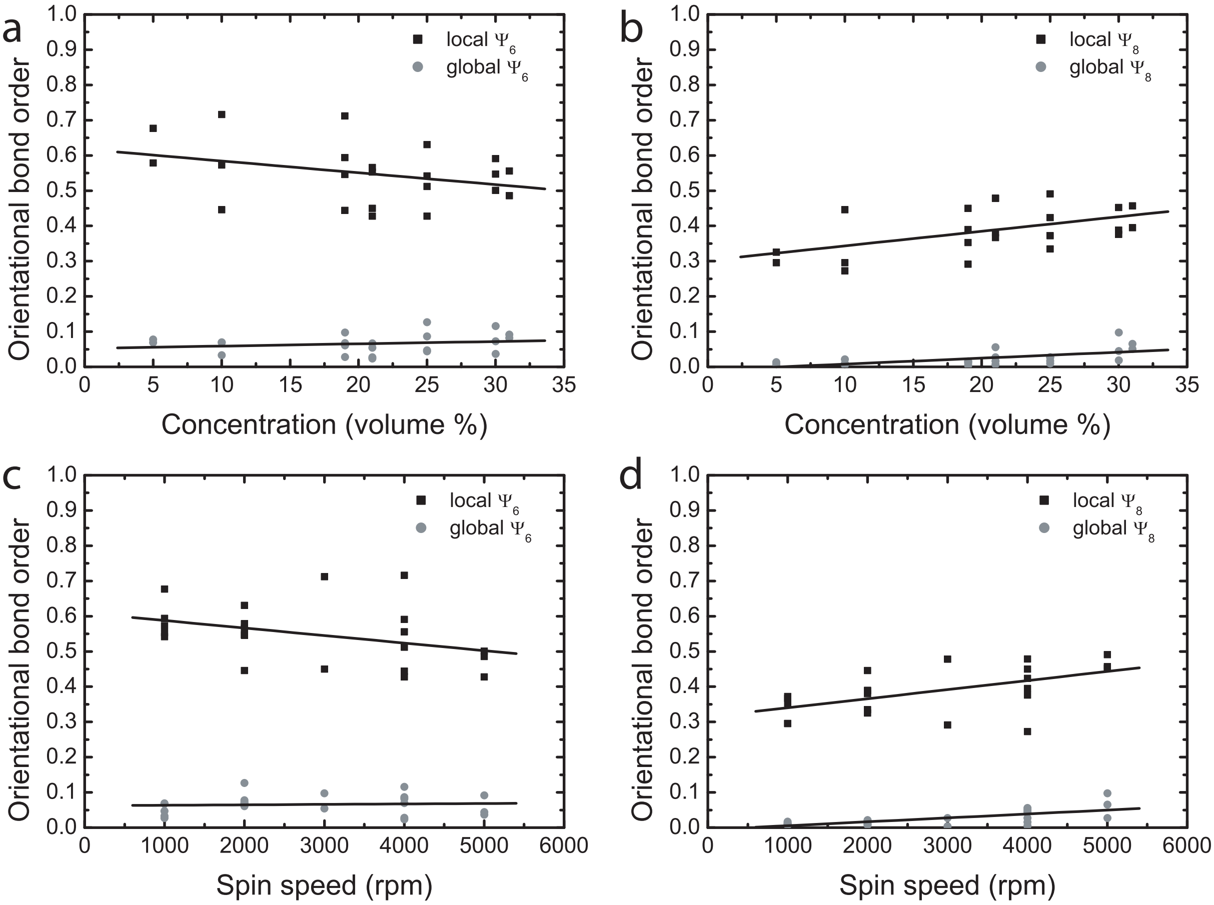

**Figure 8.12:** Graphs giving the local and global orientational bond order parameters as a function of concentration or spin speed for confocal images made of many spin coated samples of 1038 nm particles. The spread in the points results from the fact that at one value of the speed, samples at different concentration values were measured and vice versa.

In the graphs, linear fits were drawn through the points, however these are merely intended as guides to the eye and to illustrate that with increasing spin speed and with increasing concentration, the local hexagonal order decreased and the local square order increased. The globally aligned square order also increased slightly, while the globally aligned hexagonal order hardly changed. Thus, the alignment of the crystals with the (111) plane horizontal is less dependent on spin speed and concentration than the alignment of the crystals with the (200) plane horizontal.

The trends found from the order parameters agree with the trends found in the other characterization methods. However, the low degree of order does not agree with the fact that a clear diffraction pattern can be seen in white light illumination and also laser diffraction shows clear order. We must conclude that the order on a short scale is much less than the radial order on a longer length scale.

This quite counter-intuitive finding gives important clues to the mechanism of the large scale orientation of the crystals. Usually, if interference effects are observed on a length scale on the order of centimeters as with the star shaped patterns, one assumes that the underlying symmetry is a reflection of the order that starts on a local scale and then is continued to this large length scale. It is intriguing to see from the local analysis in real space that this is not the case, although the order giving rise to the stars is already present on the millimeter sized length scale probed by the laser diffraction experiments. The only way this kind of order can be manifested on a larger length scale, is if it does not originate from local interactions between the spheres, but if there is a (much) longer ranged effect that can induce the order without direct inter-particle interactions. The only field in this process that can do this is flow. It should be noted however, that although in our case strong local correlations were absent in most cases, the work of Jiang et al. demonstrates that these can be achieved as well [99].

### 8.3.5 Spin coating from ethylene glycol instead of ethanol

In the article by Mihi et al., not only dispersions in ethanol are used, but also dispersions in ethylene glycol and water (or mixtures of those). These solvents are less volatile and ethylene glycol is more viscous. It was observed that they yielded larger domains and predominantly hexagonal symmetry.

To see if we could reproduce the effect of the use of ethylene glycol and water as dispersion solvent, we spin coated 808 nm diameter $SiO_2$ particles in a mixture of ethylene glycol and water. This yielded samples with larger hexagonal domains, but equally sized square domains. Some hexagonal domains became more than 100 $\mu$m wide, making them suitable for photonic applications. For the image shown in Figure 8.13, the local $\Psi_6$ is as high as 0.79 and also the global alignment is good with a $\Psi_6$ of 0.67.

### 8.3.6 PS defects in a silica crystal

To study the possibility of incorporating defects in a colloidal crystal using the spin coating technique, we added 5% $SiO_2$-coated PS particles to a dispersion of $SiO_2$ particles. We made two dispersions with a total volume fraction of particles in the $SiO_2$/PS/ethanol

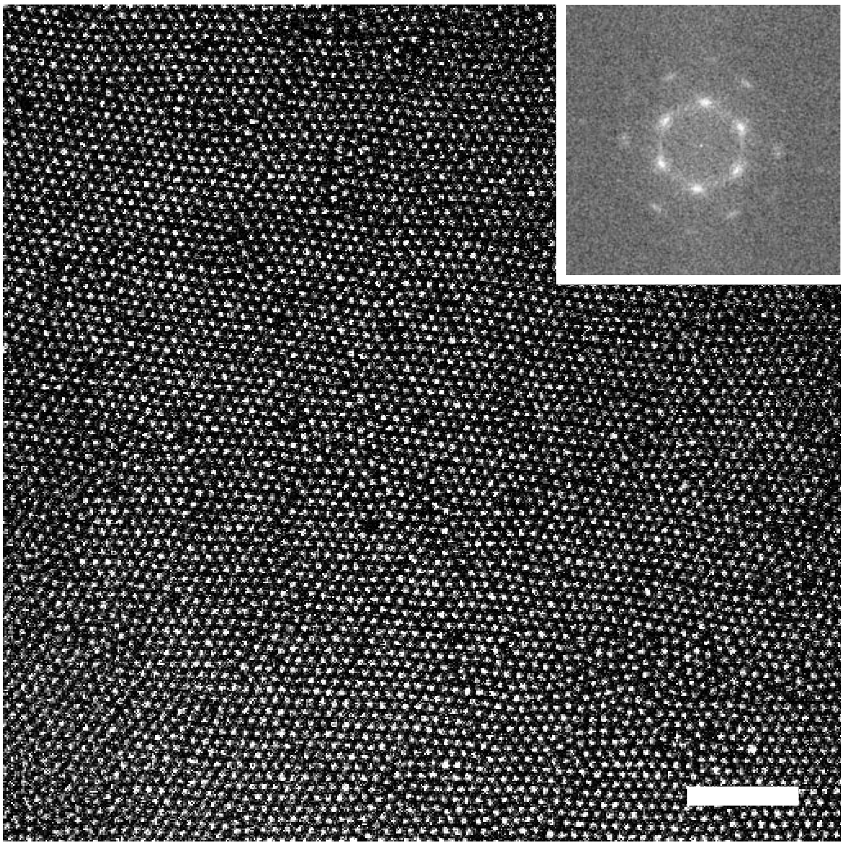

**Figure 8.13:** Confocal microscopy image of 50% 808 nm diameter $SiO_2$ particles in a mixture of ethylene glycol and water (4:1) at 1500 rpm. The scale bar is 10 $\mu$m.

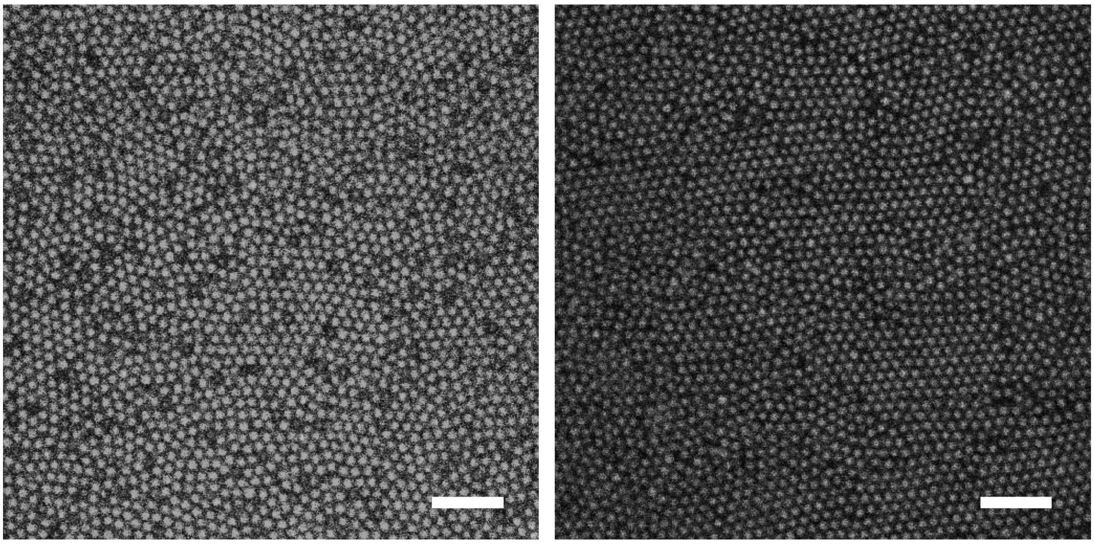

**Figure 8.14:** *(A color version of this figure can be found on page 36)* Confocal microscopy *xy* images of $SiO_2$/PS/ethanol dispersions. a) a 25% dispersion spin coated at 3000 rpm, b) a 34% dispersion spin coated at 4000 rpm. Scale bars are 5 $\mu$m.

dispersion of 25% and 34%. The dispersions were spinned at 3000 rpm and 4000 rpm, respectively, yielding the confocal microscopy images shown in Figure 8.14.

The confocal microscopy images demonstrate that the PS defects were well distributed over the colloidal crystal. However, it is not completely clear to what extent the crystal structure was perturbed by the PS defects. Some defects were situated at grain boundaries or other crystal defects. Furthermore, there was no clear diffraction star visible on the samples in white light illumination, which means that the crystal was less ordered than the samples without PS defects.

Spin coating a dispersion of 50% colloids (95% silica and 5% PS) in a mixture of ethylene glycol and $H_2O$ (weight ratio 4:1) at 1500 rpm yielded a crystal with almost the same domain size as the crystals spin coated from ethanol. For these crystals the PS-particles clearly disturbed the lattice, since otherwise much larger domains were found. This disturbance was probably caused by a small size difference between the two particles. The sizes of the particles, measured with SLS, were very close (the diameter was only 12 nm different, which is 1,5%). However, we did not study the effective diameters of the particles in the different solvents. This could give a better clue on the origin of the disturbance of the crystal structure. It could also be that the interaction between the silica colloids and the silica-coated PS colloids is not the same as the interaction between mutual silica colloids.

Since the drying-time for the crystals formed from an ethylene glycol dispersion was longer than for the crystals formed from an ethanol dispersion, the density separation was more clear: there were hardly PS particles in the bottom layer and significantly more in the layers above. As a result, the bottom layers had larger crystal grains than the top layers.

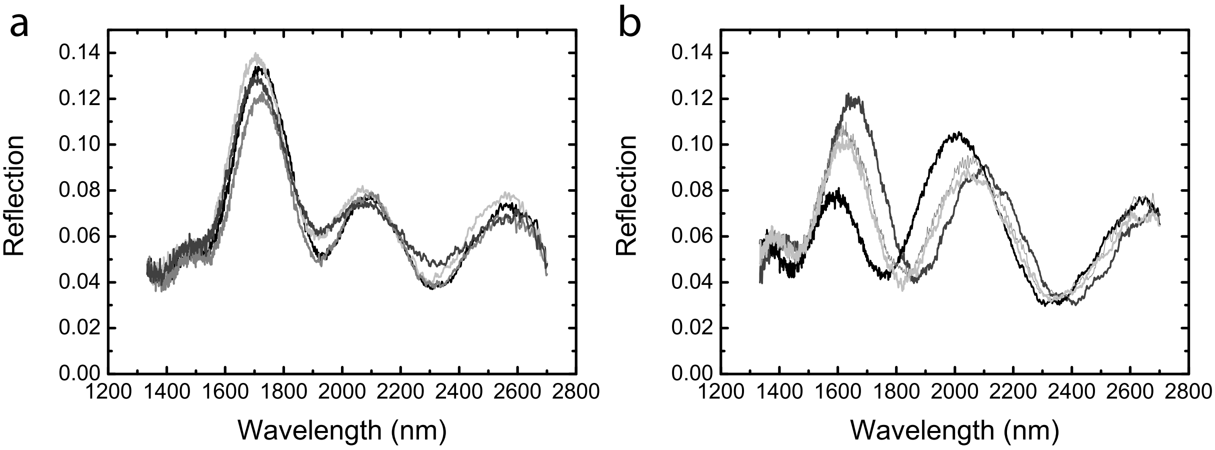

**Figure 8.15:** FTIR reflection spectra for several positions on (a) a sample made by spin coating a 25 volume % dispersion of 800 nm $SiO_2$ particles in ethanol at 4000 rpm, (b) a sample made by spin coating a 25 volume % dispersion of 800 nm $SiO_2$ particles and PS particles (number ratio 19:1) in ethanol at 3000 rpm. The lines with different colors represent spectra taken at different positions at the sample.

### 8.3.7 Reflection spectra

We recorded the reflection spectra of two samples, both originating of a dispersion with a volume fraction of 25% consisting of 800 nm $SiO_2$ particles, but one with 5% added PS-defects and one without. Measured reflection spectra at several positions for both samples are plotted in Figure 8.15.

The theoretical reflection signal for a few layers of fcc crystal of silica spheres ($n$=1.45) in air ($n$=1) oriented with the (111) plane horizontal or with the (200) plane horizontal, was calculated using the Korringa-Kohn-Rostoker (KKR) method implemented in the program 'multem' by Stefanou et al. [29]. The thin and thick glass plates below the crystal were approximated by an infinitely thick slab with the same refractive index as silica. The calculated reflection spectra are shown in Figure 8.16.

The reflection spectra for an fcc structure with the (200) planes horizontal do not have a Bragg peak in the wavelength region of interest because the form factor of these spheres has a minimum at the reciprocal vector of the reflection from the (200) planes. Domains with the (200) orientation will therefore not contribute considerably to the measured reflection spectrum.

The Bragg peak found for reflection from horizontal (111)-peaks agrees with the expected value at $\lambda_{(111)} = 2\langle n\rangle\sigma d_{(111)} = 1.7$ $\mu$m where $\langle n\rangle = 1.33$ is the volume averaged refractive index and $d_{(111)} = \sqrt{2/3}$ is the layer spacing. Based on the peak positions in the measured and calculated reflection spectra, the 7-layer fcc structure with the (111) plane horizontal agrees most with the measured structure without PS defects. The decrease in height of the main peak is probably due to a lack of order in the plane as visible in the confocal images.

The reflection spectra of the sample with PS defects shows more spread in the peak positions and peak height with the position on the sample. This implies that the sample

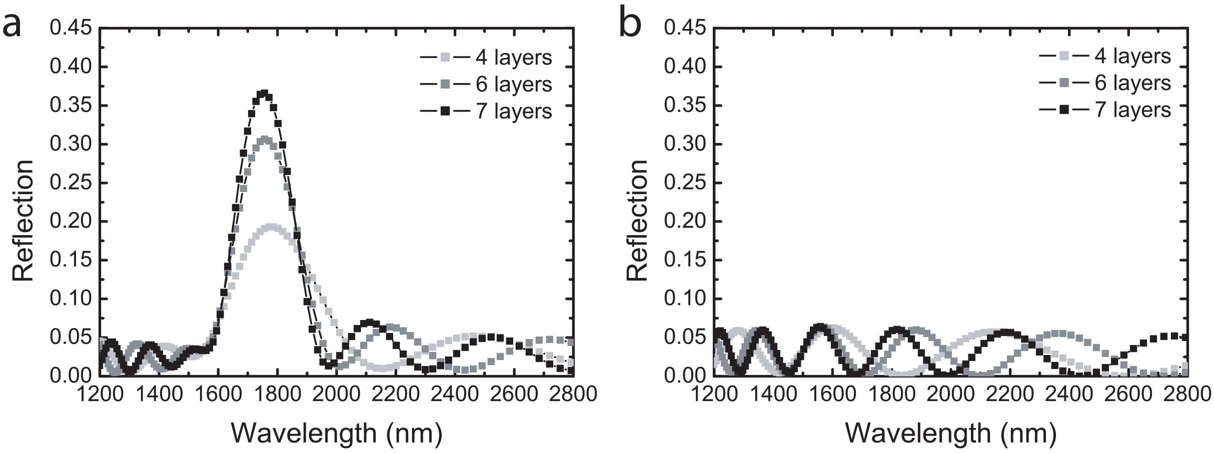

**Figure 8.16:** Reflection spectra calculated using the KKR method for a close-packed fcc crystal of 800 nm $SiO_2$ particles in air for different numbers of layers and for two different orientations: (a) with the (111) plane horizontal and (b) with the (200) plane horizontal.

is more irregular in thickness, layer spacing and range and quality of the in-plane order, which confirms our observation with confocal microscopy, that the incorporation of PS defects distorts the crystal structure of the spin coated crystals.

It is intriguing to see it can also make the 'secondary' peaks, caused by the finite thickness of the layers, higher than the main Bragg peak. This may indicate that in some places the distribution of the PS may have been inhomogeneous, but such a conclusion needs further support by calculations next to more detailed real-space analysis.

### 8.3.8 Spin coating on a templated substrate

Since the domains resulting from spin coating ethanol dispersions were small, on the order of 10 $\mu$m, the crystals were not suitable for photonic applications. To increase the domain size and improve the alignment, a templated substrate was used. Colloidal templates have been used before in combination with the controlled drying technique to grow aligned colloidal crystals [195, 196]. Here we combined the spin coating technique with epitaxial growth on a templated substrate. An array of holes of about a square millimeter in area was made in Norland OA 68 glue on a glass substrate using the soft lithography technique as described in Chapter 2.3.2. The square array was roughly aligned with the close-packed lines along the radial direction. A dispersion with a volume fraction of 33% of 1.48 $\mu$m diameter silica particles in ethanol was spin coated on a square array of holes with different spacings, of which the template with a spacing of 1.63 $\mu$m gave the best results. The samples were rotated at spin speeds of 1000, 2000, 3000 and 4000 rpm. The resulting samples had 5, 4, 3 and 2 layers, respectively. In white light illumination, there was a four-armed star for the samples made at 4000 and 3000 rpm, an unclear diffraction star for the sample made at 2000 rpm and no diffraction star at the lowest spin speed. In confocal microscopy, the bottom layers were imaged, showing that for the lowest spin speeds only few particles entered the holes of the pattern on the bottom surface and

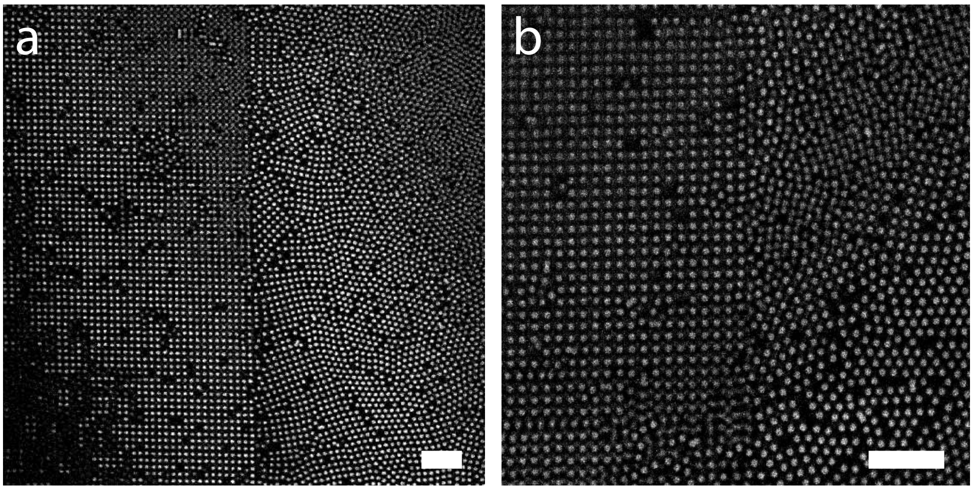

**Figure 8.17:** Confocal microscopy $xy$ images of 1.48 $\mu$m diameter silica dispersions in ethanol, spin coated at 4000 rpm on a substrate patterned with a square array of holes. The scale bars are 10 $\mu$m.

further layers did not adopt the symmetry and alignment of the bottom particles. Only at 4000 rpm, the template had a large effect: at the position of the template, the particles in the bottom layer were almost completely in the template holes and also the next (top) layer adopted this alignment and the square symmetry. At the edges of the template, the effect of the template was most clear, as can be seen in Figure 8.17.

### 8.3.9 Two crystal orientations

From the results presented in Table 8.1, a trend can be identified: at low concentrations and spin speeds, the fcc structure is oriented with its (111) plane parallel to the surface, while at higher concentrations and at higher spin speeds the (200) plane is horizontal. This trend does not agree with the alternating trend, which one would expect if the crystal orientation would be caused by optimization of the volume fraction for different confinement parameters (as described in the introductory Section 8.1).

The other possible cause for a change in preferred crystal orientation, as put forward in the introduction, is a difference in permeability for the liquid forced to flow in different directions in the crystal. During the spin coating process (both for dispersions in monomer and in volatile media), a colloidal crystal is formed which has a higher volume fraction of colloids than the original colloidal dispersion. Thus, some of the dispersion solvent is extracted from the colloidal crystal during spin coating. In the case of spin coating in a volatile medium, even all solvent leaves the crystal. This empirical notion implies that there is a solvent flow relative to the colloids. In the case that the colloidal structure has a yield stress like a crystal or a glass, liquids leaving the structure can be understood. In the case of a colloidal liquid it is harder to understand how the liquid can leave. Still, the very fast crystal formation and removal of the solvent from the crystal do imply an important role of these fluid flows in the process. The influence of the fluid flow on the crystal formation is dependent on the following factors:

- The *viscosity* and evaporation rate
- For *higher volume fractions* of colloids, solidification is expected to be faster
- The fluid flow will have more influence for *higher spin speeds* and higher spin speeds may also mean higher evaporation rates.

In the spin coating process, three different fluid flow directions play a role. First of all, after application, the dispersion is accelerated azimuthally to the same rotational speed as the substrate, resulting in an azimuthal fluid flow. Secondly, because of radial acceleration, a radial flow brings the fluid to the outside of the sample, of which a part is even expelled from the sample. Finally, the solvent completely evaporates, which happens mostly at the top surface (because of larger surface area than at the sides the crystal), resulting in a vertical fluid flow.

The crystal directions in which the three different fluid flows occur (radial, azimuthal and vertical) are indicated in Figure 8.18 for three different orientations of the crystal with respect to the radial direction: two with the hexagonal (111) plane horizontal (henceforth referred to as a hexagonal orientations) and one with the square (200) plane horizontal (referred to as a square orientation). The first orientation with the hexagonal plane horizontal, is the orientation which is found by Jiang et al. [99] for spin coating a colloidal dispersion in a monomer, with the close-packed strings in the radial direction. In our case, for spinning in a volatile medium, we also find the other hexagonal orientation (though less frequently): with the strings in the azimuthal direction. This orientation is the second orientation in the table.

The most permeable direction in the fcc crystal is the [110] direction (perpendicular to the (220) planes), as stated by Ishii et al. [204], based on pure visible inspection of the crystal directions of an fcc structure made of macroscopic balls. The visible inspection was used to look for the straightest possible channels through which fluid could flow. However, the argument that straight channels exist in the fcc crystal only in the [110] direction, does not take into account the hydrodynamic interactions of the fluid in the small interconnected channels in the microscopic sample. And more in general, hydrodynamic interactions are long-ranged, an intuitive prediction is therefore highly questionable. Nevertheless, based on the argument that flow is easiest in this direction through the crystal, Ishii et al. were able to provide an explanation for the crystal orientation seen in their flow cell.

Flow of a Newtonian fluid through periodic arrays of spheres of different volume fractions, including hydrodynamic interactions, has been discussed in several articles in the past [208–211]. In these studies, the interest was in flow through a crystal, but also in the context of sedimentation of a crystal in a fluid. For the body centered cubic structure Hurd et al. studied the friction factors for flow in different directions [212]. However, we were not able to find articles that discuss the difference in viscous drag for different fcc crystal directions. Therefore, in the following we have turned to the very simple argumentation as proposed by Ishii et al. [204]. We want to stress that with recent advances in computer simulations in which hydrodynamic effects can be fully taken into account our estimations of the friction of fluid flowing in the different directions through an fcc crystal can be tested numerically [155, 213]. In Figure 8.19 we made projections of several

| radial<br>direction<br>→ | 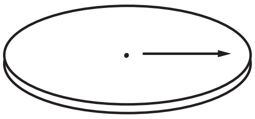 | 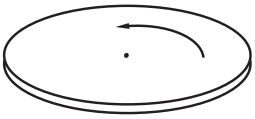 | 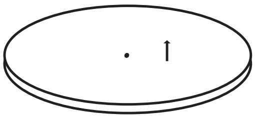 |
|---|---|---|---|
| 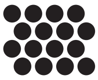 | [110] | [211] | [111] |
|  | [211] | [110] | [111] |
| 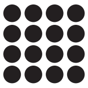 | [110] | [110] | [100] |

**Figure 8.18:** Table of the crystal directions in which the three different flows occur (radial, azimuthal and vertical) for three different crystal orientations of the crystal with respect to the radial direction. The schematic images of the crystal planes depict the horizontal plane, in which the radial direction (towards of the middle of the sample) is indicated with the horizontal arrow at the top left of the table. The [100] direction is perpendicular to the family of {200} planes, the [110] direction is perpendicular to the family of {220} planes, the [111] direction is perpendicular to the family of {111} planes and the [211] direction is perpendicular to the family of {422} planes of the fcc crystal structure.

layers of spheres in the crystal direction which are relevant for the fluid flows in the spin coating process. From these images, free channels in the crystal (as in the case of the [110] direction) can be identified and also mildly open planes are recognizable from the low overlap of the spheres. Based on the grey-level in the images for every direction, one could order them roughly at decreasing permeability: [110]-[100]-[211]-[111].

Combining the fluid flows for different crystal orientations with the permeabilities of the relevant planes, shows that the radial flow cannot explain the reorientation behavior, since this flow is in the [110] direction for both the more common hexagonal orientation and the square orientation. The evaporation direction is not an efficient direction for fluid flow in either direction, since it is in the [111] or in the [100] direction. The azimuthal flow, however, is in the [110] direction for the square orientation, but in the less permeable [211] direction for the common hexagonal orientation. The azimuthal flow is most prominent in the acceleration stage (usually identified as the second stage of the spin coating process, see Section 2.6.1), in which the deposited dispersion has to acquire the same rotation speed as the substrate. As can be seen in the supporting movie of Jiang et al. [99], the diffraction star appears almost immediately, supporting the hypothesis that the order already starts in the acceleration-stage. The hypothesis could be checked more thoroughly by carrying out the experiment with different initial accelerations. The only drawback of this method is the fact that we found that it is experimentally difficult to apply the dispersion while the substrate is still standing still. Often the dispersion dried partly already before starting the spin coating process.

The fact that Jiang et al. only found the first hexagonal orientation could be explained

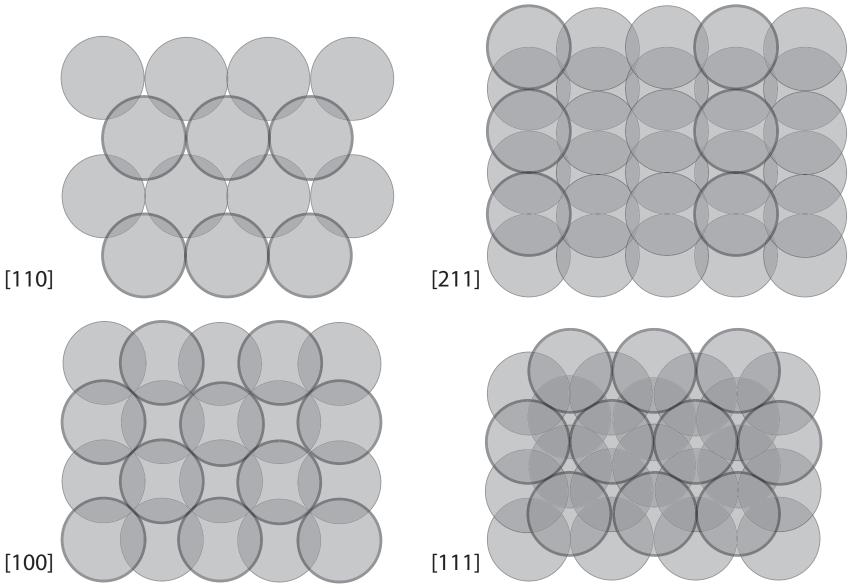

**Figure 8.19:** Schematic image of the overlap of spheres in different directions in the fcc crystal. The amount of overlap can be deduced from the grey level. The top layer of spheres is outlined with a thicker line. Only the number of unique planes in each direction is shown.

from the fact that the monomer is much more viscous than ethanol, which is used in our experiments. We hypothesize that there is less solvent moving relative to the colloids for a more viscous solvent, since the colloids are dragged along with the dispersion. The percolating flow is therefore lower for a viscous solvent. The crystal is in this case aligned by shear on the dispersion by the outward movement of part of the dispersion on one side and by the substrate on the other side. A similar argument holds for dispersions with a low volume fraction of colloids and for low spin speeds: in these cases, the colloidal crystal is aligned by shear instead of displacement of fluid relative to the colloids and therefore becomes aligned with the hexagonal layer parallel to the substrate and with the close-packed strings of colloids in the shear-flow direction (as is seen for shear-induced order [214]).

## 8.4 Conclusions

From the observations with both the real-space techniques (SEM and confocal microscopy) and the reciprocal-space techniques (laser and white light diffraction), we conclude that in the spin coating process fcc crystals are formed with an orientation where the (111) plane is horizontal at low spin speeds and low concentrations and otherwise with an orientation where the (200) plane is horizontal. For both orientations the crystals are globally aligned in the radial direction, following from the observation of star-shaped interference patterns with hexagonal or square symmetry covering the size of the structures or from laser diffraction experiments covering about millimeter sized regions. Intriguingly, the local alignment of small ordered domains along a common radial director as observed by SEM and confocal microscopy, does not clearly reflect the order seen on the millimeter and centimeter length scales in the scattering experiments. From Fourier transforms the confocal images it can be concluded that the horizontal square (200) planes are locally aligned better along a common director than the horizontal hexagonal (111) planes. A bond order parameter analysis of the confocal images demonstrates the increase in local square order for increasing spin speed or concentration and an accompanying decrease in local hexagonal order. The global (on the order of 100 $\mu$m) square order in the confocal images increased in a similar fashion, while the global hexagonal order was hardly influenced by the two parameters. We hypothesize that this last observation, in combination with the comparison of the different permeabilities of the fcc crystal directions (which should be measured or calculated and not guessed at as in the present work) may suggest that the hexagonal orientation of the fcc crystal is formed by shear when the percolating fluid flow (average flow relative to the particles) does not play an important role. The square orientation of the fcc crystal is formed by aligning the planes with lowest permeability ({220} planes) along the important flow directions (radial and azimuthal directions) by the percolating flow.

PS defects were homogeneously incorporated in the colloidal crystal. In the case of crystals made from dispersions in ethylene glycol, the grain size clearly decreased. This is probably due to a different effective radius of the PS defects and the silica hosts. An other explanation could be that the interaction between the silica hosts and the defects is not the same as the interaction between the mutual hosts.

Spin coating a crystal on a (200) templated surface gives control over the positions of the bottom particles. The second layer is also affected by the template at high spin speeds where the second layer is the top layer. Together with the observation that the bottom layer is less densely packed and less ordered, we can conclude that the ordering of the spin coated crystals starts at the top surface.

In this study we focussed on two parameters: spin speed and concentration of the dispersion, which both have a large influence on the order, orientation and alignment of the crystal. However, there are still many other parameters that can be varied (vapor pressure, dispersing solvent, substrate hydrophilicity, temperature, etc.). Further studies should give more insight in the mechanism of spin coating by varying those parameters, while simulations are required to investigate our assumptions about friction of the flow through different crystals and crystalline directions.

## 8.5 Acknowledgements

This work was partly performed together with undergraduate student Rianne ’t Hoen. We would like to thank Yu Ling Wu for the initial help with the spin coating technique. We thank Anke Kuijk and Dannis ’t Hart for $SiO_2$ particle synthesis. We would like to thank Arnout Imhof for the synthesis of the PS particles, for the help with the growth of the $SiO_2$ shell and for useful discussions. Job Thijssen is gratefully acknowledged for help with the laser diffraction and FTIR experiments and for useful tips and discussions. We thank Carlos van Kats and Zuocheng Zhou for help with the SEM imaging. Furthermore, we thank Anand Yethiraj for useful discussions.

# References

[1] T. Graham, *Liquid diffusion applied to analysis*, Philosophical Transactions of the Royal Society of London **151**, 183 (1861).

[2] A. Einstein, *Über die von der molekularkinetischen Theorie der Wärme geforderte Bewegung von in ruhenden Flüssigkeiten suspendierten Teilchen*, Annalen der Physik **17**, 548 (1905).

[3] W. Poon, *Colloids as big atoms*, Science **304**, 830 (2004).

[4] A. Vrij, E. A. Nieuwenhuis, H. M. Fijnaut, and W. G. M. Agterof, Faraday Discussions of the Chemical Society **65**, 101 (1978).

[5] P. N. Pusey and W. van Megen, *Phase behaviour of concentrated suspensions of nearly hard colloidal spheres*, Nature **320**, 340 (1986).

[6] J. Israelachvili, *Intermolecular and surface forces*, Academic Press, San Diego, 1991.

[7] A. Yethiraj and A. van Blaaderen, *A colloidal model system with an interaction tunable from hard sphere to soft and dipolar*, Nature **421**, 513 (2003).

[8] M. E. Leunissen, C. G. Christova, A. P. Hynninen, C. P. Royall, A. I. Campbell, A. Imhof, M. Dijkstra, R. van Roij, and A. van Blaaderen, *Ionic colloidal crystals of oppositely charged particles*, Nature **437**, 235 (2005).

[9] U. Dassanayake, S. Fraden, and A. van Blaaderen, *Structure of electrorheological fluids*, J. Chem. Phys. **112**, 3851 (2000).

[10] A. P. Hynninen and M. Dijkstra, *Phase diagram of dipolar hard and soft spheres: Manipulation of colloidal crystal structures by an external field*, Phys. Rev. Lett. **94**, 138303 (2005).

[11] A. P. Hynninen, C. G. Christova, R. van Roij, A. van Blaaderen, and M. Dijkstra, *Prediction and observation of crystal structures of oppositely charged colloids*, Phys. Rev. Lett. **96**, 138308 (2006).

[12] A. Yethiraj, J. H. J. Thijssen, A. Wouterse, and A. van Blaaderen, *Large-area electric-field-induced colloidal single crystals for photonic applications*, Adv. Mater. **16**, 596 (2004).

[13] J. D. Joannopoulos, R. D. Meade, and J. Winn, *Photonic crystals: Molding the Flow of Light*, Princeton University Press, Princeton (New Yersey); http://ab-initio.mit.edu/book/photonic-crystals-book.pdf, second edition, 1995.

[14] *Photonic Crystals and Light Localization in the 21st Century*, NATO Science Series (C): Mathematical and Physical Sciences, Kluwer Academic, Dordrecht, 2001.

[15] P. Vukusic and J. R. Sambles, *Photonic structures in biology*, Nature **424**, 852 (2003).

[16] V. P. Bykov, *Spontaneous emission in a periodic structure*, Soviet Physics - JETP **35**, 269 (1972).

[17] K. Ohtaka, *Energy band of photons and low-energy photon diffraction*, Phys. Rev. B **19**, 5057 (1979).

[18] E. Yablonovitch, *Inhibited Spontaneous Emission in Solid-State Physics and Electronics*, Phys. Rev. Lett. **58**, 2059 (1987).

[19] S. John, *Strong localization of photons in certain disordered dielectric superlattices*, Phys. Rev. Lett. **58**, 2486 (1987).

[20] K. M. Leung and Y. F. Liu, *Full Vector Wave Calculation of Photonic Band Structures in Face-Centered-Cubic Dielectric Media*, Phys. Rev. Lett. **65**, 2646 (1990).

[21] Z. Zhang and S. Satpathy, *Electromagnetic wave propagation in periodic structures: Bloch wave solution of Maxwell's equations*, Phys. Rev. Lett. **65**, 2650 (1990).

[22] K. M. Ho, C. T. Chan, and C. M. Soukoulis, *Existence of a photonic gap in periodic dielectric structures*, Phys. Rev. Lett. **65**, 3152 (1990).

[23] E. Yablonovitch, T. J. Gmitter, and K. M. Leung, *Photonic band structure: The face-centered-cubic case employing nonspherical atoms*, Phys. Rev. Lett. **67**, 2295 (1991).

[24] C. T. Chan, K. M. Ho, and C. M. Soukoulis, *Photonic Band Gaps in Experimentally Realizable Periodic Dielectric Structures*, Europhys. Lett. **16**, 563 (1991).

[25] K. M. Ho, C. T. Chan, C. M. Soukoulis, R. Biswas, and M. Sigalas, *Photonic band gaps in three dimensions: New layer-by-layer periodic structures*, Solid State Commun. **89**, 413 (1994).

[26] J. M. Harrison, P. Kuchment, A. Sobolev, and B. Winn, *On occurrence of spectral edges for periodic operators inside the Brillouin zone*, Journal of Physics A-Mathematical and Theoretical **40**, 7597 (2007).

[27] *http://ab-initio.mit.edu/wiki/index.php/Main_Page.*

[28] S. G. Johnson and J. D. Joannopoulos, *Block-iterative frequency-domain methods for Maxwell's equations in a planewave basis*, Optics Express **8**, 173 (2001).

[29] N. Stefanou, V. Yannopapas, and A. Modinos, *Heterostructures of photonic crystals: frequency bands and transmission coefficients*, Computer Physics Communications **113**, 49 (1998).

[30] A. Moroz, *Density-of-States Calculations and Multiple-Scattering Theory for Photons*, Phys. Rev. B **51**, 2068 (1995).

[31] J. V. Sanders and M. J. Murray, *Ordered arrangements of spheres of two different sizes in opal*, Nature **275**, 201 (1978).

[32] J. V. Sanders, *Close-packed structures of spheres of two different sizes I. Observations on natural opal*, Philos. Mag. A **42**, 705 (1980).

[33] M. J. Murray and J. V. Sanders, *Close-packed structures of spheres of two different sizes II. The packing densities of likely arrangements*, Philos. Mag. A **42**, 721 (1980).

[34] S. Hachisu and S. Yoshimura, *Optical demonstration of crystalline superstructures in binary mixtures of latex globules*, Nature **283**, 188 (1980).

[35] S. Yoshimura and S. Hachisu, *Order formation in binary mixtures of monodisperse lattices. I. Observations of ordered structures*, volume 68 of *Progress in Colloid & Polymer Science*, page 59, 1983.

[36] S. Hachisu and S. Yoshimura, in *Physics of complex and supermolecular fluids*, page 221, John Wiley and Sons Inc., New York, 1987.

[37] U. R. Pedersen, N. P. Bailey, J. C. Dyre, and T. B. Schrøder, *Crystallization of the Wahnström binary Lennard-Jones liquid*, arXiv:0706.0813v2 (2007).

[38] M. D. Eldridge, P. A. Madden, and D. Frenkel, *Entropy-driven formation of a superlattice in a hard-sphere binary mixture*, Nature **365**, 35 (1993).

[39] M. D. Eldridge, P. A. Madden, and D. Frenkel, *The stability of the $AB_{13}$ crystal in a binary hard sphere system*, Mol. Phys. **79**, 105 (1993).

[40] M. D. Eldridge, P. A. Madden, and D. Frenkel, *A computer simulation investigation into the stability of the $AB_2$ superlattice in a binary hard sphere system*, Mol. Phys. **80**, 987 (1993).

[41] M. D. Eldridge, P. A. Madden, P. N. Pusey, and P. Bartlett, *Binary Hard-Sphere Mixtures - a Comparison between Computer-Simulation and Experiment*, Mol. Phys. **84**, 395 (1995).

[42] P. Bartlett, R. H. Ottewill, and P. N. Pusey, *Superlattice formation in binary mixtures of hard-sphere colloids*, Phys. Rev. Lett. **68**, 3801 (1992).

[43] P. Bartlett, R. H. Ottewill, and P. N. Pusey, *Freezing of binary mixtures of colloidal hard spheres*, J. Chem. Phys. **93**, 1299 (1990).

[44] P. Bartlett and R. H. Ottewill, *A neutron scattering study of the structure of a bimodal colloidal crystal*, J. Chem. Phys. **96**, 3306 (1992).

[45] P. Bartlett and R. H. Ottewill, *Geometric Interactions in Binary Colloidal Dispersions*, Langmuir **8**, 1919 (1992).

[46] N. Hunt, R. Jardine, and P. Bartlett, *Superlattice formation in mixtures of hard-sphere colloids*, Phys. Rev. E **62**, 900 (2000).

[47] A. B. Schofield, *Binary hard-sphere crystals with the cesium chloride structure*, Phys. Rev. E **64**, 051403 (2001).

[48] G. H. Ma, T. Fukutomi, and N. Morone, *Preparation and Analysis of Ordered Structure of Binary Mixtures Composed of Poly(4-vinylpyridine) and Polystyrene Microgels*, J. Colloid Interface Sci. **168**, 393 (1994).

[49] S. M. Underwood, W. van Megen, and P. N. Pusey, *Observation of colloidal crystals with the cesium chloride structure*, Physica A: Statistical and Theoretical Physics **221**, 438 (1995).

[50] P. Bartlett and A. I. Campbell, *Three-dimensional binary superlattices of oppositely charged colloids*, Phys. Rev. Lett. **95**, 128302 (2005).

[51] P. D. Kaplan, J. L. Rouke, A. G. Yodh, and D. J. Pine, *Entropically Driven Surface Phase Separation in Binary Colloidal Mixtures*, Phys. Rev. Lett. **72**, 582 (1994).

[52] A. Imhof and J. K. G. Dhont, *Experimental Phase Diagram of a Binary Colloidal Hard-Sphere Mixture with a Large Size Ratio*, Phys. Rev. Lett. **75**, 1662 (1995).

[53] M. Dijkstra, R. van Roij, and R. Evans, *Phase diagram of highly asymmetric binary hard-sphere mixtures*, Phys. Rev. E **59**, 5744 (1999).

[54] D. Frenkel and A. A. Louis, *Phase separation in binary hard-core mixtures: An exact result*, Phys. Rev. Lett. **68**, 3363 (1992).

[55] C.-m. Xiao, G.-j. Jin, X.-d. Shi, and Y.-q. Ma, *Entropy-driven phase transition in binary mixtures*, Phys. Rev. E **64**, 011402 (2001).

[56] J. L. Barrat, M. Baus, and J. P. Hansen, *Density-Functional Theory of Freezing of Hard-Sphere Mixtures into Substitutional Solid Solutions*, Phys. Rev. Lett. **56**, 1063 (1986).

[57] X. Cottin and P. A. Monson, *A cell theory for solid solutions: Application to hard sphere mixtures*, J. Chem. Phys. **99**, 8914 (1993).

[58] A. R. Denton and N. W. Ashcroft, *Weighted-density-functional theory of nonuniform fluid mixtures: Application to freezing of binary hard-sphere mixtures*, Phys. Rev. A **42**, 7312 (1990).

[59] W. G. T. Kranendonk and D. Frenkel, *Computer simulation of solid-liquid coexistence in binary hard-sphere mixtures*, J. Phys.: Condens. Matter **1**, 7735 (1989).

[60] Z. D. Cheng, W. B. Russell, and P. M. Chaikin, *Controlled growth of hard-sphere colloidal crystals*, Nature **401**, 893 (1999).

[61] M. Holgado, F. García-Santamaría, A. Blanco, M. Ibisate, A. Cintas, H. Miguez, C. J. Serna, C. Molpeceres, J. Requena, A. Mifsud, F. Meseguer, and C. Lopez, *Electrophoretic deposition to control artificial opal growth*, Langmuir **15**, 4701 (1999).

[62] J. P. Hoogenboom, D. Derks, P. Vergeer, and A. van Blaaderen, *Stacking faults in colloidal crystals grown by sedimentation*, J. Chem. Phys. **117**, 11320 (2002).

[63] J. P. Hoogenboom, P. Vergeer, and A. van Blaaderen, *A real-space analysis of colloidal crystallization in a gravitational field at a flat bottom wall*, J. Chem. Phys. **119**, 3371 (2003).

[64] L. V. Woodcock, *Entropy difference between the face-centred cubic and hexagonal close-packed crystal structures*, Nature **385**, 141 (1997).

[65] P. G. Bolhuis, D. Frenkel, S. C. Mau, and D. A. Huse, *Entropy difference between crystal phases*, Nature **388**, 235 (1997).

[66] A. D. Bruce, N. B. Wilding, and G. J. Ackland, *Free energy of crystalline solids: A lattice-switch Monte Carlo method*, Phys. Rev. Lett. **79**, 3002 (1997).

[67] D. H. Van Winkle and C. A. Murray, *Layering in Colloidal Fluids near a Smooth Repulsive Wall*, J. Chem. Phys. **89**, 3885 (1988).

[68] D. J. Courtemanche and F. Vanswol, *Wetting State of a Crystal-Fluid System of Hard-Spheres*, Phys. Rev. Lett. **69**, 2078 (1992).

[69] D. J. Courtemanche, T. A. Pasmore, and F. Vanswol, *A Molecular-Dynamics Study of Prefreezing Hard-Spheres at a Smooth Hard-Wall*, Mol. Phys. **80**, 861 (1993).

[70] A. van Blaaderen, R. Ruel, and P. Wiltzius, *Template-directed colloidal crystallization*, Nature **385**, 321 (1997).

[71] A. van Blaaderen and P. Wiltzius, *Growing large, well-oriented colloidal crystals*, Adv. Mater. **9**, 833 (1997).

[72] K. H. Lin, J. C. Crocker, V. Prasad, A. Schofield, D. A. Weitz, T. C. Lubensky, and A. G. Yodh, *Entropically driven colloidal crystallization on patterned surfaces*, Phys. Rev. Lett. **85**, 1770 (2000).

[73] J. P. Hoogenboom, *Colloidal Epitaxy: A Real-Space Analysis*, PhD thesis, Utrecht University, 2002.

[74] J. P. Hoogenboom, A. K. van Langen-Suurling, J. Romijn, and A. van Blaaderen, *Hard-sphere crystals with hcp and non-close-packed structure grown by colloidal epitaxy*, Phys. Rev. Lett. **90**, 138301 (2003).

[75] J. P. Hoogenboom, A. K. van Langen-Suurling, J. Romijn, and A. van Blaaderen, *Epitaxial growth of a colloidal hard-sphere hcp crystal and the effects of epitaxial mismatch on crystal structure*, Phys. Rev. E **69**, 051602 (2004).

[76] M. Heni and H. Löwen, *Surface Freezing on Patterned Substrates*, Phys. Rev. Lett. **85**, 3668 (2000).

[77] M. Heni and H. Löwen, *Precrystallization of fluids induced by patterned substrates*, J. Phys.: Condens. Matter **13**, 4675 (2001).

[78] A. Cacciuto and D. Frenkel, *Simulation of colloidal crystallization on finite structured templates*, Phys. Rev. E **72**, 041604 (2005).

[79] Y. Xia and G. Whitesides, *Soft Lithography*, Angew. Chem. Int. Ed. **37**, 550 (1998).

[80] A. Ashkin, *Acceleration and Trapping of Particles by Radiation Pressure*, Phys. Rev. Lett. **24**, 156 (1970).

[81] A. Ashkin and J. M. Dziedzic, *Optical Levitation by Radiation Pressure*, Appl. Phys. Lett. **19**, 283 (1971).

[82] A. Ashkin, J. M. Dziedzic, J. E. Bjorkholm, and S. Chu, *Observation of a single-beam gradient force optical trap for dielectric particles*, Optics Lett. **11**, 288 (1986).

[83] A. Ashkin and J. M. Dziedzic, *Optical trapping and manipulation of viruses and bacteria*, Science **235**, 1517 (1987).

[84] M. P. MacDonald, G. C. Spalding, and K. Dholakia, *Microfluidic sorting in an optical lattice*, Nature **426**, 421 (2003).

[85] S. M. Block, D. F. Blair, and H. C. Berg, *Compliance of bacterial flagella measured with optical tweezers*, Nature **338**, 514 (1989).

[86] C. Cecconi, E. A. Shank, C. Bustamante, and S. Marqusee, *Direct Observation of the Three-State Folding of a Single Protein Molecule*, Science **309**, 2057 (2005).

[87] Y. Harada and T. Asakura, *Radiation forces on a dielectric sphere in the Rayleigh scattering regime*, Opt. Commun. **124**, 529 (1996).

[88] P. A. M. Neto and H. M. Nussenzveig, *Theory of optical tweezers*, Europhys. Lett. **50**, 702 (2000).

[89] A. Mazolli, P. A. M. Neto, and H. M. Nussenzveig, *Theory of trapping forces in optical tweezers*, Proc. R. Soc. London, Ser. A **459**, 3021 (2003).

[90] A. van der Horst, P. D. J. van Oostrum, A. Moroz, A. van Blaaderen, and M. Dogterom, *High trapping forces for high-refractive index particles trapped in dynamic arrays of counterpropagating optical tweezers*, Applied Optics **47**, 3196 (2008).

[91] D. L. J. Vossen, A. van der Horst, M. Dogterom, and A. van Blaaderen, *Optical tweezers and confocal microscopy for simultaneous three-dimensional manipulation and imaging in concentrated colloidal dispersions*, Review of Scientific Instruments **75**, 2960 (2004).

[92] H. A. Pohl, *Dielectrophoresis, The behavior of neutral matter in nonuniform electric field*, Cambridge University Press, Cambridge, 1978.

[93] D. J. Griffiths, *Introduction to electrodynamics*, page 165, Prentice-Hall, New Jersey, 1999.

[94] B. Khusid and A. Acrivos, *Effects of Conductivity in Electric-Field-Induced Aggregation in Electrorheological Fluids*, Phys. Rev. E **52**, 1669 (1995).

[95] J. van 't Hoff, *The role of osmotic pressure in the analogy between solutions and gases*, Zeitschrift fur Physikalische Chemie **1**, 481 (1887).

[96] M. E. Leunissen, *Manipulating colloids with charges & electric fields*, PhD thesis, Utrecht University, 2007.

[97] M. E. Leunissen, M. T. Sullivan, P. M. Chaikin, and A. van Blaaderen, *Dielectrophoretic compression of colloids in an electric bottle. I. Particle transport and growth mechanism of hard-sphere-like crystals*, J. Chem. Phys., accepted (2008).

[98] M. E. Leunissen and A. van Blaaderen, *Dielectrophoretic compression of colloids in an electric bottle. II. Phase transitions and crystal buckling of charged spheres with long-ranged repulsions*, J. Chem. Phys., accepted (2008).

[99] P. Jiang and M. McFarland, *Large-Scale Fabrication of Wafer-Size Colloidal Crystals, Macroporous Polymers and Nanocomposites by Spin-Coating*, J. Am. Chem. Soc. **126**, 13778 (2004).

[100] A. Mihi, M. Ocaña, and H. Míguez, *Oriented Colloidal-Crystal Thin Films by Spin-Coating Microspheres Dispersed in Volatile Media*, Adv. Mater. **18**, 2244 (2006).

[101] A. G. Emslie, F. T. Bonner, and L. G. Peck, *Flow of a Viscous Liquid on a Rotating Disk*, J. Appl. Phys. **29**, 858 (1958).

[102] D. Meyerhofer, *Characteristics of resist films produced by spinning*, J. Appl. Phys. **49**, 3993 (1978).

[103] J. H. J. Thijssen, *Characterization of photonic colloidal crystals in real and reciprocal space*, PhD thesis, Utrecht University, 2007.

[104] K. Becker, J. M. Lupton, J. Muller, A. L. Rogach, D. V. Talapin, H. Weller, and J. Feldmann, *Electrical control of Forster energy transfer*, Nat. Mater. **5**, 777 (2006).

[105] E. V. Shevchenko, D. V. Talapin, C. B. Murray, and S. O'Brien, *Structural characterization of self-assembled multifunctional binary nanoparticle superlattices*, J. Am. Chem. Soc. **128**, 3620 (2006).

[106] J. J. Urban, D. V. Talapin, E. V. Shevchenko, C. R. Kagan, and C. B. Murray, *Synergismin binary nanocrystal superlattices leads to enhanced p-type conductivity in self-assembled PbTe/Ag-2 Te thin films*, Nat. Mater. **6**, 115 (2007).

[107] P. Bartlett, P. N. Pusey, and R. H. Ottewill, *Colloidal Crystallization under Time-Averaged Zero Gravity*, Langmuir **7**, 213 (1991).

[108] P. Bartlett and R. H. Ottewill, *Gravitational Effects on the Phase-Behavior of Dispersions*, Adv. Colloid Interface Sci. **50**, 39 (1994).

[109] X. Cottin and P. A. Monson, *Substitutionally Ordered Solid-Solutions of Hard-Spheres*, J. Chem. Phys. **102**, 3354 (1995).

[110] E. Trizac, M. D. Eldridge, and P. A. Madden, *Stability of the AB crystal for asymmetric binary hard sphere mixtures*, Mol. Phys. **90**, 675 (1997).

[111] A. E. Saunders and B. A. Korgel, *Observation of an AB phase in bidisperse nanocrystal superlattices*, Chemphyschem **6**, 61 (2005).

[112] K. P. Velikov, C. G. Christova, R. P. A. Dullens, and A. van Blaaderen, *Layer-by-layer growth of binary colloidal crystals*, Science **296**, 106 (2002).

[113] G. Tommaseo, G. Petekidis, W. Steffen, G. Fytas, A. B. Schofield, and N. Stefanou, *Hypersonic acoustic excitations in binary colloidal crystals: Big versus small hard sphere control*, J. Chem. Phys. **126**, 014707 (2007).

[114] L. Filion, unpublished (2008).

[115] N. A. M. Verhaegh and A. van Blaaderen, *Dispersions of Rhodamine-Labeled Silica Spheres - Synthesis, Characterization, and Fluorescence Confocal Scanning Laser Microscopy*, Langmuir **10**, 1427 (1994).

[116] H. Giesche, *Synthesis of Monodispersed Silica Powders .1. Particle Properties and Reaction-Kinetics*, J. Eur. Ceram. Soc. **14**, 189 (1994).

[117] J. C. Crocker and D. G. Grier, *Methods of digital video microscopy for colloidal studies*, J. Colloid Interface Sci. **179**, 298 (1996).

[118] A. D. Hollingsworth and D. A. Saville, *Dielectric spectroscopy and electrophoretic mobility measurements interpreted with the standard electrokinetic model*, J. Colloid Interface Sci. **272**, 235 (2004).

[119] A. Yethiraj, A. Wouterse, B. Groh, and A. van Blaaderen, *Nature of an electric-field-induced colloidal martensitic transition*, Phys. Rev. Lett. **92**, 058301 (2004).

[120] C. P. Royall, J. Dzubiella, M. Schmidt, and A. van Blaaderen, *Nonequilibrium Sedimentation of Colloids on the Particle Scale*, Phys. Rev. Lett. **98**, 188304 (2007).

[121] M. T. Sullivan, K. Zhao, A. D. Hollingsworth, R. H. Austin, W. B. Russel, and P. M. Chaikin, *An electric bottle for colloids*, Phys. Rev. Lett. **96**, 015703 (2006).

[122] K. Busch, S. Lölkes, R. B. Wehrspohn, and H. Föll (ed.), *Photonic Crystals: Advances in Design, Fabrication, and Characterization*, Wiley-VCH, Berlin, 2004.

[123] K. Busch, G. von Freymann, S. Linden, S. Mingaleev, L. Tkeshelashvili, and M. Wegener, *Periodic nanostructures for photonics*, Physics Reports **444**, 101 (2007).

[124] M. Maldovan, C. K. Ullal, W. C. Carter, and E. L. Thomas, *Exploring for 3D photonic bandgap structures in the 11 f.c.c. space groups*, Nat. Mater. **2**, 664 (2003).

[125] A. Moroz, *Metallo-dielectric diamond and zinc-blende photonic crystals*, Phys. Rev. B **66**, 115109 (2002).

[126] A. J. Garcia-Adeva, *Band structure of photonic crystals with the symmetry of a pyrochlore lattice*, Phys. Rev. B **73**, 073107 (2006).

[127] A. J. Garcia-Adeva, *Band gap atlas for photonic crystals having the symmetry of the kagome and pyrochlore lattices*, New J. Phys. **8**, 87 (2006).

[128] T. T. Ngo, C. M. Liddell, M. Ghebrebrhan, and J. D. Joannopoulos, *Tetrastack: Colloidal diamond-inspired structure with omnidirectional photonic band gap for low refractive index contrast*, Appl. Phys. Lett. **88**, 241920 (2006).

[129] M. Deubel, G. von Freymann, M. Wegener, S. Pereira, K. Busch, and C. M. Soukoulis, *Direct laser writing of three-dimensional photonic-crystal templates for telecommunications*, Nat. Mater. **3**, 444 (2004).

[130] F. García-Santamaría, H. T. Miyazaki, A. Urquía, M. Ibisate, M. Belmonte, N. Shinya, F. Meseguer, and C. López, *Nanorobotic Manipulation of Microspheres for On-Chip Diamond Architectures*, Adv. Mater. **14**, 1144 (2002).

[131] A. van Blaaderen, *Colloids under external control*, MRS Bull. **29**, 85 (2004).

[132] C. Lopez, *Materials aspects of photonic crystals*, Adv. Mater. **15**, 1679 (2003).

[133] D. J. Norris, E. G. Arlinghaus, L. L. Meng, R. Heiny, and L. E. Scriven, *Opaline photonic crystals: How does self-assembly work?*, Adv. Mater. **16**, 1393 (2004).

[134] H. S. Sözüer, J. W. Haus, and R. Inguva, *Photonic Bands - Convergence Problems with the Plane-Wave Method*, Phys. Rev. B **45**, 13962 (1992).

[135] R. Biswas, M. M. Sigalas, G. Subramania, and K. M. Ho, *Photonic band gaps in colloidal systems*, Phys. Rev. B **57**, 3701 (1998).

[136] A. Moroz and C. Sommers, *Photonic band gaps of three-dimensional face-centred cubic lattices*, J. Phys.: Condens. Matter **11**, 997 (1999).

[137] Z. Y. Li and Z. Q. Zhang, *Fragility of photonic band gaps in inverse-opal photonic crystals*, Phys. Rev. B **62**, 1516 (2000).

[138] X. D. Wang, T. C. Leung, B. N. Harmon, and P. Carra, *Circular Magnetic-X-Ray Dichroism in the Heavy Rare-Earth-Metals*, Phys. Rev. B **47**, 9087 (1993).

[139] Z. L. Zhang, A. S. Keys, T. Chen, and S. C. Glotzer, *Self-assembly of patchy particles into diamond structures through molecular mimicry*, Langmuir **21**, 11547 (2005).

[140] D. R. Nelson, *Toward a tetravalent chemistry of colloids*, Nano Lett. **2**, 1125 (2002).

[141] A. V. Tkachenko, *Morphological diversity of DNA-colloidal self-assembly*, Phys. Rev. Lett. **89**, 148303 (2002).

[142] V. N. Manoharan, M. T. Elsesser, and D. J. Pine, *Dense packing and symmetry in small clusters of microspheres*, Science **301**, 483 (2003).

[143] V. N. Manoharan and D. J. Pine, *Building materials by packing spheres*, MRS Bull. **29**, 91 (2004).

[144] Y. A. Vlasov, X. Z. Bo, J. C. Sturm, and D. J. Norris, *On-chip natural assembly of silicon photonic bandgap crystals*, Nature **414**, 289 (2001).

[145] G. A. Mansoori, N. F. Carnahan, K. E. Starling, and J. T. W. Leland, *Equilibrium Thermodynamic Properties of the Mixture of Hard Spheres*, J. Chem. Phys. **54**, 1523 (1971).

[146] R. J. Speedy, *Pressure and entropy of hard-sphere crystals*, J. Phys.: Condens. Matter **10**, 4387 (1998).

[147] D. Frenkel and B. Smit, *Understanding Molecular Simulations*, Academic, New York, 2002.

[148] J. M. Polson, E. Trizac, S. Pronk, and D. Frenkel, *Finite-size corrections to the free energies of crystalline solids*, J. Chem. Phys. **112**, 5339 (2000).

[149] A. P. Hynninen, L. Filion, and M. Dijkstra, to be published (2008).

[150] Y. L. Wu, *Control over colloidal crystallization*, PhD thesis, Utrecht University, 2007.

[151] Y. L. Wu, J. H. J. Brand, J. L. A. van Gemert, J. Verkerk, H. Wisman, A. van Blaaderen, and A. Imhof, *A new parallel plate shear cell for in situ real-space measurements of complex fluids under shear flow*, Review of Scientific Instruments **78**, 103902 (2007).

[152] T. Biben, J. P. Hansen, and J. L. Barrat, *Density Profiles of Concentrated Colloidal Suspensions in Sedimentation Equilibrium*, J. Chem. Phys. **98**, 7330 (1993).

[153] C. P. Royall, E. C. M. Vermolen, A. van Blaaderen, and H. Tanaka, *Controlling glass formation with binary hard spheres: a real space analysis*, J. Phys.: Condens. Matter **20**, 404225 (2008).

[154] E. Sanz, M. E. Leunissen, A. Fortini, M. Dijkstra, and A. van Blaaderen, *Gel formation in oppositely charged colloids: mechanism and relation to the phase diagram*, Journal of Physical Chemistry, accepted **112**, 10861 (2008).

[155] A. Wysocki, C. P. Royall, R. Winkler, G. Gompper, H. Tanaka, A. van Blaaderen, and H. Löwen, *Direct observation of hydrodynamic instabilities in driven non-uniform colloidal dispersions*, Submitted (2008).

[156] A. P. Hynninen, J. H. J. Thijssen, E. C. M. Vermolen, M. Dijkstra, and A. van Blaaderen, *Self-assembly route for photonic crystals with a bandgap in the visible region*, Nat. Mater. **6**, 202 (2007).

[157] S. Simeonov, U. Bass, and A. R. McGurn, *Photonic band structure of zinc blende type periodic dielectric media*, Physica B **228**, 245 (1996).

[158] K. Edagawa, S. Kanoko, and M. Notomi, *Photonic amorphous diamond structure with a 3D photonic band gap*, Phys. Rev. Lett. **100**, 013901 (2008).

[159] W. Y. Zhang, X. Y. Lei, Z. L. Wang, D. G. Zheng, W. Y. Tam, C. T. Chan, and P. Sheng, *Robust photonic band gap from tunable scatterers*, Phys. Rev. Lett. **84**, 2853 (2000).

[160] Z. Wang, C. T. Chan, W. Zhang, N. Ming, and P. Sheng, *Three-dimensional self-assembly of metal nanoparticles: Possible photonic crystal with a complete gap below the plasma frequency*, Phys. Rev. B **64**, 113108 (2001).

[161] E. Palik, *Handbook of Optical Constants of Solids*, Academic, New York, 1985.

[162] A. R. Williams and J. v.-W. Morgan, *Multiple scattering by non-muffin-tin potentials: general formulation*, Journal of Physics C: Solid State Physics **7**, 37 (1974).

[163] W. H. Butler, A. Gonis, and X. G. Zhang, *Multiple-Scattering Theory for Space-Filling Cell Potentials*, Phys. Rev. B **45**, 11527 (1992).

[164] W. H. Butler, A. Gonis, and X. G. Zhang, *Basis Functions for Arbitrary Cells in Multiple-Scattering Theory*, Phys. Rev. B **48**, 2118 (1993).

[165] K. Busch and S. John, *Photonic band gap formation in certain self-organizing systems*, Phys. Rev. E **58**, 3896 (1998).

[166] H. Míguez, F. Meseguer, C. López, A. Blanco, J. S. Moya, J. Requena, A. Mifsud, and V. Fornés, *Control of the photonic crystal properties of fcc-packed submicrometer SiO2 spheres by sintering*, Adv. Mater. **10**, 480 (1998).

[167] A. van Blaaderen and P. Wiltzius, *Real-Space Structure of Colloidal Hard-Sphere Glasses*, Science **270**, 1177 (1995).

[168] P. R. ten Wolde, M. J. Ruiz-Montero, and D. Frenkel, *Numerical calculation of the rate of crystal nucleation in a Lennard-Jones system at moderate undercooling*, J. Chem. Phys. **104**, 9932 (1996).

[169] S. Auer and D. Frenkel, *Prediction of absolute crystal-nucleation rate in hard-sphere colloids*, Nature **409**, 1020 (2001).

[170] S. Auer and D. Frenkel, *Numerical simulation of crystal nucleation in colloids*, in *Advanced Computer Simulation Approaches for Soft Matter Sciences I*, volume 173 of *Advances in Polymer Science*, pages 149–208, 2005.

[171] P. N. Pusey, W. Van Megen, P. Bartlett, B. J. Ackerson, J. G. Rarity, and S. M. Underwood, *Structure of Crystals of Hard Colloidal Spheres*, Phys. Rev. Lett. **63**, 2753 (1989).

[172] J. Zhu, M. Li, R. Rogers, W. Meyer, R. H. Ottewill, S.-. S. S. Crew, W. B. Russel, and P. M. Chaikin, *Crystallization of hard-sphere colloids in microgravity*, Nature **387**, 883 (1997).

[173] U. Gasser, E. R. Weeks, A. Schofield, P. N. Pusey, and D. A. Weitz, *Real-space imaging of nucleation and growth in colloidal crystallization*, Science **292**, 258 (2001).

[174] S. Auer and D. Frenkel, *Line tension controls wall-induced crystal nucleation in hard-sphere colloids*, Phys. Rev. Lett. **91**, 015703 (2003).

[175] M. Dijkstra, *Capillary freezing or complete wetting of hard spheres in a planar hard slit?*, Phys. Rev. Lett. **93**, 108303 (2004).

[176] A. Cacciuto, S. Auer, and D. Frenkel, *Onset of heterogeneous crystal nucleation in colloidal suspensions*, Nature **428**, 404 (2004).

[177] V. W. A. de Villeneuve, R. P. A. Dullens, D. Aarts, E. Groeneveld, J. H. Scherff, W. K. Kegel, and H. N. W. Lekkerkerker, *Colloidal hard-sphere crystal growth frustrated by large spherical impurities*, Science **309**, 1231 (2005).

[178] D. L. J. Vossen, *Optical Tweezers in concentrated colloidal dispersions*, PhD thesis, Utrecht University, 2004.

[179] U. M. B. Marconi and P. Tarazona, *Dynamic density functional theory of fluids*, J. Chem. Phys. **110**, 8032 (1999).

[180] U. M. B. Marconi and P. Tarazona, *Dynamic density functional theory of fluids*, J. Phys.: Condens. Matter **12**, 413 (2000).

[181] S. van Teeffelen, C. N. Likos, and H. Löwen, *Colloidal crystal growth at externally imposed nucleation clusters*, Phys. Rev. Lett. **100**, 108302 (2008).

[182] A. van Blaaderen, J. P. Hoogenboom, D. L. J. Vossen, A. Yethiraj, A. van der Horst, K. Visscher, and M. Dogterom, *Colloidal epitaxy: Playing with the boundary conditions of colloidal crystallization*, Faraday Discuss. **123**, 107 (2003).

[183] R. C. Hayward, D. A. Saville, and I. A. Aksay, *Electrophoretic assembly of colloidal crystals with optically tunable micropatterns*, Nature **404**, 56 (2000).

[184] M. E. Leunissen, H. R. Vutukuri, and A. van Blaaderen, *Directing colloidal self-assembly with biaxial electric fields*, Submitted (2008).

[185] C. Murray, *Experimental studies of melting and hexatic order in two-dimensional colloidal suspensions*, in *Bond-orientational order in condensed matter systems*, edited by K. Strandburg, pages 137–215, Springer-Verlag, New York, 1992.

[186] J. A. Weiss, D. W. Oxtoby, D. G. Grier, and C. A. Murray, *Martensitic Transition in a Confined Colloidal Suspension*, J. Chem. Phys. **103**, 1180 (1995).

[187] V. W. A. de Villeneuve, L. Derendorp, D. Verboekend, E. C. M. Vermolen, W. K. Kegel, H. N. W. Lekkerkerker, and R. P. A. Dullens, *Grain boundary pinning in doped hard sphere crystals*, Submitted (2008).

[188] V. N. Astratov, A. M. Adawi, S. Fricker, M. S. Skolnick, D. M. Whittaker, and P. N. Pusey, *Interplay of order and disorder in the optical properties of opal photonic crystals*, Phys. Rev. B **66**, 165215 (2002).

[189] R. Rengarajan, D. Mittleman, C. Rich, and V. Colvin, *Effect of disorder on the optical properties of colloidal crystals*, Phys. Rev. E **71**, 016615 (2005).

[190] P. Jiang, J. F. Bertone, K. S. Hwang, and V. L. Colvin, *Single-crystal colloidal multilayers of controlled thickness*, Chemistry of Materials **11**, 2132 (1999).

[191] S. H. Park and Y. N. Xia, *Assembly of mesoscale particles over large areas and its application in fabricating tunable optical filters*, Langmuir **15**, 266 (1999).

[192] K. Wostyn, Y. X. Zhao, B. Yee, K. Clays, A. Persoons, G. de Schaetzen, and L. Hellemans, *Optical properties and orientation of arrays of polystyrene spheres deposited using convective self-assembly*, J. Chem. Phys. **118**, 10752 (2003).

[193] R. M. Amos, J. G. Rarity, P. R. Tapster, T. J. Shepherd, and S. C. Kitson, *Fabrication of large-area face-centered-cubic hard-sphere colloidal crystals by shear alignment*, Phys. Rev. E **61**, 2929 (2000).

[194] T. Sawada, Y. Suzuki, A. Toyotama, and N. Iyi, *Quick fabrication of gigantic single-crystalline colloidal crystals for photonic crystal applications*, Japanese Journal of Applied Physics Part 2-Letters **40**, 1226 (2001).

[195] J. P. Hoogenboom, C. Retif, E. de Bres, M. V. de Boer, A. K. van Langen-Suurling, J. Romijn, and A. van Blaaderen, *Template-induced growth of close-packed and non-close-packed colloidal crystals during solvent evaporation*, Nano Lett. **4**, 205 (2004).

[196] C. J. Jin, M. A. McLachlan, D. W. McComb, R. M. De La Rue, and N. P. Johnson, *Template-assisted growth of nominally cubic (100)-oriented three-dimensional crack-free photonic crystals*, Nano Lett. **5**, 2646 (2005).

[197] Y. A. Vlasov, V. N. Astratov, A. V. Baryshev, A. A. Kaplyanskii, O. Z. Karimov, and M. F. Limonov, *Manifestation of intrinsic defects in optical properties of self-organized opal photonic crystals*, Phys. Rev. E **61**, 5784 (2000).

[198] V. Yannopapas, N. Stefanou, and A. Modinos, *Effect of stacking faults on the optical properties of inverted opals*, Phys. Rev. Lett. **86**, 4811 (2001).

[199] L. Teh, N. Tan, C. Wong, and S. Li, *Growth imperfections in three-dimensional colloidal self-assembly*, Appl. Phys. A **81**, 1399 (2005).

[200] P. Pieranski, L. Strzelecki, and B. Pansu, *Thin Colloidal Crystals*, Phys. Rev. Lett. **50**, 900 (1983).

[201] S. Neser, C. Bechinger, P. Leiderer, and T. Palberg, *Finite-Size Effects on the Closest Packing of Hard Spheres*, Phys. Rev. Lett. **79**, 2348 (1997).

[202] A. B. Fontecha, H. J. Schope, H. Konig, T. Palberg, R. Messina, and H. Löwen, *A comparative study on the phase behaviour of highly charged colloidal spheres in a confining wedge geometry*, J. Phys.: Condens. Matter **17**, 2779 (2005).

[203] A. Fortini and M. Dijkstra, *Phase behaviour of hard spheres confined between parallel hard plates: manipulation of colloidal crystal structures by confinement*, J. Phys.: Condens. Matter **18**, 371 (2006).

[204] M. Ishii, M. Harada, and H. Nakamura, *In situ observations of the self-assembling process of colloidal crystalline arrays*, Soft Matter **3**, 872 (2007).

[205] M. Qi, E. Lidorikis, P. T. Rakich, S. G. Johnson, J. D. Joannopoulos, E. P. Ippen, and H. I. Smith, *A three-dimensional optical photonic crystal with designed point defects*, Nature **429**, 538 (2004).

[206] T. Ruhl, P. Spahn, H. Winkler, and G. P. Hellmann, *Large Area Monodomain Order in Colloidal Crystals*, Macromol. Chem. Phys. **205**, 1385 (2004).

[207] W. J. Li, T. Fu, and S. L. He, *Preparation of free-standing silica 3D colloidal crystal film at water-air interface*, Materials Science and Engineering a-Structural Materials Properties Microstructure and Processing **441**, 239 (2006).

[208] H. Hasimoto, *On the periodic fundamental solutions of the Stokes equations and their application to viscous flow past a cubic array of spheres*, J. Fluid. Mech. **5**, 317 (1959).

[209] K. Ishii, *Viscous Flow pas Multiple Planar Arrays of Small Spheres*, J. Phys. Soc. Jpn. **46**, 675 (1978).

[210] A. S. Sangani and A. Acrivos, *Slow flow through a periodic array of spheres*, Int. J. Multiphase Flow **8**, 343 (1982).

[211] A. Zick and G. Homsy, *Stokes flow through periodic arrays of spheres*, J. Fluid. Mech. **115**, 13 (1982).

[212] A. Hurd, N. Clark, R. Mockler, and W. O'Sullivan, *Friction factors for a lattice of Brownian particles*, J. Fluid. Mech. **153**, 401 (1985).

[213] J. T. Padding and A. A. Louis, *Hydrodynamic interactions and Brownian forces in colloidal suspensions: Coarse-graining over time and length scales*, Phys. Rev. E **74**, 031402 (2006).

[214] B. J. Ackerson, *Shear Induced Order of Hard-Sphere Suspensions*, J. Phys.: Condens. Matter **2**, 389 (1990).

# Summary

The colloidal particles that are studied in this thesis are solid spheres with a diameter of approximately a micrometer. These spheres, when dispersed in a fluid, behave in a thermodynamically similar way as atoms and molecules: at low concentrations they form a fluid phase, while at high concentrations they can crystallize into a colloidal crystal to gain entropy. The analogy with molecular crystallization combined with the easy access to real-space data (because of longer time and length scales as compared to molecules), makes this system ideal for studying crystallization and nucleation processes. Furthermore, colloidal crystals are studied because of their applicability in new developing technologies based on light: the length scale of the periodically varying refractive index in the crystals is of the same order as the wavelength of visible light, giving the possibility to open up an optical band gap, similar to the energy band gap in semiconductors. Whether or not a photonic band gap opens depends sensitively on the crystal lattice, the refractive index contrast and the quality of the colloidal crystals. Increased control over crystallization and nucleation processes involved in the self-assembly of a crystal, can increase the tunability of the colloidal crystals and therefore increase the possibilities for producing photonic crystals.

In **Chapter 1**, a general introduction is given on colloids and the crystals that they can form. A large section of the chapter is dedicated to photonic crystals and photonic band structure calculations. The end of the chapter focuses on binary colloidal crystals, which consist of two types of colloids and give new options for opening up a photonic band gap.

In **Chapter 2**, a few methods are introduced which can be used to manipulate colloidal crystallization. The sedimentation behavior of colloids can be influenced by a structured bottom surface, dictating the orientation and lattice of the crystal that grows on top by so called epitaxial growth. Several methods are described which can be used to structure the surface at a micrometer scale.

Nucleation in the bulk of a sample can be induced by a small seed structure of tracer particles, trapped by optical tweezers: a strongly focused laser beam that catches optically dense particles by the gradient of its light field. The theory of optical trapping and the setup of the optical tweezers are described in this chapter.

Compression by dielectrophoretic forces is used throughout this thesis to increase the volume fraction of colloidal dispersions, to induce crystallization. This technique uses a similar gradient field as optical tweezers.

The last technique is spin coating, which is used in several experiments described in this thesis. The colloidal dispersion is deposited on a fast spinning disc, where most of the fluid is spun off or evaporates, leaving a radially aligned colloidal crystal. This very

fast method for creating colloidal crystals is discussed at the end of this chapter.

The colloidal NaCl structure is a binary colloidal crystal with potential for photonic applications, as is shown in **Chapter 3**. Colloidal crystals with a NaCl structure were fabricated by combining several external fields (sedimentation, epitaxial growth, electric fields and dielectrophoresis) to optimize the quality and stacking of the crystals. The crystals were studied by confocal microscopy, revealing stress-induced defects at places where the epitaxial template did not match the lattice parameters of the equilibrium crystal structure. We were able to dry the NaCl crystals, which facilitated further processing for photonic applications and gave the opportunity to study the crystals by scanning electron microscopy.

A second binary colloidal crystal, with the structure of the Laves phase $MgCu_2$, is the focus of **Chapter 4**. This colloidal crystal structure consists of large spheres on a diamond lattice and slightly smaller spheres on a pyrochlore lattice. Both of these single-component lattices are good candidates for opening up a photonic band gap. The stability of the colloidal Laves phases was studied by simulations. It was found that the three binary Laves phases are stable in a large area of the phase diagram. However, the free energy difference between the three structures is very small, so all three will coexist in a dispersion. Therefore, an epitaxial growth procedure was designed for selectively growing only the $MgCu_2$ structure. In the second half of the chapter, the results are presented of experiments on several colloidal systems with size ratios in the range where the Laves structures were found to be stable. In these experiments the separation of these binary systems under several forms of shear and flow was observed.

In **Chapter 5**, photonic band structure calculations are discussed on the binary Laves structures and their single component constituents. Two methods to calculate band structures are compared and their convergence is discussed. Band structures of the metallodielectric diamond and pyrochlore structures (with a metal core or a metal shell) yielded large photonic band gaps.

The study of nucleation in the bulk of a dispersion is presented in **Chapter 6**. Optical tweezers were used to fix a seed structure of tracer particles in the bulk of the host dispersion. This induced nucleation of the host dispersion at the seed structure. The host particles were unaffected by the laser because of the refractive index matching solvent. Using confocal microscopy, the effect of the seed structure on the host dispersion could be studied for different symmetries and lattice spacings of the seed structure. The volume fraction of the dispersion could be changed in situ by dielectrophoretic compression.

Dielectrophoretic compression is also the main manipulation technique used in **Chapter 7**. A method is presented to fabricate large single-domain colloidal crystals by epitaxial growth on a small templated bottom surface. Dielectrophoretic forces were deployed for pushing the epitaxially grown crystal forward, to be able to continually grow colloidal crystals of an orientation defined by the template. By confocal microscopy, similar stress-induced defects were found as in the growth of NaCl crystals by epitaxial growth.

In the last chapter, **Chapter 8**, we tried to unravel the mechanism of colloidal crystal formation by spin coating colloidal dispersions in volatile media. It was found before that this process could yield face centered cubic crystals with two different orientations. Because the fabrication process is very fast, in situ study of the crystallization mechanism was impossible. Instead, we based our conclusions on the structure of the end product, while varying the spin speed and the initial volume fraction. The structure was studied by visual inspection of white light diffraction, by laser diffraction and in real-space by scanning electron microscopy and confocal microscopy. These observations point towards the spin-up acceleration as the main parameter that determines the orientation of the crystals. The reflectivity of the spin coated crystals was measured by Fourier transform infra-red spectroscopy and compared with calculations using the Korringa-Kohn-Rostoker method. Further, the possibility of incorporating point defects in the structure for creating a photonic defect state in the Bragg peak was investigated.

# Samenvatting

De colloïdale deeltjes die bestudeerd worden in dit proefschrift zijn massieve bolletjes met een diameter van ongeveer een micrometer. Deze bolletjes gedragen zich, wanneer ze gedispergeerd zijn in een vloeistof, thermodynamisch analoog aan atomen en moleculen: bij lage concentraties vormen ze een vloeistof-fase, terwijl ze bij hoge concentraties kunnen kristalliseren tot een colloïdaal kristal om entropie te winnen. De analogie met moleculaire kristallisatie, gecombineerd met het feit dat colloïden makkelijker rechtstreeks te bestuderen zijn (vanwege de langere tijd- en lengteschalen dan bij moleculen), maakt dit systeem ideaal voor het bestuderen van kristallisatie- en nucleatieprocessen. Bovendien worden colloïdale kristallen bestudeerd vanwege hun toepasbaarheid in nieuwe technologieën gebaseerd op licht: de lengteschaal van de periodiek variërende brekingsindex in de kristallen is van dezelfde orde van grootte als de golflengte van zichtbaar licht. Dit geeft de mogelijkheid tot het openen van een fotonische band gap, analoog aan de energetische band gap in halfgeleiders. Of een band gap opent hangt sterk af van het kristalrooster, het brekingsindex-contrast en de kwaliteit van de colloïdale kristallen. Meer controle over de kristallisatie- en nucleatieprocessen, die een rol spelen in de zelf-organisatie van een kristal, kan de kans vergroten dat een fotonische band gap opent in een colloïdaal kristal.

In **Hoofstuk 1** wordt een algemene introductie gegeven over colloïden en de kristallen die zij kunnen vormen. Een groot deel van het hoofdstuk is gewijd aan fotonische kristallen en berekeningen van fotonische bandenstructuren. Het eind van het hoofdstuk richt zich op binaire colloïdale kristallen, die uit twee soorten colloïdale deeltjes bestaan en die nieuwe mogelijkheden scheppen voor het openen van een fotonische band gap.

In **Hoofdstuk 2** worden een paar methodes geïntroduceerd die kunnen worden gebruikt voor de beïnvloeding van colloïdale kristallisatie. Het sedimentatiegedrag van colloïden kan worden beïnvloed door een gestructureerd bodemoppervlak, dat de oriëntatie en het kristalrooster bepaalt van het kristal dat er bovenop groeit. Dit wordt epitaxiale groei genoemd. Verschillende methodes worden beschreven om een structuur op micrometer-schaal te maken op een oppervlak.

Nucleatie in het midden van een dispersie kan worden geïnduceerd door een kleine kiem van tracerdeeltjes vast te houden met optical tweezers (een optisch pincet): een sterk gefocusseerde laserstraal vangt de optisch dichte deeltjes in de gradiënt van het lichtveld. De theorie van het optisch trappen (vasthouden) en de opstelling van de optical tweezers worden in dit hoofdstuk beschreven.

Compressie door diëlectroforetische krachten wordt door heel dit proefschrift heen gebruikt voor het verhogen van de volumefractie van de colloïdale dispersies om kristallisatie te induceren. Bij deze techniek wordt ook een veldgradiënt gebruikt, net als bij optical tweezers.

De laatste techniek is spincoaten, een techniek die gebruikt is in verschillende experimenten in dit proefschrift. Een colloïdale dispersie wordt opgebracht op een snel ronddraaiende schijf, waarna het grootste gedeelte van de vloeistof eraf gespind wordt of verdampt. Hierbij vormt een radieel uitgelijnd colloïdaal kristal. Deze zeer snelle methode voor het maken van colloïdale kristallen wordt besproken aan het eind van dit hoofdstuk.

De colloïdale NaCl structuur is een binair kristal dat veelbelovend is voor fotonische toepassingen, zoals aangetoond wordt in **Hoofdstuk 3**. Colloïdale kristallen met een NaCl-structuur zijn gefabriceerd door de combinatie van verschillende externe velden (sedimentatie, epitaxiale groei, electrische velden en diëlectroforese) om de kwaliteit van de kristallen en de stapelingsvolgorde van de lagen te optimaliseren. De kristallen zijn bestudeerd met confocale microscopie, waarbij stress-geïnduceerde defecten aan het licht kwamen op plaatsen waar de roosterparameters van de epitaxiale structuur op de bodem niet overeenkwam met de roosterparameters van het evenwichtskristal. Het is gelukt om de NaCl-kristallen te drogen, wat de verdere verwerking voor fotonische toepassing vergemakkelijkt. Bovendien gaf dit de mogelijkheid om de kristallen te bestuderen met scanning electronenmicroscopie.

Een tweede binair colloïdaal kristal, met de structuur van de Laves fase $MgCu_2$, is het onderwerp van **Hoofdstuk 4**. Dit colloïdaal kristal bestaat uit grotere bollen op een diamantrooster en enigszins kleinere bollen op een pyrochloorrooster. De kristalroosters van beide aparte componenten zijn geschikt om een fotonische band gap te openen. De stabiliteit van de colloïdale Laves fasen is bestudeerd met simulaties. Er is gevonden dat de drie binaire Laves fasen stabiel zijn in een groot parametergebied. Het vrije-energieverschil tussen de drie structuren is echter zeer klein, dus zullen deze drie tegelijk in een dispersie voorkomen. Daarom is een procedure ontworpen, gebaseerd op epitaxiale groei, om selectief de $MgCu_2$-structuur te groeien. In de tweede helft van dit hoofdstuk worden de resultaten gepresenteerd van de experimenten aan verschillende colloïdale systemen die een grootteverhouding hadden waarvan gevonden was dat de Laves structuren daarbij stabiel zijn. In deze experimenten werd waargenomen dat de binaire systemen scheidden onder invloed van verschillende vormen van shear (afschuifstroming) en stroming.

In **Hoofdstuk 5** worden de fotonische bandenstructuurberekeningen besproken van de binaire Laves structuren en van de structuren van hun aparte componenten. Twee methodes voor het berekenen van fotonische bandenstructuren worden vergeleken en hun convergentie wordt bediscussieerd. Uit de bandenstructuren van de metallodiëlectrische diamant- en pyrochloorstructuren (met een metalen kern of een metalen schil) bleek dat deze structuren grote fotonische band gaps hebben.

De studie van nucleatie in het midden van de dispersie is uiteengezet in **Hoofdstuk 6**. Optical tweezers zijn gebruikt voor het fixeren van een kiem van tracerdeeltjes in het midden van de gastdispersie. Dit induceerde nucleatie van de dispersie op de kiemstructuur. De gastdeeltjes werden niet beïnvloed door de laser doordat het dispersiemedium dezelfde brekingsindex had als deze deeltjes. Het effect van de kiem op de gastdispersie kon bestudeerd worden met confocale microscopie voor verschillende symmetrieën en voor verschillende roosterafstanden van de kiem. De volumefractie van de dispersie kon tegelijkertijd veranderd worden met diëlectroforetische compressie.

Diëlectroforetische compressie is ook de voornaamste techniek voor beïnvloeding van de kristallisatie in **Hoofdstuk 7**. Hier wordt een methode gepresenteerd voor het fabriceren van grote één-kristallen door epitaxiale groei op een klein structuurtje op het bodemoppervlak. Diëlectroforetische krachten werden ingezet om de epitaxiaal gegroeide kristallen voort te duwen, zodat een colloïdaal kristal met een door de bodemstructuur gedefinieerde oriëntatie continu kon groeien. Met confocale microscopie zijn vergelijkbare stress-geïnduceerde defecten gevonden als bij de epitaxiale groei van NaCl-kristallen.

In het laatste hoofstuk, **Hoofdstuk 8**, is getracht om het mechanisme van kristalformatie door het spincoaten van een colloïdale dispersie in een vluchtig medium te ontrafelen. Eerder is aangetoond dat dit proces vlakkengecentreerde kubische kristallen oplevert met twee verschillende oriëntaties. Vanwege het feit dat het spincoatingproces erg snel verloopt, is in-situ studie van het kristallisatiemechanisme niet mogelijk. Daarom baseerden we onze conclusies op de structuur van het eindproduct, voor verschillende waarden van de spinsnelheid en van de initiële volumefractie. De structuur is bestudeerd door visuele inspectie van wit-lichtdiffractie, door laserdiffractie en rechtstreeks door scanning electronenmicroscopie en confocale microscopie. Uit deze observaties kon geconcludeerd worden dat de opspinversnelling de parameter is, die de oriëntatie van de kristallen het meest beïnvloedt. De reflectie van de spincoatkristallen is gemeten met Fourier transform infra-rood spectroscopie en dit is vergeleken met berekeningen volgens de Korringa-Kohn-Rostoker methode. Verder is de mogelijkheid bekeken om puntdefecten in de kristalstructuur op te nemen om een fotonische defect-toestand te creëren.

# Dankwoord

De afgelopen vier jaar zijn echt heel erg snel gegaan! Maar als ik terugdenk dan blijken er toch heel veel mensen mijn pad te zijn gekruist die allemaal direct of indirect hun steentje hebben bijgedragen aan mijn promotieonderzoek. In deze laatste paar pagina's van mijn proefschrift wil ik deze mensen graag bedanken.

Allereerst wil ik Alfons van Blaaderen bedanken, die als promotor en dagelijks begeleider de grootste rol heeft gespeeld bij de totstandkoming van dit proefschrift. Jouw enthousiasme en jouw onuitputtelijke verzameling nieuwe ideeën hebben mij erg geïnspireerd en gestimuleerd in de afgelopen jaren. De gesprekken met jou gaven altijd iets meer informatie en opties voor nieuwe experimenten dan waar ik vooraf op gehoopt had. Maar dat gaf me dan tegelijkertijd ook de vrijheid om daarin mijn eigen weg te zoeken. Bedankt voor alle mogelijkheden die je mij hebt gegeven.

Tijdens deze 4 jaar heb ik heel wat kamergenoten versleten. Paddy Royall, Andrew Campbell, Joan Penninkhof, Patrick Johnson, Zuocheng Zhou, Daisuke Nagao, and Peter van Oostrum, thank you for introducing me to all the things I needed to know to survive here and thanks for the good company in our office! Peter heeft het nog het langste uitgehouden met mij. Peter, bedankt voor alle nuttige discussies en natuurlijk ook voor vele minder nuttige gesprekken die we de afgelopen jaren gevoerd hebben. En natuurlijk bedankt voor de fijne samenwerking zowel in New York als hier in Utrecht.

Astrid van der Horst en Dirk Vossen hebben mij in het begin ingewerkt op de tweezeropstelling en ze hebben me op weg geholpen met mijn eerste experimenten, allebei heel erg bedankt hiervoor! Ook Jacob Hoogenboom heeft mij een heel eind op weg geholpen met het maken van de templates, al heeft het nog een hele tijd geduurd voordat alles precies werkte zoals ik wilde. Jacob, bedankt voor de hulp aan het begin van mijn promotie, maar ook voor alle discussies dit jaar, nu je weer tijdelijk terug bent. Chris Rétif heeft mij op Amolf erg geholpen bij het maken van templates met e-beam lithografie, bedankt hiervoor!

Arnout Imhof en Marjolein Dijkstra wil ik bedanken voor verschillende fijne samenwerkingen en discussies gedurende de afgelopen jaren. Jullie vaste aanwezigheid heeft een hele goede invloed op de (werk- en sociale) sfeer in de groep. Dit laatste geldt zeker ook voor Carlos van Kats. Carlos, ik zou niet weten hoe het lab er uit zou zien zonder al jouw kennis over syntheses en over waar alles ligt in het lab of over waar het anders wel te verkrijgen is. Hoeveel mensen ik in de afgelopen jaren wel niet doorverwezen heb met de mededeling "Ik weet zeker dat Carlos dat wel weet"... (sorry hiervoor ;-) María Delgado Flores wil ik natuurlijk bedanken voor de secretariële ondersteuning van de groep, maar vooral ook voor de vele gezellige gesprekken.

Job Thijssen, ook jou wil ik bedanken voor een hele prettige samenwerking, voornamelijk op het gebied van de fotonische berekeningen. Jouw precieze en grondige werkwijze zal ik nooit kunnen evenaren, maar ik zal toch af en toe proberen om een klein beetje in de buurt te komen. Ook wil ik je bedanken voor de hulp met scattering- en FITR-experimenten en het onderhoud van de confocale microscopen.

Also Alexander Moroz has helped me a lot with the photonic calculations, first of all by providing his KKR-code and but also by his feedback during the years. Alexander, thank you for your help.

Antti-Pekka Hynninen, thank you for the nice cooperation on the binary Laves structures. And sorry for the fact that my experimental Laves structures were forming quite a bit slower than your simulated ones (or even did not form at all up till now).

I want to thank the people of the Center for Soft Matter Research van NYU for the opportunity to spend some time in the lab at New York University at the beginning of 2007.

Michiel Hermes, ik wil jou graag bedanken voor je experimentele en computertechnische hulp, je simulaties en alle discussies die we in de afgelopen tijd gevoerd hebben.

Laura Filion, ik wil jou graag bedanken (en dat kan nu best in het Nederlands :) voor de berekeningen, de discussies over binaire kristallen en natuurlijk voor de lekkere “suppers”.

Yu Ling Wu wil ik graag bedanken voor de uitleg van het spincoaten, de demonstratie van het polymeriseren van “haar” monomeer (o ja, en die van Job) en voor de hulp met het shearen, zowel met de hand als met de Hippos. En natuurlijk ook voor de gezellige etentjes, samen met Rianne van Eerd. Rianne kende ik al uit Nijmegen en eigenlijk ben ik via haar tip, via Yu Ling en met de aanbevelingen van Mirjam tussen de colloïden terecht gekomen. Yu Ling en Rianne, allebei bedankt voor de gezellige tijd!

De meest opmerkzame samenwerking was toch wel met Mirjam Leunissen. Ik kende je natuurlijk al uit Nijmegen, dus ik wist al wel een beetje wat ik kon verwachten. Maar toch heb ik verschillende keren versteld gestaan van je aanstekelijk enthousiaste werkhouding en je experiment-vullende repertoire van (enigzins commercieel ingestelde) liedjes in het lab. Onze zangrepertoires overlapten helaas alleen op het nummer "er is nog kaas", maar dat mocht de zangpret niet drukken. Bedankt voor de vele dagen die we samen al tweezerend gevuld hebben!

Verder wil ik alle studenten met wie ik samengewerkt heb bedanken: Leonie, Gerben, Rianne, Floor en Thomas, het was leuk om jullie te mogen begeleiden!

Ook was het erg prettig te kunnen samenwerken met onze collega’s in de Fysische en Colloïd Chemie groep. Ik heb veel geleerd uit lezingen van en discussies met verschillende mensen in deze groep en ik wil alle fcc-ers hiervoor bedanken. Het meest heb ik samengewerkt met Volkert de Villeneuve, met wie ik samen een grote bol probeerde te tweezeren in een zee van kleintjes. We hebben de kleintjes er niet helemaal van weten te overtuigen om zich niets aan te trekken van de laser, maar ik vond het wel prettig om met je samen te werken, bedankt!

Náást het werk heb ik ook heel wat beleefd met allerlei collega’s. Ik herinner me barbecues aan de Lek, in tuinen en op dakterrassen, een etentje aan de Oude Gracht (met surrealistische zangers op een boot) en in het Wilhelminapark, volleybaltoernooien (al dan niet in het donker), vele borrels, concerten, balletten, wandelen in Han-sur-Lesse, kanoën, wadlopen, boerengolven, Sinterklaassurprises en -gedichten, schaatsen, zwemmen en als hoogtepunten (in meters) het skiën in Oostenrijk, en het kamperen en wandelen op Corsica. Ahmet, Albert, Alejandro, Alessandro, Andrea, Andrei, Anke, Ben, Carmen, Chantal, Catherine, Christina, Daniela, Dannis, Didi, Dirk, Eduardo, Eelco, Esther, Emanuela, Floor, Frank, Gulşen, Henk, Jamal, Jan, Johan, Jos, Lia, Lucas, Marjolein, Marlous, Matthieu, Maurice, Menno, Myrthe, Niels, Peter, Rao, René, Rob, Roel, Sandra, Slava, Stéphane, Teun, Wessel, Willem and everyone I mentioned before and everyone I accidently forgot, thank you for all your help and the "gezelligheid", both during working hours and outside!

Mijn familie en vrienden hebben dan misschien wel niet rechtstreeks een bijdrage geleverd aan het onderzoek dat in dit boekje wordt gepresenteerd, maar zonder hun steun en gezelschap zou ik niet zo'n fijne tijd hebben gehad. Femke, Tom en Marieke, in alle lange email-conversaties met onzinnige subjects heb ik veel blijdschap en frustraties kunnen uiten, dankjewel voor jullie "luisterend oor". In de afgelopen twee jaar heb ik heel wat energie kwijt gekund bij de gezellige trainingen (en andere activiteiten) van de schaatsvereniging Softijs, bedankt hiervoor! Via Softijs heb ik ook Rogier ontmoet. Rogier, dankjewel voor je steun en liefde in het afgelopen jaar en hopelijk gaan er nog vele jaren samen volgen. Tenslotte wil ik mijn hele familie bedanken. Jullie zijn al het langst in mijn leven en hebben mij altijd onvoorwaardelijk gesteund. Lieve papa, mama en Sander, dankjewel voor alles wat jullie voor mij doen en betekenen.

# Curriculum Vitae

Esther Christianne Maria Vermolen was born on April 14$^{\text{th}}$ 1982 in Arnhem, the Netherlands. In 1999 she obtained the Gymnasium degree at the secondary school Nederrijn College in Arnhem (later renamed to Olympus College).

In September 1999 she started her chemistry studies at the University of Nijmegen (later renamed to Radboud University). She received her first-year diploma (propedeuse) of chemistry in August 2000 (cum laude). During her second year, she also started physics courses, after which she finished the first year of physics in August 2002 (cum laude). Her B.Sc. research project was performed in the Solid State Chemistry group at the University of Nijmegen, with the title *Investigation of growth spirals on crystals of potassium hydrogen phthalate using atomic force microscopy.* She obtained her B.Sc. diploma in September 2003 (cum laude).

For her M.Sc. degree, she performed two minor researches (both half a year), one at the Solid State Chemistry group at the University of Nijmegen, entitled *Molecular modelling study of epitaxial growth of anthraquinone on NaCl using GULP, GDIS and Monty* and one at the Experimental Solid State Physics II group at the University of Nijmegen, entitled *Second harmonic generation study of surface phenomena in liquid crystal displays.* During this project she had the opportunity to present part of this work in an oral presentation at the OLC 2003, the 10th International topical meeting on optics of liquid crystals.

She performed her major M.Sc. research in the Solid State NMR group at the University of Nijmegen, of which a three month period was spent at the National Institute for Chemical and Biological Physics in Tallinn, Estonia. The resulting thesis was entitled *Nutation NMR of quadrupole nuclei.* The literature thesis, also written in this group, was entitled *Quantum computing and the physical implementation using NMR.* In August 2004, she received her M.Sc. degree (cum laude).

During her chemistry studies, she was a teaching assistant for several undergraduate courses, she was an Account Manager for the “Bèta Bedrijven Beurs” (organization of company fairs) for two years and during the same period she was a member of the Symposium Committee of the Chemistry Student Association “Sigma”, of which one year as chairman.

In 2004 she started her PhD-project in the Soft Condensed Matter group of Prof. Dr. Alfons van Blaaderen, which resulted in the work described in this thesis. During her PhD, she supervised several problem classes for undergraduate students and she was a member of the PhD committee of the Debye Institute for NanoMaterials Science. Part of the work described here was presented as oral presentations at

- SFB-TR6 Colloids in External Fields, Corsica (2006)
- Physics@FOM, Veldhoven (2008)
- Photonics 2008, Eindhoven
- 7th Liquid Matter Conference, Lund, Sweden (2008)

and at poster sessions of several national and international conferences.

# Publications

This thesis is partly based on the following publications:

- A.-P. Hynninen, J. H. J. Thijssen, E. C. M. Vermolen, M. Dijkstra, A. van Blaaderen, *Self-assembly route for photonic crystals with a bandgap in the visible region*, Nature Materials 6(3), 202 (2007)
- C. P. Royall, E. C. M. Vermolen, Alfons van Blaaderen, and Hajime Tanaka, *Controlling competition between crystallisation and glass formation in binary colloids with an external field*, Journal of Physics: Condensed Matter 20, 404225 (2008)
- E. C. M. Vermolen, A. Kuijk, M. Hermes, J. H. J. Thijssen, A. van Blaaderen, *Fabrication of large binary colloidal crystals with a NaCl-structure using a combination of external fields*, submitted (2008)
- E. C. M. Vermolen, J. H. J. Thijssen, A. van Blaaderen, A. Moroz, M. Megens, *Photonic band structure calculations for diamond and pyrochlore crystals*, submitted (2008)

Other publications:

- M. I. Boamfa, S. V. Lazarenko, E. C. M. Vermolen, A. Kirilyuk and T. Rasing, *Magnetic field alignment of liquid crystals for fast display applications*, Advanced Materials 17, 610 (2005)
- V. W. A. de Villeneuve, L. Derendorp, D. Verboekend, E. C. M. Vermolen, W. K. Kegel, H. N. W. Lekkerkerker and R. P. A. Dullens, *Grain boundary pinning in doped hard sphere crystals*, submitted (2008)